

*ÉCOLE DOCTORALE DES SCIENCES CHIMIQUES*

**CNRS 7199 Conception et Application de Molécules Bioactives**

# THÈSE

Présentée par :

**Mohamed Attia**

Soutenue le : Novembre 3, 2016

Pour obtenir le grade de

**Docteur de l'université de Strasbourg**

Discipline/ Spécialité : Chimie

**Agent de contraste à base de nano-émulsion pour  
l'imagerie biomédicale ciblée**

**THÈSE dirigée par :**

**Pr. VANDAMME Thierry**

Professeur, université de Strasbourg

**RAPPORTEURS :**

**Pr. BERG-BESTEL Isabelle**

Professeur, université de Bordeaux

**Dr. EDWARDS Florence**

Maître de Conférences - HDR, Institut de Chimie Moléculaire de Reims

---

**AUTRES MEMBRES DU JURY :**

**Dr. ANTON Nicolas**

Maître de conférences, université de Strasbourg



*This thesis is dedicated to  
my beloved*

*Father and Mother,*

*For sacrifices, endless love, encouragement and  
Patience make me able to get such success and honor*

*Brothers and sister*

*Who never allowed me to give up on the pursuit of my dream*

*Zhra*

*My lovely wife for her love, patience and understanding*

*Ammar*

*My little man who was my big gift that gives to my life another  
meaning and another hope*



# *Table of contents*

<b>Acknowledgment</b> .....	i
<b>Abbreviation</b> .....	iv
<b>Résumé de thèse</b> .....	viii
<b>Introduction of thesis</b> .....	1
<b>Chapter One</b> .....	10
<b>Chapter 1.1: Nano-emulsions for drug delivery and biomedical imaging</b> .....	11
Abstract .....	12
1. Introduction .....	13
2. Formulation processes .....	14
2.1. Generalities .....	14
2.2. High-pressure methods .....	15
2.3. Ultrasounds-based methods .....	16
2.4. Low-energy methods .....	17
3. Applications of nano-emulsions for drug delivery and biomedical imaging .....	19
3.1. Nano-emulsions as nanomedicines .....	19
3.2. Clinical applications of nano-emulsions .....	24
3.3. Nano-emulsions in biomedical imaging .....	27
3.3.1. <i>Nano-emulsions in X-ray imaging</i> .....	28
3.3.2. <i>Nano-emulsions in magnetic resonance imaging (MRI)</i> .....	28
3.3.3. <i>NEs as fluorescent probes in Fluorescent imaging</i> .....	30
3.3.4. <i>Nano-emulsions as multimodal imaging probes and theragnostics</i> .....	31
4. Conclusion .....	33
5. References .....	33
<b>Chapter 1.2: Biodistribution of X-Ray Iodinated Contrast Agent in Nano-Emulsions Is Controlled by the Chemical Nature of the Oily Core</b> .....	38
1. Abstract .....	39
2. Introduction .....	39
3. Results and Discussion .....	40
4. Conclusion .....	50
5. Experimental section .....	50
5.1. General Synthesis of Hexa-iodinated Monoglyceride and Hexa-iodinated Castor Oil ..	50
5.2. Characterization of Hexa-iodinated Monoglyceride and Hexa-iodinated Castor Oil ....	50
5.3. Preparation of Iodinated Nano-Emulsions .....	50
5.4. Characterization of Nano-Emulsions .....	50
5.5. In Vitro Mouse Macrophage Uptake .....	51
5.6. Micro-CT Imaging .....	51
6. References and notes .....	51
<b>Chapter 1.3: Biodistribution and Toxicity of X-Ray Iodinated Contrast Agent in Nano-emulsions in Function of Their Size</b> .....	54
1. Abstract .....	55
2. Introduction .....	56

3. Experimental section .....	57
3.1. Materials .....	57
3.2. Methods .....	57
3.2.1. <i>Synthesis and Characterization of Cholecalciferoyl 2,3,5-Triiodobenzoate</i> .....	57
3.2.2. <i>Formulation of Triiodinated Cholecalciferol Nano-Emulsions</i> .....	57
3.2.3. <i>Characterization of Nano-Emulsions by Dynamic Light Scattering (DLS)</i> .....	58
4. In Vitro Studies .....	58
4.1. Cell Culture .....	58
4.2. Stability of Nano-Emulsion Droplets in Serum .....	59
4.3. In Vitro Cytotoxicity (MTT-Assay) .....	59
4.4. Cellular Uptake Experiment .....	59
5. Micro-CT Imaging .....	59
5.1. In Vitro Experiments .....	59
5.2. In Vivo Experiments .....	59
6. Results and discussion .....	60
7. Conclusion .....	65
8. References .....	65
<b>Chapter Two</b> .....	68
<b><u>Chapter 2.1: Targeting agents conjugated to nano-carriers to increase drug efficiency</u></b> ....	69
1. Introduction .....	70
2. Nano-carriers as drug delivery systems (DDs) .....	71
3. Tumor-targeted drug delivery systems .....	73
3.1. Passive targeting .....	73
3.1.1. <i>Nano-carriers' characteristics affect passive targeting strategy</i> .....	74
3.2. Active targeting (Tuning surface functionality) .....	75
3.2.1. <i>Tumor cell targeting</i> .....	77
3.2.2. <i>Vascular targeting (Endothelial cells)</i> .....	78
3.2.3. <i>Targeting the mildly acidic tumor microenvironment</i> .....	79
3.2.4. <i>Nuclear targeting</i> .....	79
4. Examples of targeted nano-carriers .....	82
5. Expert opinion .....	84
6. References .....	85
<b><u>Chapter 2.2: Functionalizing nano-emulsions with carboxylate: impact on the biodistribution and pharmacokinetics on mice</u></b> Abstract .....	93
Abstract .....	95
Keywords .....	95
1. Introduction .....	96
2. Experimental section .....	98
2.1. Materials .....	98
2.2. Methods .....	98
2.2.1. <i>Axisymmetric drop shape analysis (ADSA)</i> .....	98

2.2.2.	<i>Formulation of carboxylate-decorated nano-emulsions</i>	99
2.2.3.	<i>Dynamic light scattering, <math>\zeta</math> potential measurements</i>	99
2.2.4.	<i>Cryo TEM preparations and observations</i>	99
2.2.5.	<i>Quantification of carboxylates available on the nanodroplets</i>	100
2.2.6.	<i>Synthesis and characterization of 2,4,6-triiodophenyl oleate</i>	100
2.2.7.	<i>NMR analysis</i>	100
2.2.8.	<i>Cell culture and in vitro studies</i>	101
2.2.9.	<i>Micro-CT Imaging</i>	101
2.2.9.1.	<i>In vitro experiments</i>	101
2.2.9.2.	<i>In vivo experiments</i>	101
3.	Results and discussion	102
3.1.	Surface tension study of the PMAO at the oil / water interface	102
3.2.	Formulation of nano-emulsions with PMAO	104
3.3.	Quantification of the carboxylate at the oil / water interface of nano-emulsion droplets	105
3.4.	In vitro studies	106
3.5.	In vivo imaging	108
4.	Conclusion	111
5.	Acknowledgments	112
6.	References	112
	<b>Supplementary part</b>	114
1.	The goal	115
2.	General method of preparation	115
3.	Results and discussion	115
3.1.	Hydrodynamic diameter	115
3.2.	Zeta potential	116
3.3.	Cellular uptake experiments	117
4.	Conclusion	118
	<b>Chapter 2.3: Functionalization of nano-emulsions with an amino- silica shell at the oil- water interface</b>	120
1.	Introduction	121
2.	Experimental section	122
2.1.	Materials	122
2.2.	Methods	122
2.2.1.	<i>Formulation of amino-decorated lipid nano-emulsions</i>	122
2.2.2.	<i>Quantification of primary amines available on the nano- capsules</i>	123
2.2.3.	<i>Grafting of activated coumarin blue (7-(diethylamino) coumarin-3-carboxylic acid N-succinimidyl ester dye) on primary amines decorating the nanocapsules</i>	123
2.2.4.	<i>Physicochemical characterization of nano-emulsions</i>	123
2.2.4.1.	<i>Transmission electron microscopy</i>	123
2.2.4.2.	<i>Fluorescence spectroscopy</i>	123

2.2.4.3.	<i>Fluorescence correlation spectroscopy (FCS)</i> .....	123
2.2.4.4.	<i>Atomic force microscopy coupled with fluorescence microscopy</i> .....	124
3.	Results and discussion .....	124
4.	Conclusion .....	128
5.	References .....	128
	<b>Chapter Three</b> .....	131
	<b><u>Chapter 3.1: Inorganic nanoparticles for micro CT imaging</u></b> .....	132
1.	Introduction .....	133
2.	General nanoparticulate systems for imaging purposes .....	134
3.	Stringent requirements for ideal imaging probes .....	136
4.	Biodistribution and pharmacokinetics of the developed CAs .....	137
5.	General steps in the formation of inorganic NPs .....	138
6.	AuNPs as a CT CA .....	139
6.1.	Synthesis of AuNPs .....	140
6.2.	Chemical and biochemical properties .....	143
6.2.1.	<i>Surface engineering of AuNPs, coating, and functionalization with ligands for active targeting</i> .....	143
6.3.	In vitro and in vivo studies (targeting) .....	146
7.	Gold-hybrid NPs .....	149
7.1.	Gold-iron hybrid NPs .....	149
7.2.	Gold-gadolinium hybrid NPs .....	152
7.3.	Gold-silica nanosystems and other hybrids .....	153
8.	Miscellaneous multifunctional CAs .....	154
9.	Silver-based CA .....	156
10.	Bismuth-Based Agents .....	157
11.	Platinum-based NPs .....	161
12.	MRI and optical imaging and their current inorganic NP-based CAs .....	161
12.1.	Inorganic NPs for MRI .....	161
12.2.	Quantum dots for optical imaging .....	156
13.	Lesser known elements and derivatives-based inorganic nanoparticulate CAs .....	167
13.1.	Thorium: a well-known efficient, but carcinogenic, colloidal X-ray CA .....	167
13.2.	Tantalum-based nanoparticulate and radiopaque CA .....	168
13.3.	Europium chelate-based NPs for magnetic and optical bioimaging .....	168
13.4.	Ytterbium lanthanide element for X-ray, optical imaging, and MRI .....	169
14.	Conclusion .....	169
15.	References .....	170
	<b><u>Chapter 3.2 : One-step synthesis of iron oxide polypyrrole nanoparticles encapsulating ketoprofen as model of hydrophobic drug</u></b> .....	185
1.	Introduction .....	186
2.	Experimental part .....	187
2.1.	Reagents and materials .....	187

2.2. Preparation of ketoprofen doped iron/PPy-PEG nanocomposites as drug delivery system .....	187
2.3. Infrared spectroscopy (IR) .....	188
2.4. Differential scanning calorimetry (DSC) .....	188
2.5. Transmission electron microscopy (TEM) .....	188
2.6. Scanning electron microscopy (SEM) .....	188
2.7. UV–vis absorption spectroscopy .....	188
2.8. Encapsulation efficiency (EE%) .....	188
2.9. In vitro release study .....	188
2.10. MRI experiments .....	188
3. Results and discussion .....	188
3.1. FTIR analysis .....	189
3.2. DSC characterization .....	189
3.3. Determination of the particle size and morphology of the NCs .....	191
3.3.1. <i>TEM characterization</i> .....	192
3.3.2. <i>SEM images</i> .....	192
3.4. Encapsulation efficiency of ketoprofen (EE) .....	193
3.5. In vitro release study .....	193
4. Conclusion .....	194
5. References .....	194
<b>Conclusion and perspectives</b> .....	197
<b>Appendices</b> .....	204



# *Acknowledgment*

Because this may be my only opportunity to thank these individuals in writing, I may be a bit more verbose in my thanks than necessary.

I wish to express my warmest gratitude to all those persons whose comments, questions, criticism, support and encouragement, personal and academic, have left a mark on this work. Regrettably, but inevitably, the following list of names will be incomplete, and I hope that those who are missing will forgive me, and will still accept my sincere appreciation of their influence on my work.

First and foremost I offer my deepest gratitude to my advisor, Professor Thierry Vandamme, for his continuous support and challenging throughout all my PhD study and research, for his patience, motivation, enthusiasm, and immense knowledge. His guidance helped me in all the time of research and writing of this thesis. His smart supervision made me to be independent and achieve my work professionally.

My sincere thanks and appreciation also goes to Dr. Nicolas Anton, co-advisor, for providing me the benefits of his own numerical experience. As well as writings and direct communication provided me to understand and enrich my ideas, continuous following up, proofreading and checking my dissertation and all publications. Nicolas has been always there to listen and give advice. I am deeply grateful to him for the long discussions that helped me sort out the technical details of my work. I am also thankful to him for encouraging the use of consistent notation in my writings and for carefully reading and commenting on countless revisions of all my published articles.

I wish to express my gratitude to my dissertation committee members, Professor Isabelle Berg-Bestel, Dr. Florence Edwards and Dr. Yves FRERE for their time and extreme patience.

I thank my fellow labmates in biogalenic group: Justine Wallyn, Thi Trinh Lan Nguyen, Shukai Ding, Salman Akram, Asad Urehman, and Sidy Muhammad, in addition to Minjie Zhao and Manuela Chiper for the stimulating discussions, and for all the fun we have had all the time, beside the respect and love between each other and interesting research collaboration.

Many thanks to our collaborators: Andrey klemchenko, Mayeul collot, Christophe Serra, I have appreciated their collaboration and the impressive work achieved together.

I also wish to thank those institutions, which have supported me to implement my PhD work, National Research Centre in Egypt, my home institution, University of Strasbourg (Faculty of Pharmacy in Illkirch, IGBMC institution in Illkirch, ICPEES institution in Cronenbourg) and University of Lyon.

In regards to the TEM and SEM facilities, I would like to thank Nadia Messadeque for her sincere and serious work and interest.

For in vivo experiments, I have to thank Caroline Bouillot at CERMEP, Lyon University and my colleague Alexandru Parlog at IGBMC institute, Strasbourg University for their professional work on animals.

I gratefully acknowledge the funding source that made my Ph.D. work possible. I was funded by ministry of higher education and Scientific research of Egypt that funded me during all my PhD years.

I have to acknowledge my friends in Strasbourg, Mohamad Kassem, Redouane Bouchaala, and Ali Ayadi for their permanent conduct, for love and fun, they were real friends. I hope this friendship to continue forever.

As long as I'm writing names down, I cannot neglect that of my best and most constant friends during all my undergraduate studies years, Samah Attia, Yosri Mahmoud, Ahmed Nawar, Abdalla Samir and Mohamed Alshorbagy.

Most importantly, none of this would have been possible without the love and patience of my family: my parents for their wise counsel and sympathetic ear and for supporting me spiritually throughout my life. My gratitude to them is beyond words.

My thanks extend to my brothers, sister, and other extended family for raising me with a love of science and supported me in all my pursuits.

And most of all for my loving, supportive, encouraging, and patient wife, Zhra and my son, Ammar whose faithful support during the final stages of this Ph.D. is so appreciated. They are the basic source of light granting me the happiness in my life. Thank you.

Mohamed Fathy Attia  
University of Strasbourg  
November 3, 2016

# *Abbreviations*

---

<b><math>^{13}\text{C}</math>-NMR</b>	Carbon nuclear magnetic resonance
<b><math>^1\text{H}</math>NMR</b>	Proton nuclear magnetic resonance
<b>Ab</b>	Antibody
<b>ADSA</b>	Axisymmetric drop shape analysis
<b>AFM-Fluo</b>	Atomic force microscopy coupled with fluorescence microscopy
<b>AgNPs</b>	Silver nanoparticles
<b>AK</b>	Actinic keratosis
<b>ALA</b>	Aminolaevulinic acid
<b>API</b>	Active pharmaceutical ingredients
<b>APTES</b>	Aminopropyltriethoxy silane
<b>APTMS</b>	3-(Aminopropyl) trimethoxysilane
<b>AuNPs</b>	Gold nanoparticles
<b>BF200 ALA</b>	BF200 aminolaevulinic acid
<b>BiGNPs</b>	Bismuth glyconanoparticles
<b>BPCA</b>	Blood pool contrast agent
<b>CB</b>	Coumarin blue dye
<b><math>\text{CDCl}_3</math></b>	Deuterated chloroform
<b>CDK</b>	Cyclin-dependent kinase
<b>CLSM</b>	Confocal laser scanning microscope
<b>CMC</b>	Critical micelle concentration
<b>CNR</b>	Contrast-to-noise ratio
<b>CNS</b>	Central nervous system
<b>CNTs</b>	Carbon nanotubes
<b>CT</b>	Computed tomography
<b>CTAB</b>	Cetyltrimethylammonium bromide
<b>DCC</b>	N,N'-Dicyclohexylcarbodiimide
<b>DDS</b>	Drug delivery system
<b>DEs</b>	Dendrimers
<b>DLS</b>	Dynamic light scattering
<b>DMAP</b>	4-Dimethylaminopyridine
<b>DMEM</b>	Dulbecco's modified Eagle medium
<b>DMF</b>	Dimethylformamide
<b>DMSO</b>	Dimethyl sulfoxide
<b>DOTA</b>	1,4,7,10-Tetraazacyclododecane-1,4,7,10-tetraacetic acid
<b>DOX</b>	Doxorubicin drug
<b>DSC</b>	Differential scanning calorimetry
<b>DSPE-PEG2000</b>	1,2-Distearoyl-sn-glycero-3-phosphoethanolamine-N-[amino(polyethylene glycol)-2000]
<b>DTDTPA</b>	Dithiolated diethylenetriamine-pentaacetic acid
<b>DTPA-PE</b>	Diethylenetriaminepentaacetic acid phosphoethanolamine
<b>DTX</b>	Docetaxel
<b>EDTA</b>	Ethylenediaminetetra acetic acid
<b>EE</b>	Encapsulation efficiency
<b>EGFR</b>	Epidermal growth factor receptor

---

---

<b>EPR</b>	Enhanced permeation and retention
<b>FAR</b>	Folic acid receptor
<b>FBS</b>	Fetal bovine serum
<b>FCS</b>	Fluorescence correlation spectroscopy
<b>FRET</b>	Forster resonance energy transfer
<b>FTIR</b>	Fourier transform infrared spectroscopy
<b>GI</b>	Gastrointestinal tract
<b>HBSS</b>	Hank's balanced salt solution
<b>HER</b>	Herceptin
<b>HLB</b>	Hydrophilic-lipophilic balance
<b>HU</b>	Hounsfield unit
<b>IONPs</b>	Iron oxide nanoparticles
<b>KDa</b>	Kilo Dalton
<b>keV</b>	Kilo electronvolt
<b>KHz</b>	Kilo hertz
<b>LC</b>	Lipid chitosan
<b>LD</b>	Lethal dose
<b>LNP</b>	Lipid nanoparticle
<b>m-PAA</b>	Modified-polyacrylic acid
<b>MAL</b>	5-Aminolaevulinic acid
<b>MB</b>	Methylene blue
<b>MCT</b>	Medium chain triglycerides
<b>MHz</b>	Mega-hertz
<b>MPS</b>	Mononuclear phagocyte system
<b>MRI</b>	Magnetic resonance imaging
<b>MSOT</b>	Multispectral optoacoustic tomography
<b>MTD</b>	Magnetic targeted drug delivery
<b>MTT</b>	3-(4,5-Dimethylthiazol-2-yl)-2,5-diphenyltetrazolium bromide
<b>MTX</b>	Methotrexate
<b>Mw</b>	Molecular weight
<b>NEs</b>	Nano-emulsions
<b>NGR</b>	Arginylglycylaspartic acid
<b>NIR</b>	Near infrared
<b>NIRF</b>	Near infrared fluorescence
<b>NLS</b>	Nuclear location sequence
<b>NMR</b>	Nuclear magnetic resonance
<b>NMs</b>	Nanomaterials
<b>NPC</b>	nuclear pore complex
<b>NPs</b>	Nanoparticle
<b>OR</b>	Oil ratio
<b>PAV</b>	Prednisolone acetate valerate
<b>PBS</b>	Phosphate buffer saline
<b>PDI</b>	Polydispersity index
<b>PDT</b>	Photo dynamic therapeutic agents

---

---

<b>PEG</b>	Polyethylene glycol
<b>PEI</b>	Poly(ethyleneimine)
<b>PET</b>	Positron emission tomography
<b>PFCs</b>	Perfluorocarbons
<b>PFPE</b>	Perfluoropolyether
<b>PLGA-PEG</b>	(Poly(D,L-lactic-co-glycolic acid)-block-polyethyleneglycol)
<b>PMAO</b>	Poly(maleic anhydride-alt-1-octadecene)
<b>PPy</b>	Polypyrrole
<b>PTT</b>	Photothermal therapy
<b>PVP</b>	polyvinyl pyrrolidone
<b>PXT</b>	Paclitaxel drug
<b>QDs</b>	Quantum-dots
<b>RES</b>	Reticuloendothelial system
<b>RGD</b>	Arginylglycylaspartic acid
<b>SEM</b>	Scanning electron microscope
<b>SiNPs</b>	Silica nanoparticles
<b>SLNPs</b>	Solid lipid nanoparticles
<b>SNR</b>	Signal-to-noise ratio
<b>SOR</b>	Surfactant / (surfactant + oil) weight ratio
<b>SOWR</b>	(Surfactant+oil) / (surfactant + oil + water) weight ratio
<b>SPECT</b>	Single photon emission computed tomography
<b>SPIO</b>	Superparamagnetic iron oxide
<b>t<sub>1/2</sub></b>	Half-life time
<b>TEM</b>	Transmission electron microscopy
<b>TEOS</b>	Tetraethoxyortho-silicates
<b>TIBA</b>	2,3,5-Triiodobenzoic acid
<b>TIPh</b>	2,4,6-Triiodophenol
<b>TIPhO</b>	2,4,6-Triiodophenyl oleate
<b>TIRF</b>	Total Internal Reflection Fluorescence Microscopy
<b>TME</b>	Tumor microenvironment
<b>TOAB</b>	Tetraoctylammonium bromide
<b>TPF</b>	Two-photon fluorescence
<b>TPGS</b>	D- $\alpha$ -Tocopherol Polyethylene Glycol 1000 Succinate
<b>TXT</b>	Taxotere®
<b>VEGF</b>	Vascular endothelial growth factor
<b>VPF</b>	Ascular permeability factor
<b>Z</b>	Atomic number

---

# *Résumé de thèse*

Cette thèse a pour objectif de réaliser la formulation de nano-émulsions injectables contenant des agents iodés destinés à l'imagerie biomédicale pour la recherche préclinique. Les nano-émulsions sont préparées par un processus spontané d'émulsification de basse énergie et les agents iodés utilisés contiennent des atomes d'iode directement fixés sur des cycles benzéniques eux-mêmes greffés à des composés lipophiles. Ces composés sont préparés en utilisant des réactions chimiques simples. Ces composés iodés peuvent être incorporés ou peuvent constituer la partie centrale des nano-émulsions huile/eau. Cette dissertation doctorale comprend l'étude de plusieurs facteurs qui affectent la biodistribution et la pharmacocinétique des nano-émulsions ainsi que les profils de toxicité de ces nano-émulsions. Pour réaliser des nano-émulsions efficaces, les paramètres physico-chimiques telles que la taille, la charge en surface, la morphologie, la fonctionnalisation en surface etc. de ligands ont dû être optimisés. Ces particules (phase interne des nano-émulsions L/H) doivent montrer une accumulation sélective afin de réaliser une vectorisation active et/ou passive visant des mécanismes spécifiques afin de maximiser l'efficacité pour la représentation ou le traitement tout en réduisant au minimum les effets secondaires et indésirables. Des sondes fluorescentes lipophiles aussi bien que des agents thérapeutiques anticancéreux peuvent être incorporés dans la phase interne lipophile des nano-émulsions pour produire des objets nanométriques multifonctionnels.

Au cours des dernières décennies, il a été recommandé de recourir à l'imagerie médicale pour visualiser l'intérieur d'un organisme vivant de manière non invasive. Les récentes techniques découvertes permettent non seulement un meilleur diagnostic mais offrent également de nouveaux espoirs pour le traitement de beaucoup de maladies telles que le cancer, les dysfonctionnements cardiaques, les désordres cérébraux, etc. En effet, l'imagerie médicale peut actuellement être considérée comme une véritable porte ouverte pour détecter et identifier des tumeurs et des lésions avec précision et pour faciliter ainsi des opérations chirurgicales. D'ailleurs, ces outils permettent une meilleure compréhension de la fonction et du mécanisme de fonctionnement des organes (en grande partie encore inconnus pour certains d'entre eux) fortement complexes et encore mystérieux comme le cerveau.

Plusieurs techniques de représentations ont été mises en application comme la tomodensitométrie (rayon X micro-CT), l'imagerie par résonance magnétique (IRM), l'imagerie optique, la médecine nucléaire et l'imagerie par ultrasons. L'utilisation de ces techniques d'imagerie permet indirectement de visualiser la physiologie ou le métabolisme du corps humain ou des animaux. L'image obtenue permet par exemple de montrer l'évolution ou les mouvements d'une substance dans le tissu vivant au cours du temps afin d'assurer une « surveillance en ligne », pour donner une reconstitution tridimensionnelle d'un organe ou d'un tissu. Les images quantitatives représentent également les valeurs mesurées de certains paramètres biologiques en volume donné.

Afin d'augmenter la qualité de l'image, il est habituel d'ajouter dans les formulations administrées des agents radio-opaques de contraste au patient, selon la technique utilisée et la voie de

---

l'administration envisagée. Par exemple, il est bien documenté que l'utilisation de la suspension orale de sulfate de baryum (pour obtenir des images du tube digestif), la molécule iodée ou l'or lié à la technique utilisant des rayons X, les traces d'oxyde de fer ou le gadolinium iodées soient combinées avec la technique d'IRM, de sondes fluorescentes ou l'utilisation de quantum dots nécessaires pour une imagerie par fluorescence.

Dans cette thèse, nous nous sommes focalisés sur la technique d'imagerie à rayons X ainsi que sur ses agents de contraste qui sont constitués de nano-émulsions contenant des huiles iodées. Actuellement, la technique d'imagerie à rayons X est la meilleure technique d'imagerie et ce, due à la puissance liée à sa technique, sa rapidité d'obtention d'images et son coût peu onéreux, sa capacité d'obtenir rapidement des images reconstituées en 2D et en 3D, présentant une haute résolution spatiale non invasive permettant une meilleure détection d'éléments de tailles allant de 1 à 100  $\mu\text{m}$ , et par conséquent permet de révéler des informations structurelles et fonctionnelles de lésions, permettant également la détection d'une tumeur aussi petite que 300  $\mu\text{m}$ . La technique d'imagerie optique est prometteuse due à son faible coût comparée aux autres techniques d'imagerie. Cependant, cette technique donne un faible signal de pénétration dans le corps de l'animal. En ce qui concerne l'imagerie nucléaire, les problèmes principaux sont liés au stockage et à l'approvisionnement en matériaux radioactifs. En plus des problèmes liés à l'exposition des irradiations, elle cause des effets secondaires importants chez le patient.

Les agents iodés de contraste sont les composés les plus généralement utilisés dans la technique de  $\mu\text{-CT}$  aux rayons X. La plupart des agents iodés de contraste contiennent un cycle benzénique tri-iodé en positions 2,3,5 ou un cycle benzénique tri-iodé en positions 2,4,6. Ces dérivés tri-iodés ont été développés au cours des 50 dernières années et leurs applications en imagerie médicale a fait suite à la découverte des rayons X. Ces composés ont été utilisés pour leurs propriétés d'auto-assemblage permettant de la sorte de limiter leur excrétion rénale et de là pour leurs propriétés de rémanence vasculaire.

Le développement de nouveaux agents à base d'iode est principalement liée à la nécessité de surmonter les limitations des produits commerciaux actuels. Par exemple, malgré les propriétés contrastantes élevées résultantes de la forte concentration en iode dans le Xenetix® (iobitridol), soit 300 mg/ml, ce produit commercial donne aisément après injection par voie intraveineuse une imagerie du torrent sanguin mais est rapidement éliminée de l'organisme du fait de sa petite taille moléculaire.

Un autre exemple est le Fenestra® VC qui a une rémanence de plus de 2 heures dans le torrent sanguin après administration par voie parentérale. Par conséquent ce produit ne possède pas les propriétés permettant une visualisation du torrent sanguin et une propriété contrastante spécifique au niveau du foie. De plus, l'osmolalité des émulsions contenant des dérivés iodés est plus importante que celle observée physiologiquement. Le procédé de préparation de ces émulsions contenant de l'iode est relativement compliqué et onéreux. On peut également citer la complexité

---

liée à la formulation qui pose des problèmes d'extrapolation d'échelles en vue d'une commercialisation.

Afin d'éviter les problèmes mentionnés ci-dessus, deux solutions existent pour améliorer l'imagerie médicale, la première concerne les modalités d'imagerie en mettant en place des techniques d'imagerie bi- ou multi-modale afin de rassembler tous les avantages de cette technique dans un seul appareillage (solution physique), c'est la raison pour laquelle 43% des imageries sont multimodales. La seconde solution consiste à améliorer la qualité des agents de contraste (solution chimique).

Dans le cadre de notre travail de recherches nous nous sommes focalisés sur la chimie de l'agent de contraste ainsi que sur la manière de générer d'excellentes sondes d'imagerie afin de surmonter les écueils rencontrés lors de leurs utilisations en clinique.

Tous les aspects des nouveaux agents de contraste développés utilisés à des fins biomédicales doivent être optimisés en comprenant la chimie des agents de contraste (synthèse et fonctionnalisation de surface), la physique du mécanisme générant le signal ainsi que les profils de pharmacocinétique et de toxicité et finalement leur application sur les animaux et les êtres humains. Ces conditions peuvent être résumées dans les points suivants :

- i) La taille des agents de contraste ne devrait pas être trop petite pour éviter une filtration rénale rapide et néanmoins être inférieure à 200 nanomètres pour permettre le mécanisme d'optimisation passive qui dépend de la perméation augmentée et de l'effet de rétention (EPR). Ce processus est lié à la taille des pores des vaisseaux sanguins lorsque les nanoparticules ont une taille comprise entre 20 et 200 nm leur permettant de diffuser en dehors des vaisseaux sanguins et de s'accumuler spécifiquement dans certains tissus/organes. A l'inverse, des nanoparticules trop grosses ont tendance à être maintenues dans la circulation sanguine
  - ii) la stabilité des agents de contraste formulés avec une composition et un protocole de formulation donnés sous forme de nano-émulsions iodées constituées de gouttelettes de phase huileuse dispersée et recouvertes en surface par des chaînes de polyéthylène-glycol de manière à présenter une stabilité acceptable allant de quelques mois à un an.
  - iii) des systèmes nanoparticulaires biocompatibles, biodégradables et qui puissent être biodistribués, c'est la raison pour laquelle les formulations doivent être constituées de matériaux approuvés par la FDA et montrer une toxicité négligeable. Afin d'atteindre ces objectifs, le recouvrement de polyéthylène-glycol doit être ancré en surface afin d'éviter une reconnaissance trop rapide par le système réticulo-endothélial et par conséquent d'augmenter leur temps de circulation dans le torrent sanguin. Cette stratégie doit pouvoir donner l'opportunité aux sondes nanométriques d'imagerie de s'accumuler dans des organes déterminés.
  - iv) efficacité des agents de contraste : dans nos études nous avons augmenté la capacité de charge utile des molécules contrastantes en greffant de manière covalente des molécules iodées aux huiles constituant le cœur huileux des nano-émulsions prévenant de la sorte leur libération prématurée. Idéalement de faibles quantités injectées doivent pouvoir donner un contraste
-

suffisant dans l'organe ou le tissu qu'il est souhaitable de visu des nanoparticules. Un mécanisme de vectorisation active peut également être envisagé par la bioconjugaison avec des ligands spécifiques évitant de la sorte une localisation non souhaitée.

v) le produit final doit être abordable pour le patient sachant que le prix dépend largement des étapes de synthèse et de préparation. Les molécules iodées étudiées dans le cadre de cette thèse sont réalisées par une simple réaction d'estérification suivie par une technique d'émulsification spontanée de faible énergie.

Dans la première étude (chapitre 1.2), nous avons étudié le rôle de la nature chimique du noyau de la gouttelette huileuse des nano-émulsions utilisées en tant qu'agents de contraste pour l'imagerie aux rayons-X sur leurs pharmacocinétiques et leurs biodistribution. Pour ce faire, nous avons formulé des nano-émulsions PEGylées avec deux huiles iodées (*e.g.* monoglycéride hexa-iodé et de l'huile de ricin hexa-iodée) et comparé à une nano-émulsion à base de vitamine E iodée. Toutes les formulations sont réalisées par émulsification spontanée et stabilisées par un surfactant non ionique PEGylé. Grâce à l'utilisation de la diffusion dynamique de la lumière et de la microscopie électronique à transmission, nous avons pu mettre en évidence que les trois nano-émulsions iodées sont caractérisées par des morphologies, des tailles ainsi qu'une composition de surface comparables. En outre, elles ont présenté une concentration très élevée en iode, ce qui a conduit à des propriétés plus fortes d'atténuation aux rayons X comparé à la nano-émulsion iodée commerciale Fenestra®VC. Les trois nano-émulsions étaient administrées par voie intra-veineuse chez les souris et suivies par la tomographie (micro-CT). Elles ont montré un pouvoir contrastant important dans le sang avec une demi-vie semblable, soit environ 6 heures mais accumulées dans sur des sites différents comme indiqué sur le schéma 1 par les images 3D pour le deux émulsions.

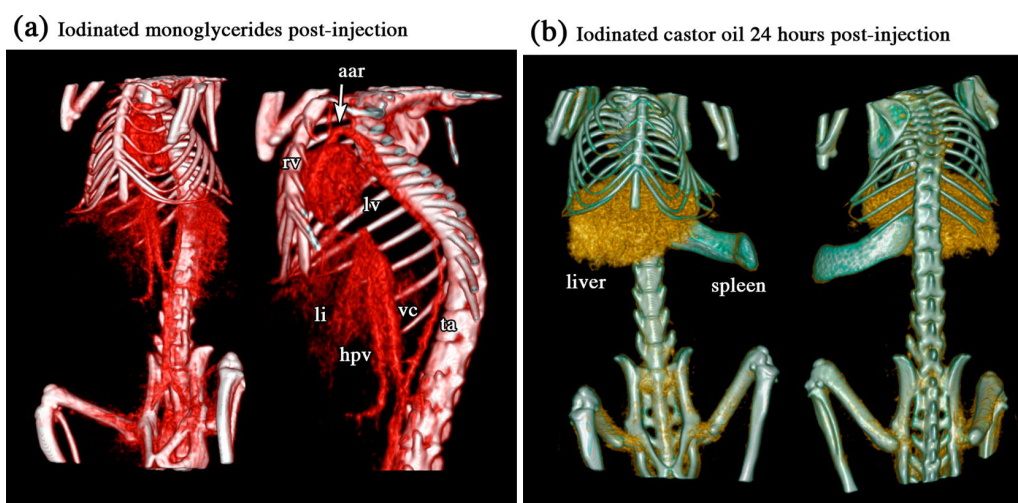


**Figure 1:** volume rendu 3D par micro-CT, (a) 5 minutes après injection des monoglycérides iodés et (b) 24 h après injection d'huile de ricin iodée. Annotations : (Aar) voûte aortique, (rv) ventricule droit, (vg) ventricule gauche, (Li) emplacement du foie, (vc) veine cave, (hvp) veine porte hépatique, (at) aorte thoracique.

Alors que les monoglycérides iodés montraient une faible accumulation dans le foie et dans la rate, une accumulation élevée a été observée dans la rate pour l'huile de ricin iodée et dans le foie pour la vitamine E. Ces données ont clairement mis en évidence le rôle important de la composition de l'huile constituant le cœur des gouttelettes de la nano-émulsion pour obtenir un contraste important aux rayons X pour des cibles spécifiques telles que le foie, la rate, ou seulement le sang. Ces différences de biodistribution ont été en partie attribuées aux différences de capture des gouttelettes huileuses nanométriques par les macrophages *in vitro*, comme le met très bien en évidence la figure 2 par leur pénétration dans les cellules.

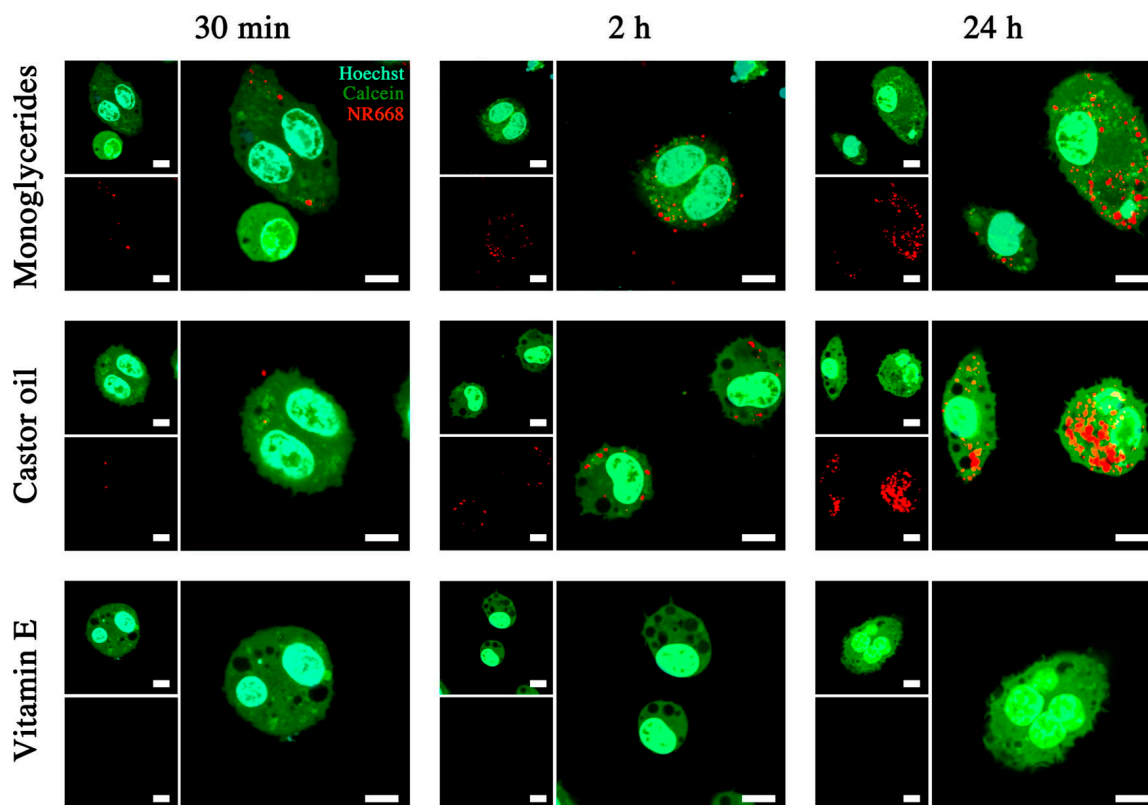


**Figure 2:** Suivi de la prise des nano-émulsions iodées chargées de NR668 par les macrophages murins (cellules RAW264.7). Des noyaux ont été marqués avec une cyanine provenant de chez Hoechst et les cellules avec de la calcéine AM (vert). Le NR668 (Nile Red modifié lipophile) chargé dans le noyau huileux des gouttelettes des nano-émulsions permet de suivre la localisation des gouttelettes une fois internalisées par les cellules. Les monoglycérides iodés, l'huile de ricin iodée, et la vitamine E iodée ont été formulés sous forme de nano-émulsions et incubés pendant différentes périodes : 30 minutes, 2 h, et 24 h. En haut à gauche les photographies montrent la cellule et les noyaux. En bas à gauche les photographies montrent le signal du NR668 et plus grande photographie montre chacun des deux fusionnés.

Une autre particularité de ces nano-émulsions est leur long temps de demi-vie dans le foie ou la rate (plusieurs semaines, en fonction des cibles et de la nature chimique de l'huile), qui permet une rétention suffisante pour faire de l'imagerie par micro-CT. Ce travail a par conséquent permis de considérer ces agents de contraste nanoparticulaire pour la représentation par rayons X

d'organes sélectionnés. Leur utilisation potentielle pour l'imagerie clinique a pu également être envisagée.

Le but de la deuxième étude (chapitre 1.3) consistait en l'étude de l'impact du facteur de la taille de l'agent iodé de contraste aux rayons X dans les nano-émulsions, sur leur toxicité et leur devenir *in vivo*. Pour réaliser cela, un nouveau composé, le cholécalférol (vitamine D3) de triiodobenzoate, a été synthétisé, formulé sous forme de nano-émulsions, et suivi après administration intraveineuse (i.v.) chez les souris par imagerie aux rayons X. La caractérisation physico-chimique et l'optimisation du processus ont permis d'identifier un bon compromis entre les propriétés contrastantes aux rayons X, la monodispersité et la stabilité. Ceci a également permis de sélectionner deux formulations avec différentes tailles, des diamètres hydrodynamiques de 55 et de 100 nanomètres, ayant néanmoins des compositions identiques. Des expériences *in vitro* ont été réalisées sur deux variétés de cellules, à savoir des hépatocytes (BNL-CL2) et des macrophages (RAW264.7). Les études de viabilité cellulaires, la quantification de l'internalisation a été déterminée par fluorimétrie comme indiquée à la figure 3. L'internalisation cellulaire a été observée par microscopie confocale. Cette technique a révélé des différences claires entre les deux formulations, ainsi qu'entre les deux types de variétés de cellules.

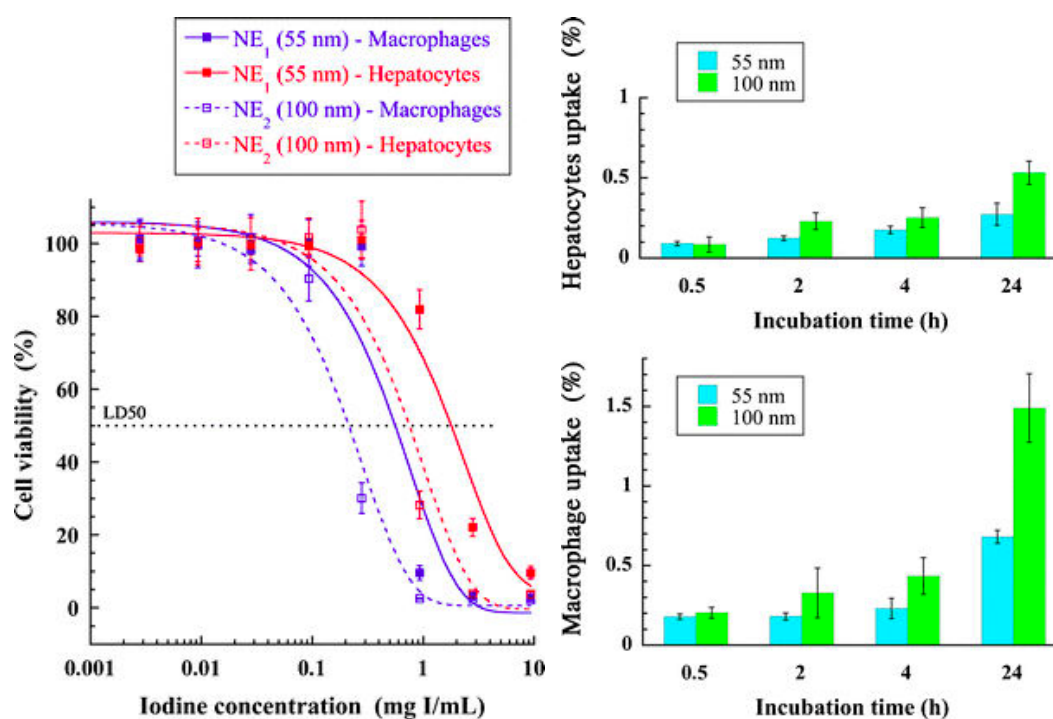


**Figure 3:** Viabilité (gauche) des macrophages RAW264.7 murins (courbes bleues) et des hépatocytes BNL-CL2 (courbes rouges) après 24h00 d'incubation avec les nano-émulsions iodées. Les concentrations de nano-émulsions ont été exprimées en concentrations en iode par mL. Les symboles remplis et les symboles ouverts correspondent aux nano-émulsions iodées NE1 et NE2, respectivement. Quantification d'internalisation des nano-émulsions par des hépatocytes et des macrophages en fonction du temps d'incubation et de la taille des gouttelettes (droite). Après l'incubation avec les nano-émulsions chargées avec NR668, les hépatocytes ou les macrophages ont été lavés, lysés

avec du DMSO et étudié par la fluorimétrie. L'internalisation a été exprimée en pourcentage de la fluorescence lié aux cellules comparé à la fluorescence de la solution du milieu de culture.

Après injection par voie intraveineuse (i.v.) des deux nano-émulsions iodées chez les souris, elles ont montré une amélioration du contraste comme mentionné à la figure 4.

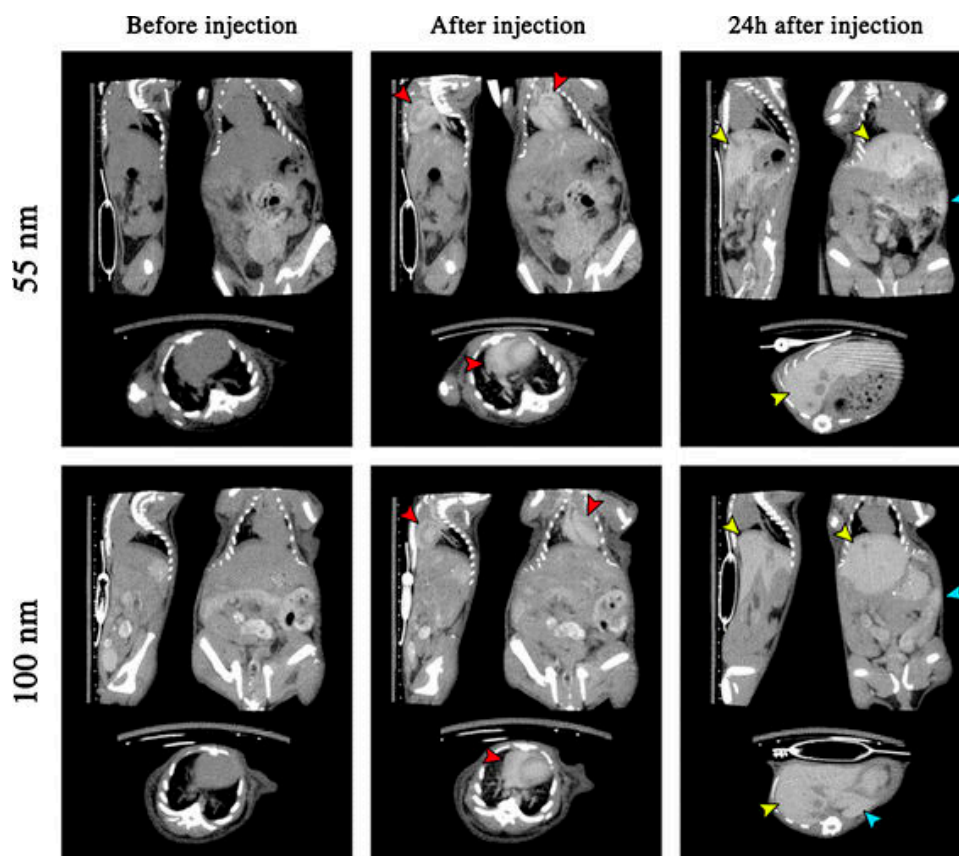


**Figure 4:** représentation *in vivo* par micro-CT (intensité maximum de projection) des nano-émulsions iodées de cholécalciférol de deux tailles différentes (55 et 100 nanomètres) ayant exactement la même composition, avant et après 24 h suite à l'injection. Les photos montrent les sections sagittales et coronales des souris, aussi bien que les tranches transversales par le cœur, le poumon, et les tranches de vertèbre et transversales pour le foie et la rate. Le cœur est indiqué par des flèches rouges, le foie par les flèches jaunes, et la rate par les flèches bleues.

Les balayages par CT ont fourni les paramètres de pharmacocinétique et les biodistributions. Nous avons finalement mis en évidence que la taille dans les nano-émulsions n'a pas un impact réel sur la pharmacocinétique et les biodistributions. En revanche, on observe une influence forte sur leur toxicité. En effet, les nano-émulsions de 100 nanomètres se sont avérées être plus toxiques que celles de 55 nanomètres quelle que soit la variété des cellules (hépatocytes ou macrophages). Cette observation réalisée par microscopie confocale est vraisemblablement attribuable à une prise plus élevée par les cellules et confirmée par la quantification fluorimétrique, corroborant les résultats observés *in vitro*. Cette différence majeure a pu être attribuée à la différence de toxicité et d'internalisation cellulaire liée à la taille des gouttelettes.

Au regard de l'imagerie *in vivo*, l'ensemble des courbes de pharmacocinétique et de biodistribution dans le sang, le foie, la rate et le rein étaient tout à fait semblables. Ces résultats indiquent que la taille des nano-émulsions n'a aucune réelle influence sur le devenir *in vivo* jusqu'à 48h après injection. Après ce temps, la nano-émulsion NE2 induisait la mort chez la souris, alors que l'imagerie suite à l'injection de la nano-émulsion NE1 peut être poursuivie 50 jours sans aucune difficulté comme démontré à la figure 5.

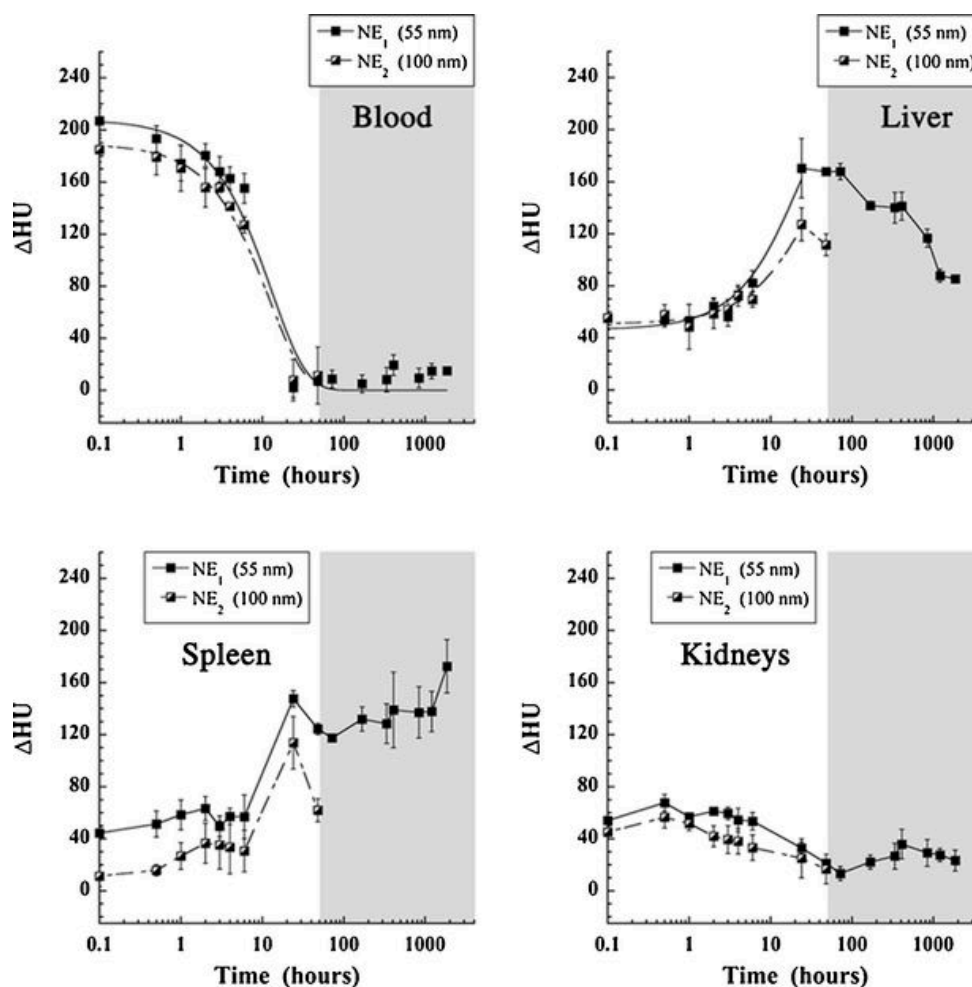


**Figure 5:** Mesures quantitatives de l'atténuation de rayons X du cœur, du foie, de la rate et du rein après administration intraveineuse de nano-émulsions iodées de cholécalférol. NE1 et NE2 se rapportent à des nano-émulsions de composition semblable mais ayant différentes tailles, à savoir 55 et 100 nanomètres, respectivement ;  $n=6$  pour chaque nano-émulsion. La limite entre la partie blanche et grise indique le temps à partir duquel les souris qui avaient reçues les NE2 mouraient, alors que celles ayant reçues les NE1 survivaient.

Au chapitre 2.2, nous avons étudié la décoration de la surface des nano-émulsions avec des groupes carboxyliques. Puisque les interfaces des systèmes émulsionnés sont dynamiques, la modification chimique d'un tel système est par définition un défi, sachant que les espèces fonctionnelles adsorbées ou les ligands peuvent potentiellement être désorbés, selon les équilibres

d'adsorption/désorption. Ce phénomène limite réellement la concentration et la stabilité des entités potentiellement greffées. Le deuxième but de cette étude est d'étudier l'effet potentiel de la charge extérieure des nano-émulsions sur leurs pharmacocinétiques et leurs biodistributions *in vivo*. Cette étude a été réalisée grâce à une méthode fiable et innovatrice pour fonctionnaliser des gouttelettes de lipides, basée sur un polymère lipophile (PMAO), le poly (anhydride-alt-1-octadécène maléique), soluble dans le noyau des gouttelettes et qui peut être hydrolysé à l'interface huile/eau. L'hydrolyse du PMAO à l'interface huile/eau a été étudiée et validée par des méthodes physico-chimiques, la tension superficielle et des mesures du potentiel  $\zeta$  ainsi que par des mesures basées sur des méthodes colorimétriques qui sont à l'origine adaptées aux systèmes nanoparticulaires. La figure 6 schématise une nano-goutte huileuse fonctionnalisée en surface avec des groupes carboxyliques.

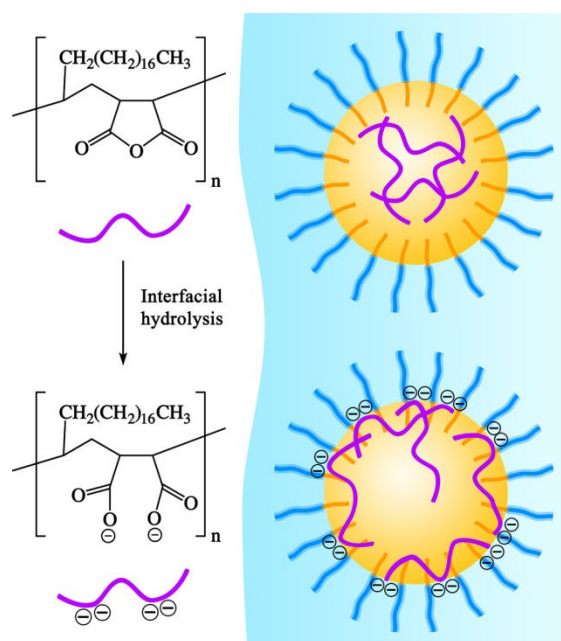


**Figure 6:** Illustration schématique de l'étude : le PMAO, soluble dans le noyau huileux des gouttelettes d'une nano-émulsion s'hydrolyse à l'interface en créant des carboxylates fortement ancrés et disponibles à la surface des gouttelettes.

Trois nano-émulsions différentes ont été préparées et variaient seulement dans la charge extérieure (une neutre, une négative dû à la présence du polymère de PMAO et des nano-émulsions chargées positivement provenant de la couche de chitosan déposée à la surface des gouttelettes et discuté dans la partie supplémentaire de cette étude). Les charges positives ne donnaient pas lieu à une interaction *in vitro* avec les cellules Hela, c'est la raison pour laquelle nous avons réalisé des comparaisons seulement entre les particules neutres et négatives pour des expériences *in vivo*. Dans les études *in vitro*, la présence des carboxylates à l'interface donne lieu à des interactions avec des cellules. L'internalisation des gouttelettes chargées négativement est beaucoup plus importante que celle observée avec les particules neutres. Cette différence a été

confirmée avec des études longitudinales réalisées *in vivo* avec des souris après administration i.v., suivie par une imagerie aux rayons X, la modification extérieure a comme conséquence une différence significative dans la pharmacocinétique et la biodistribution, avec une capture plus importante pour la rate et le foie. Cette différence est représentée à la figure 7.

**Figure 7:** Imagerie *in vivo* par micro-CT, études longitudinales de biodistribution des nano-émulsions d'O-TIB après administration i.v. chez des souris. Des Nano-émulsions sans PMAO (*TIPhO NE*) et avec PMAO à 1,5 % en poids d'huile (*TIPhO-PMAO NE*) ont été comparées ; n = 3 pour chaque type de nano-émulsion. A gauche : l'analyse quantitative des valeurs d'atténuations aux rayons X, les régions d'intérêt (ROIs, *regions of interest*) ont été placées dans le cœur, le foie, la rate et les reins. A droite : projection maximum d'intensité aux heures représentatives : sections coronales de souris post-injection et après 6 heures suite à l'injection (montrant le cœur et le foie), et sections transversales 6 heures après injection (montrant la rate). Les flèches sur les graphiques indiquent les correspondances pendant 6 heures.

Dans cette étude nous avons établi la preuve de concept d'une nouvelle méthode de fonctionnalisation de gouttelettes lipidiques et avons démontré que la modification de surface peut avoir un impact significatif sur leur interaction avec les cellules, leurs pharmacocinétiques et leurs biodistribution *in vivo*.

Le but de la quatrième étude (chapitre 2.3) est de poursuivre la fonctionnalisation des gouttelettes d'émulsion à leur interface huile/eau. Comme nous l'avons mentionné ci-dessus la surface des nano-gouttelettes d'huile est une interface dynamique huile/eau stabilisée par des agents tensio-actifs, et sa modification chimique avec des ligands greffés est un véritable défi. Dans cette étude, nous avons développé un nouveau protocole également pour assurer la modification de surface des nano-gouttelettes grâce à une coque de silice terminée par des fonctions amines. Le

---

précurseur lipophile de silice est un aminopropyltriéthoxysilane (APTES) qui a été ajouté à l'huile avant la formulation, et transformé en coquille de silice après la fabrication de nano-gouttelettes par sono-chimie qui évite l'addition du catalyseur dans le mélange. Le processus complet est décrit à la figure 8.

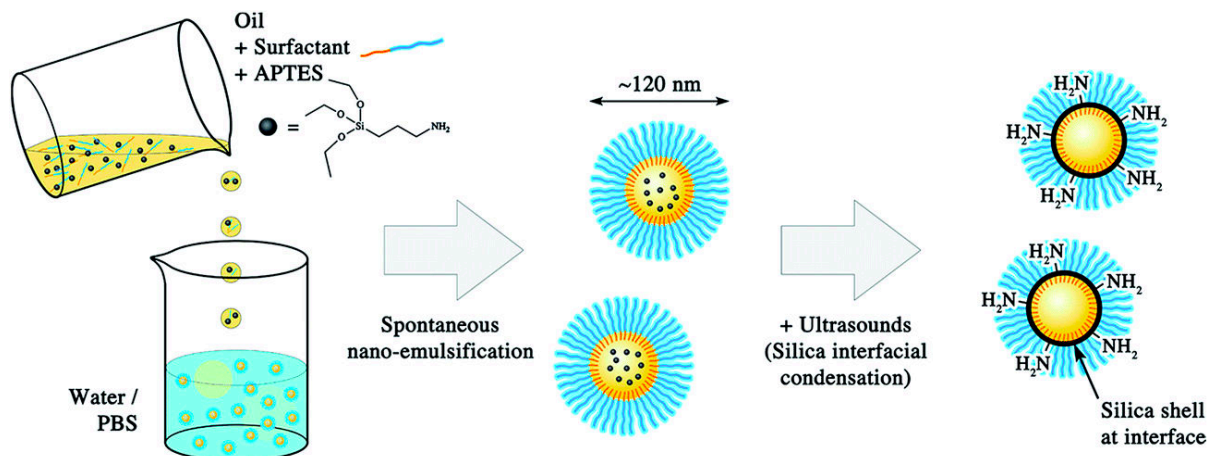


**Figure 8:** Schéma général décrivant la formulation des gouttelettes fonctionnalisées par des fonctions amines de nano-émulsions.

En comparaison des méthodes existantes pour fonctionnaliser des nano-gouttelettes comme la post-insertion de lipides fonctionnalisés, cette procédure nouvelle apporte de réels avantages : greffage covalent des groupements fonctionnels sur la surface de nano-gouttelettes c'est à dire fortement ancrées sur les nanocapsules de silice avec également un grand nombre de sites réactifs par capsule (jusqu'à  $9 \times 10^4$ ,  $\sim 2$  groupements aminés par  $\text{nm}^2$ ). La fabrication d'une coquille de silice est simple, rapide, et n'affecte ni le processus de formulation ni la taille des gouttelettes. La quantification du nombre de groupements aminés a permis de comprendre l'impact des paramètres de formulation, comme la taille des gouttelettes ou la concentration en APTES, le nombre de groupements  $\text{NH}_2$  réactifs décorant les nanocapsules. La surface des nanocapsules ont été fonctionnalisées (41%) par un ligand fluorescent modèle (bleu de coumarine) soutenant la fonction carboxylique sur les fonctions amines disponibles à la surface de nanocapsules. Les preuves de la réussite d'un greffage ont été obtenues par transfert d'énergie de spectrofluorométrie, de résonance de Forster (FRET), par microscopie atomique de force (AFM) couplée avec la représentation de fluorescence et de spectroscopie de corrélation de fluorescence (FCS) comme mentionné à la figure 9. Ce protocole simple pour réaliser la fonctionnalisation à l'interface liquide/liquide des gouttelettes de lipide peut constituer une réelle avance pour les applications potentielles de gouttelettes pour lesquelles une décoration en surface est souhaitable pour le greffage de ligands.

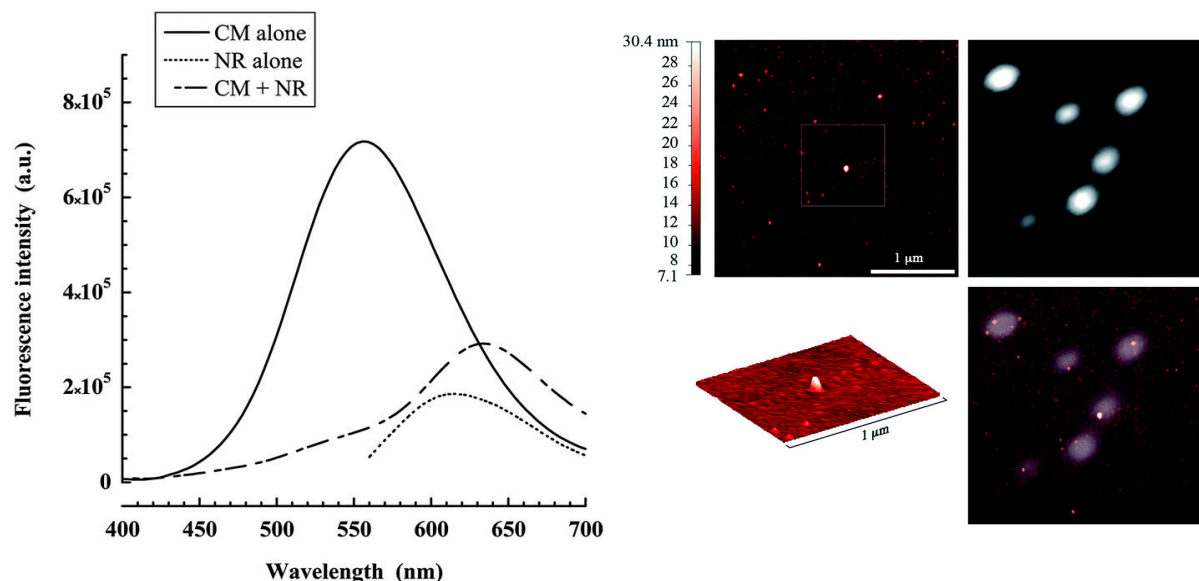


**Figure 9:** Gauche : Spectres d'émission pour des expériences et des contrôles de FRET. Les systèmes étudiés sont des nanocapsules décorées avec du bleu de coumarine (CM seule), ou des nanocapsules seulement chargées avec du Nile Rouge (seul NR), ou finalement des nanocapsules décorées avec de la coumarine bleue et chargées avec le Nil Rouge (CM + NR) ;  $[APTES]_{\text{huile}} = 0,5 \text{ M}$ . Photographies de droite : Microscopie combinée d'AFM et de fluorescence des nanocapsules décorées avec de la coumarine bleue (huile  $[APTES]_{\text{huile}} = 0,5 \text{ M}$ ). Gauche : photographie AFM avec une représentation 3D des nanocapsules. Droite : acquisition correspondante de fluorescence montrant la correspondance entre l'AFM et la fluorescence.

La dernière étude (chapitre 3.2) concerne une nouvelle synthèse en seule étape de nanocapsules hybrides multifonctionnelles d'oxyde de fer / polypyrrole encapsulant un principe actif hydrophobe et décorées avec du polyéthylène glycol. Le processus global est basé sur la polymérisation oxydante chimique in situ du pyrrole avec la réduction du chlorure ferrique ( $\text{FeCl}_3$ ) en présence de kétoprofène en tant que principe actif modèle et agents tensio-actifs PEGylés (Solutol HS15). Le produit final est un nanocomposite constitué du polypyrrole et un mélange de  $\text{FeO}/\text{Fe}_2\text{O}_3$ . Différentes concentrations de kétoprofène ont été encapsulées dans le nanocomposite et ont été caractérisées par spectroscopie infrarouge à transformée de Fourier (FTIR) et l'analyse enthalpique différentielle (DSC). La figure 10 décrit le processus de formulation.

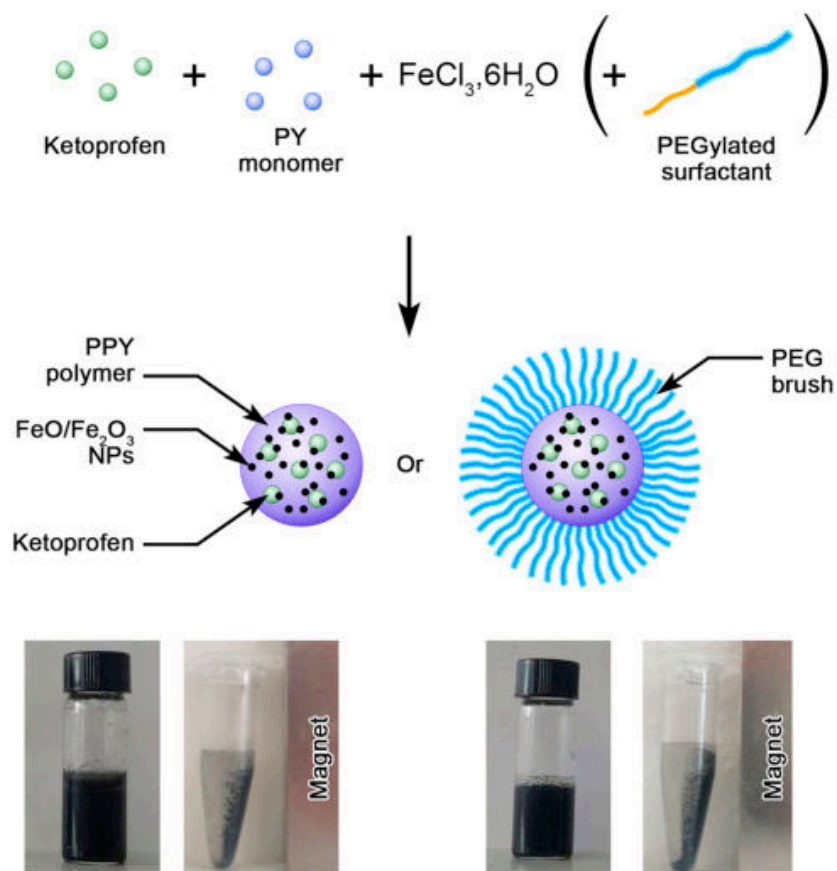


**Figure 10:** Représentation schématique du procédé de fabrication et des structures des nanocomposites de polypyrrole avec et sans surfactant non ionique comme agent stabilisateur. La photographie du bas montre l'aspect macroscopique des suspensions ainsi que le comportement général suite à un contact avec un aimant.

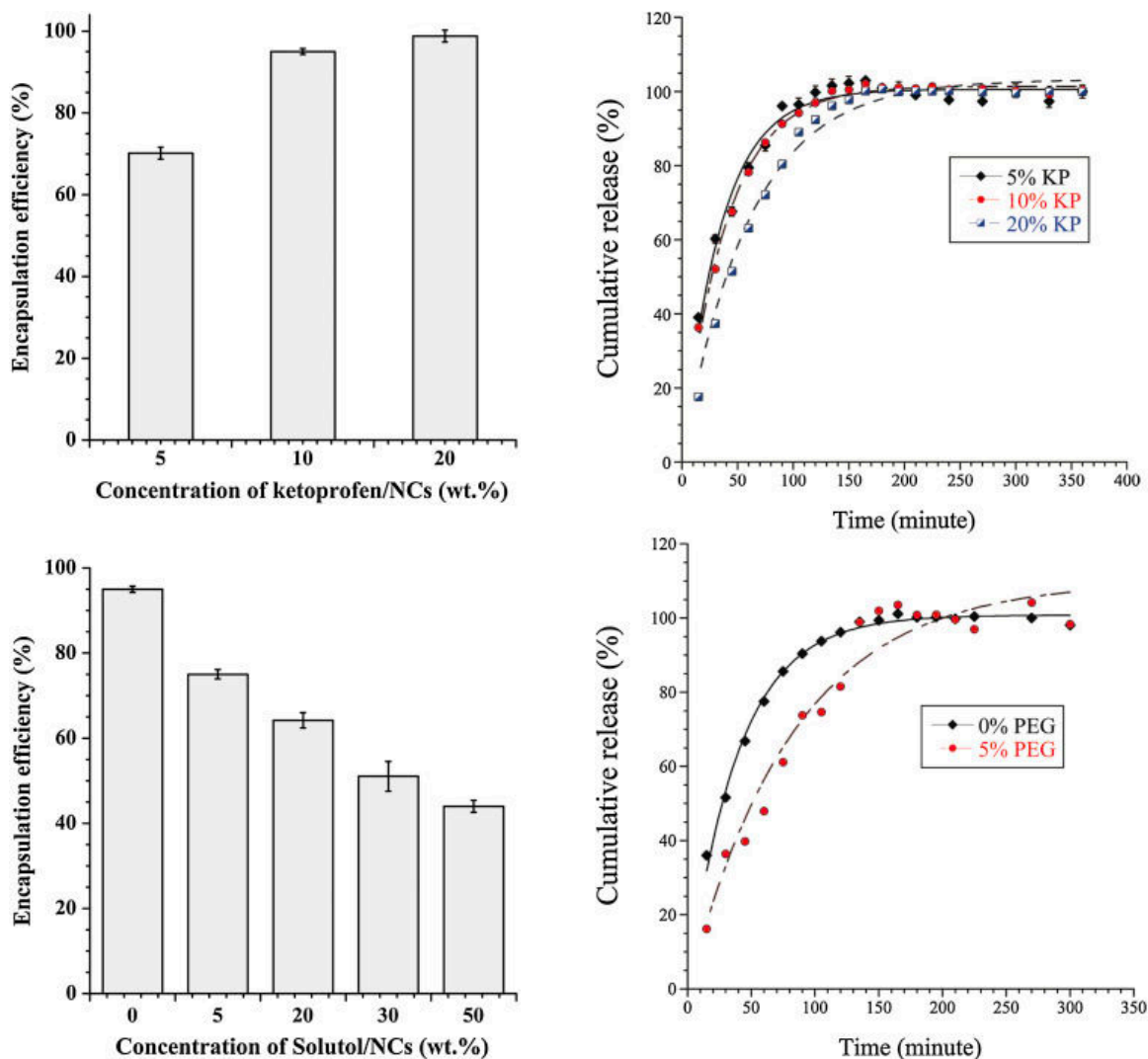


**Figure 11:** Gauche : Efficacités d'encapsulation du principe actif présent dans les particules composites. Trois concentrations de kétoprofène chargées à 0 % en poids de solutol (NCs non-PEGylées) (dessus). Différentes concentrations de Solutol HS15® (agent tensio-actif de PEGylé) à un rapport constant de 23% en poids de principe actif/ pyrrole (en bas) (n = 3). Droite : Profils de libération in vitro de trois formulations différentes nanocomposites non pégylées chargées à 5 %, 10 % et 20 % de kétoprofène (dessus). Formulations avec 0%, 5% et 10% en kétoprofène PEGylées (en bas). Les mesures ont été réalisées trois fois.

Le polypyrrole (PPy), polymère qui est très utilisé pour des applications d'ingénierie tissulaire, offre également un certain nombre de fonctionnalités supplémentaires, par exemple sa structure hydrophobe avec des électrons délocalisés permet des liaisons avec des molécules de principes actifs aromatiques tel que le kétoprofène (interaction ionique) et permettant d'augmenter la capacité de charge du principe actif. Ce processus ouvre de nouvelles possibilités pour la modification extérieure des nanocomposites de polypyrrole par des molécules PEGylées

terminées avec des groupements actifs fonctionnels qui peuvent moduler la charge extérieure ou promouvoir le bioconjugation.

Pour conclure, dans le cadre de cette dissertation doctorale, nous avons réussi à synthétiser de nouveaux agents de contraste destinés à l'imagerie CT aux rayons X qui peuvent être vectorisés, qui ne présentent pas de toxicité, qui peuvent contraster le torrent sanguin : monoglycérade hexaiodé, huile de ricin hexa-iodée, cholécalciférol triiodé, oléate triiodé. Les agents de contraste qui en résultent possèdent des concentrations élevées en iode ont montré une augmentation du contraste à la fois *in vitro* et *in vivo*. Nous avons étudié le mécanisme de vectorisation active par l'intermédiaire de la fonctionnalisation de l'interface huile/eau de gouttelettes de phase interne d'émulsions nanométriques, tout d'abord en greffant des groupements aminés par l'intermédiaire d'enrobage de silice terminée par des fonctions aminées et en second lieu par le greffage de groupements carboxyliques sur des nanogouttelettes grâce à du PMAO qui est un polymère comportant des fonctions carboxyliques latérales et introduit dans la phase huileuse. Les différents groupements ont été quantifiés par différentes méthodes, l'une mettant en œuvre des techniques spectroscopiques (méthode colorimétrique basée sur l'utilisation de fluorescamine) et par d'autres méthodes colorimétriques (méthode au colorant bleu coumarine). Nous avons également étudié l'influence des paramètres physico-chimiques tels que la taille, la composition chimique et la composition ou la charge en surface et de leurs influences sur leur pharmacocinétique, la biodistribution et la toxicité.

# *Introduction to thesis*

Nanomedicine is an emerged field springing up after the fusion between nanotechnology and medicine, and had been widely spreaded in biomedical applications. Nanotechnology is an interdisciplinary scientific field focusing on methods, materials, and tools on the nanometer scale. This combination seeks to benefit patients by providing prevention, early diagnosis, and effective treatment for prevalent, for disabling, and for currently incurable medical conditions.

Diagnostic nanomedicine is an early discovering disease, and it is essential step necessary for ideal treatment. Notably, it can be served for better understanding the basis of disease by detection of unhealthy cells and distinguishing them from the normal ones, to analyze the complex biological systems and processes, used for cellular and molecular imaging and nuclear trafficking and to precisely determine for example the location and the size of solid tumors or metastasis. In addition to monitoring therapy response, guiding drug discovery/development and for image-guided surgery.

Due to the key features of the nanometric size that matches mostly with biological compartments since the cells and the nucleus are of the nanosize range, several nanocarriers have been developed for delivering therapeutics/contrast agents to the active site either for diagnosis or treatment. These nanoparticles are mainly composed of organic molecules (polymeric NPs, liposomes, nano-emulsions, micelles and dendrimers), inorganic materials or hybrid nanoparticles. Taking the benefit of their safety, biocompatibility, and suitability to biological environment into consideration.

As well as different NPs are designed especially in biomedical imaging to serve different purposes such as They can improve visualization through increasing signals intensity, the capability to be selectively uptaked by microphages, or to enhance the sensitivity.

To date, the five major imaging modalities used are computed tomography imaging (X-ray micro-CT), magnetic resonance imaging (MRI), optical imaging, nuclear medicine (PET, SPECT) and ultrasound imaging. X-ray emerged imaging modality is the best amongst all other imagers because it is high powerful technique, fast and cost-effective, enables rapid two-dimension 2D and three-dimension 3D reconstructed images, presenting noninvasive high spatial resolution allowing better detection from 1-100 $\mu$ m, and therefore can reveal structural and functional information on lesions allowing the detection of a tumor as small as 300  $\mu$ m. The optical imaging technique is promising due to the low cost compared to other imagers, however it

---

reveals low signal penetration in the animal body. For the nuclear imaging, they have problems in storage and supply of their radioactive materials. In addition to the radiation exposure to the patient causes severe side effects.

The same principle applied in all techniques, this schematic representation describes the X-ray preclinical imaging process. Briefly, The mouse is intravenously injected by contrast agent and exposed to X-rays (electron beams) emitted from X-ray scanner and then immediately interact with contrast materials. The revealed signals are received by detector providing finally 2D and 3D images containing detailed informatives about blood vasculatures, such lesions and tumors.

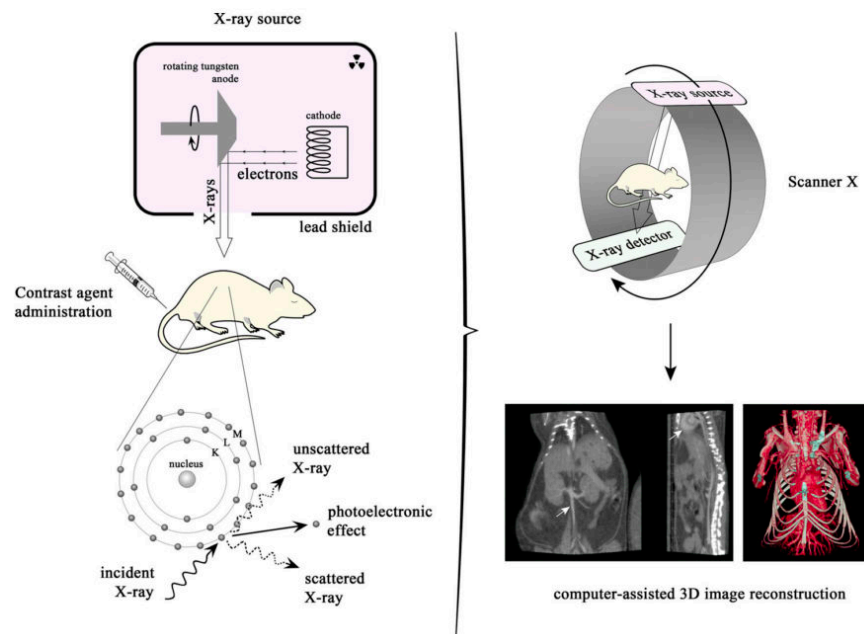


**Figure 1:** Schematic description about the principle of preclinical X-ray micro-computed tomography.

In spite of the superior characteristics of the computed tomography over other modalities, but the drawbacks limit their use in the preclinical research or in the clinics lie in the contrast agents that have either poor contrast efficiency or toxicity profiles or even the high cost of some imaging agents.

To our mind the two solutions presented to improve the imaging process, the first linked to the imaging modality, by engineering bi- or multi- modal imaging techniques in order to gather the advantages of all techniques in one apparatus (physical solution), this is why 43% of the images

are multimodal. The second solution is designing superior imaging agents associated with the imaging tools (chemical solution).

In our research work we will focus on the chemistry of contrast agent, and how to generate excellent imaging probes to overcome the defects faced by the clinically used CAs.

The all aspects of the novel developed contrast agents used in biomedical imaging must be optimized, including the chemistry of the CAs (synthesis preparations and surface functionalization), the physics of the signal-generating mechanism and up to the pharmacokinetic and toxicity profiles and finally their application on animals and humans. These requirements can be summarized in few items :

i) The size of the contrast agents should not to be extremely small to avoid the rapid renal filtration and not bigger than 200 nm to follow passive targeting mechanism that depends on enhanced permeation and retention effect (EPR). This process linked to the pores size of the blood vessels, when NPs are in the range of 20-200 nm allowing them to extravasate from the blood vessels and accumulate to specific organs/tissues. In contrast, the too big NPs tend to be entrapped and circulated in the blood stream.

ii) Stability of the CAs which results from the composition and the protocol of formulation i.e. iodinated nano-emulsions consist of oily core and PEGylated coating exhibit huge stability reaches from few months up to one year.

iii) Biocompatibility, biodegradability and biodistribution nanoparticulate systems, this is why the formulations should be constituted of FDA approved materials and showing negligible toxicity. To that goal, PEGylated shell should be anchored in the nanoparticulate surface to inhibit their fast recognition by RES system and thus increase their circulation time in the blood stream. This helps finally to give opportunity to the nano imaging probes to passively accumulated to definite organs.

iv) Efficacy of the CAs, in our studies we increased the payload capacity of the contrast material *via* grafting iodinated molecules by covalent bond to the oily core of the nano-emulsions, preventing them from leaking out after formulation. At delivering high amounts of contrast medium, small injected doses are sufficient to improve the contrast enhancement. The efficiency also depends on their targeting to desired cells/tissues of interest, this can be achieved by passive targeting mechanism that has significant correlation with the physicochemical properties of the

---

nanoparticles. As well as active targeting mechanism in order to bioconjugate them with specific bindings and avoiding the undesired locations.

v) The end product should be affordable to the patient, so that the price depends largely on few preparation steps combined with environmentally friendly synthesis. To this end we proceeded very simple esterification reaction followed by low energy spontaneous emulsification technique.

This PhD thesis encompasses several integrated points allowing deeply investigate the basic requirements needed for the nanoparticulate systems as described above to enhance their efficacy, biocompatibility, how to increase their blood circulation times, and so on. Tailoring the nanoparticles is crucial parameter since it potentially affects the *in vivo* biodistribution and pharmacokinetics. Therefore the size, the shape, the surface chemistry the surface charge, etc. must be conditioned and studied to deliver the nanoparticles bearing active pharmaceutical ingredient API to the target site.

These following studies have mainly been applied on iodine-containing nano-emulsions as efficient contrast agents for X-ray CT imaging and to investigate the *in vivo* pathway of such NPs, their half life times, active and/or passive accumulated sites and elimination pathway mechanism. In addition, to evaluate their efficacy and cytotoxicity in both *in vitro* and *in vivo*.

In the first study (chapter 1.2), we will present new developed contrast agents (efficient, nontoxic and blood pool CAs) and study the relationship between the chemical structure of the constituted nano-emulsions in function of their biodistribution and pharmacokinetics. We will select two oils (monoglyceride (Capmul<sup>®</sup> MCM C8) and triglyceride (castor oil)) and will modify them by triiodobenzoic acid thanks to the free hydroxyl groups of the oils forming iodinated oils. Next, the formulation of both iodinated molecules by spontaneous emulsification technique in presence of cremophore elp as surfactant, keeping in mind the surfactant/oil ratio (SOR%) controls the size of the final nano-emulsion. This is why, two formulations will be optimized to produce good monodispersed particles, 131 nm of iodinated monoglyceride nano-emulsion and 200 nm of iodinated castor oil. They will be characterized by DLS and TEM and *in vitro* X-ray attenuation (HU) values of iodinated NEs will be evaluated by preclinical X-ray  $\mu$ -CT demonstrating high iodine concentration loaded as high as 96 mgI/ml and 76 mgI/ml for both monoglyceride and triglyceride respectively. MTT cytotoxicity experiments and cellular uptake

---

studies will be performed on three different cell lines, namely HeLa cells, hepatocytes (BNL-CL2) and murine macrophages (RAW264.7). The results show negligible toxicity for both emulsions and monoglycerid NE tends to penetrate the hepatocytes more than spleenocytes, unlike the castor oil NE that is remarkably uptaked only by murine macrophage cells. The following, they will be intravenously administrated to mice showing high contrasting in the heart after administration immediately and will circulated in the blood stream up to 9 hours ( $t_{1/2}$ ), then will be eliminated from the blood and accumulate into liver and spleen organs. The coherent results of the *in vitro* and *in vivo* data ensure that the biodistribution and the pharmacokinetics of the nano-emulsions are influenced by the chemical nature of their oily cores.

The second study will outline how the size of the nano-emulsions affect *in vitro* (interaction with cells) and *in vivo* biodistribution and/or the toxicity by using X-ray micro-computed tomography. Iodiated vitamin D<sub>3</sub> (cholecalciferol) will be the contrast agent used to achieve this goal. Two different sizes, 55 nm and 100 nm of iodinated vitamin D<sub>3</sub> nano-emulsions will be prepared based on the different weight ratios between iodinated vitamin D<sub>3</sub> and labrafac oil which introduced to improve the homogeneity between the oil phase and the cremophore elp before adding phosphate buffer saline (aqueous phase). The resulted nanodroplet nano-emulsion characterizes by DLS to measure the size the droplet. Cell viability and cellular uptake studies will be performed on two cell lines hepatocytes and macrophages as mentioned above. Next, the iodinated nano-emulsions will be i.v. administrated to the mice revealing interesting results by using X-ray scanner coherrently suited with the *in vitro* observations. We will show finally that the size of the nano-emulsion has negligible impact on the pharmacokinetics and biodistributions, but has real affect on toxicity.

The aim of the following proposed work is to investigate to what extent the surface charge likely to modulate the *in vivo* pathway and/or the toxicity of the nanoparticles. This work will be conducted in *in vitro* (HeLa cells) and *in vivo* (mice) models. To this end, We will formulate different kinds of nano-emulsions *i.e.* neutral, positive and negative charge nano-emulsions based on iodinated oleate nano-emulsions. The lipophilic polymer poly(maleic anhydride-alt-1-octadecene) (PMAO) will be solubilized in the droplet core, and able to hydrolyze at the oil / water interface. physico-chemical methods, surface tension and zeta potential measurements,

---

size and morphology will be adapted by DLS and Cryo-TEM. Beside the quantification of the carboxylic groups by using (methylene blue dye method) will be performed. *In vitro* studies reveal that the presence of carboxylates at interface has a heavy impact on the interactions with cells, as the internalization of negatively charged droplets is much higher than neutral ones. This difference is confirmed with longitudinal studies performed *in vivo* in mice after i.v. administration, followed by X-ray imaging, the surface modification resulted in a significant difference in pharmacokinetics and biodistributions, with enhanced spleen and liver uptake. In this work we establish the proof of concept of a new method for functionalizing lipid droplets, and demonstrate that surface modification can have a significant impact on their interaction with cells, pharmacokinetics and biodistribution *in vivo*. We will compare these results with the positively charge nano-emulsion, in the presence of chitosan layer deposited on the nanodroplets surfaces. In the supplementary part below, we will show that no interaction (no cell penetration) at all in case of the positively charged nano-emulsions.

The fourth study aiming to functionalize the nanodroplet nano-emulsion with amino groups presented in the oil/water interface of the nanocapsules. Very simple and novel method applied thanks to aminopropyletrirthoxysilane (APTES) as a precursor to cover the droplet by silica shell ended by active functions (NH<sub>2</sub>) The idea here is to achieve active targeting technology by crosslinking the amino droplets with carboxylate ligands to target specific receptors. The generated nanocapsules will be characterized by DLS and TEM beside other microscopic and spectroscopic techniques. Thereafter, the amino groups on the droplets surfaces will be quantified precisely by fluorescamine dye method. The following step will be the conjugation of amino capsules with coumarine blue (carboxylic dye ligand model). The formation of the peptide bonds will be confirmed by fluorescence correlation spectroscopy (FCS) and free resonance energy transefer analysis (FRET).

In the last section, we will design a multifunction polymeric nanoparticles in one step synthesis by *in situ* chemical oxidative polymerization to pyrrole monomer. The base of this study is to encapsulate ketoprofen with high concentrations as hydrophobic drug model into polypyrrole nanocomposites, containing magnetic particles which came from the precursor ferric chloride FeCl<sub>3</sub>.6H<sub>2</sub>O to add magnetism properties to the nanoparticles. Meanwhile they will be externally

---

coated by polyethylene glycole shell to increase the hydrophilicity and the biocompatibility. The generated NCs, then will be characterized by TEM, SEM, DSC and FTIR instrumentations. The encapsulation efficiency and the drug release studies will be undertaken as well as the relaxometry will be assessed.



---

---

# *Chapter one*

---

---

## **Chapter 1.1: Nano-emulsions for drug delivery and biomedical imaging**

In this review we will discuss in details the preparation methods used for the nano-emulsion formulations. We will focus on the fundamental advantages of the nano-emulsions that making them potential candidate in the biomedical applications. The tunable size, the nontoxicity, the biodistribution and the high payload capacity of lipophilic molecules in their cores, all these characteristics made them to be among the nanocarriers that have successful clinical advances. This review aims to present a general overview about the all aspects of the nano-emulsion starting from their different formulations followed by biomedical applications, including clinical applications. Nano-emulsions serve as efficient contrast agents by encapsulating radiopaque molecules for X-ray CT imaging, or containing lipophilic fluorescent dyes in their cores. Their diagnostic applications extended to magnetic resonance imaging (MRI) when they incorporate iron oxides or  $Gd^{3+}$  chelates. Moreover, nano-emulsion offer real potential as theragnostics. Due to the vast number of applications, they considered as a promising nanoprobes in nanomedicines.

## Abstract

Over the last decade, nano-emulsion has gained a considerable interest in biomedical applications. The reason is simple, and lies in the combination of several advantages of this nano-carrier. Nano-emulsion consists of a dispersion of oil nano-droplets in a water phase, sizing from 20 to 200 nm. First advantage of nano-emulsions is their huge stability; Second is their very simple formulation; Third is their non-toxicity; And fourth is their very important loading capability of lipophilic or oil-soluble molecules in the oily core of the nano-droplets. On the other hand, if the formulation is easy, tailoring the nano-emulsions for a given application, optimizing the processes, functionalizing the droplets surface, and targeting organs or cancerous tumors remains a challenge. This chapter aims to draw an overview of the different aspects of nano-emulsions formulations and applications. A first part regards the different fabrication processes, followed by biomedical applications of nano-emulsions, *in vivo* fate, biodistribution, pharmacokinetics, targeting, applications as nanomedicines and drug delivery systems. Clinical applications of nano-emulsions are also discussed, as well as their applications as contrast agent for the main different imaging modalities, X-ray imaging, fluorescence imaging and magnetic resonance imaging.

## Keywords

Nano-emulsion; Formulation; High-energy method; Low-energy method; Nanomedicines; Targeting; Surface functionalization; Biomedical imaging.

## 1. Introduction

Conventional emulsions, also called macro-emulsions, are typically sizing around the micrometer or larger. This is advantageous as regards the formulation process since they can be simply generated with conventional mechanical methods, like rotor-stator devices, but disadvantageous as regards their stability. Size range of macro-emulsions originates many physical destabilization processes, mainly gravitational-based phenomena that favor droplet flocculation and ultimately coalescence. On the other hand, the term “nano-emulsions” refers also to emulsions with the same structure than macro-emulsions but with drastic differences in both their stability properties and formulation processes. First, nano-emulsions (also known as miniemulsions, fine-dispersed emulsions, submicron emulsions and so forth) can be formulated from 10-20 nm up to 200-300 nm. In general, emulsions are thermodynamically unstable systems because the free energy  $\Delta G_f$  is greater than zero. The physical destabilization of emulsions is related to the spontaneous trend to reduce interfacial area between the two immiscible phases. The minimization of interfacial area is attained by two mechanisms: (i) flocculation generally followed by coalescence, and (ii) Ostwald ripening. The global expression  $\Delta G_f = \gamma \Delta A - T \Delta S_f$  (with  $\gamma$  the water-oil interfacial tension,  $\Delta A$  the water-oil interfacial area gained with emulsification,  $T \Delta S_f$  the entropy of droplet formation), means that the emulsion instability only comes from  $\Delta A$ .

In the case of nano-emulsions, the stability comes from two phenomena; their nano-scale size range inhibits the effect of gravitation to the benefit of Brownian motion, and induces the predominance of the steric stabilization between droplets. As a consequence, Ostwald ripening is the only process that destabilizes the droplet giving a typical stability over several months. Actually, this kinetic stability is the main typical characteristic of nano-emulsions, making them prime candidate for numerous applications from nanomedicine, pharmaceuticals, to agro-food industries. In nano-emulsion systems, the very small size of droplets will prevent the droplets undergoing reversible processes like flocculation and creaming (or sedimentation), and thus preventing the coalescence. However, the stability of nano-emulsions actually appears as a paradox since  $\Delta A$  of nano-emulsions is definitively higher than the one of macro-emulsions, thus resulting in higher  $\Delta G_f$ . On the other hand, the inhibition of the destabilization processes predominates, resulting in very stable nano-emulsions. Stability of nano-emulsions is an experimental fact, and very easily obtained with simple formulation procedures.

As we saw above the main property of nano-emulsions is their stability, but another interesting point due to the Brownian properties of the droplets is their ability to diffuse in all the available volume to give a very homogeneous dispersion of droplets. Therefore after encapsulating a given active principle (e.g. drugs, contrast agents) in oil nano-droplets, these hydrophobic or lipophilic molecules are homogeneously dispersed in the aqueous phase. The nano-scale of nano-emulsions droplets is also an advantage for biological and medical applications since they have privileged interactions with living cells, tissues, organs of pathologies, and they are as well compatible with the parenteral administration. In that way

---

nano-emulsions naturally found many applications in various fields and notably in nanomedicines as lipid nano-carriers.

## 2. Formulation processes

### 2.1. Generalities

Emulsification consists of dispersing one fluid into another non-miscible one, creating interface through the increasing of  $\Delta A$ . The properties of the generated emulsion, *i.e.* size distribution and stability, are closely linked not only to the composition, chemical nature of the phases and stabilizing agents, ratio of viscosities of the dispersed and bulk phases, but also on the formulation protocol, temperature and time of processing, shear rate, cooling time, and type of emulsification apparatus. In addition, besides these criteria, the emulsion stability is strongly related to the size distribution of the dispersion after formulation. In the case of nano-emulsion, monodispersity will have a direct impact on the inhibition of Ostwald ripening, since the difference of the pressure between the bigger and smaller droplets will be reduced. The formulation of emulsions is conditioned by the energy supplied by the formulation device. Actually, most of apparatuses currently used for the fabrication of macro-emulsions do not allow decreasing the droplet size below 1  $\mu\text{m}$  because of low emulsification yields due to the dissipation of the mechanical energy in heat. It is for example the case of rotor / stator apparatus like UltraTurrax<sup>®</sup> and colloidal mills. Only some methods allow the fabrication of nano-emulsions. Table 1 gathers the main methods for the formulation of emulsions along with the range of the generated droplet sizes (with limiting  $f_v^d < 30\%$  to avoid droplet recombination during processing).

**Table 1:** Summary of the accessible sizes in function of the emulsification apparatuses (\* the ones generally compatible with the formulation of nano-emulsions).

Emulsification method	Typical size
Mechanical stirring	1 $\mu\text{m}$ – 15 $\mu\text{m}$
Colloidal Mills	10 $\mu\text{m}$ – 50 $\mu\text{m}$
* High-pressure homogenization	50 nm – 5 $\mu\text{m}$
Membrane	0.2 $\mu\text{m}$ – 100 $\mu\text{m}$
* Microfluidizer <sup>®</sup>	10 nm – 1 $\mu\text{m}$
* Ultrasonication	20 nm – 1 $\mu\text{m}$
* Low-energy methods	10 nm – 200 nm

It follows that the three main possibilities for the formulation of nano-emulsions are: (i) high-pressure homogenization, (ii) ultrasound based methods (using sonotrode), and (iii) low-energy emulsification. In the following sections, these processes will be presented and the conditions to reach nanometric-sized droplets will be discussed. It is to be noted that in the case of high-energy methods (high pressure or sonication), the formulation of nano-emulsions obligatory follows a preliminary step of pre-emulsification. The initial phase containing all components like emulsifiers, additives, and maintained at controlled temperature, undergoes

a stage of dispersion that consist in creating a strong shearing that favors the breaking-up of the drops. Apparatuses indicated for this step are generally turbines type (*e.g.* Rushton type), that provide a high shearing along with an efficient recirculation of the liquid, giving rise to a premix emulsion between 10 and 100  $\mu\text{m}$ . Then, the second step, homogenization step, will decrease the droplet size below 500 nm, narrow the size distribution, eventually improving the stability.

## 2.2. High-pressure methods

High-pressure homogenization is a very common industrial process, notably in the formulation of agri-food liquid or semi-liquid products. The premix emulsion is projected under high pressure from 30 to 1'000 bar through a homogenization head of particular geometry (see Fig. 1), and undergoes a combination of elongation and shear flows, impacts, and cavitations. The resulting size distributions are reproducible with a mean size ranging from 50 nm to 5  $\mu\text{m}$ .

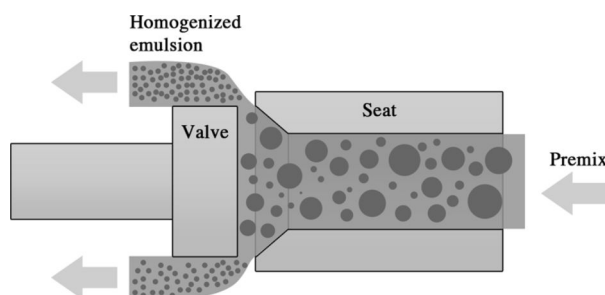


**Figure 1:** Conceptual representation of high-pressure homogenizer chamber.

High-pressure emulsification arises from the competition between the droplets break-up due to deformation enhanced by the high-speed flow, and their recombination due to coalescence enhanced by collisions. The main parameters influencing the size and dispersity of the nano-emulsions are (i) the number of passages in the homogenizer, (ii) the value of the volume fraction of dispersed phase  $\phi_v^d$ , (iii) the value of the pressure applied, and (iv) the concentration  $C$  of stabilizing agent like surfactants, proteins, polymers. We can note that the stabilizing agent concentration  $C$  is a critical parameter, since, if  $C$  is lower than  $cmc / 10$  ( $cmc$  is the critical micelle concentration), the droplet size does not decrease lower than 300 nm. This is due to the predominance of the coalescence against the stabilization of the fragmented droplets. On the other hand, when  $C$  is typically higher than  $cmc \times 10$ , the surfactants molecules are efficient to stabilize the droplets formed after fragmentation, allowing to decrease the size up to 50 nm. Of course, a further increase of  $C$  can reach the interface saturation that cannot allow a further decrease of the size. In addition, as easily understandable, this is only in this regime of surfactant concentration that the effect of the applied pressure is effective, actually the size follow a power law [1].

### ***2.3. Ultrasounds-based methods***

This formulation method consists in applying a strong ultrasonic energy in a small volume sample under circulation. This is performed with a specific sonotrode that concentrate the energy in a surrounding volume (see Fig. 2). Ultrasonic emulsification is thus only efficient in this small volume around the sonotrode, and thus the fluid circulation in the sample is still necessary for optimizing the process, and as well involves a minimum time before stabilization of the droplet sizes. The frequencies of ultrasound are from 16 kHz to 1 MHz, and generated by a plane surface vibrating on a sinusoidal way with amplitude between 1 and 200  $\mu\text{m}$ . Cavitation bubble alternatively undergo contraction and dilatations, and the micrometric globules of the premix emulsions are broken-up by the successive implosions of the cavitation bubble. The droplet fragmentation of the droplets gradual decreases their average diameter. This is illustrated in Fig. 2 (middle) that shows the nano-emulsion mean size describes an exponential decay up to stabilization, for a simple system composed of medium chain triglycerides (oily core), nonionic surfactant (stabilizing agent) and water as continuous phase [2]. The figure shows the follow-up of the mean size and polydispersity indexes (PDI). PDI reflects the quality and monodispersity of the dispersion, such that a suspension is considered of good monodispersity (good quality) if the value of PDI is below 0.2-0.15, and of very good monodispersity (very good quality) if the PDI is below 0.1. The exponential profiles reported, for a similar system can be “stretched” if the energy supplied is decreased, as illustrated in Fig. 2 (bottom). This result is actually important for understanding the process, as well as its design and optimization. If ultrasound-based technologies are compared with high-pressure homogenizers, the properties of the resulting emulsions are generally similar. However, high-pressure homogenizers are widely used in industrial processes, whereas ultrasonifiers are more adapted for the laboratory scale, research and development stages.

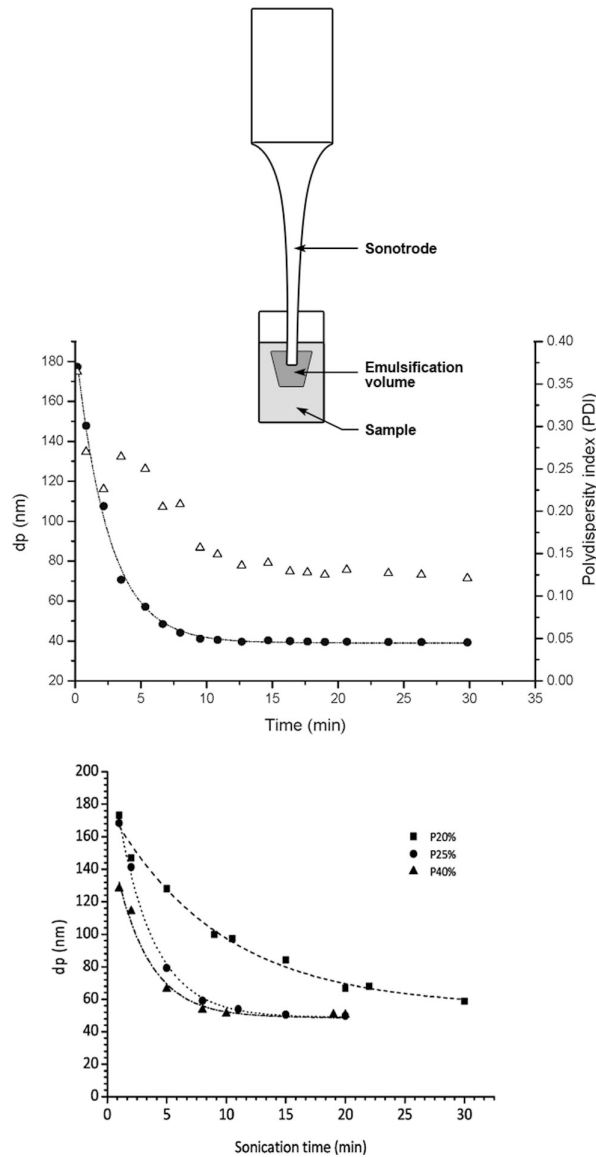


**Figure 2:** (Reprinted adapted with permission from Ref. [2]). Schematic of a sonication-based nano-emulsification process. *Top:* evolution of droplet size distribution along the sonication process: particle mean diameter (black disks), and polydispersity index (open triangles). *Bottom:* evolution of droplet size distribution along the sonication process in function of the power of the sonicator.

## 2.4. Low-energy methods

Low-energy methods allow the formulation of nano-emulsions similar to those described above (with high pressure and sonication methods), but without mechanical energy. In this case, the increase of  $\Delta A$  is obtained by taking benefit of the intrinsic physicochemical properties of the phases and stabilizing agents.

Low-energy methods are simple, cost-effective formulation processes and are very attractive. However, the low-energy methods are very studied but almost only on the fundamental point of view, and much less used in industrial processes than high-energy ones. This is likely due to several points, like the fact 1) that these methods only allow nano-emulsification and not

homogenization of premix (*e.g.* not suitable for homogenizing milk), or 2) that the physicochemical properties of the dispersion cannot always be finely controlled, or finally 3) that they involve a non-negligible amount of surfactants that is not always compatible with all the specifications (impact on the taste in agrifood industries, or induce a toxicity, etc.).

Low-energy methods in general are based on spontaneous emulsification, or self-emulsification. It is to be noted that other low-emulsification methods are reported, like phase inversion temperature methods of solvent diffusion, but it has recently been shown that their principle is based on the spontaneous emulsification described below. Spontaneous emulsification occurs when two immiscible fluids are brought in contact and gently homogenized. In a few seconds a kinetically stable nano-emulsion is formed. In contrast with high-energy methods, spontaneous emulsification allows a similar gain in  $\Delta A$  without energy input. Spontaneous emulsification takes benefit of the physicochemical properties of the water, oil, and surfactant for generating the nano-droplets through a spinodal decomposition-like process.

Numerous explanations aimed understanding of this phenomenon, however, it is only recently than a universal and simple mechanism was proposed [3], thus including all the spontaneous emulsification processes. Illustrated in Fig. 3, the spontaneous emulsification was attributed to the penetration of the water phase in the oily one, resulting in breaking-up the oil phase at the nanometric scale.

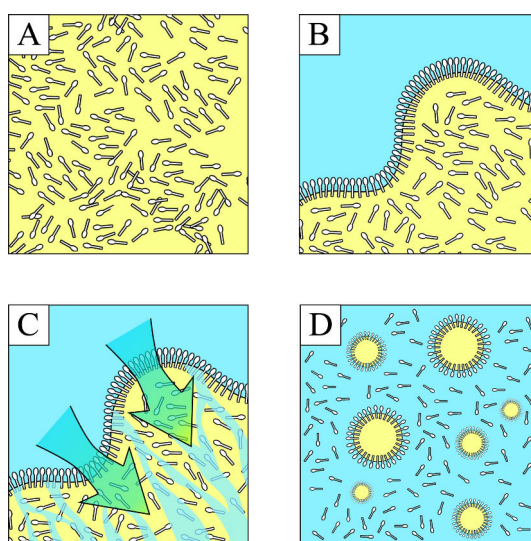


**Figure 3:** (adapted from Ref. [3]) Schematic representation of the mechanism driving the spontaneous emulsification.

Let us consider the oil phase homogeneously mixed with surfactant molecules in specific conditions (*e.g.* temperature) that make them lipophilic (Fig. 3A). Then, once this surfactant / oil phase is in contact with water (Fig. 3B), aqueous phase penetrates the oil one solubilizing the surfactant molecules (Fig. 3C). Surfactants stabilize the newly-formed oil nano-droplets generating the nano-emulsions (Fig. 3D), generally sizing from 20 nm to 200-300 nm. In addition, spontaneous nano-emulsions give suspension with a very good

monodispersity excepted when we reach the limit of the feasibility region, *e.g.* at low surfactant concentrations, where the polydispersity indexes suspensions can increase higher than 0.2-0.3. It follows that spontaneous emulsification is driven by the physicochemical properties of the surfactant and its solubility towards the oily and aqueous phases. On the other hand, when a spontaneous emulsification process is efficient to give nano-emulsions, its own size can be finely controlled by the surfactant concentration, namely the higher is the surfactant concentration, the lower is the average nano-emulsion size [3]. It is noteworthy that not all the surfactant/oil couples are compatible with the spontaneous nano-emulsification, and this is one of the main reasons why sometimes it is necessary to shift to high-energy methods. However, we can define some necessary conditions for the spontaneous emulsification, like the complete solubility of the surfactant to the oily phase. This affinity can be relative and be artificially improved with temperature, for example with nonionic surfactants that become lipophilic at high temperature (above their cloud point in general). Then with a sudden mixing with the aqueous phase at room temperature (*i.e.* colder water) the surfactant affinity for oil is suddenly decrease beneficially to the one of water, enhancing the water penetration. Another important factor that impact on the process is simply the chemical nature of each compound, not only the properties of nonionic surfactant but also the nature of oil, the nature of surfactant, and the additives in the aqueous phase.

### **3. Applications of nano-emulsions for drug delivery and biomedical imaging**

#### ***3.1. Nano-emulsions as nanomedicines***

The drugs used for Humans present a main pharmacological activity, but also adverse effects. Thus improving the efficiency of a drug by inhibiting its adverse effects results in increasing its benefit-to-risk ratio. Nanotechnologies, in general, and nano-emulsions being a realistic solution, allow increasing its benefit-to-risk ratio in modifying the becoming of the drug in the organism. This aspect is particularly crucial in antitumor treatments, aiming a very specific targeting on tumor cell without affecting healthy cells. The main strategy consists in associating the drug with a nano-carrier, which will influence the drug biodistribution and elimination. In this case, the drug may follow the *in vivo* fate of the nanocarrier, closely related to its physicochemical properties like size, electrostatic charge, chemical composition, functionalization. Optimizing this operation results in increasing the targeting of the drug towards the tissues in which we want this last one has to be active, increasing the time in contact, while limiting its diffusion to those it could be toxic. This targeting ideally improves the drug efficiency. Actually, the design, the development and the optimization of an efficient vector are not only related to the understanding and expertise in the formulation process of the nanocarriers, sometimes delicate at the nanometric scale, but also on the knowledge of the different physiological, histological, biological and biochemical aspects of the tissues in living organisms. Actually, the biodistribution of the drug will be driven by the interactions and *in vivo* behavior of the nanocarrier in the body. In addition, in function of the

---

administration route, the nano-carrier will be in contact with different tissues and its pathway can be different.

As regards lipid nano-emulsions as drug delivery systems, and considering that the potential drugs are solubilized in oil cores without premature leakage, their targeting properties will be defined by the interactions of the lipid droplets in function of the administration route. Let us now focus on the different administration ways, and evaluate the different potentialities for targeting lipid nano-droplets.

Intravenous administration constitutes the main administration route adopted for research investigations or preclinical studies since blood is the ultimate location desired for a drug before targeting. However, beside physiological compatibilities like sterility, osmolarity and pH, the size of the nanocarrier is a main issue in their design. Once in the bloodstream, the nano-droplets will circulate in the blood pool, migrate to the heart by the vena cava, then in the lung to be back in heart by the pulmonary vena, and in the arterial circulation by the aorta. In this context, the risk of pulmonary emboli that arises above 5 mm is prevented by the size of nano-emulsions below 200-300 nm. Then, their elimination is performed by the macrophages of the reticuloendothelial system (RES) and particularly in liver and spleen. Kupfer cells in liver are particular macrophages very efficient for nanoparticles uptake; they are located in the border of hepatic sinuses, and constitute 25% of the liver cells and 90% of the macrophages in the body. Spleen is well an efficient trap for nanoparticles. Then, their elimination is performed through the bile by transcytosis within the gall bladder. On the other hand, when the particles are smaller than 5-10 nm they are filtrated by kidneys, and this happens in some applications with, *e.g.* micelles or small hydrophilic contrast agents.

It appears that the therapeutic efficiency of drugs can be improved by their potential targeting through nano-carriers, and thus depend on their time of circulation in the blood stream. The longer is this circulation time, the longer will be the contact with the target tissues. It follows that increasing the circulation time of the nano-carriers in bloodstream (*i.e.* making them stealth towards RES) is a key factor for improving the drug efficiency. Actually, before the macrophage uptake by phagocytosis as discussed above, the nanoparticles are recognized through opsonization, by fixation onto their surface of blood proteins called opsonin. Two parameters are known to inhibit this phenomenon, the size of the particles and the chemical nature of the surface. Indeed, the limit of 100 nm is generally considered as an efficient limitation of the RES recognition, as well as the decoration of the surface with neutral hydrophilic polymers like polyethylene glycol (PEG).

In the case of nano-emulsions, we have seen that the different formulation processes give rise to oil nano-droplet suspensions of similar physicochemical properties. Therefore the size and surface composition should be mainly related to the choice of stabilizing agent. Precisely, a large class of stabilizing agents, *i.e.* nonionic surfactants, fulfills such specifications and allows the simple formulation of small PEGylated nano-droplets. Nonionic surfactants are generally composed of a PEG chain as hydrophilic part connected to a more or less simple aliphatic chain. Owing to their high surfactant properties (HLB > 15-16) they allow to reach very small size below 200 or even 100 nm, and owing to the PEG part of the surfactant the resulting droplets are naturally protected from opsonization. Spontaneous emulsification has

emerged as a very efficient method to produce stealth nano-emulsion droplets. Some examples are reported in Fig. 4, for different kinds of nanoparticles comparing nano-emulsions, polymeric nanocapsules and inorganic nanoparticles. Their morphologies are illustrated in TEM micrographs and the longitudinal quantification of their concentration in blood are reported for all nanoparticles.

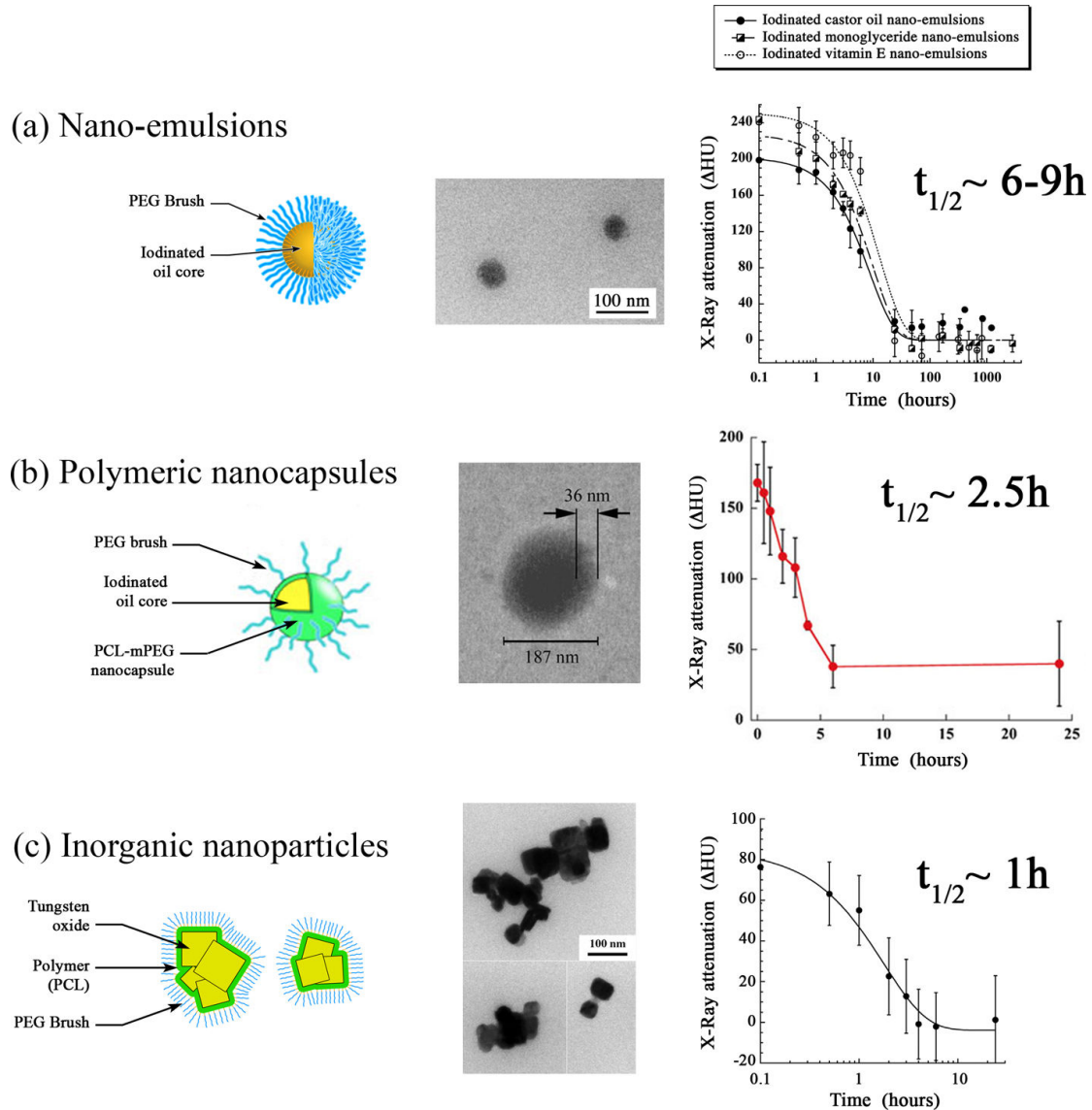


**Figure 4:** (adapted from Ref. [4-6]) Comparison of the residence time in bloodstream for different kinds of nanoparticles: (a) nano-emulsions, (b) polymeric nano-capsules, and (c) inorganic nanoparticle. The figure presents a schematic illustration of the nanoparticle structure (left), transmission electron micrograph (middle), and X-ray attenuation (proportional to the blood concentration of nanoparticles) in function of time post-intravenous administration in mice.

In fact, these nanoparticles differ in their mean sizes, with nano-emulsions around 80 nm, and, inorganic nanoparticles or polymeric capsules around 200 nm. However we have to consider that the size distributions of these kinds of suspensions largely overlap, and thus the average size should not be considered as main factors influencing the blood clearance. Another basic factor that impacts on the blood pharmacokinetics, beyond the surface

functionalization, is the nature of the particle core itself. In Fig. 4 (a), blood concentration of nano-droplets (*i.e.* proportional to X-ray contrast) are compared for droplets of similar size and made with the same surfactant (PEG-35 ricinoleate) but with different iodinated oils constituting their core. One can see a slight difference in the curve profiles, resulting in half-lives varying from 6 h to 9 h. However, when the surface is drastically modified with a polymeric capsule (Fig. 4 (b)), the clearance is much more decreased up to 2.5 h, and finally reaches 1 h with inorganic (tungsten oxide crystals) (Fig. 4 (c)). Obviously the nature of the nanoparticles influence the opsonization process due to the surface charge, electronic density or protein attractions by other low-energy forces [7], but we can note as well that in the case of nano-emulsions the PEG coverage is actually optimal since any other material enters in the surface composition.

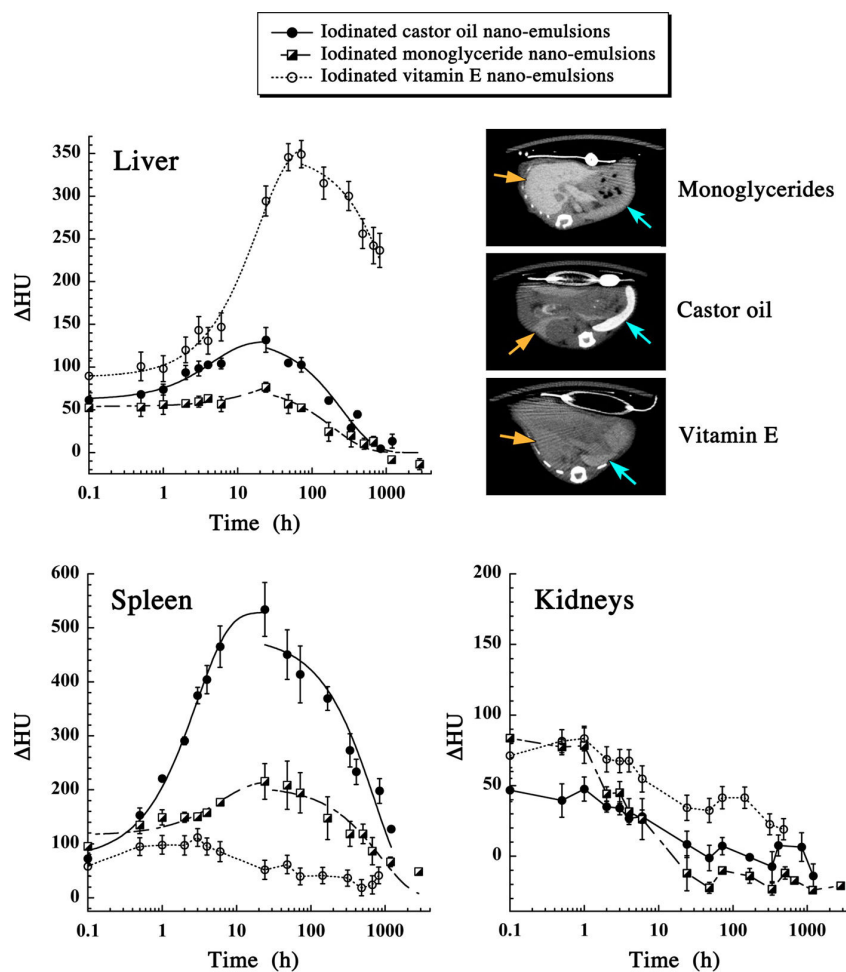


**Figure 5:** (adapted from Ref. [4]) Quantification of the droplet concentration in liver, spleen and kidneys (through X-ray attenuation, DHU) after *i.v.* administration of iodinated nano-emulsions with similar size and physicochemical properties, but different oil cores made with iodinated vitamin E, iodinated castor oil, and iodinated monoglyceride. To illustrate the differences in contrast at 24 h post-injection, transverse slices through the liver and spleen are presented. Liver is indicated by orange arrows and spleen by blue arrows ( $n = 3$  mice/group).

Besides the considerations on blood circulation time, the drug targeting process is associated to the nano-carriers accumulation into the aimed tissues during this blood circulation phase.

This means that it is related to accumulation phenomena, specific to the nature of the nano-carrier and/or surface functionalization. This accumulation can be the direct consequence of the size, chemical nature or charge of the nano-carriers (so-called passive targeting), but can also be induced by the decoration of the surface by ligands specific to the receptors overexpressed in the target tissues (so-called active targeting). Sometimes the natural elimination pathways of the vectors towards the liver or spleen are used for the specific drug delivery in these organs, and can be also called passive targeting (of liver or spleen). In this case, we have disclosed the passive accumulation in these organs thanks to X-ray imaging that allows the longitudinal non-invasive *in vivo* quantification of the biodistribution. Figure 5 illustrates the biodistribution in liver, spleen and kidney of nano-emulsions with similar size and physicochemical properties, but different oil cores made with iodinated vitamin E, iodinated castor oil, and iodinated monoglyceride (as in Fig. 4 (a) above). The quantification of their biodistribution with time emphasize drastic differences between the different organs, iodinated vitamin E is more accumulated in liver while iodinated castor oil prefers spleen, and on the contrary iodinated monoglyceride does not show an organ specificity and is simply more rapidly eliminated from the organism. It follows that the passive accumulation of nano-droplets through elimination pathway is a powerful tool for imaging pathologies actually located in these organs as described in [8-11] in liver and spleen.

On the other hand, passive targeting includes the passive accumulation in tumors, for instance implanted subcutaneously, and considered to be undergone through the enhanced permeation and retention effect (EPR effect), targeting. EPR effect results from the passive accumulation of drug or nanocarriers due to their extravasation through leaky vasculature. It is well established that for certain pathologies like tumors, infarctus, inflammation areas, and under certain circumstances, the endothelial lining of the blood vessel wall becomes more permeable than in the normal state [12, 13]. Thus, large molecules and nanoparticles ranging from 10 to 500 nm can leak from the vessel and accumulate in interstitial space, *i.e.* co-localize with the pathology. Actually, the efficiency of the passive EPR tumor accumulation is basically related to the time of the agent in bloodstream: the higher is the exposure, the higher is the accumulation. Thus, a prolonged time in blood is obtained with non-renal clearable entities (size > 5 nm) [14] decorated with well solvated and flexible polymer chain (PEG) was shown to slow down their opsonization and clearance by the RES [15, 16]. The major examples reported in literature refer to liposomal formulations that accumulate in subcutaneous xenografted tumors [17-19]. The direct visualization of this accumulation phenomenon is provided by X-ray imaging techniques, and reveals the gradual enhancement of the contrast over time in the tumor surrounding regions. Some examples of EPR targeting with nano-emulsions were reported and have proved the compatibility of lipid droplets with EPR effect in general. For instance, in Ref. [20], the authors report the formulation of nano-emulsions made with PEGylated surfactants (PEG 660-hydroxystearate) stabilizing medium chain triglyceride core. These lipid nano-droplets encapsulated anticancer molecule, docetaxel (DTX), at a concentration of 3wt.% of the nano-droplet. The passive EPR accumulation the model tumor occurred thanks to the nano-carriers, studied and compared to a commercial control formulation (*i.e.* solubilized in micelles) of DTX (Taxotere<sup>®</sup>, TXT).

---

C26 colon adenocarcinoma cells in growth medium were injected subcutaneously in three different locations on the back of each mouse, which produced three separate tumors. The formulations were administered when each tumor grew to a volume of about 20 mm<sup>3</sup>, approximately 10 days after cell inoculation. These results are reported in Fig. 6, where the two above-described formulations were injected at similar doses of 15 mg/kg, comparing the pharmacokinetics and biodistributions of DTX in tumor. The results disclose a clear-cut and significant accumulation in tumor of the DTX encapsulated in nano-emulsions compared to the control roughly constant, while in liver, spleen and kidney the two curve profiles are similar. This clearly evidences the EPR effect induced by the lipid nano-carrier.

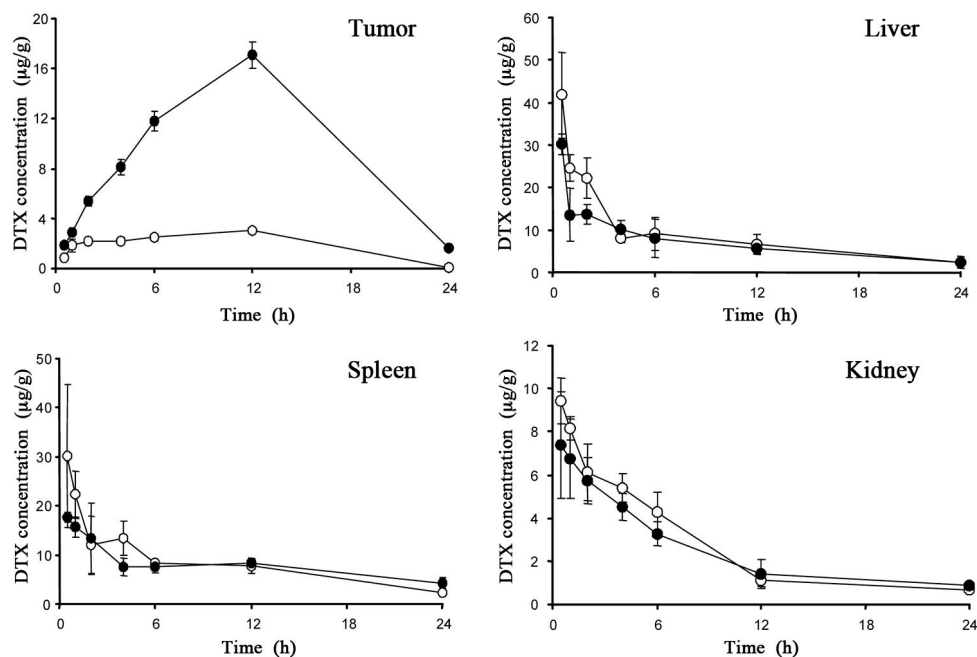


**Figure 6:** (adapted from Ref. [20]) Illustration of the passive targeting of nano-emulsions to xenografted subcutaneous tumor in mice after i.v. administration of nano-emulsions encapsulating DTX (closed circles) and of control injection of TXT (open circles). The drug dose level of 15 mg/kg and the concentration in the nanocarrier is 3wt.% (n = 4 mice/group).

Actually in literature, EPR accumulation is generally illustrated with liposomes, for example in biomedical imaging [17-19, 21]. Herein for nano-emulsions, a similar size range and lipid nature gives rise to the similar efficiency in the passive accumulation of lipid nano-emulsion droplets in tumors, that can allow to draw a realistic parallel with the liposomes EPR accumulation. As a last remark, the passive targeting of nano-emulsions, performed with post-insertion in nano-emulsion droplets of function lipids, remains anecdotal and not very efficient [22], likely due to the difficulty to increase the ligand concentration decorating the particle surface.

### 3.2. Clinical applications of nano-emulsions

Some nano-emulsions have already clinical applications and are authorized in different countries. We will present you in this part, different applications of such commercialized

emulsions. Then, a description of current clinical assays on nano-emulsions will be performed. Mainly, nano-emulsions in commercialized formulations are used to improve drug solubility in water and therefore drug bioavailability. To illustrate these facts one can mention two examples. The first is Neoral<sup>®</sup> (Novartis Pharma, Rueil-Malmaison, France), an oral cyclosporine emulsion for transplantation [23]. The second is Propofol Lipuro<sup>®</sup> (B Braun AG, Melsungen, Germany), an emulsion of propofol in soy oil for intravenous administration [24]. This last is used for anesthesia in intensive care units. Another advantages of nano-emulsions are the possibility to inject oil intravenously and to improve emulsion stability. This is for example the case for Medialipide<sup>®</sup> (B Braun Medical, Boulogne, France), a commercialized oil-in-water emulsified lipid utilized for parenteral nutrition [25]. To be administrated, strictly speaking oil droplets size should be less than 5 microns but in practice the characterizing size is the average size of the lognormal distribution meaning that the population contains droplets much bigger than the average size. It follows that nano-emulsions to be compatible with parenteral administration have a size range below the micrometer.

We identified the current clinical assays on nano-emulsions using the Cochrane library. It is noteworthy that in this part, we will not present the assays using nano-emulsions as model for the evaluation of different treatments or drugs on hyperlipidemia. Experiments based on *ex vivo* model like explanted human tooth are likewise not considered.

Actually, these clinical assays could be classified in 3 applications: anesthesiology, dermatology and vaccines. One publication concerned a comparative study of emulsified propofol with Solutol<sup>®</sup> HS15 (BASF) in nanometric size and propofol in soybean oil emulsion for anesthesia during endoscopy. This phase II assay was performed on 150 patients (being 33 to 54 years old) [26]. The authors observed equivalence between emulsified propofol and propofol in nanometric emulsion form concerning its efficacy, safety and the side effects. However, it is worth to note that it was a lower incidence of pain during injection with propofol in nanometric emulsion form: 53.3 % of patients instead of 82.7 % with propofol in soybean oil emulsions. In additions, the incidence of nausea and vomiting was reduced with nano-emulsified propofol from 10.7 % to 2.7 % of the patients. A lack of this work is the absence of comparative study with Propofol Lipuro<sup>®</sup>, propofol emulsion containing medium-chain triglycerides [27]. Indeed, this last formulation induced less injection pain than non-lipid forms of propofol. A hypothesis was a reduction or an absence of free propofol with Propofol Lipuro<sup>®</sup>. With a comparative study between Propofol Lipuro<sup>®</sup> and nano-emulsified propofol with Solutol<sup>®</sup> HS15 could be a good approach to verify this hypothesis.

Concerning dermatological applications, different applications of nanometric emulsion based drugs are clinically tested. A first clinical assay was conducted on 482 subjects for the development of drug against cold sores [28]. The developed active substance (NB-001) was formulated at different dosages (0.1, 0.3 or 0.5 wt.%) in nanometric emulsions. At the first signs or symptoms of a cold sore episode, this medicine was applied 5 times per day, approximately 3 to 4 hours apart, for 4 days. Emulsions at a drug concentration of 0.3 wt.%

---

showed the best efficiency by a 1.3 days improvement in the mean time to healing compared to placebo ( $p = 0.006$ ). This could be explained by a better skin penetration of the active substance at this concentration. Concerning drug safety, no serious side effects or dermal irritation at any concentration were observed. In additions, no active substance was detected in subject bloods. Compared to other medicine for cold sores, the observed efficacy was similar to oral nucleoside analogues and greater than topical formulations which present a reduction of healing time by only one half day. The originality of this new formulation is the lack of drug distribution in blood preventing most of side effects for an efficacy comparable to oral formulations.

The two next studies focused on drug evaluation for the treatment of distal subungual onychomycosis [29, 30]. The formulation consisted of emulsions with a mean droplet size of 180 nm containing a new active substance (NB-002). The first study corresponds to a phase II assay on 432 subjects having mild to moderate subungual onychomycosis of the toenails [30]. The treatment was applied to all toenails and on 5 mm of adjacent skin for 42 weeks. The droplet size and emulsion composition allow selective uptake into the skin without irritation via hair follicles and skin pores. In additions, the droplet size of the formulation destabilized fungal hyphae and spores leading to a formulation efficiency of 84% compared to 13% with blank emulsion. No serious side effect was observed during this assay. Nevertheless, the most observed side effect was nail discoloration and concerned globally 10 subjects on 432. The second assay is a post-hoc analysis of the first study on 227 subject to assess the post-treatment mycologic cure and effective treatment rates of a 42-week treatment regimen of NB-002 compared to vehicle [29]. At 4 and 8 weeks post-treatment, an evaluation of the treatment efficiency. At all emulsion concentration of NB-002, the mycologic cure rates 8 weeks post treatment was ranged from 4.2 to 16.9 % versus 5.3 % in blank emulsion. These assays showed clear antifungal activity with clinically significant nail clearing of NB-002. For more, the emulsion form had also an activity on treatment efficacy.

Several phase III assays concerned the use of nano-emulsions of BF200 5-aminolaevulinic acid (BF200 ALA) for actinic keratosis (AK) photo-treatment compared to a registered 5-aminolaevulinic acid cream (MAL) or placebo [31] [31-34]. BF-200 ALA (Biofrontera Bioscience GmbH) is a gel formulation of 5-aminolaevulinic acid (ALA) with nano-emulsion. This formulation was designed to prevent ALA instability and improve skin penetration [31, 32]. For the illumination, different devices were used three hours after drug administration: narrow emission spectrum LED (590 to 670 nm; Aktilite CL128<sup>®</sup>) or broad emission spectrum LED (580 to 1400 nm; PhotoDyn 750<sup>®</sup>). These assays were performed on 13 to 663 patients presenting a light to mild AK on face and/or bald scalp. The protocol included one drug application followed by a LED luminescence. In cases of residual AK lesions corresponding mostly to grade II and III AK, a second treatment was performed 12 weeks after the first [33, 34]. Then, patients were followed during 3 to 12 months to determine influence of different treatment protocols on AK recurrence [31, 33, 34]. Concerning the results, since 2010 and confirmed by all other works, the authors concluded that treatment efficacy depends on both drug design and luminescence technique. Narrow spectrum light sources presented the best results. For example, on 600 patients with MAL or

---

BF200 ALA, this technique had a healing rate compared to broad spectrum lamps of 71.5 % versus 61.3 % and 84.8 % versus 65.7 % respectively [33]. It was to note that only with placebo broad spectrum lamps had better results 21.6 % versus 12.8 % with narrow spectrum light sources. In point of view of used drug formulations, BF200 ALA presented the best efficacy compared to MAL and placebo in all assays. The healing rates on 600 patients for BF200 ALA compared to MAL were 78.2 % versus 64.2 % ( $p = 0.05$ ) with a remission rate at three months for BF200 ALA of 90.4 % [33]. This difference could be explained by the observation on 13 patients of better histological clearance at three month with BF200 ALA compared to MAL: 61.5 % compared to 38.5 % ( $p = 0.375$ ) [34]. At 12 months after last treatment, BF200 ALA showed the best remission rates at 47 % versus 36 % for MAL [33]. Concerning the safety of BF200 ALA, the observed side effects were similar with MAL [33, 34]. All these results demonstrated that BF-200 ALA is a very effective and superior to a registered MAL. In additions efficacies and adverse events are also depended to the different light sources used.

Two publications report vaccines against influenza [35, 36]. In both assays, emulsions had the role of adjuvant. In the first work, the authors used a glucopyranosyl lipid A, an emulsion designed to be an intramuscular vaccine [35]. They performed a phase I/II assay on 392 patients (being 18 to 49 years old) receiving two administrations at D1 and D21. 42 days after the first vaccine administration, up to 82% of the tested patients presented seropositivity to the different influenza stems. Concerning vaccine security, this study revealed that the half of patients presented light to mild side effects. In some cases, the authors determined serious side effects requiring the use of antihypertensive drugs. In the second work, the author used a new adjuvant W805EC corresponding to nano-emulsion. Indeed, nasal mucosa is the main entry for influenza virus [36]. The authors performed a phase I assay on 199 patients receiving a single intra-nasal administration of vaccine for 3 different influenza strains. The innovation was to design a vaccine for an intra-nasal administration in order to induce both systemic and mucosal immunity. Despite immunization process with a single administration through an original administration route, more than 70 % of the volunteers were sero-protected for the 3 influenza strains through systemic and mucosal immunity. W805EC as adjuvant presented a good tolerance during this clinical assays: absence of serious side effects and observation of side effects similar with intra-nasal administration of PBS (Phosphate buffer saline).

### ***3.3. Nano-emulsions in biomedical imaging***

Another fundamental application of nano-emulsions concerns their use as contrast agents for biomedical imaging. The formulations strategies can be actually close to the formulations of medicines, with on the whole different purposes. Imaging is an important preliminary aspect of some treatments like cancer treatment, providing real-time monitoring with minimal invasiveness and tissue destruction. Biomedical imaging is often used for prediction, screening, staging, prognosis, biopsy guidance, therapy planning, and guidance. Computed X-ray tomography, magnetic resonance imaging, fluorescence and ultrasound have been traditional techniques of anatomical imaging. Ultrasound is commonly used as an external

---

stimulus due to its accessibility, cost-effectiveness, and ability to be used in conjunction with multimodal systems. Besides, optical imaging tools, PET, SPECT, and photoacoustic imaging techniques, nano-emulsions have been widespread used in biomedical fields, daily consuming, particularly in cosmetics and even food industry owing to the huge stability, the encapsulation efficiency, and the high safety of these nano-emulsions.

As mentioned above, the key to their success hinges on their oily cores which act as reservoir allowing solubilization and nano-encapsulation of hydrophobic molecules like drugs, contrast agents, organic fluorophores, and/or inorganic NPs at very high concentrations. Other fundamental point for their applications *in vivo* is the non-toxicity since there are lonely fabricated with parenteral-compatible materials. Herein we will shed more light on specific examples to show the importance of the excellent behaviors of nano-emulsions as contrast agent for imaging. And this could be categorized into integrated classes:

### ***3.3.1. Nano-emulsions in X-ray imaging***

One of the earliest developed contrast agents-based nano-emulsions for micro-computed tomography (CT) are Fenestra VC<sup>®</sup> and Fenestra LC<sup>®</sup> in order to overcome the incompatibility of clinic products like small hydrophilic iodinated molecules. These latter undergo a rapid elimination from the kidneys causing renal failure and do not allow performing scans in preclinical studies.

Introducing the nanotechnology into the medicine made significant progress in micro-CT imaging. Over the last few years, our group has developed several efficient formulations of nano-emulsion-based contrast agents for preclinical X-ray imaging. The ideal solution to ensure a high encapsulation and prevent any release is the synthesis of oily molecules grafted with X-ray contrasting atoms like iodine, and then formulated as nano-emulsions. These droplets are coated with hydrophilic polymer (PEG) to reduce their opsonization that prolongs their residence time in the blood stream. For these applications, as discussed above, the size in the range is 50-250 nm, avoiding a fast clearance by the reticulo-endothelial system [37], but as well large enough to prevent a rapid elimination by kidneys [38]. From these considerations, some examples of iodinated nano-emulsions were proposed as contrast agents for X-ray micro CT such as iodinated  $\alpha$ -tocopherol nano-emulsions [39], iodinated monoglyceride nano-emulsions (glyceryl monocaprylate), iodinated triglyceride nano-emulsions (castor oil) [40], and iodinated cholecalciferol nano-emulsions [41] and studied *in vivo*. The preclinical investigations, briefly discussed in the previous sections, concerned the pharmacokinetics, biodistributions, toxicity and contrasting efficiencies of nano-emulsions, eventually disclosing their outstanding efficacy for X-ray biomedical imaging.

### ***3.3.2. Nano-emulsions in magnetic resonance imaging (MRI)***

It is approved that some moieties like IONPs, Gd<sup>3+</sup> chelates, and/or perfluorocarbons PFCs in combination with MRI modality are able to enhance the imaging performance. We will restrain here on the nano-emulsion formulations loading those contrast agents, and it is as

well to note that many other examples reports association of MRI contrast agent combined with imaging agents for other modalities.

Recently, a multifunctional and biodegradable nanocarrier system based on oil-in-water nano-emulsions with three different mean diameters (30, 60, and 95 nm) were developed, and used as tumor targeting agent through EPR effect [42]. The formulation is performed with iron oxide nanoparticles having a hydrophobic coating, dispersed in the soybean oil, solubilizing simultaneously a near infrared fluorophore. These nano-emulsions are injected in nude mice and their accumulation in subcutaneous tumors followed. The optimized quantity of iron oxide nanocrystals induces a remarkably high transverse relaxivity ( $R_2$ ), which is desirable for T2-weighted MRI imaging. The multimodal *in vivo* MRI and fluorescence imaging is shown in Figure 7.

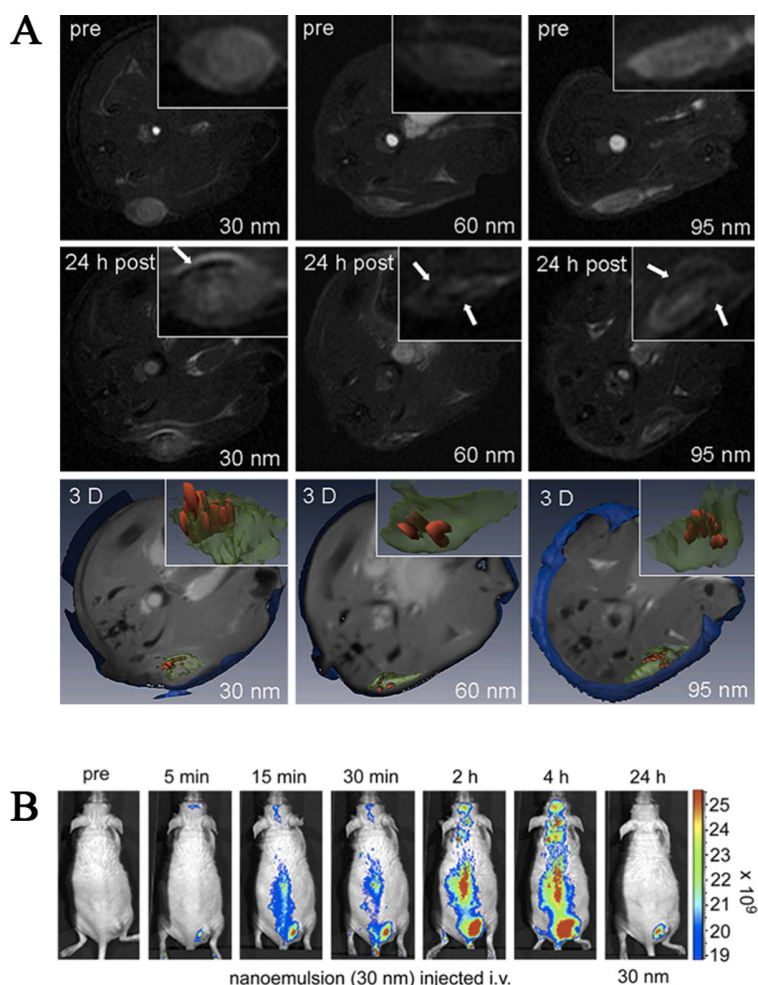


**Figure 7:** (adapted from Ref. [42]) MRI images of nude mice bearing subcutaneous EW7 tumors, injected with the three different nano-emulsions of 30 nm, 60 nm and 90 nm. (A) T2-weighted MRI images of the pre-scans, , after 24 h after intravenous injection, and 3D images that show the proton density MR image (grey), the whole tumor in 3D (transparent green) and the areas of iron oxide deposition in red. (B) *In vivo* NIR fluorescence imaging series showing the accumulation of the 30 nm nano-emulsion.

Another example of MRI imaging with nano-emulsions concerns the use of perfluorocarbons (PFCs) as oily phase. PFCs are synthetic organic compounds in which all or most of the hydrogen atoms have been replaced with fluorine atoms. The  $^{19}\text{F}$  isotope of PFC's is biologically and chemically inert and thus provides excellent sensitivity *in vivo*. PFCs nano-

emulsions have been used for  $^{19}\text{F}$  MRI cell tracking [43-46] as an alternative to SPIO agents, thanks to the high NMR sensitivity of the  $^{19}\text{F}$  atom. As well, they have been shown to label *in vivo* the monocytes and macrophages, and give positive signals at sites of inflammation [46, 47].

### **3.3.3. NEs as fluorescent probes in Fluorescent imaging**

Fluorescence is one of the most powerful and commonly used tools in biophysical studies of biomembrane structure and dynamics that can be applied on different levels, from lipid monolayers and bilayers to living cells, tissues, and whole animals. Nano-emulsions are also very suited for encapsulating fluorescent probes at high concentrations either organic dyes or inorganic quantum-dots (QDs), thus enabling a multimodal imaging as shown previously in Fig. 7. We have shown that the slight modification of classical dyes enable the increase of their concentration in oil without an excessive loss of quantum yield, resulting in ultrabright nano-droplets with no dye leakage [48]. This can be performed using classical dyes derivatives, like Nile Red. Actually, we disclosed that in living animal model (zebrafish), classical Nile Red dye encapsulated in nano-emulsions shows a strong release towards the surrounding tissues, whereas modified lipophilic Nile Red does not leak and allows accurate imaging of the blood. In 2010, Goutayer *et al.* [49] were able to formulate a new lipid nanoparticles (LNP) loading lipophilic fluorescent dye (DiD), then functionalized with the cRGD peptide binding to  $\alpha v\beta_3$  integrin, a well-known angiogenesis biomarker, allowing their *in vivo* tracking using fluorescence imaging. *In vitro* study on HEK293( $\beta_3$ ) cells over-expressing the  $\alpha v\beta_3$  integrins demonstrates the functionalization, specific targeting, and internalization of cRGD-functionalized LNP in comparison with LNP-cRAD or LNP-OH used as negative controls. Following their intravenous injection in Nude mice, LNP-cRGD can accumulate actively in slow-growing HEK293( $\beta_3$ ) cancer xenografts, leading to tumor over skin fluorescence ratio of  $1.53 \pm 0.07$  ( $n = 3$ ) 24 h after injection. Figure 8 indicates the *in vivo* imaging in the study.

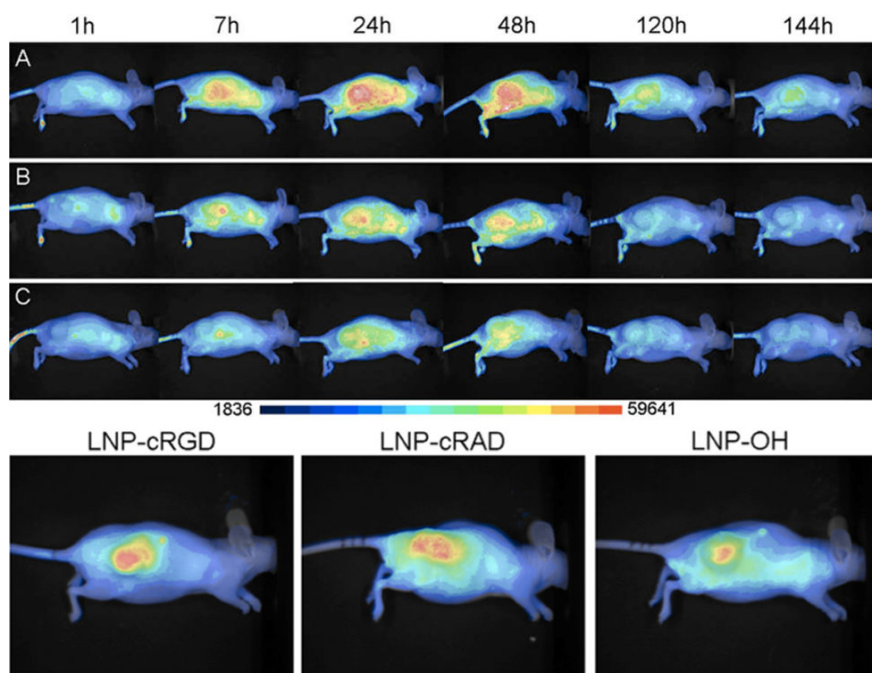


**Figure 8:** (adapted from Ref. [49]) *In vivo* injection of LNP-cRGD (A), LNP-cRAD (B), or LNP-OH (C) in HEK293(b3) xenografted nude mice.

### 3.3.4. Nano-emulsions as multimodal imaging probes and theragnostics

The main characteristic of nano-emulsions is their cargo structure that allows solubilizing and dispersing lipophilic compounds in the droplet's core, even if the molecules are very different. This property allows encapsulating different contrast agents for different imaging modalities, but also contrasts agents and drugs, so-called theragnostics agents.

A study has been performed by Jiali Ding *et al.* [50] to design CT / fluorescence dual-modal nano-emulsion platform for investigating atherosclerotic plaques. Hydrophobic QDs were embedded in iodinated oil, which subsequently were dispersed in water to form multimodal contrast agent. The simultaneous X-ray contrasting properties and fluorescence properties were proved. These authors show that the nano-emulsion droplets entered murine macrophage cells and human liver cells, conferring them bimodal imaging properties. *In vivo* evaluation on atherosclerotic rabbits showed that bimodal nano-emulsions are detected to target specifically macrophages and allows visualizing atherosclerotic plaques.

On the other hand, the co-encapsulation of contrast agent and drug, *i.e.* theragnostics, has seen a real emergence in the last decade since it opens a real chance to monitor the actual dosage and amount of drug delivery in real time. This is even more interesting when non-invasive imaging techniques are more and more efficient, thus offering the possibility to follow quantitatively the drug targeting within a living organism. An interesting example reports a multimodal theragnostics nano-emulsion, containing MRI and fluorescent contrast agent (IONPs and Cy7, respectively), along with a glucocorticoid prednisolone acetate valerate (PAV) used for cancer treatment [51]. The droplets were functionalized with  $\alpha\text{v}\beta_3$ -specific RGD peptides, and administrated in subcutaneous tumors-bearing mice (at doses of

30 mg of FeO/kg and 10 mg of PAV/kg). The results, reported in Fig. 9 show a significant accumulation of the contrast agents in the tumor region, while tumor growth profiles revealed a potent inhibitory effect in all of the PAV containing nano-emulsion (compared to the control without PAV).

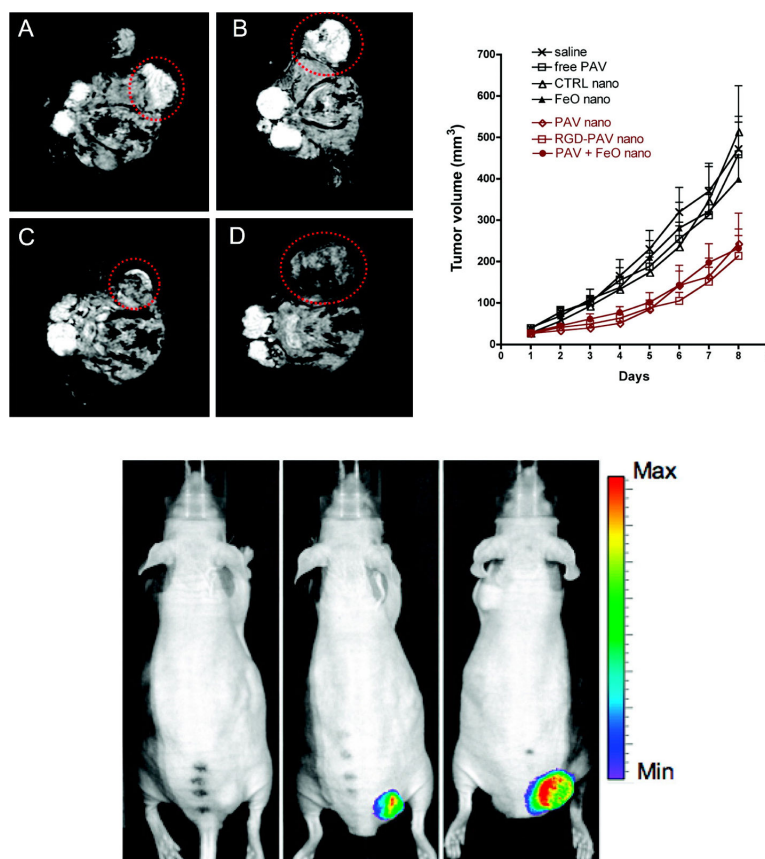


**Figure 9:** (adapted from Ref. [51]) (A-D) *In vivo* MRI imaging of xenografted tumor in mice (transverse sections), red circles indicate the tumors; (A) Selected MR images of PAV nano-emulsions and (B) control nano-emulsions. (C) MR images of PAV + FeO nano-emulsion and (D) FeO NE injected mice. Red circles indicate the tumors. In (A) and (B) tumors appeared bright compared to surrounding muscle tissue, and in (C) and (D), tumor areas appeared hypo-intense, indicative of FeO accumulation. Starting at day 6, tumor growth profiles showed statistically significant tumor growth inhibition ( $P < 0.001$ ) in all of the PAV nano-emulsions treated groups compared to saline, control nano-emulsions, FeO nano-emulsions, and free PAV injected groups. *Bottom:* *In vivo* NIRF images of a mouse injected with unlabeled NE (left) and mice (two different sized tumors) injected with Cy7 NE (middle and right) at the end of the study.

Another study [52] was reported for fabrication of DTPA-PE-Gd<sup>3+</sup> complexes nano-emulsions encapsulating paclitaxel hydrophobic drug and their T1 relaxation times measured. Based on NMR and MRI results, it was concluded that this system could act as a contrast agent. *In vitro* cell experiments also confirmed the drug delivery efficacy of the nano-emulsions, since they penetrated the cell membrane and killed the cancerous cells. O'Hanlon *et al.* [53] have synthesized the NIR-labeled perfluoropolyether nano-emulsions for drug delivery and imaging. In brief, PFPE-tyramide was successfully formulated into a non-steroidal anti-inflammatory drug, celecoxib (0.2 mg/mL)-carrying nano-emulsions with dual imaging modalities, <sup>19</sup>F MR and NIR. The results obtained by DLS, <sup>19</sup>F NMR, NIR fluorescence microscopy, and biological studies indicate that the nano-emulsion formulation

may be useful for parenteral administration of celecoxib.

## 4. Conclusion

To summarize, we can say that nano-emulsions are stable nano-cargo with important loading capability. These unique features open the doors of mixing the nature of encapsulating materials, enable a wide range of applications from biomedical imaging to therapies. In addition, any application of nanoparticulate systems is conditioned by the toxicity, biodistribution, pharmacokinetics and potentialities to target specific sites, and this chapter has been precisely focused on these different points to show the extent in which nano-emulsions are promising in many fields related to nanomedicines and imaging.

## 5. References

- [1] Taisne L, walstra B, Cabane B. Transfer of oil between emulsion droplets. *J Colloid Interface Sci.* 1996;184:378-90.
  - [2] Delmas T, Piraux H, Couffin AC, Texier I, Vinet F, Poulin P, et al. How to prepare and stabilize very small nanoemulsions. *Langmuir.* 2011;27:1683-92.
  - [3] Anton N, Vandamme TF. The universality of low-energy nano-emulsification. *Int J Pharm.* 2009;377:142-7.
  - [4] Attia M, Anton N, Chiper MC, Akasov R, Anton H, Messaddeq N, et al. Biodistribution of X-ray iodinated contrast agent in nano-emulsions is controlled by the chemical nature of the oily core. *ACS Nano.* 2014;8:10537-50.
  - [5] Hallouard F, Briançon S, Anton N, Li X, Vandamme TF, Fessi H. Poly(ethylene glycol)-poly( $\epsilon$ -caprolactone) iodinated nanocapsules as contrast Agents for X-ray imaging. *Pharm Res.* 2013;30:2023-35.
  - [6] Jakhmola A, Anton N, Anton H, Messaddeq N, Hallouard F, Klymchenko A, et al. Poly- $\epsilon$ -caprolactone tungsten oxide nanoparticles as a contrast agent for X-ray computed tomography. *Biomaterials.* 2014;35:2981-6.
  - [7] Owens DE, Peppas NA. Opsonization, biodistribution and pharmacokinetics of polymeric nanoparticles. *Int J Pharm.* 2006;307:93-102.
  - [8] Boll H, Nittka S, Doyon F, Neumaier M, Marx A, Kramer M, et al. Micro-CT based experimental liver imaging using a nanoparticulate contrast agent: a longitudinal study in mice. *PloS ONE.* 2011;6:e25692-e7.
  - [9] Almajdub M, Nejari M, Poncet G, Magnier L, Chereul E, Roche C, et al. In vivo high-resolution X-ray microtomography for liver and spleen tumor assessment in mice. *Contrast Media Mol Imaging.* 2007;2:88-93.
  - [10] Martiniova L, Schimel D, Lai EW, Limpunfthip A, Kvetnansky R, Pacak K. In vivo micro CT imaging for liver lesions in small animal models. *Methods.* 2010;50:20-5.
  - [11] Aprahamian M, Bour G, Akladios CY, Fylaktakidou K, Greferath R, Soler L, et al. Myo-InositolTrisPyroPhosphate treatment leads to HIF-1 $\alpha$  suppression and eradication of early hepatoma tumors in rats. *ChemBioChem.* 2011;12:777-83.
-

- [12] Hobbs SK, Monsky WL, Yuan F, Roberts WG, Griffith L, Torchilin VP, et al. Regulation of transport pathways in tumor vessels: role of tumor type and microenvironment. *Proc Natl Acad Sci USA*. 1998;95:4607-12.
  - [13] Jain RK. Transport of molecules, particles, and cells in solid tumors. *Annu Rev Biomed Eng*. 1999;1.
  - [14] Fang J, Nakamura H, Maeda H. The EPR Effect: Unique Features of Tumor Blood Vessels for Drug Delivery, Factors Involved, and Limitations and Augmentation of the Effect. *Adv Drug Deliv Rev*. 2001;63:136-51.
  - [15] Klibanov AL, Maruyama K, Torchilin VP, Huang L. Amphipathic polyethyleneglycols effectively prolong the circulation time of liposomes. *FEBS Lett*. 1990;268(1):235-7.
  - [16] Torchilin V-P, Trubetskoy V-S. With polymers can make nanoparticles drug carriers long circulating? *Adv Drug Deliv Rev*. 1995;16(2-3):141-55.
  - [17] Zheng J, Jaffray D, Allen C. Quantitative CT Imaging of the Spatial and Temporal Distribution of Liposomes in a Rabbit Tumor Model. *Mol Pharm*. 2009;6(2):571-80.
  - [18] Karathanasis E, Suryanarayanan S, Balusu SR, McNeeley K, Sechopoulos I, Karellas A, et al. Imaging nanoprobe for prediction of outcome of nanoparticle chemotherapy by using mammography. *Radiology*. 2009;250:398-406.
  - [19] Anayama T, Nakajima T, Dunne M, Zheng J, Allen C, Driscoll B, et al. A novel minimally invasive technique to create a rabbit VX2 lung tumor model for nano-sized image contrast and interventional studies. *PloS One*. 2013;8:e67355.
  - [20] Khalid MN, Simard P, Hoarau D, Dragomir A, Leroux JC. Long circulating poly(ethylene glycol)-decorated lipid nanocapsules deliver docetaxel to solid tumors. *Pharm Res*. 2006;23(4):752-8.
  - [21] Li X, Anton N, Zuber G, Vandamme TF. Contrast agents for preclinical targeted X-ray imaging. *Adv Drug Deliv Rev*. 2014;76:116-33.
  - [22] Béduneau A, Hindré F, Clavreul A, Leroux JC, Saulnier P, Benoit JP. Brain targeting using novel lipid nanovectors. *J Control Release*. 2008;126:44-9.
  - [23] ANSM. Résumé des caractéristiques du produit - NEORAL 100 mg/ml, solution buvable - Base de données publique des médicaments.
  - [24] ANSM. Résumé des caractéristiques du produit - PROPOFOL LIPURO 1 % (10 mg/ml), émulsion injectable ou pour perfusion - Base de données publique des médicaments.
  - [25] ANSM. Résumé des caractéristiques du produit - MEDIALIPIDE 20 POUR CENT, émulsion pour perfusion - Base de données publique des médicaments.
  - [26] Rodrigues TA, Alexandrino RA, Kanczuk ME, Gozzani JL, Mathias LA, Da ST. A comparative study of non-lipid nanoemulsion of propofol with solutol and propofol emulsion with lecithin. *Rev Bras Anesthesiol*. 2012;62:325-34.
  - [27] Dubey PK, Kumar A. Pain on Injection of Lipid-Free Propofol and Propofol Emulsion Containing Medium-Chain Triglyceride: A Comparative Study. *Anesth Analg*. 2005;101:1060-2.
  - [28] Kircik L, Jones TM, Jarratt M, Flack MR, Ijzerman M, Ciotti S, et al. Treatment with a novel topical nanoemulsion (NB-001) speeds time to healing of recurrent cold sores. *J Drugs Dermatol*. 2012;11:970-7.
-

- [29] Ijzerman M, Backer J, Flack M, Robinson P. Forty-two-week safety study of topical nanoemulsion (NB-002) for the treatment of mild to moderate distal subungual onychomycosis: A randomized, double-blind, vehicle-controlled trial. *J Am Acad Derm.* 2010;62:AB77.
- [30] Ijzerman M, Backer J, Flack M, Robinson P. Efficacy of topical nanoemulsion (NB-002) for the treatment of distal subungual onychomycosis: A randomized, double-blind, vehicle-controlled trial. *J Am Acad Derm.* 2010;62:AB76.
- [31] Szeimies R-M, Radny P, Sebastian M, Borrosch F, Dirschka T, Krähn-Senftleben G, et al. Photodynamic therapy with BF-200 ALA for the treatment of actinic keratosis: results of a prospective, randomized, double-blind, placebo-controlled phase III study. *Br J Dermatol.* 2010;163:386-94.
- [32] Dirschka T, Radny P, Dominicus R, Mensing H, Brünig H, Jenne L, et al. Photodynamic therapy with BF-200 ALA for the treatment of actinic keratosis: results of a multicentre, randomized, observer-blind phase III study in comparison with a registered methyl-5-aminolaevulinate cream and placebo. *Br J Dermatol.* 2012;166:137-46.
- [33] Dirschka T, Radny P, Dominicus R, Mensing H, Brünig H, Jenne L, et al. Long-term (6 and 12 months) follow-up of two prospective, randomized, controlled phase III trials of photodynamic therapy with BF-200 ALA and methyl aminolaevulinate for the treatment of actinic keratosis. *Br J Dermatol.* 2013;168:825-36.
- [34] Neittaanmäki-Perttu N, Karppinen Tt, Grönroos M, Tani Tt, Snellman E. Daylight photodynamic therapy for actinic keratoses: a randomized double-blinded nonsponsored prospective study comparing 5-aminolaevulinic acid nanoemulsion (BF-200) with methyl-5-aminolaevulinate. *Br J Dermatol.* 2014;171:1172-80.
- [35] Treanor JJ, Essink B, Hull S, Reed S, Izikson R, Patriarca P, et al. Evaluation of safety and immunogenicity of recombinant influenza hemagglutinin (H5/Indonesia/05/2005) formulated with and without a stable oil-in-water emulsion containing glucopyranosyl-lipid A (SE+GLA) adjuvant. *Vaccine.* 2013;31:5760-5.
- [36] Stanberry LR, Simon JK, Johnson C, Robinson PL, Morry J, Flack MR, et al. Safety and immunogenicity of a novel nanoemulsion mucosal adjuvant W805EC combined with approved seasonal influenza antigens. *Vaccine.* 2012;30:307-16.
- [37] Kulkarni SA, Feng SS. Effects of Particle Size and Surface Modification on Cellular Uptake and Biodistribution of Polymeric Nanoparticles for Drug Delivery. *Pharm Res.* 2013;30:2512-22.
- [38] Choi HS, Liu W, Misra P, Tanaka E, Zimmer JP, Ipe BI, et al. Renal Clearance of Nanoparticles. *Nat Biotechnol.* 2007;25:1165-70.
- [39] Li X, Anton N, Zuberá G, Zhao M, Messaddeq N, Hallouard F, et al. Iodinated  $\alpha$ -tocopherol nano-emulsions as non-toxic contrast agents for preclinical X-ray imaging. *Biomaterials.* 2013;34:481-91.
- [40] Attia MF, Anton N, Chipier M, Akasov R, Anton H, Messaddeq N, et al. Biodistribution of X-Ray Iodinated Contrast Agent in Nano-Emulsions Is Controlled by the Chemical Nature of the Oily Core. *ACS Nano.* 2014;8:10537-50.
-

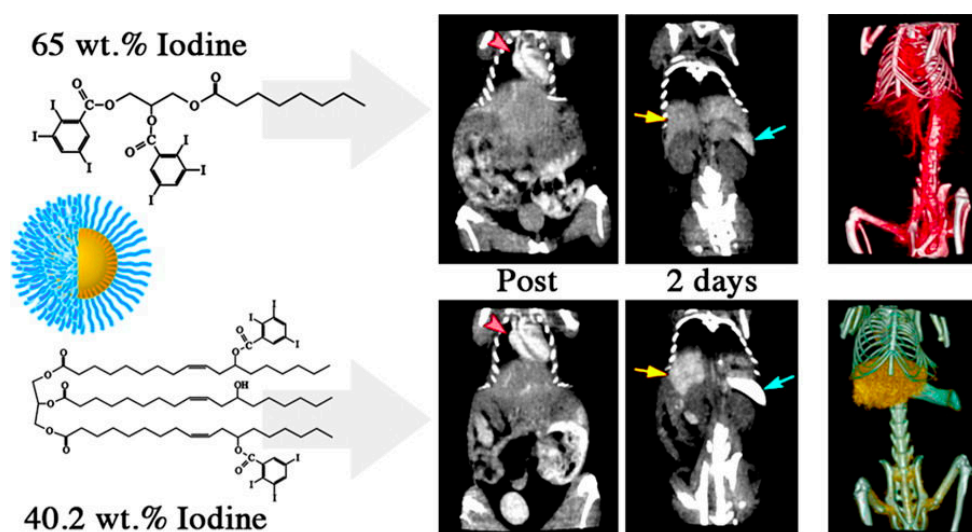
- [41] Attia MF, Anton N, Akasov R, Chipper M, Markvicheva E, Vandamme TF. Biodistribution and Toxicity of X-Ray Iodinated Contrast Agent in Nano-emulsions in Function of Their Size. *Pharm Res.* 2015;33:603-14.
- [42] Jarzyna PA, Skajaa T, Gianella A, Cormode DP, Samber DD, Dickson SD, et al. Iron oxide core oil-in-water emulsions as a multifunctional nanoparticle platform for tumor targeting and imaging. *Biomaterials* 2009;30:6947-54.
- [43] Partlow KC, Chen J, Brant JA, Neubauer AM, Meyerrose TE, Creer MH, et al. 19F magnetic resonance imaging for stem/progenitor cell tracking with multiple unique perfluorocarbon nanobeacons. *FASEB J.* 2007;21:1647-54.
- [44] Lanza GM, Winter PM, Neubauer AM, Caruthers SD, Hockett FD, Wickline SA. 1H/19F magnetic resonance molecular imaging with perfluorocarbon nanoparticles. *Curr Top Dev Biol* 2005;70:57-76.
- [45] Ahrens ET, Flores R, Xu H, Morel PA. In vivo imaging platform for tracking immunotherapeutic cells. *Nat Biotechnol.* 2005;23:983-7.
- [46] Nöth U, Morrissey SP, Deichmann R, Jung S, Adolf H, Haase A, et al. Perfluoro-15-crown-5-ether labelled macrophages in adoptive transfer experimental allergic encephalomyelitis. *Artif Cells Blood Substit Immobil Biotechnol.* 1997;25:243-54.
- [47] Flögel U, Ding Z, Hardung H, Jander S, Reichmann G, Jacoby C, et al. In vivo monitoring of inflammation after cardiac and cerebral ischemia by fluorine magnetic resonance imaging. *Circulation.* 2008;118:140-8.
- [48] Klymchenko AS, Roger E, Anton N, Anton H, Shulov I, Vermot J, et al. Highly lipophilic fluorescent dyes in nano-emulsions: towards bright non-leaking nano-droplets. *RSC Advances.* 2012;2:11876-86.
- [49] Goutayer M, Dufort S, Jossierand V, Royère A, Heinrich E, Vinet F, et al. Tumor targeting of functionalized lipid nanoparticles: Assessment by in vivo fluorescence imaging. *Eur J Pharm Biopharm.* 2010;75:137-47.
- [50] Ding J, Wang Y, Ma M, Zhang Y, Lu S, Jiang Y, et al. CT/fluorescence dual-modal nanoemulsion platform for investigating atherosclerotic plaques. *Biomaterials.* 2013;34:209-16.
- [51] Gianella A, Jarzyna PA, Mani V, Ramachandran S, Calcagno C, Tang J, et al. Multifunctional Nanoemulsion Platform for Imaging Guided Therapy Evaluated in Experimental Cancer. *ACS Nano.* 2011;5:4422-33.
- [52] Tiwari S, Tan YM, Amiji M. Preparation and In Vitro Characterization of Multifunctional Nanoemulsions for Simultaneous MR Imaging and Targeted Drug Delivery. *J Biomed Nanotechnol.* 2006;2:1-8.
- [53] O'Hanlon CE, Amede KG, O'Hear MR, Janjic JM. NIR-labeled perfluoropolyether nanoemulsions for drug delivery and imaging. *J Fluor Chem.* 2012;137:27-33.



## Chapter 1.2 : Biodistribution of X-Ray Iodinated Contrast Agent in Nano-Emulsions Is Controlled by the Chemical Nature of the Oily Core

In this first part, we developed two new nontoxic and blood pool contrast agents based on nano-emulsions (NEs) used for preclinical X-ray imaging. Iodinated monoglyceride (Capmul MCM C8) and iodinated triglyceride (castor oil) were initially synthesized by grafting triiodobenzoic acid to the parent oils followed by their formulations using spontaneous emulsification technique in the presence of Cremophore ELP<sup>®</sup> as PEGylated surfactant. The size and the morphology of the generated nanodroplets nano-emulsion were determined by dynamic light scattering (DLS) and transmission electron microscope (TEM) giving rise to 131 nm and 200 nm of size for both monoglyceride NE and triglyceride NE respectively and showing spherical immense black color under TEM. Their *in vitro* experiments involving toxicity issues and cellular uptakes were evaluated, revealing negligible toxicity. *In vivo i.v.* injection performed on Swiss mice, then were scanned by X-ray imaging modality for pre- and post-injection and up to 50 days. The results demonstrated high contrasting in blood vessels ( $t_{1/2} = 8-9$  hours), after that NEs were eliminated from the blood and began to accumulate in specific organs. Monoglyceride NE showed higher accumulation in liver than in spleen, triglyceride NE, however, was highly accumulated in spleen compared to liver. The mice have been scanned after the NEs were totally removed from the body that confirmed by after X-ray scanning 50 days.

This study approved that the discrepancy in the chemical structure of the oily core of the nano-emulsion impacts their biodistribution and pharmacokinetics.



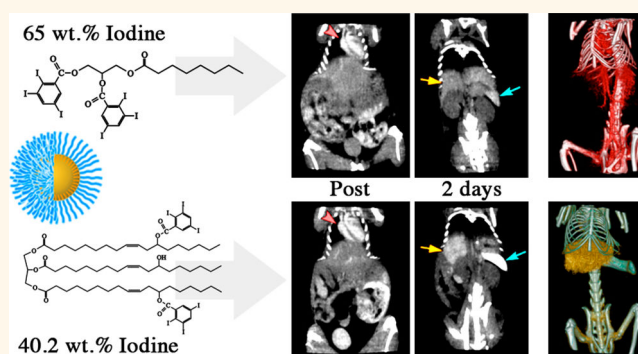
# Biodistribution of X-Ray Iodinated Contrast Agent in Nano-Emulsions Is Controlled by the Chemical Nature of the Oily Core

Mohamed F. Attia,<sup>†,‡</sup> Nicolas Anton,<sup>\*,†,‡</sup> Manuela Chiper,<sup>†,‡</sup> Roman Akasov,<sup>†,‡,§</sup> Halina Anton,<sup>†,‡</sup> Nadia Messaddeq,<sup>||</sup> Sylvie Fournel,<sup>†,‡</sup> Andrey S. Klymchenko,<sup>†,‡</sup> Yves Mély,<sup>†,‡</sup> and Thierry F. Vandamme<sup>†,‡</sup>

<sup>†</sup>University of Strasbourg, Faculty of Pharmacy, 74 route du Rhin, 67401 Illkirch Cedex, France, <sup>‡</sup>CNRS UMR 7199, Laboratoire de Conception et Application de Molécules Bioactives, University of Strasbourg, 74 route du Rhin, 67401 Illkirch Cedex, France, <sup>§</sup>Shemyakin-Ovchinnikov Institute of Bioorganic Chemistry, Russian Academy of Sciences, Miklukho-Maklaya Str., 16/10117997, Moscow, Russia, <sup>||</sup>CNRS UMR 7213, Laboratoire de Biophotonique et Pharmacologie, University of Strasbourg, 74 route du Rhin, 67401 Illkirch Cedex, France, and <sup>||</sup>IGBMC (Institut de Génétique et de Biologie Moléculaire et Cellulaire), Inserm U964, CNRS UMR7104, Université de Strasbourg, 1 rue Laurent Fries, 67404 Illkirch, France

**ABSTRACT** In this study, we investigated the role of the chemical nature of the oil droplet core of nano-emulsions used as contrast agents for X-ray imaging on their pharmacokinetics and biodistribution. To this end, we formulated PEGylated nano-emulsions with two iodinated oils (*i.e.*, iodinated monoglyceride and iodinated castor oil) and compared them with another iodinated nano-emulsion based on iodinated vitamin E. By using dynamic light scattering and transmission electron microscopy, the three iodinated nano-emulsions were found to exhibit comparable morphologies, size, and surface composition.

Furthermore, they were shown to be endowed with very high iodine concentration, which leads to stronger X-ray attenuation properties as compared to the commercial iodinated nano-emulsion Fenestra VC. The three nano-emulsions were *i.v.* administered in mice and monitored by microcomputed tomography (micro-CT). They showed high contrast enhancement in blood with similar half-life around 6 h but very different accumulation sites. While iodinated monoglycerides exhibited low accumulation in liver and spleen, high accumulation in spleen was observed for iodinated castor oil and in liver for vitamin E. These data clearly highlighted the important role of the oil composition of the nano-emulsion core to obtain strong X-ray contrast enhancement in specific targets such as liver, spleen, or only blood. These differences in biodistribution were partly attributed to differences in the uptake of the nanodroplets by the macrophages *in vitro*. Another key feature of these nano-emulsions is their long half-elimination time (several weeks), which offers sufficient retention for micro-CT imaging. This work paves the way for the design of nanoparticulate contrast agents for X-ray imaging of selected organs.



**KEYWORDS:** X-ray imaging · micro-CT · contrast agent · nano-emulsion · targeting

During the past decade, X-ray micro-computed tomography (micro-CT) emerged as a key imaging modality for biomedical research. Micro-CT provides high-resolution, noninvasive, structural, and functional imaging at low cost compared to magnetic resonance imaging and without tedious experimental protocols compared to nuclear imaging.<sup>1,2</sup> However, in spite of the strong progress recently achieved on microscanners, with a notable reduction of the voxel size down to 10  $\mu\text{m}$  or acquisition times lower than 5 min, their use is still

limited by the poor efficiency of the available contrast agents. Indeed, in the absence of contrast agents, micro-CT only allows differentiating bones (electron-dense) from soft tissues including organs or fluids.<sup>3</sup> Therefore, micro-CT is often used in association with another imaging modality (like single-photon emission computed tomography, SPECT) in order to help locate the SPECT signal within the whole animal body, such as for tumor location. The possibilities offered by X-ray scanners are largely improved by using electron-dense contrast

\* Address correspondence to nanton@unistra.fr.

Received for review July 18, 2014 and accepted October 3, 2014.

Published online October 04, 2014  
10.1021/nn503973z

© 2014 American Chemical Society

agents, which allow direct visualization of the biological compartments in which they accumulate,<sup>3,4</sup> providing thus structural and potentially functional, non-invasive imaging with high resolution. As discussed in previous reports,<sup>1,2,5</sup> there are fundamental differences between contrast agents designed for clinical X-ray scanners and those formulated for micro-CT. Clinical contrast agents were designed as small hydrophilic iodinated molecules, which are excreted by the kidney only a few minutes after i.v. administration. Since clinical agents were developed before modern and fast scanners were available, considerable investments were made by industry to adapt the scanners to the contrast agents and make them fast. However, these contrast agents are less appropriate for micro-CT since their renal clearance kinetics is comparable to the image acquisition times of this modality. Therefore, high doses or multiple administrations are needed to improve the contrast, which results in significant side effects, like nephropathy, acute kidney injury, or renal failure. With the objective of using micro-CT for imaging soft tissues and organs with pathologies like tumors, new contrast agents were developed in the past decade. To slow down or avoid their renal elimination, the idea was to increase the size of the contrast agents above the 50–100 nm diameter of the glomerulus pores.<sup>2,5–11</sup> To this end, several nanoparticle systems were developed in the form of iodinated liposomes, polymeric micelles, dendrimers, inorganic nanoparticles (based on gold, bismuth, silver, tungsten),<sup>4,12</sup> and iodinated nano-emulsions.<sup>2,5</sup> The main constraint, directly linked to the contrast enhancement, is the concentration of heavy atoms, which has to be as high as possible. Moreover, the toxicity of the nanoparticles should be as low as possible, which depends on the chemical nature of the nanoparticle components (lipid, polymer, inorganic compounds) and the loading dose required for obtaining a good contrast. Finally, the last important aspect of the formulation of nanoparticulate CT contrast agent concerns their surface properties that can strongly influence their pharmacokinetics and/or biodistribution after injection. As a rule, decorating the nanoparticle surface with polyethylene glycol (PEG) increases their circulation time in the bloodstream.<sup>13–15</sup> Actually, long circulating systems (also called “blood pool contrast agents”) not only allow performing angiography with micro-CT but also are used for the formulation of targeted systems, based on the fact that the longer the vascular circulation, the longer the time in contact with the potential targets in the whole body.<sup>2</sup> In general, innovation in CT contrast agents is based on already well-known scaffolds<sup>8,16,17</sup> such as gold and iodinated liposomes, through improved formulation, chemical nature, and surface functionalization.

An overview of the recent literature on micro-CT nanoparticulate contrast agents shows that the major difficulty encountered in designing these contrast

agents comes from the need to concentrate the contrasting atoms within the nanoparticles,<sup>2,4</sup> so that nontoxic doses of nanoparticles could be injected. Only few families of nanoparticles allow formulating contrast agents at high concentrations in heavy atoms, representative examples being inorganic particles based on elements like gold,<sup>18–22</sup> bismuth,<sup>23</sup> or tantalum<sup>24</sup> and iodinated lipid-based nanoparticles like liposomes and nano-emulsions. In our previous studies,<sup>5,25</sup> we have shown that iodinated nano-emulsions appear as one of the best compromises to provide very high contrast without toxicity. Compared to inorganic nanoparticles,<sup>4</sup> lipid nano-emulsions are easier to synthesize and formulate, enable complete clearance from the body, and offer the possibility to use the oily core of the nanodroplets as a reservoir for drugs. In addition, micro-CT allows monitoring with time the biodistribution of the contrast agent in the living animal. This is fundamental to understand the influence of the physicochemical properties of the formulations on their *in vivo* biodistribution and pharmacokinetics, in order to optimize the processes and adapt the contrast agents to the imaging targets. Moreover, coencapsulating the active principle in the oily core of the iodinated nano-emulsion droplets, coupled with the possibility to follow up the *in vivo* biodistribution, offers new therapeutic potentials like “online” monitoring and quantification of the actual dosage of active principles brought on various sites.

The objective of the present study was to investigate how the composition of nano-emulsions (*i.e.*, the chemical nature of the iodinated lipid core of droplets) can control the biodistribution of the contrast agent and thus the contrast enhancement. To this end, two new iodinated lipids were synthesized, namely, iodinated monoglycerides and iodinated castor oil (structures are shown in Figure 1a), and formulated as nano-emulsions by the spontaneous emulsification method (Figure 1b). Formulation processes were optimized, and both new iodinated nano-emulsions were characterized by dynamic light scattering (DLS), transmission electron microscopy (TEM), and by MTT cell viability assays *in vitro*. Then, *in vivo* contrasting properties, biodistribution, and pharmacokinetics were evaluated in mice with micro-CT and followed up over 2 months. The efficiency of the accumulation in liver, spleen, and kidneys, as a function of the nature of iodinated oil, was assessed and compared with that of nano-emulsions prepared with iodinated vitamin E. While kinetics of blood clearance appeared similar between the two types of oils, the accumulations in organs (liver, spleen) after blood clearance were found to significantly differ.

## RESULTS AND DISCUSSION

After synthesis and purification, the iodinated oils were formulated into nano-emulsions following the same protocol. Process optimizations were carried out

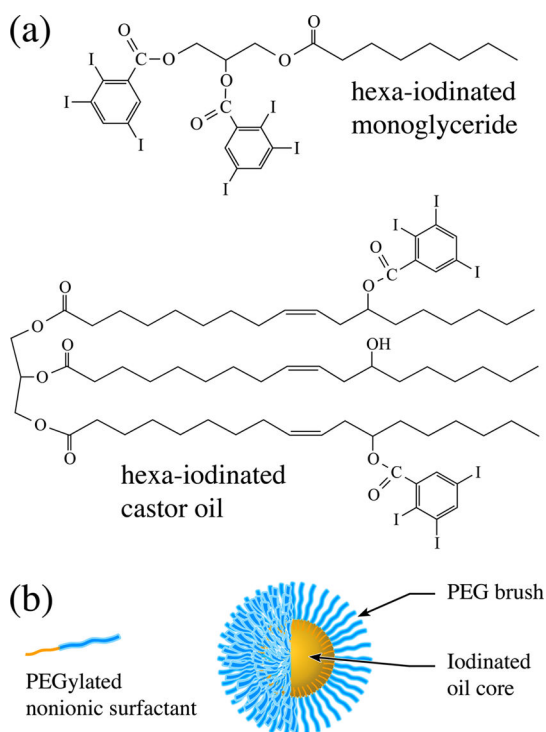


**Figure 1.** (a) Chemical structures of iodinated monoglyceride and castor oil. (b) Schematic representation of an iodinated nano-emulsion droplet.

by following the impact of the surfactant amount (SOR) on the droplet sizes (hydrodynamic diameter). This point is illustrated in Figure 2a<sub>1</sub>,b<sub>1</sub>, both comparing emulsification process before (open symbols) and after (filled symbols) oil iodination for (a) monoglyceride and (b) castor oil.

The trend generally observed in such diagrams, and globally confirmed here, is a decrease in the droplet size with increasing surfactant amounts. We have previously shown<sup>26</sup> that spontaneous nanoemulsification is induced by the sudden solubilization of the surfactant by the aqueous phase, which breaks up the oil/surfactant phase into oil droplets dispersed in water. The process is governed by the surfactant affinities (*i.e.*, solubility) for the oil and water phases. Surfactants have to be first soluble in oil to ensure a perfect homogeneity (helped by temperature since non-ionic PEGylated surfactants are thermosensitive) and then even more soluble in water to ensure fast water penetration and droplet breaking up. In Figure 2a<sub>1</sub>,b<sub>1</sub>, emulsification appears less efficient for non-iodinated oils, probably due to their higher hydrophobicity as compared to non-iodinated oils that decrease the solubility of surfactants and thus slow down the water breaking-up step. Moreover, the viscosity appears much higher for iodinated than for non-iodinated oils, which may further contribute to slow the water fractionation process and increase the droplet size. As a result, in the conditions indicated in gray in Figure 2a<sub>1</sub>,b<sub>1</sub>, emulsification of iodinated oils is

impeded and nano-emulsions do not form. In contrast, iodinated nanoformulations with droplets of small size and narrow PDI were obtained for high SOR values. However, as SOR increases, the iodine content of the droplets decreases as a result of their decreased size. As a consequence, formulations selected for contrast agent applications should be a compromise to ensure that droplet size and PDI are compatible with *i.v.* administration and sufficient iodine content for getting optimal contrast in imaging. The selected formulations are indicated by arrows in Figure 2a<sub>1</sub>,b<sub>1</sub>; they correspond to SOR values of 60 and 65%, respectively, for iodinated monoglyceride and iodinated castor oil. The size distributions of the two formulations are reported in Figure 2a<sub>2</sub>,b<sub>2</sub>, while their TEM images are given in Figure 2a<sub>3</sub>,b<sub>3</sub>. For iodinated monoglycerides, a narrow log-normal size distribution of the nanoparticles, centered at 130 nm, is observed. This narrow size distribution is confirmed by TEM, showing homogeneous droplets. For iodinated castor oil, the log-normal size distribution is also narrow, being centered at 200 nm and largely overlapping the size distribution of the former nanoparticles. Thus, both formulations provide particles of similar size. The TEM pictures of iodinated castor oil nanodroplets confirmed the homogeneity of the spherical dispersion of droplets (Figure 2b<sub>3</sub>). However, at the highest magnification, in contrast with Figure 2a<sub>3</sub>, a core/shell segregation indicated by arrows was observed. This separation between the oily dense core and the non-ionic surfactant at the interface likely arises from a loss of miscibility between these compounds after the temperature drop during emulsification. This difference in physicochemical properties could also explain the somewhat different dependence of their diameter as a function of the SOR (Figure 2a<sub>1</sub>,b<sub>1</sub>). However, it is interesting to note that, in spite of the dramatic changes in the oil properties due to iodination, the spontaneous emulsification process still leads to droplets with good monodispersity.

The strong interest of lipid nano-emulsions comes from their potential to provide nontoxic aqueous dispersions with very high concentrations in iodine. Indeed, the selected nano-emulsions present outstanding amounts in weight of iodine *versus* oils of 64.5 and 40.2% for iodinated monoglyceride and castor oil, respectively. When it is assumed that the amount of surfactant at the nanodroplet interface is negligible compared to the amount of oil in the nanodroplet, similar percentages could be deduced for the iodine content of the nanodroplets. Moreover, an iodine content of 10.3 and 5.6% could be calculated for the whole nano-emulsions (respectively, for monoglyceride and castor oil).

The actual amount of iodine in the formulations was further assessed *in vitro* through their contrasting properties in the micro-CT scanner, by comparison to a

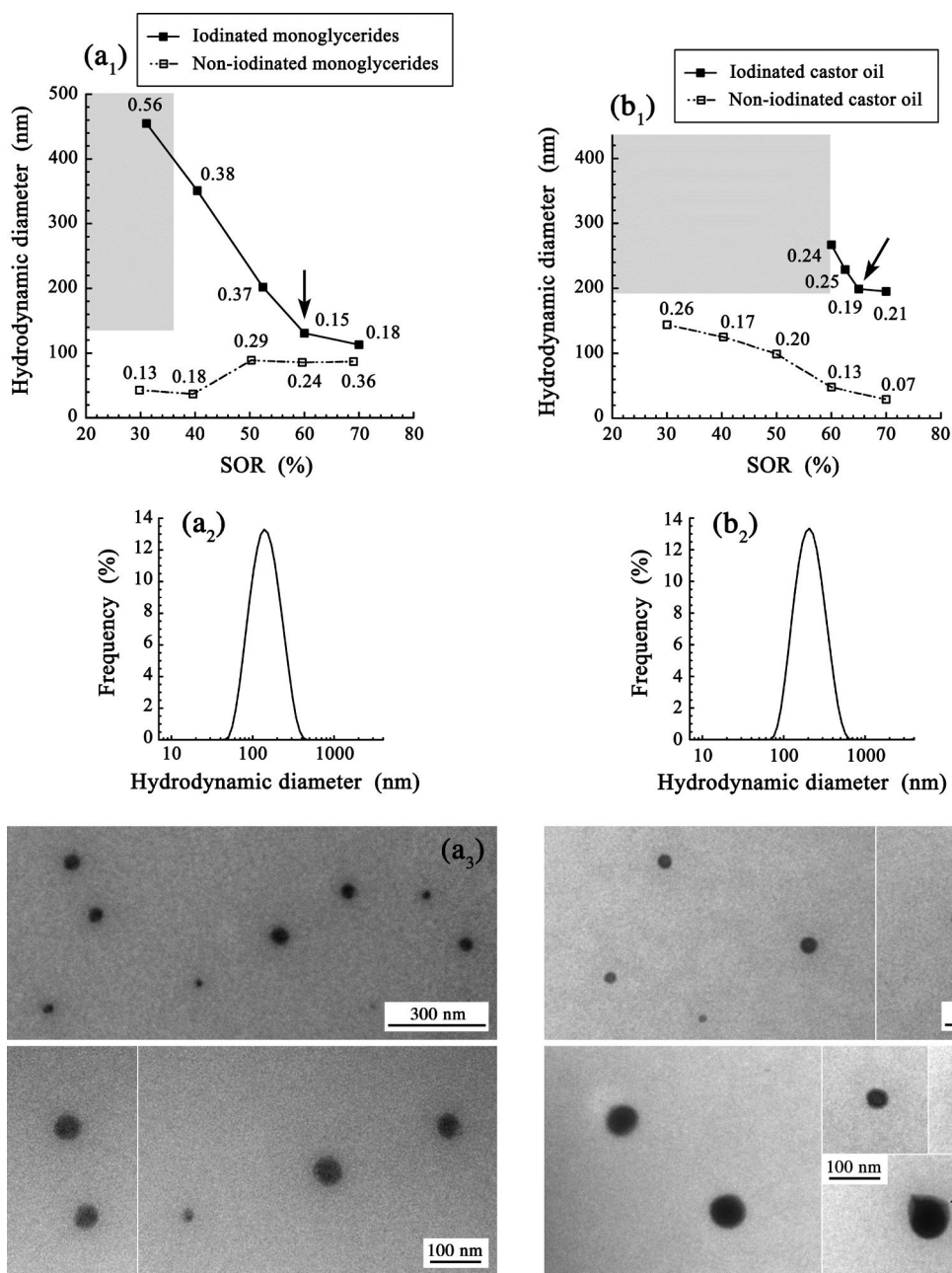


**Figure 2.** DLS and TEM characterization of nano-emulsions of (a) hexa-iodinated monoglyceride and (b) hexa-iodinated castor oil. (a<sub>1</sub>,b<sub>1</sub>) Present the impact of the surfactant concentration (SOR = surfactant/(surfactant + oil) weight ratio) on the hydrodynamic size and polydispersity index (PDI, labeled for each point in the graph) measured by DLS. The gray areas show the regions in which nano-emulsions do not form (either size or PDI are too high). The arrows indicate the optimized formulations selected for the *in vivo* studies: SOR = 60% for iodinated monoglycerides, and SOR = 65% for iodinated castor oil. (a<sub>2</sub>,b<sub>2</sub>) Size distributions of the optimized formulations (corresponding to the arrows in (a<sub>1</sub>) and (b<sub>1</sub>)). (a<sub>3</sub>,b<sub>3</sub>) TEM micrographs of nano-emulsions with optimized formulations (corresponding to the arrows in (a<sub>1</sub>) and (b<sub>1</sub>)).

calibration curve made with iobitridol (XenetiX 300). The results are reported in Figure 3, together with the commercial iodinated nano-emulsion Fenestra VC, and another formulation based on tri-iodinated vitamin E ( $\alpha$ -tocopheryl 2,3,5-triiodobenzoate) from our previous work.<sup>5</sup>

As expected, the X-ray attenuation was found to linearly grow with iodine concentration. Quantification from the iobitridol standard gives iodine concentrations of the selected formulations (arrows in Figure 2)

of 93.1 mg/mL of iodine for iodinated monoglyceride nano-emulsions and of 76.0 mg/mL of iodine for iodinated castor oil nano-emulsions, in full line with the concentration expected theoretically as calculated from the chemical structure. This high theoretical concentration is thought to play a major role in the signal/noise ratio and the imaging resolution in X-ray scanners. This point has been illustrated recently by the imaging of tumor microvascularization,<sup>8</sup> which is especially challenging. Indeed, the blood pool is the

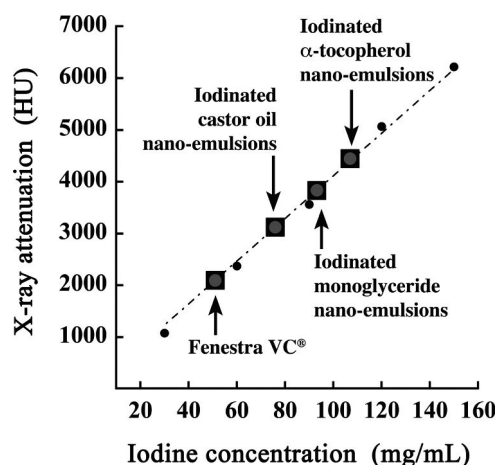


Figure 3. *In vitro* evaluation of the X-ray attenuation properties of hexa-iodinated monoglyceride and hexa-iodinated castor oil nano-emulsions using a calibration curve made with iobitridol (filled circles). The values of radiopacity of two other iodinated nano-emulsions, namely, iodinated  $\alpha$ -tocopherol and Fenestra VC (reproduced with permission from ref 5; copyright 2013 Elsevier), are also reported for comparison.

biological compartment with the largest volume, so that dilution of the contrasting atoms will be high, leading to a strong decrease of the signal/noise ratio. An additional difficulty is related to the small size of the capillaries or microvessels, which requires high-resolution imaging. To obtain the required signal-to-noise ratio and resolution, the X-ray attenuation signal was increased by increasing the contrasting properties of the contrast agent, using a liposomal suspension highly concentrated in iodine (around 110 mg/mL of iodine).

Then, *in vitro* toxicity of iodinated nano-emulsion suspensions was assessed by MTT assays after incubation of the nano-emulsions for 24 h with cells at different concentrations (Figure 4). The toxicity was globally similar for iodinated monoglycerides and iodinated castor oil, with  $LD_{50}$  values of 0.4 mg/mL of iodine for human cervix epithelial HeLa and mouse hepatocyte BNL-CL2 cells. Toxicity was slightly less for the mouse macrophage cell line RAW264.7 with a  $LD_{50}$  around 2 mg/mL of iodine. Considering that the iodinated nano-emulsion suspensions are administered at 7.59  $\mu$ L/g of mouse for imaging experiments, the corresponding iodine concentration in the animal body (obtained from Figure 3) is 0.67 and 0.57 mg/g of mouse for the iodinated monoglycerides and iodinated castor oil, respectively. Both values are close to the  $LD_{50}$  values for HeLa and BNL-CL2 cells, but it has to be kept in mind that the conditions in the MTT assays are more drastic than those *in vivo* because, during the 24 h incubation, the cells are in prolonged contact with the droplets as well as with free surfactants. In contrast, these surfactants are generally rapidly cleared from blood *in vivo*.<sup>25</sup>

Once administered in mice by i.v., the nano-emulsions were immediately spread in the whole

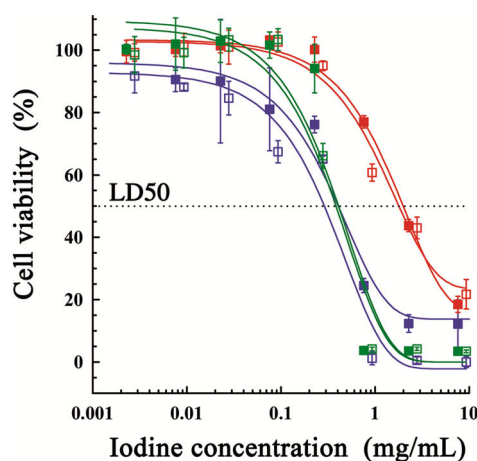
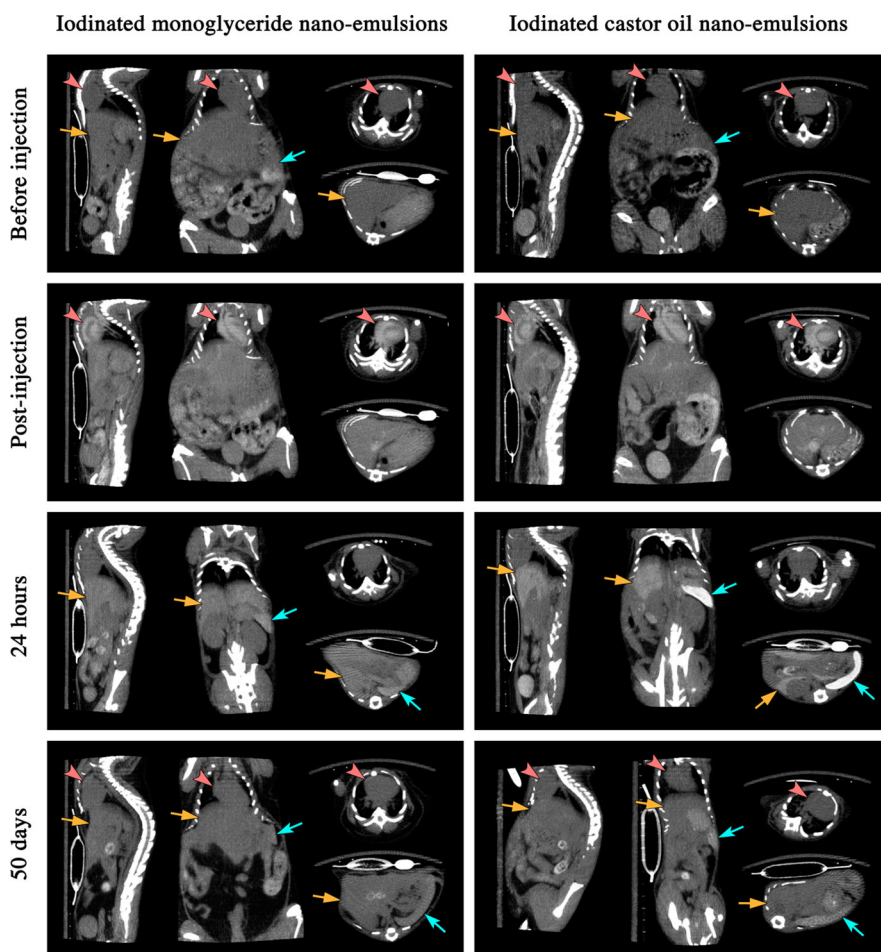


Figure 4. Cytotoxicity MTT experiments. Cells were incubated for 24 h with various concentrations of iodinated nano-emulsions. The nano-emulsion concentrations were expressed in iodine concentrations per mL. Open symbols correspond to iodinated monoglyceride nano-emulsions, and filled symbols correspond to iodinated castor oil nano-emulsions. Blue: HeLa cells. Green: BNL-CL2 hepatocytes. Red: RAW264.7 murine macrophages.

animal vasculature. No clinical sign of disorder or toxicity was observed in any mice, during and after injection and through all the experiment duration. The weight of mice was measured and followed all along the micro-CT acquisitions period, that is, 50 days (see Supporting Information), showing fully normal evolution. *In vivo* contrast enhancement induced by these contrast agents is illustrated at different representative acquisition times in Figure 5. Immediately after injection (5 min), a strong contrast enhancement arises in the whole vasculature system, showing a clear delineation of the blood pool. In this early stage after administration, the distribution and contrast enhancements induced by both iodinated formulations appear very similar, as expected from the identical surface composition of both nano-emulsions and their similar iodine concentrations. However, the *in vivo* behaviors of the two nano-emulsions differ when blood clearance mechanisms and elimination begin. This is illustrated at 24 h postinjection, where both nano-emulsions are totally eliminated from the blood pool but accumulate in different organs. The most pronounced difference between the two formulations is observable in the spleen, which shows a strong contrast with liver for the iodinated castor oil but not for the iodinated monoglycerides. Finally, 50 days after injection, the contrast between spleen and liver was dramatically reduced, indicating that iodinated oils are gradually eliminated from the body.

Three-dimensional volume rendering of the blood vessels provided by iodinated monoglyceride nano-emulsions, 5 min after injection, is presented in Figure 6a. The blood compartment in the heart as well as vessels, aortic arch (aar) and thoracic aorta (ta), is clearly visible. Liver irrigation is nicely visible, as well.



**Figure 5.** *In vivo* micro-CT imaging (maximum projection intensity) of iodinated monoglycerides (left column) and iodinated castor oil (right column) nano-emulsions, at different representative times after i.v. injection. Each picture shows sagittal and coronal sections of the mice, as well as transverse slices through the heart, lung, and vertebra and transverse slices through the liver and spleen. Heart is indicated by red arrowheads, liver by orange arrows, and spleen by blue arrows.

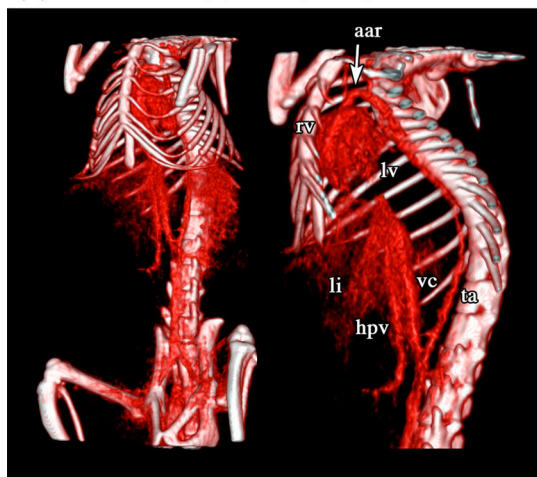
Three-dimensional volume rendering of liver and spleen induced by iodinated castor oil nano-emulsions 24 h after injection is given in Figure 6b. The strong contrast enhancement in spleen results in a very clear image that provides distinct details of the organ surface. In contrast, the liver appears less clearly, suggesting that the contrast agent is not homogeneously distributed and less concentrated than in the spleen. However, since the liver “compartment” dilutes more the contrast agent than the spleen, due to its much larger volume, it results in a difference in contrast enhancement that may not reflect the real amounts of contrast agent accumulated in the organs. This point was explored below with the quantification of the contrast agent in the different organs, by expressing the percent of injected dose as a function of the acquisition time. This approach shows that, though the contrast is higher in spleen than in liver, the total amount of contrast agent is higher in the liver. Since 3D image reconstructions were easily obtained due to the pronounced contrast induced by these iodinated systems, the latter appear thus as

potent contrast agents for global structural imaging in micro-CT.

Quantification of contrast enhancement was followed up in blood (ROI in heart), liver, spleen, and kidneys over the 50 days of acquisition. Contrast enhancement is expressed as  $\Delta\text{HU}(t)$ , which is equal to the value of X-ray attenuation (normalized in Hounsfield units, HU) at acquisition time  $t$  subtracted by the one of the same region, before contrast agent administration. Pharmacokinetics and biodistribution in each organ of the two iodinated nano-emulsions are reported in Figure 7, in comparison with a previously described nano-emulsion of iodinated vitamin E ( $\alpha$ -tocopherol).<sup>5</sup> Interestingly, these three formulations are identical in their surfactant and bulk composition and only differ by the nature of their oily core.

The contrast enhancement and kinetics in the blood pool appeared very similar for the three formulations. This can be easily understood considering that blood clearance is mediated by mechanisms involving recognition of particles through their surface properties. Since all iodinated nano-emulsions tested have the

(a) Iodinated monoglycerides post-injection



(b) Iodinated castor oil 24 hours post-injection

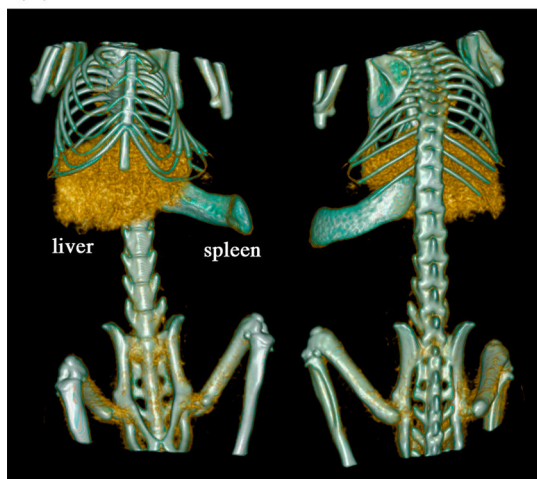


**Figure 6.** *In vivo* micro-CT 3D volume rendering, (a) 5 min after injection of iodinated monoglycerides and (b) 24 h after injection of iodinated castor oil. Annotations: (aar) aortic arch, (rv) right ventricle, (lv) left ventricle, (li) location of liver, (vc) vena cava, (hpv) hepatic portal vein, (ta) thoracic aorta. Two movies corresponding to these volume rendering (a) and (b) are available as Supporting Information (movie1.mov and movie2.mov).

same surface composition, this readily explains their very close blood clearance kinetics, giving half-life values of 6.1, 6.7, and 9.0 h for iodinated monoglyceride, castor oil, and vitamin E nano-emulsions, respectively. All three contrast agents can thus be used as blood pool contrast agents and have actually longer circulation half-lives than the majority of contrast agents reported in the literature. It is, however, worth noting that some liposomal iodinated formulations<sup>7</sup> can reach iodine concentrations as high as 150 mg/mL of iodine with half-lives around 24 h. Here, after 24 h, the value of  $\Delta$ HU in the blood was observed to go back to zero. The performances of iodinated nano-emulsions can be further compared with those of other commercially available contrast agents such as, for instance, gold-based nanoparticles (AuroVist)<sup>27</sup> and

rare earth-based nanoparticles (ExiTron nano 12000)<sup>28</sup> on the same animal model. In the present study, we obtained an initial contrast enhancement  $\Delta$ HU = 200–240 HU that corresponds to an increase of the contrast of 300–330%, which is significantly higher than the 260 and 170% values reported in the literature<sup>27</sup> for AuroVist 15 nm and ExiTron Nano 12000, respectively. To allow the comparison of the data of Figure 7 (expressed in  $\Delta$ HU) with values expressed in percentage of contrast enhancement (as both can be found in literature), we reported in Figure S2 (Supporting Information) that the pharmacokinetics data expressed in percentage of contrast enhancement with the reference before injection can be fixed at 100%. On the other hand, the half-life around 6 or 9 h is optimal for CT scans and comparable or better than that reported for the two commercial contrast agents.

The  $\Delta$ HU values of our iodinated nano-emulsions in the liver and the spleen increased progressively with time, reaching a maximum 24 h postinjection. To verify whether the potential aggregation of nanodroplets in blood circulation could explain the differences in these pharmacokinetics, the size of nano-emulsions incubated in fetal bovine serum (FBS) for different times and at different dilutions was studied by DLS. The results reported in Figure S3 (Supporting Information) show almost invariant size for all experimental conditions, thus confirming the high stability of these iodinated nano-emulsions in FBS. After this maximum, the  $\Delta$ HU values slowly decreased. Finally, the highest  $\Delta$ HU values in the kidneys were observed within the first hour and then progressively decreased with time. Thus, these data suggest that the nanodroplets gradually eliminated from the blood circulation accumulate mainly in liver and spleen. After 24 h, once nano-emulsions are cleared from the bloodstream, the contrast enhancement also starts decreasing in liver and spleen, indicating that they are progressively eliminated from these organs.

In contrast to vitamin E nano-emulsions for which the elimination is governed by hepatocyte-selective uptake,<sup>5</sup> the accumulation of the iodinated monoglyceride and castor oil nano-emulsions in the spleen suggests an elimination by the reticulo-endothelial system.<sup>5</sup> Interestingly, iodinated castor oil nano-emulsions show an outstanding contrast for the spleen, with a maximum  $\Delta$ HU value of  $530 \pm 50$  HU. The maximum  $\Delta$ HU values obtained with iodinated monoglyceride nano-emulsions for the same organ were somewhat lower, being  $220 \pm 30$  HU. In comparison, much lower contrast was seen in the liver with these two formulations since their maximum  $\Delta$ HU values were  $130 \pm 15$  and  $76 \pm 6$  HU, respectively.

To get further information on their pharmacokinetics, the elimination and accumulation kinetics of all three iodinated formulations were fitted with classical monocompartmental exponential eqs 1 and 2,

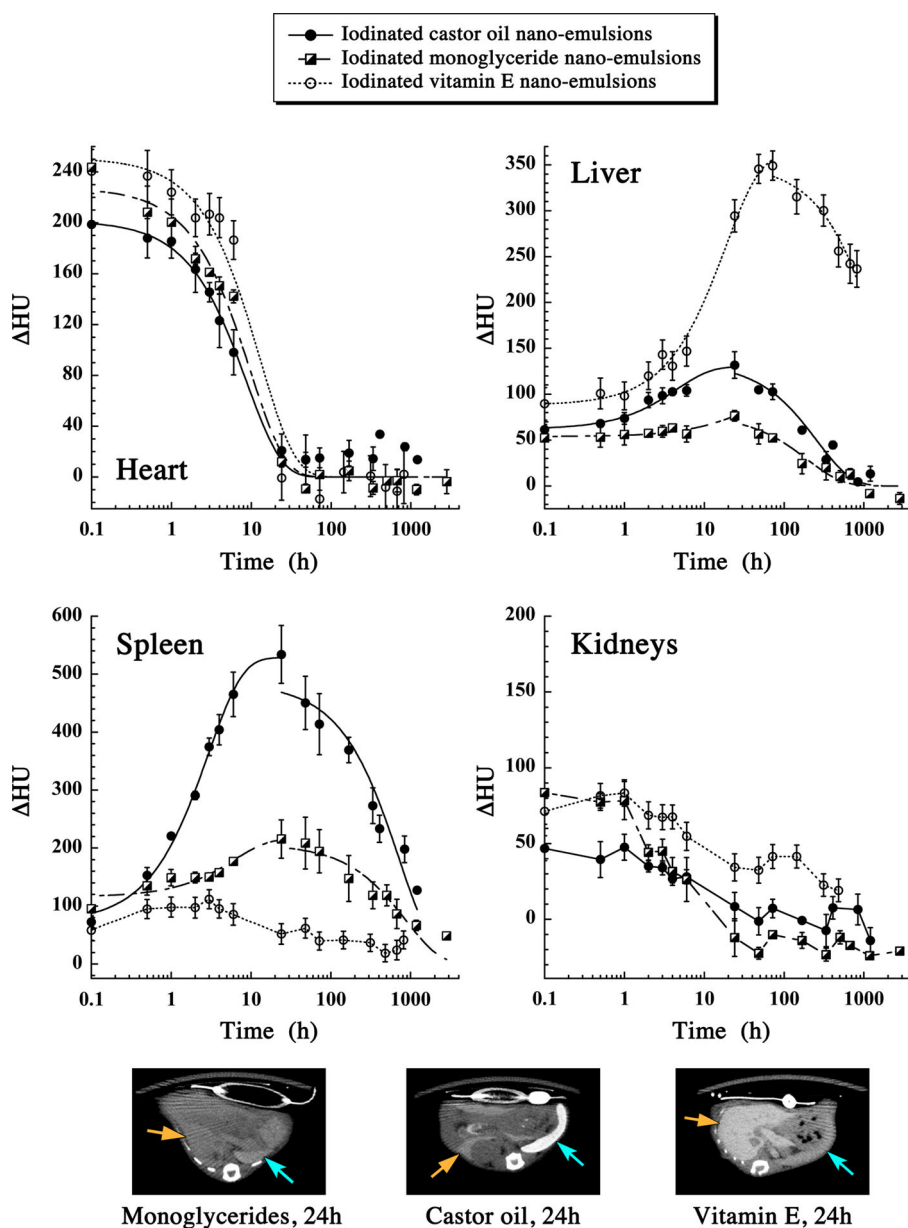


Figure 7. Dependence of the X-ray attenuation with time after i.v. administration of iodinated nano-emulsions. Iodinated monoglycerides and iodinated castor oil nano-emulsions are compared to each other in heart, liver, spleen, and kidneys and also compared with iodinated vitamin E ( $\alpha$ -tocopherol) nano-emulsions from literature (data for iodinated vitamin E reproduced with permission from ref 5; copyright 2013 Elsevier);  $n = 3$  for each nano-emulsion. Curves were fitted with eq 1 for the heart and eqs 2 and 3 for the liver and spleen (eq 2 for accumulation and eq 3 for elimination). To illustrate the differences in contrast at 24 h postinjection, transverse slices through the liver and spleen are presented. Liver is indicated by orange arrows and spleen by blue arrows.

respectively:

$$\Delta HU(t) = \Delta HU_0 \times \exp(-k_1 t) \quad (1)$$

$$\Delta HU(t) = \Delta HU_0 + \Delta HU_\infty \times (1 - \exp(-k_2 t)) \quad (2)$$

where  $\Delta HU_0$  is the initial value of the contrast enhancement in blood (after injection),  $\Delta HU_\infty$  is the contrast enhancement at the end of the accumulation process (i.e., increment above the  $\Delta HU_0$  value),  $k_1$  is the blood elimination rate constant, and  $k_2$  is the accumulation rate constant. Afterward, once blood clearance is over at 24 h, the clearance from liver and spleen

becomes visible, following a monoexponential decrease given by eq 3:

$$\Delta HU(t) = \Delta HU_0 \times \exp(-k_3(t - 24)) \quad (3)$$

where  $k_3$  is the liver or spleen elimination rate. The values of the different parameters (Table 1) were obtained from the fits shown in Figure 7 for the elimination of the iodinated compounds from blood ( $k_1$  and  $t_{1/2}$ ), their accumulation in liver and spleen ( $k_2$ ), and their elimination from liver and spleen ( $k_3$  and  $t_{1/2}$ ). For the blood clearance, the values of the elimination rate  $k_1$  are comparable for the three formulations,

**TABLE 1. Pharmacokinetics Parameters for the Iodinated Nano-Emulsions<sup>a</sup>**

	iodinated castor oil			iodinated monoglyceride			iodinated vitamin E		
	blood	liver	spleen	blood	liver	spleen	blood	liver	spleen
$\Delta HU_0$ (HU)	202	62	72	228	54	116	245	88	58
$k_1$ (h <sup>-1</sup> )	0.113			0.103			0.077		
$t_{1/2}$ (h)	6.1			6.7			9.0		
$k_2$ (h <sup>-1</sup> )		0.224	0.345		0.037	0.164		0.054	
$\Delta HU_{max}$ (HU)		132	534		76	216		349	111
$k_3$ (h <sup>-1</sup> )		0.0039	0.0014		0.0051	0.0012		0.00054	
$t_{1/2}$ (days)		7.4	21.1		5.6	24.9		53	

<sup>a</sup>  $\Delta HU_{max} = \Delta HU_0 + \Delta HU_{\infty}$ .

being only slightly higher for the iodinated castor oil and monoglycerides (0.113 and 0.103 h<sup>-1</sup>) than for vitamin E (0.077 h<sup>-1</sup>). This difference is probably due to the major role of the spleen in the clearance process for the iodinated castor oils and monoglycerides nano-emulsions. Indeed, the values of the accumulation rate  $k_2$  (0.345 and 0.164 h<sup>-1</sup>, for the iodinated castor oil and monoglyceride, respectively) in the spleen are at least 3-fold higher than the corresponding rate in the liver for vitamin E (0.054 h<sup>-1</sup>) for which the role of spleen is negligible. It is also interesting to note that the kinetics of accumulation in liver and spleen are comparable for iodinated castor oil ( $k_2^{liver} = 0.224$  h<sup>-1</sup> and  $k_2^{spleen} = 0.345$  h<sup>-1</sup>) but not for monoglycerides ( $k_2^{liver} = 0.037$  h<sup>-1</sup> and  $k_2^{spleen} = 0.164$  h<sup>-1</sup>).

Once the blood is cleared from the contrast agent, the metabolism and elimination of iodinated oils from the liver or spleen remain the only observable kinetics. These elimination kinetics are much slower than the accumulation kinetics ( $k_3 \ll k_2$ , Table 1). Globally, the iodinated castor oil and monoglycerides present similar elimination kinetics, with half-lifetimes of about 1 week in the liver and 3 weeks in the spleen. It follows that these contrast agents are largely removed from the body within 50 days. Finally, contrast enhancement in kidneys begins in the range of 50 to 90 HU and decreases along with the blood clearance. This signal likely corresponds to the renal filtration of a part of the nanodroplets, that is, the smaller population of the log-normal distribution, but can also be induced by elimination of metabolites after their passage in liver or spleen.

The raw contrast enhancement given by the value of  $\Delta HU$  is fundamental for imaging applications but does not give a direct idea of the biodistribution of the contrast agent in organs or biological compartments since their volumes are different. To determine the real biodistribution of the contrast agents, we expressed the percentages of injected dose for each compartment or organ of interest: blood pool, liver, and spleen. Taking into account that the liver of a Swiss mouse represents  $4.37 \pm 0.19\%$  of its body weight and the spleen represents  $0.48 \pm 0.13\%$ ,<sup>29</sup> we recalculated

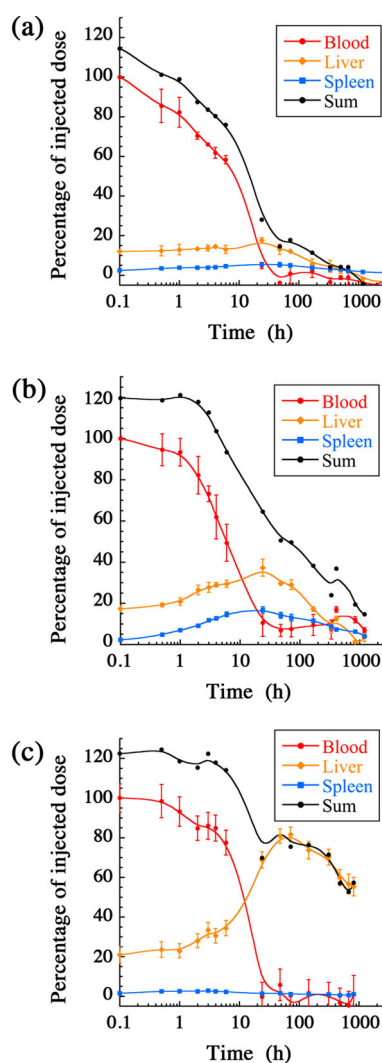


**Figure 8.** Accumulation and elimination of iodinated mono-glycerides (a), castor oil (b), and vitamin E (c) in different organs. The contrast agents were expressed as the percentage of injected dose, using the images from Figure 7 and placing the ROIs in the blood pool (red), liver (orange), and spleen (blue). The summed percentages (black) are also shown.

the amount of contrast agent (as % of injected dose) in the different organs at different acquisition times (Figure 8). Using this representation, mono-glycerides

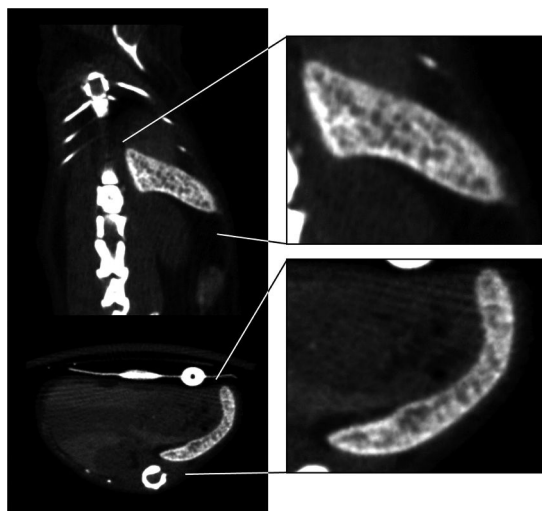


**Figure 9.** Micro-CT imaging and maximum intensity projections. Magnified representations of the spleen, 24 h after injection of iodinated castor oil: sagittal (top left), coronal (top right), and transverse (bottom) section.

(Figure 8a) show a moderate accumulation in liver (around 17% at the maximum, 24 h) and negligible accumulation in spleen ( $\sim 5\%$  at 24 h). In contrast, castor oil (Figure 8b) accumulates much stronger in the liver (40% at 24 h) but less in the spleen (20% at 24 h). Its global elimination kinetics is close to that of monoglycerides, with a gradual clearance after 24 h (compare black curves in Figure 8a,b). In the case of vitamin E (Figure 8c), the accumulation is much higher in the liver (reaching 80% of the injected dose at 48 h) with nearly nothing in the spleen. Its elimination kinetics is also quite different, showing a longer retention time in the liver. Thus, a different mechanism may be involved in the accumulation and elimination of vitamin E as compared to monoglycerides and castor oil. Noticeably, the initial presence of the contrast agent in liver comes from the blood irrigating the liver that contains contrast agents, explaining the apparent sum values (overall blood + liver) higher than 100%.

The main results from these data are (i) the similar kinetics of the blood clearance that is likely due to the similar surface composition of the nano-emulsion droplets, inducing a similar behavior from the blood clearance system; and (ii) the clear differences in their elimination pathway. Spleen accumulation could be linked to recognition by immune cells. In Figure 9, which focuses on the spleen at the maximum contrast enhancement (24 h after injection of iodinated castor oil nano-emulsion), one can observe a heterogeneity in the distribution of the contrast agent within the spleen.

The less contrasted domains correspond to the white pulp, consisting of lymphoid tissues mainly composed of leucocytes from different lineages, such as lymphocytes. In contrast, the more contrasted part corresponds to the red pulp in which the blood is filtered and which is composed of venous cavities filled

with red blood cells, lymphocytes, and macrophages.<sup>30</sup> Therefore, the accumulation of the contrast agent in the spleen is likely linked to the differential recognition of the oil droplets or leaked oil by immune cells as a function of their chemical structure. The slight shift in the size distribution between both formulations (see Figure 2) could also have been invoked to explain the differences in the accumulation behaviors since the smaller particles may be more excreted by kidneys while the larger ones may be trapped by the spleen. However, the difference in the values of the contrast is so high ( $\Delta\text{HU}_{\text{max}}$  values are  $220 \pm 30$  and  $530 \pm 30$  HU) that it can only be explained by alternative reasons, such as differences in the affinities of the droplets or their content for the spleen tissues or enhanced recognition by immune cells, especially macrophages. Interestingly, vitamin E nano-emulsions are not accumulated in spleen but in liver through specific hepatocyte uptake. The marginal accumulation of iodinated vitamin E nanodroplets in the spleen may result from their low ability in comparison to iodinated monoglycerides and castor oil to be taken up by macrophages. To confirm this hypothesis, iodinated nano-emulsion droplets were loaded with a lipophilic dye (NR668) and incubated with mouse macrophages to follow their uptake. NR668 is a Nile Red derivative bearing aliphatic chains, ensuring the dye remains encapsulated within the nano-emulsion lipid droplets, even in the presence of a serum-containing medium or when injected in a zebrafish model.<sup>31</sup> Nanodroplets with different iodinated oils, formulated together with 1 wt % of NR668, showed fluorescence maxima centered in the range of 590–605 nm, indicating that the dye was successfully encapsulated inside the apolar core.<sup>31</sup> Iodinated monoglyceride and castor oil nano-emulsion droplets were observed to be gradually taken up by the macrophages (Figure 10). After 30 min incubation, macrophages only engulfed a few droplets near the plasma membrane. Their number significantly increased after 2 h incubation, gradually highlighting the whole cell periphery (see image with only red channel of NR668). Finally, after 1 day of incubation, the whole cytoplasm is filled with nano-emulsion droplets. In sharp contrast, the fluorescence of NR668 was not detectable in macrophages incubated with iodinated vitamin E nano-emulsions, validating our hypothesis that this poor uptake may be responsible for the low accumulation of iodinated vitamin E droplets in the spleen. To check whether this difference in the nanodroplet uptake between monoglyceride, castor oil, and vitamin E is specific to the macrophage cell type, we compared by fluorescent microscopy the uptake of NR668-loaded nano-emulsion droplets (made with the three different iodinated oils) by murine hepatocytes BNL-CL2 and macrophages RAW264.7, after 30 min and 24 h incubation (Figure S4, Supporting Information). In hepatocytes, no internalization of nano-emulsion droplets

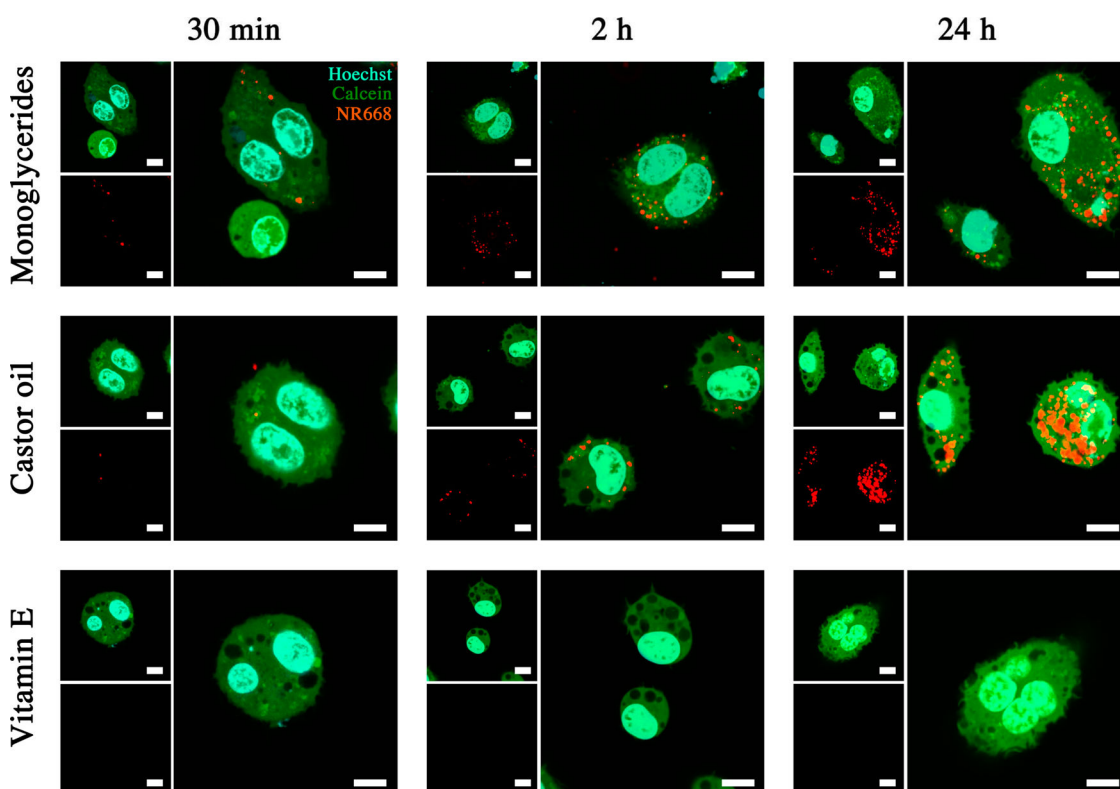


**Figure 10.** Monitoring of the uptake of NR668-loaded iodinated nano-emulsions by murine macrophages (RAW264.7 cells). Nuclei were stained with Hoechst (cyan) and cells with calcein AM (green). NR668 (a lipophilic modified Nile Red) loaded in the oil core of the nano-emulsion droplets allows following the location of the droplets once engulfed by the cells. Iodinated monoglycerides, iodinated castor oil, and iodinated vitamin E were formulated as nano-emulsions and incubated for different times: 30 min, 2 h, and 24 h. Top left insets show the cell and nuclei. Bottom left insets show the signal of NR668, and the larger right picture shows both merged.

was observed with all three iodinated oils, confirming that the uptake by macrophages of nano-emulsions made from castor oil and monoglycerides (Figure 10) is selective.

These data clearly show that the oil nature has a strong impact on macrophage uptake, even formulated as nanodroplets with similar surface composition. They allow understanding of the selective accumulation in the spleen of iodinated monoglycerides and castor oil. To confirm our microscopy observations, a quantification of the internalized NR668 was performed by fluorometry of the cellular lysate in DMSO (Figure 11).

These data confirmed the uptake of nanodroplets containing monoglycerides and castor oil. The measured values appear similar for the two oils, with some difference arising only after 24 h, a condition that is relatively far from the conditions used *in vivo*. Importantly, even at such long incubation time, the vitamin E nanodroplets do not penetrate into cell cytoplasm. This confirms that vitamin E droplets and/or the vitamin E oil are not recognized by macrophages, and that the blood clearance in this case occurs through the gradual accumulation of the droplets in hepatocytes. This difference in the clearance mechanism can also explain the longer half-life (9.0 h) of vitamin E

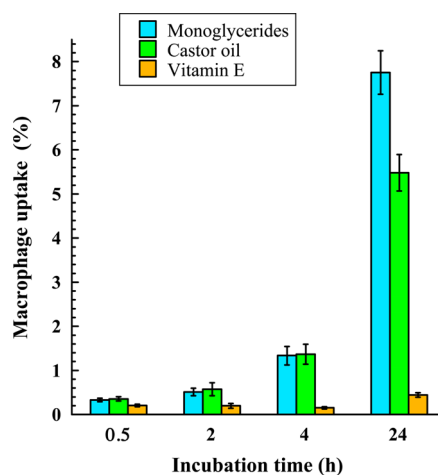


**Figure 11.** Quantification of nano-emulsion uptake by macrophages as a function of incubation time and oil nature. After incubation with NR668-loaded nanodroplets, the macrophages were washed, lysed with DMSO, and measured by fluorometry. Uptake was expressed as the percentage of fluorescence associated with cells versus the amount of fluorescence present in the feed solution.

nano-emulsions compared to castor oil (6.1 h) and monoglycerides (6.7 h). The results of macrophage uptake explains the difference in accumulation in liver and spleen between vitamin E and the two other oils

but does not permit one to conclude on the difference of accumulation between iodinated monoglycerides and iodinated castor oil, likely due to additional factors arising *in vivo*, as compared to *in vitro* cell experiments.

## CONCLUSION

This study shows that iodinated nano-emulsions with comparable morphologies, sizes, surface composition, and only differing in the chemical nature of the iodinated oil droplet core display significantly different pharmacokinetics and biodistributions. Herein we propose two novel formulations based on hexa-iodinated monoglyceride and hexa-iodinated castor oil, formulated by spontaneous emulsification and stabilized by PEGylated non-ionic surfactant. Besides the very high contrasting properties of these X-ray contrast

agents, we show that, after *i.v.* administration, both nano-emulsions present similar blood elimination kinetics with  $t_{1/2}$  around 6 h, followed then by different *in vivo* behavior, with the iodinated castor oil showing a much stronger accumulation in the spleen. Comparison with another iodinated nano-emulsion based on iodinated vitamin E that accumulates only in liver further demonstrates that these nanoparticulate systems can provide strong X-ray contrast enhancement in specific targets such as liver, spleen, or only blood as a function of the oil used in the nano-emulsion formulation. Our data further revealed that the nature of the iodinated oil affects the uptake of nanodroplets by the macrophages, thus explaining in part the observed differences in biodistribution. The half-elimination time of these contrast agents is on the scale of weeks, offering sufficient retention for micro-CT imaging applications. Their potential use for clinical imaging could be envisioned, as well.

## EXPERIMENTAL SECTION

2,3,5-Triiodobenzoic acid, castor oil, *N,N'*-dicyclohexylcarbodiimide, 4-dimethylaminopyridine, deuterated chloroform ( $\text{CDCl}_3$ ), ethyl acetate, cyclohexane, dichloromethane, sodium bicarbonate, sodium sulfate anhydrous, sodium chloride Hoechst 33258, calcein AM, dimethyl sulfoxide (DMSO), and 3-(4,5-dimethylthiazol-2-yl)-2,5-diphenyltetrazolium bromide (MTT) solutions were purchased from Sigma-Aldrich (St. Louis, MO). Glycerol monocaprylate (Capmul MCM C8) was kindly gifted by Abitec (Columbus, OH). Non-ionic surfactant (Kolliphor ELP) from BASF (Ludwigshafen, Germany) was kindly donated by Laserson, Etampes, France. Kolliphor ELP (formerly named "Cremophor ELP") is a parenteral-grade non-ionic surfactant made by reacting ethylene oxide to castor seed oil at a molar ratio of 35.<sup>32</sup> Phosphate buffered saline, Dulbecco's modified Eagle medium (DMEM), and fetal bovine serum were from PAN Biotech (Aidenbach, Germany).

**General Synthesis of Hexa-iodinated Monoglyceride and Hexa-iodinated Castor Oil.** 2,3,5-Triiodobenzoic acid (TIBA) (10 g, 0.02 mol), 4-dimethylaminopyridine (0.75 g, 0.007 mol), and *N,N'*-dicyclohexylcarbodiimide (4.5 g, 0.022 mol) were sequentially added to a solution containing either glycerol monocaprylate (1.84 g, 0.0085 mol) or castor oil (7.92 g, 0.0085 mol), in dichloromethane at room temperature. The reaction mixture was stirred overnight at room temperature. Then, dicyclohexylurea and other precipitates were removed by filtration. The organic phase was washed twice with saturated aqueous  $\text{NaHCO}_3$  and once with saturated NaCl solution and then dried over anhydrous  $\text{Na}_2\text{SO}_4$ . The solvent was removed by rotary evaporator, and the resulting oil was purified by gradient elution silica gel column chromatography using cyclohexane and ethyl acetate as eluents. Both purified products were obtained as dense and yellowish viscous oils. The reaction yields were 58% for hexa-iodinated monoglyceride and 47% for hexa-iodinated castor oil. The chemical structure of these two iodinated oils is presented in Figure 1a. Hexa-iodinated monoglyceride and hexa-iodinated castor oil have theoretical iodine content of 64.5 and 40.2 wt %, respectively. It should be noted that the difference in molecular weights between these two molecules can also play a role in their X-ray attenuation properties, which are the highest for the heaviest one (*i.e.*, iodinated castor oil).

**Characterization of Hexa-iodinated Monoglyceride and Hexa-iodinated Castor Oil.**  $^1\text{H}$  NMR spectra were recorded with a Bruker Top Spin 3.0 operating at 400 MHz using deuterated chloroform ( $\text{CDCl}_3$ ) as a solvent. Chemical shifts ( $\delta$ ) were expressed in parts per million, taking tetramethylsilane as internal reference. *Hexa-iodinated monoglycerides:*  $^1\text{H}$  NMR ( $\text{CDCl}_3$ ,  $\delta/\text{ppm}$ ) 8.2 (s, 2H,

ortho), 7.7 (s, 2H, para), 4.6 (d, 2H,  $\text{phCOO}-\text{CH}_2-\text{CH}$ ), 4.4 (m, 1H,  $\text{CH}_2-\text{CH}-\text{CH}_2$ ), 4.3 (d, 2H,  $\text{OCH}_2-\text{CH}$ ), 2.3 (t, 2H,  $\text{CO}-\text{CH}_2-\text{CH}_2$ ), 1.5 (m, 2H,  $\text{COCH}_2-\text{CH}_2-\text{CH}_2$ ), 1.3 (m, 8H,  $\text{CH}_2-\text{CH}_2$ )<sub>4</sub>- $\text{CH}_3$ ), 0.8 (t, 3H,  $\text{CH}_3$ ). *Hexa-iodinated castor oil:*  $^1\text{H}$  NMR ( $\text{CDCl}_3$ ,  $\delta/\text{ppm}$ ) 8.2 (s, 2H, ortho), 7.6 (s, 2H, para), 5.5 (dd, 6H,  $(\text{CH}=\text{CH})_3$ ), 5 (m, 1H,  $\text{OCH}_2-\text{CH}-\text{CH}_2$ ), 4.2 (d, 4H,  $(\text{COO}-\text{CH}_2-\text{CH})_2$ ), 3.5 (m, 3H,  $\text{CH}_2-\text{CH}-\text{OCOPh}$ ), 2.4 (t, 6H,  $(\text{OCO}-\text{CH}_2-\text{CH}_2)_3$ ), 2.2 (t, 6H,  $(\text{CH}-\text{CH}_2-\text{CH}=\text{CH})_3$ ), 2.1 (m, 6H,  $(\text{CH}_2-\text{CH}_2-\text{CH}=\text{CH})_3$ ), 2 (s, 1H, OH), 1.5 (m, 6H,  $(\text{COCH}_2-\text{CH}_2-\text{CH}_2)_3$ ), 1.3 (q, 6H,  $(\text{PhCOO}-\text{CH}-\text{CH}_2)_3$ ), 1.2 (m, 48H,  $(\text{CH}-\text{CH}_2)_4-\text{CH}_3$ )<sub>3</sub>,  $(\text{CH}=\text{CHCH}_2-\text{CH}_2)_4-\text{CH}_2$ )<sub>3</sub>), 0.8 (t, 9H,  $(\text{CH}_3)_3$ ).

**Preparation of Iodinated Nano-Emulsions.** Nano-emulsions of iodinated monoglyceride and iodinated castor oil were formulated by the spontaneous nano-emulsification method as previously reported.<sup>26,33–35</sup> Formulation parameters are defined as surfactant/(surfactant + oil) weight ratio (SOR) and (surfactant + oil)/(surfactant + oil + water) weight ratio (SOWR).<sup>26</sup> (i) Iodinated monoglyceride nano-emulsions are formulated with SOR = 60% and SOWR = 40%. Hexa-iodinated monoglyceride (0.32 g) was first mixed with the non-ionic hydrophilic surfactant (0.48 g), maintained at 70 °C, and homogenized by help of several vortex mixing and use of a sonication bath (around 10 min). Next, PBS, used as an aqueous phase (1.20 g), was added to the surfactant/oil mixture under gentle magnetic stirring, giving rise within seconds to spontaneous formation of stable nano-emulsions. A nano-emulsion droplet is schematically represented in Figure 1b. (ii) Iodinated castor oil nano-emulsions are formulated at SOR = 65% and SOWR = 40%. The formulation process, similar to the one described above, uses hexa-iodinated castor oil (0.28 g), non-ionic surfactant (0.52 g), and PBS (1.2 g). The SOR values used for both formulations were selected to obtain nano-emulsions with optimal nano-emulsion size, monodispersity, and iodine content, as described in the Results and Discussion section (Figure 2).

**Characterization of Nano-Emulsions.** *Dynamic Light Scattering.* Size distributions and polydispersity indices (PDI) were measured by DLS with a NanoZS Malvern apparatus (Malvern, Orsay, France). The helium/neon laser, 4 mW, was operated at 633 nm, with the scatter angle fixed at 173° and the temperature maintained at 25 °C. DLS data were analyzed using a cumulant-based method.

*Transmission Electron Microscopy.* The X-ray attenuation properties of iodine nanodroplets also result in good contrast in TEM. Therefore, samples were used without any staining agent and were diluted (1/10) with Milli-Q water. A drop of the suspension was placed on a carbon grid (carbon type-A, 300 mesh, copper, Ted Pella Inc. Redding, PA) and dried at 40 °C.

Observations were carried out using a Philips Morgagni 268D electron microscope.

**Cytotoxicity Assays.** Cytotoxicity assays were performed using HeLa human cervix epithelial adenocarcinoma cells, BNL-CL2 mouse hepatocyte, and RAW264.7 murine leukemia virus-transformed monocyte cells. HeLa cells were selected because they are considered to be a standard cell line that allows direct comparison of experimental data. RAW264.7 cells were chosen because their properties are very similar to those of normal macrophages.<sup>36</sup> RAW264.7 cells are a well-suited model for macrophages,<sup>37–39</sup> showing notably similar patterns of uptake and cytotoxicity as primary macrophages.<sup>39</sup> Cells were seeded in 96-well plates at a concentration of  $10^4$  cells per well in 100  $\mu$ L of medium (DMEM) containing 10% FBS and 1 wt % of commercial solution of penicillin and streptomycin. Cells were then incubated overnight at 37 °C under a controlled atmosphere (5% CO<sub>2</sub> and 80% H<sub>2</sub>O). Next, the culture medium was replaced by the same medium but containing variable concentrations of iodine encapsulated nano-emulsions (see details below). After incubation for 24 h, the medium was removed and the cells were washed with PBS. Then, the wells were filled with cell culture medium containing MTT, incubated for 4 h at 37 °C, and the formazan crystals formed were dissolved by adding 100  $\mu$ L of DMSO. UV absorbance was measured at 570 nm with a microplate reader (Varioskan Flash, Thermo Scientific, USA). Experiments were carried out in triplicate and expressed as a percentage of viable cells compared to the control group.

**In Vitro Mouse Macrophage Uptake. Confocal Microscopy.** The cellular uptake and intracellular localization were determined in RAW264.7 cells (mouse macrophages) using a Leica TCS SP confocal scanning system (Leica, Germany). To follow the nano-emulsion droplets, we used a modified lipophilic Nile Red (NR668) that was solubilized at 0.1% (wt/wt) in the iodinated oils before formulation of nano-emulsions. NR668 synthesis was previously reported.<sup>31</sup> Cells were cultured overnight in cell culture glass chambers slides at a density of  $5 \times 10^4$  cells per well before their exposition to the dye-loaded nano-emulsions in DMEM at a concentration corresponding to 0.1 mg/mL, supplemented with 10% of FBS, for 30 min, 2 h, and 24 h at 37 °C in a 5% CO<sub>2</sub> humidified atmosphere. After incubation, cells were stained with calcein AM (10  $\mu$ M, 15 min of incubation in HBSS) and with Hoechst 33342 (50  $\mu$ M, 10 min of incubation in HBSS). After six washes in HBSS to remove all nonpenetrated nano-emulsion droplets, cells were mounted in the fluorophore protector CC/mount and observed with a Leica confocal microscope equipped with an argon/neon laser and a 63 $\times$  oil immersion objective. The excitation wavelengths used were 360 nm for Hoechst 33342, 488 nm for calcein, and 543 nm for NR668, and the fluorescence signals were collected in the 380–460 nm range for Hoechst, 500–530 nm range for calcein, and 560–650 nm range for Nile Red 668, respectively. The images were processed with Fiji software.

**Quantification of Macrophage Uptake.** Cellular uptake was quantified by fluorescence spectroscopy. Mouse macrophage RAW264.7 cells were cultured as described in the paragraph above, except that cells were lysed with DMSO and not mounted for microscopy analysis. The effectiveness of washing and lysing was checked with fluorescence microscopy observations. The concentration of encapsulated NR668 in the cell lysate was quantified by fluorimetry with an excitation wavelength of 550 nm and an emission wavelength of 630 nm (with a microplate reader Varioskan Flash, Thermo Scientific, USA). Uptake was expressed as the percentage of fluorescence associated with cells versus the amount of fluorescence in the feed solution.

**Micro-CT Imaging.** The experiments were performed in agreement with the Committee of Animal Research and Ethics of the University of Lyon-1.

**In Vitro Experiments.** The X-ray attenuation properties of iodinated nano-emulsions were evaluated at various concentrations with a micro-CT scanner (1076 Skyscan, Kartuizersweg, Belgium). Experimental parameters were as follows: X-ray, 49 keV, 129  $\mu$ A; resolution, 35  $\mu$ m; pitch, 0.4°; aluminum filters, 0.5 and 632 ms. Iodine concentration of nano-emulsions was

determined using a calibration curve established with a commercial hydrophilic contrast agent (XenetiX 300, *i.e.*, iobitridol), correlating iodine concentration and radiopacity.

**In Vivo Experiments.** *In vivo* imaging experiments were performed with a micro-CT scanner (INVEON, Siemens, Munich, Germany). The experimental X-ray parameters were as follows: X-ray, 50 keV, 500  $\mu$ A; resolution, 111.25  $\mu$ m; pitch, 2°; aluminum filters, 0.5 and 900 ms. The acquisitions were performed on Swiss mice,  $n = 3$ , for each type of nano-emulsion. Before acquisition, mice were anesthetized with isoflurane. Then, iodinated nano-emulsions were intravenously injected (using a catheter) in the tail vein, with an injection volume corresponding to 10% of the blood volume (*i.e.*, 7.6  $\mu$ L of nano-emulsions per gram of mouse). Scans were performed before administration, immediately after injection, and after 30 min, 1 h, 2 h, 3 h, 4 h, 6 h, 1 day, 2 days, 3 days, 7 days, 14 days, 21 days, 28 days, and 50 days. The micro-CT raw data were treated with OsiriX viewer to establish 2D maximum projection slices and 3D volume rendering images and then to quantify the signal by placing the region of interests in the heart, liver, spleen, and kidneys.

**Conflict of Interest:** The authors declare no competing financial interest.

**Acknowledgment.** Experimental part (*in vivo* imaging) of this study was performed on CERMEP-imagerie du vivant, Bron, F-69677, France, imaging facilities. The authors thank the technical staff of the platform. M.C. would like to acknowledge Grant "Attractivité IDEX 2013" within the University of Strasbourg, France.

**Supporting Information Available:** Additional figures and movies as described in the text. This material is available free of charge via the Internet at <http://pubs.acs.org>.

## REFERENCES AND NOTES

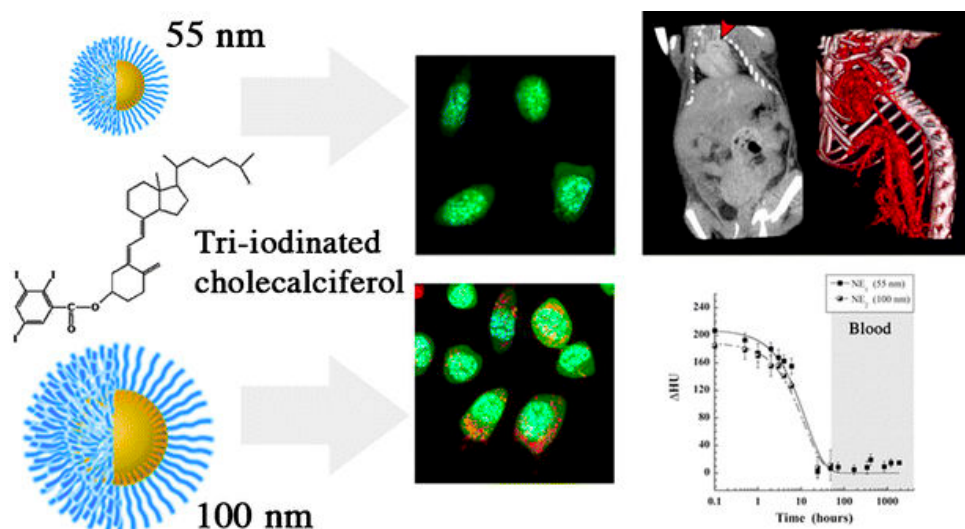
- Li, X.; Anton, N.; Zuber, G.; Vandamme, T. F. Contrast Agents for Preclinical Targeted X-ray Imaging. *Adv. Drug Delivery Rev.* **2014**, *76*, 116–133.
- Anton, N.; Vandamme, T. F. Nanotechnology for Computed Tomography: A Real Potential Recently Disclosed. *Pharm. Res.* **2014**, *31*, 20–34.
- Hallouard, F.; Anton, N.; Choquet, P.; Constantinesco, A.; Vandamme, T. F. Iodinated Blood Pool Contrast Media for Preclinical X-ray Imaging Applications: A Review. *Biomaterials* **2010**, *31*, 6249–6268.
- Jakhmola, A.; Anton, N.; Vandamme, T. F. Inorganic Nanoparticles Based Contrast Agents for X-ray Computed Tomography. *Adv. Healthcare Mater.* **2012**, *1*, 413–431.
- Li, X.; Anton, N.; Zuber, G.; Zhao, M.; Messaddeq, N.; Hallouard, F.; Fessi, H.; Vandamme, T. F. Iodinated Alpha-Tocopherol Nano-Emulsions as Non-toxic Contrast Agent for Preclinical X-ray Imaging. *Biomaterials* **2013**, *34*, 481–491.
- van Tellingen, O.; Beijnen, J.; Verweij, J.; Scherrenburg, E.; Nuijten, W.; Sparreboom, A. Rapid Esterase-Sensitive Breakdown of Polysorbate 80 and Its Impact on the Plasma Pharmacokinetics of Docetaxel and Metabolites in Mice. *Clin. Cancer Res.* **1999**, *5*, 2918–2924.
- Badea, C. T.; Athreya, K. K.; Espinosa, G.; Clark, D.; Ghafouri, A.; Li, Y.; Kirsch, D. G.; Johnson, G.; Annappagada, A.; Ghaghada, K. B. Computed Tomography Imaging of Primary Lung Cancer in Mice Using a Liposomal-Iodinated Contrast Agent. *PLoS One* **2012**, *7*, e34496.
- Toy, R.; Hayden, E.; Camann, A.; Berman, Z.; Vicente, P.; Tran, E.; Meyers, J.; Pansky, J.; Peiris, P. M.; Wu, H.; Exner, A.; Wilson, D.; Ghaghada, K. B.; Karathanasis, E. Multimodal *In Vivo* Imaging Exposes the Voyage of Nanoparticles in Tumor Microcirculation. *ACS Nano* **2013**, *7*, 3118–3129.
- de Vries, A.; Custers, E.; Lub, J.; van den Bosch, S.; Nicolay, K.; Grull, H. Block-Copolymer-Stabilized Iodinated Emulsions for Use as CT Contrast Agents. *Biomaterials* **2010**, *31*, 6537–6544.
- Wisner, E. R.; Weichert, J. P.; Longino, M. A.; Counsell, R. E.; Weisbrode, S. E. A Surface-Modified Chylomicron

- Remnant-like Emulsion for Percutaneous Computed Tomography Lymphography: Synthesis and Preliminary Imaging Findings. *Invest. Radiol.* **2002**, *37*, 232–239.
11. Pan, D.; Williams, T. A.; Senpan, A.; Allen, J. S.; Scott, M. J.; Gaffney, P. J.; Wickline, S. A.; Lanza, G. M. Detecting Vascular Biosignatures with a Colloidal, Radio-opaque Polymeric Nanoparticle. *J. Am. Chem. Soc.* **2009**, *131*, 15522–15527.
  12. Jakhmola, A.; Anton, N.; Anton, H.; Messaddeq, N.; Hallouard, F.; Klymchenko, A.; Mely, Y.; Vandamme, T. F. Poly- $\epsilon$ -Caprolactone Tungsten Oxide Nanoparticles as a Contrast Agent for X-ray Computed Tomography. *Biomaterials* **2014**, *35*, 2981–2986.
  13. Brigger, I.; Dubernet, C.; Couvreur, P. Nanoparticles in Cancer Therapy and Diagnosis. *Adv. Drug Delivery Rev.* **2002**, *54*, 631–651.
  14. Haley, B.; Frenkel, E. Nanoparticles for Drug Delivery in Cancer Treatment. *Urol. Oncol.* **2008**, *26*, 57–64.
  15. Torchilin, V. P.; Trubetsky, V. S. Which Polymers Can Make Nanoparticulate Drug Carriers Long-Circulating?. *Adv. Drug Delivery Rev.* **1995**, *16*, 141–155.
  16. Betzer, O.; Shwartz, A.; Motiei, M.; Kazimirsky, G.; Gispan, I.; Damti, E.; Brodie, C.; Yadid, G.; Popovtzer, R. Nanoparticle-Based CT Imaging Technique for Longitudinal and Quantitative Stem Cell Tracking within the Brain: Application in Neuropsychiatric Disorders. *ACS Nano* **2014**, *8*, 9274–9285.
  17. Cole, L. E.; Vargo-Gogola, T.; Roeder, R. K. Detection of Breast Microcalcifications in a Murine Model Using Targeted Gold Nanoparticles. *ACS Nano* **2014**, *8*, 7486–7496.
  18. Kattumuri, V.; Katti, K.; Bhaskaran, S.; Boote, E. J.; Casteel, S. W.; Fent, G. M.; Robertson, D. J.; Chandrasekhar, M.; Kannan, R.; Katti, K. V. Gum Arabic as a Phytochemical Construct for the Stabilization of Gold Nanoparticles: *In Vivo* Pharmacokinetics and X-ray-Contrast-Imaging Studies. *Small* **2007**, *3*, 333–341.
  19. Hainfeld, J. F.; Slatkin, D. N.; Focella, T. M.; Smilowitz, H. M. Gold Nanoparticles: A New X-ray Contrast Agent. *Br. J. Radiol.* **2006**, *79*, 248–253.
  20. Kim, D.; Park, S.; Lee, J. H.; Jeong, Y. Y.; Jon, S. Antibiofouling Polymer-Coated Gold Nanoparticles as a Contrast Agent for *In Vivo* X-ray Computed Tomography Imaging. *J. Am. Chem. Soc.* **2007**, *129*, 7661–7665.
  21. Eck, W.; Nicholson, A. I.; Zentgraf, H.; Semmler, W.; Bartling, S. Anti-Cd4-Targeted Gold Nanoparticles Induce Specific Contrast Enhancement of Peripheral Lymph Nodes in X-ray Computed Tomography of Live Mice. *Nano Lett.* **2010**, *10*, 2318–2322.
  22. Chanda, N.; Kattumuri, V.; Shukla, R.; Zambre, A.; Katti, K.; Upendran, A.; Kulkarni, R. R.; Kan, P.; Fent, G. M.; Casteel, S. W.; Smith, C. J.; Boote, E.; Robertson, J. D.; Cutler, C.; Lever, J. R.; Katti, K. V.; Kannan, R. Bombesin Functionalized Gold Nanoparticles Show *In Vitro* and *In Vivo* Cancer Receptor Specificity. *Proc. Natl. Acad. Sci. U.S.A.* **2010**, *107*, 8760–8765.
  23. Rabin, O.; Manuel Perez, J.; Grimm, J.; Wojtkiewicz, G.; Weissleder, R. An X-ray Computed Tomography Imaging Agent Based on Long-Circulating Bismuth Sulphide Nanoparticles. *Nat. Mater.* **2006**, *5*, 118–122.
  24. Oh, M. H.; Lee, N.; Kim, H.; Park, S. P.; Piao, Y.; Lee, J.; Jun, S. W.; Moon, W. K.; Choi, S. H.; Hyeon, T. Large-Scale Synthesis of Bioinert Tantalum Oxide Nanoparticles for X-ray Computed Tomography Imaging and Bimodal Image-Guided Sentinel Lymph Node Mapping. *J. Am. Chem. Soc.* **2011**, *133*, 5508–5515.
  25. Hallouard, F.; Briançon, S.; Anton, N.; Li, X.; Vandamme, T. F.; Fessi, H. Iodinated Nano-Emulsions as Contrast Agents for Preclinical X-ray Imaging, Impact of the Free Surfactants on the Pharmacokinetics. *Eur. J. Pharm. Biopharm.* **2013**, *83*, 54–62.
  26. Anton, N.; Vandamme, T. F. The Universality of Low-Energy Emulsification. *Int. J. Pharm.* **2009**, *377*, 142–147.
  27. Nebuloni, L.; Kuhn, G. A.; Müller, R. A Comparative Analysis of Water-Soluble and Blood-Pool Contrast Agents for *In Vivo* Vascular Imaging with Micro-CT. *Acad. Radiol.* **2013**, *20*, 1247–1255.
  28. Boll, H.; Nittka, S.; Doyon, F.; Neumaier, M.; Marx, A.; Kramer, M.; Groden, C.; Brockmann, M. A. Micro-CT Based Experimental Liver Imaging Using a Nanoparticulate Contrast Agent: A Longitudinal Study in Mice. *PLoS One* **2011**, *6*, e25692.
  29. Church, R. J.; Wu, H.; Mosedale, M.; Sumner, S. J.; Pathmasiri, W.; Kurtz, C. L.; Pletcher, M. T.; Eaddy, J. S.; Pandher, K.; Singer, M.; Batheja, A.; Watkins, P. B.; Adkins, K.; Harrill, A. H. A Systems Biology Approach Utilizing a Mouse Diversity Panel Identifies Genetic Differences Influencing Isoniazid-Induced Microvesicular Steatosis. *Toxicol. Sci.* **2014**, *140*, 481–492.
  30. Tarantino, G.; Savastano, S.; Capone, D.; Colao, A. Spleen: A New Role for an Old Player?. *World J. Gastroenterol.* **2011**, *17*, 3776–3784.
  31. Klymchenko, A.; Roger, E.; Anton, N.; Anton, H.; Shulov, I.; Vermot, J.; Mely, Y.; Vandamme, T. F. Highly Lipophilic Fluorescent Dyes in Nano-Emulsions: Towards Bright Non-leaking Nano-Droplets. *RSC Adv.* **2012**, *2*, 11876–11886.
  32. Szebeni, J.; Muggia, F. M.; Alving, C. R. Complement Activation by Cremophor EL as a Possible Contributor to Hypersensitivity to Paclitaxel: An *In Vitro* Study. *J. Natl. Cancer Inst.* **1998**, *90*, 300–306.
  33. Anton, N.; Benoit, J. P.; Saulnier, P. Design and Production of Nanoparticles Formulated from Nano-Emulsion Templates—A Review. *J. Controlled Release* **2008**, *128*, 185–199.
  34. Anton, N.; Gayet, P.; Benoit, J. P.; Saulnier, P. Nano-Emulsions and Nanocapsules by the Pit Method: An Investigation on the Role of the Temperature Cycling on the Emulsion Phase Inversion. *Int. J. Pharm.* **2007**, *344*, 44–52.
  35. Anton, N.; Vandamme, T. F. Nano-Emulsions and Micro-emulsions: Clarifications of the Critical Differences. *Pharm. Res.* **2011**, *28*, 978–985.
  36. Raschke, W. C.; Baird, S.; Ralph, P.; Nakoinz, I. Functional Macrophage Cell Lines Transformed by Abelson Leukemia Virus. *Cell* **1978**, *15*, 261–267.
  37. Albanese, A.; Walkey, C. D.; Olsen, J. B.; Guo, H.; Emili, A.; Chan, W. C. Secreted Biomolecules Alter the Biological Identity and Cellular Interactions of Nanoparticles. *ACS Nano* **2014**, *8*, 5515–5526.
  38. Guo, L.; Panderi, I.; Yan, D. D.; Szulak, K.; Li, Y.; Chen, Y. T.; Ma, H.; Niesen, D. B.; Seeram, N.; Ahmed, A.; Yan, B.; Pantazatos, D.; Lu, W. A Comparative Study of Hollow Copper Sulfide Nanoparticles and Hollow Gold Nanospheres on Degradability and Toxicity. *ACS Nano* **2013**, *7*, 8780–8793.
  39. Herd, H.; Daum, N.; Jones, A. T.; Huwer, H.; Ghandehari, H.; Lehr, C. M. Nanoparticle Geometry and Surface Orientation Influence Mode of Cellular Uptake. *ACS Nano* **2013**, *7*, 1961–1973.



## Chapter 1.3 : Biodistribution and Toxicity of X-Ray Iodinated Contrast Agent in Nano-emulsions in Function of Their Size

In this present study we focused on another important key parameter which extremely affects both the pharmacokinetics and toxicity profiles in general, that is the nanoparticle size. To this end, we developed two nano-emulsions based on the same oily core (iodinated cholecalciferol) and the only different aspect is the size. First, the vitamin D3 (cholecalciferol) was grafted by iodinated compound through esterification reaction yielding triiodocholecalciferol, followed by formulation of 55 nm and 100 nm of droplet diameter in terms of oil/surfactant ratio. The hydrodynamic diameters were measured by DLS giving narrow distribution size and monodispersed particles. *In vitro* MTT assays were done on hepatocytes (BNL-CL2) and macrophages (RAW 264.7) showing negligible toxicity, as well as, the stability of fetal bovine serum (FBS) and cellular uptake studies were evaluated. The *in vivo* *i.v.* injection was carried out on nude mice to explain finally the effect of the size on the biodistribution and the toxicity. Actually, this study does not emphasized that the nano-droplet size impacts pharmacokinetics, but has rather a strong effect on the toxicity *in vitro* and *in vivo*.



# Biodistribution and Toxicity of X-Ray Iodinated Contrast Agent in Nano-emulsions in Function of Their Size

Mohamed F. Attia<sup>1,2,3</sup> · Nicolas Anton<sup>1,2</sup> · Roman Akasov<sup>1,2,4</sup> · Manuela Chiper<sup>1,2</sup> · Elena Markvicheva<sup>4</sup> · Thierry F. Vandamme<sup>1,2</sup>

Received: 7 September 2015 / Accepted: 21 October 2015 / Published online: 28 October 2015  
© Springer Science+Business Media New York 2015

## ABSTRACT

**Purpose** This study aimed to investigate the impact of the size of X-ray iodinated contrast agent in nano-emulsions, on their toxicity and fate *in vivo*.

**Methods** A new compound, triiodobenzoate cholecalciferol, was synthesized, formulated as nano-emulsions, and followed after i.v. administration in mice by X-ray imaging (micro computed tomography). Physicochemical characterization and process optimization allowed identifying a good compromise between X-ray contrasting properties, monodispersity and stability. This also allowed selecting two formulations with different sizes, hydrodynamic diameters of 55 and 100 nm, but exactly the same composition. *In vitro* experiments were performed on two cell lines, namely hepatocytes (BNL-CL2) and macrophages (RAW264.7).

**Results** Cell viability studies, cell uptake observations by confocal microscopy, and uptake quantification by fluorimetry, disclosed clear differences between two formulations, as well as between two types of cell lines. After i.v. injection of the two

iodinated nano-emulsions in mice, CT scans provided the quantification of the pharmacokinetics and biodistributions. We finally showed that the size in the nano-emulsions has not a real impact on the pharmacokinetics and biodistributions, but has a strong influence on their toxicity, corroborating the *in vitro* results.

**Conclusions** This study shows that the size of the nanocarrier significantly matters, likely due to highly different interactions with cells and tissues.

**KEY WORDS** cholecalciferol · contrast agent · emulsion size · micro-CT · nano-emulsion

## ABBREVIATIONS

CDCI <sub>3</sub>	Deuterated chloroform
CT	Computed tomography
DCC	N,N'-dicyclohexylcarbodiimide
DLS	Dynamic light scattering
DMAP	4-dimethylaminopyridine
DMEM	Dulbecco's modified Eagle medium
DMSO	Dimethyl sulfoxide
EPR	Enhanced permeation and retention
FBS	Fetal bovine serum
HBSS	Hank's balanced salt solution
microCT	Micro computed tomography
MRI	Magnetic resonance imaging
MTT	3-(4,5 dimethylthiazol-2-yl)-2,5-diphenyltetrazolium bromide
NPs	Nanoparticles
OR	Oil ratio
PBS	Phosphate buffered saline
PDI	Polydispersity index
PEG	Polyethyleneglycol
PET	Positron emission tomography
RES	Reticuloendothelial system
SOR	Surfactant / (surfactant + oil) weight ratio

**Electronic supplementary material** The online version of this article (doi:10.1007/s11095-015-1813-0) contains supplementary material, which is available to authorized users.

✉ Nicolas Anton  
nanton@unistra.fr

<sup>1</sup> University of Strasbourg, Faculty of Pharmacy, 74 route du Rhin 67401 Illkirch Cedex, France

<sup>2</sup> CNRS UMR 7199, Laboratoire de Conception et Application de Molécules Bioactives, équipe de Pharmacie Biogénérique, University of Strasbourg, route du Rhin No. 74, F-67401 Illkirch Cedex, France

<sup>3</sup> National Research Center, P.O. 12622, Cairo, Egypt

<sup>4</sup> Shemyakin-Ovchinnikov Institute of Bioorganic Chemistry, Russian Academy of Sciences, Miklukho-Maklaya Str., 16/10 117997 Moscow, Russia

SOWR	(surfactant + oil) / (surfactant + oil + water) weight ratio
SPECT	Single photon emission computed tomography
TIBA	2,3,5-Triiodobenzoic acid
TMS	Tetramethylsilane

## INTRODUCTION

Advanced diagnosis is becoming a prime and essential step for ideal treatment by means of detecting pathogens and showing the specific locations of unhealthy cells. In this context, non-invasive and minimally invasive *in vivo* imaging techniques constitute a powerful arsenal for clinical diagnostics, and are currently seeing an unprecedented development. Several imaging modalities such as X-ray computed tomography (X-Ray CT), magnetic resonance imaging (MRI), positron emission tomography (PET) and single photon emission computed tomography (SPECT) or combination among two or more different modalities (multi-modals) are utilized for obtaining high resolution and potential visibility of internal bodily structures. They are generally complementary with their specific balance between advantage and drawbacks. Herein, we are focusing on X-ray imaging, that can be considered as an interesting compromise between cost, with a good spatial resolution, and without managing radioactive wastes as it is the case for nuclear imaging. On the other hand, extents X-ray imaging is very limited without using contrast agents, can only reveals bones structures and in any case soft tissues and biological compartment like blood vessels, tissues, organs. Contrast agents must be administrated along with the X-ray scanning, in order to improve contrast enhancement. Relevance and potency of “ideal” contrast agent are still largely dependent on their *in vivo* behavior, biodistribution and pharmacokinetics. More precisely, in this work, our interest concerns the development of contrast agents for preclinical X-ray CT (microCT), using scanners designed for small laboratory animals, and in this case the clinical contrast agents are not applicable since they undergo a fast blood clearance by kidneys avoiding animal imaging, and *a fortiori* targeted imaging. Strictly speaking, renal cut off size is 5.5 nm. However, when we refer to a suspension of nanoparticles (NPs) the whole distribution should be higher to this threshold to avoid renal clearance. This is generally why we can consider that increasing the size of the contrast agent in the form of NPs bigger than 50 nm (diameter) prevents the early renal clearance. The ideal NP contrast agent must fulfill a number of stringent requirements, briefly enumerated in the following: (i) the contrast agent should be easily dispersible and highly stable in a variety of local *in vivo* environments; (ii) the contrast agent should exhibit limited nonspecific binding and be resistant to reticuloendothelial system (RES) uptake (1,2), generally done with a specific surface coating with polyethyleneglycol (PEG)

(3–5). As a result, the blood circulation time is prolonged, increasing the chance for the nanoparticles to bind with specific targets. (iii) Specifically for preclinical microCT imaging, the contrast agent must be big enough (average diameter > 50 nm) to avoid the fast renal clearance as discussed above (6). (iv) Depending of the application, a control of the surface composition can be necessary to promote the particle targeting to specific sites (7,8); this can be achieved through passive targeting, e.g., according to enhanced permeation and retention effect (EPR), or mediated by ligand decoration of the surface (e.g., antigen, cell, tissue). (v) A very important point that oriented the nature of the particle is the loading rate of a radiopaque material. Indeed, X-ray imaging modality is related to a very high concentration of contrasting materials administrated along with a nontoxicity (9,10). (vi) The facile synthesis resulting in high yield of purified compounds make them promising candidates and thereby translated successfully into clinical advances. Ideally, those kinds of materials will be efficient for long-term quantitative imaging at low doses and be safely cleared from the body after the imaging is completed. To gather all these points, iodine-based nano-emulsions, have recently been developed showing huge stability, high biocompatibility and great potential in medical applications, such as image-guided surgery, advanced diagnosis (e.g., to recognize tumor regions), personalized medicine or theragnostics.

We previously reported (11) the formulation of non-toxic iodinated nano-emulsions based on natural compounds like vitamin E, triglycerides, monoglycerides. The choice of the system is driven by the hypothesis that molecules that naturally occur in living organisms would exhibit a better compatibility and non-toxicity. In the present study, we propose to evaluate a new molecule that has never been explored as a contrast agent, namely cholecalciferol (or vitamin D<sub>3</sub>) covalently modified with a triiodobenzene functionality. Cholecalciferol is an essential lipid soluble vitamin, one of the important ingredients in a human daily diet. It is photosynthesized in the human body from 7-dehydrocholesterol when exposed to U.V. wavelengths of light (12,13), and it is metabolized in the liver and kidney (14–17). Inspired by its biocompatibility, biodegradability and structural similarity with cholesterol, which is an important component of cellular membranes, and due to its poor water-solubility and low bioavailability, cholecalciferol is often encapsulated within lipid-based delivery systems for improving its bioaccessibility.

Herein, we focus on iodinated cholecalciferol as a non-toxic model contrast agent, in order to follow the expected blood pool imaging and then its passive accumulation in liver. In previous reports, we showed that the nature of the iodinated oil constituting the droplet core has a drastic influence on the biodistribution of the contrast agent (11). In the present study, we propose to keep constant the formulation composition and to focus only on the effect of the size of the

nanoparticulate contrast agent on its *in vivo* behavior and distribution. In fact, in literature, many studies showed that physicochemical factors can affect biodistribution and toxicity of nanoparticles (18–20). It is well approved that the particle size and surface charge can affect the efficiency and pathway of cellular uptake for liposomes (21), quantum dots (22), polymeric NPs (23,24), gold NPs (25), and silica NPs (26) by influencing the adhesion of the particles and their interaction with cells (27). However, this question has never been pointed out for nano-emulsions, and, in the case of iodinated nano-emulsions, can potentially serve in controlling the properties of the contrast agents. Above the smallest sizes that induce the renal clearance (i.e., below 50 nm), a legitimate question concerns the potential impact of the nanoparticle size regarding the immune system and organs cell uptake, and thus its influence on the biodistribution. In this study, we synthesized a new contrast agent, triiodobenzoate cholecalciferol that was formulated as PEGylated nano-emulsions through spontaneous emulsification with two different and representative sizes (average diameters) of 55 and 100 nm. These formulations were studied *in vitro* and their imaging properties, pharmacokinetics and biodistribution were followed *in vivo* by micro-CT after i.v. administration in mice.

## EXPERIMENTAL SECTION

### Materials

Cholecalciferol (Vitamin D<sub>3</sub>), 2,3,5-Triiodobenzoic acid (TIBA), 4-dimethylaminopyridine (DMAP), N,N'-dicyclohexylcarbodiimide (DCC), dichloromethane, ethyl acetate, cyclohexane, sodium hydrogen carbonate, sodium sulfate anhydrous, sodium chloride, Hoechst 33258, calcein AM, deuterated chloroform (CDCl<sub>3</sub>), dimethyl sulfoxide (DMSO) and 3-(4,5 dimethylthiazol-2-yl)-2,5-diphenyltetrazolium bromide (MTT) solutions were purchased from Sigma Aldrich (St. Louis, MO), Labrafac® WL1349 (Gattefossé S.A., Saint-Priest, France) is a mixture of capric and caprylic acid triglycerides. Non-ionic surfactant (Kolliphor ELP®) from BASF (Ludwigshafen, Germany) is a parenteral grade non-ionic surfactant made by reacting ethylene oxide with castor seed oil at an ethylene oxide to oil molar ratio of 35 (28). The product mainly consists of a PEG chain (35 ethylene glycol units) grafted onto a molecule of castor oil, Phosphate buffered saline (PBS), Dulbecco's modified Eagle medium (DMEM), Penicillin/Streptomycin solution (10.000 Units Penicillin/ml and 10 mg Streptomycin/ml) and fetal bovine serum (FBS) were obtained from PAN Biotech (Aidenbach, Germany), and 0.22 μm syringe filters were purchased from Fisher (Germany).

### Methods

#### Synthesis and Characterization of Cholecalciferoyl 2,3,5-Triiodobenzoate

The incorporation of iodine into the oily molecule was performed via a simple esterification reaction. Thus 2,3,5-triiodobenzoic acid (5 g, 0.01 mol), 4-dimethylaminopyridine (0.183 g, 0.0015 mol) and N,N'-dicyclohexylcarbodiimide (2.26 g, 0.011 mol) were sequentially added to a solution of cholecalciferol (3.08 g, 0.008 mol) in dichloromethane (250 mL) at room temperature. The reaction mixture was kept under stirring overnight at room temperature, and then dicyclohexylurea and other precipitates were removed by filtration. The organic phase was further washed twice with aqueous NaHCO<sub>3</sub> (5%), once with saturated NaCl solution and dried over anhydrous Na<sub>2</sub>SO<sub>4</sub>. The solvent was removed in vacuum and the obtained precipitate was then purified by gradient elution chromatography on silica gel using cyclohexane and ethyl acetate as eluents. The reaction yield was 43% and the final product obtained as a yellow needle-like crystals revealed a high iodine content (approximately 44% of the molecular weight). The synthesis scheme of cholecalciferoyl 2,3,5-triiodobenzoate is shown in Fig. 1 (top).

#### <sup>1</sup>H-NMR Analysis

<sup>1</sup>H-NMR spectra were recorded with a Bruker Top Spin 3.0 operating at 400 MHz using deuterated chloroform (CDCl<sub>3</sub>) as a solvent. Chemical shifts (δ) were expressed in parts per million (ppm), taking tetramethylsilane (TMS) as internal reference. The resulting <sup>1</sup>H-NMR data appear coherent with the iodine-grafted cholecalciferol structure by revealing another two new signals that correspond to the two CH aromatic groups at 8.21 and 7.58 ppm of benzene ring (see Supplementary information).

Cholecalciferoyl 2,3,5-triiodobenzoate: <sup>1</sup>H NMR (CDCl<sub>3</sub>, δ/ppm): 8.21 (s, 1H, H<sup>6</sup>), 7.58 (s, 1H, H<sup>4</sup>), 6.18 (dd, 1H, H<sup>16</sup>), 5.95 (dd, 1H, H<sup>15</sup>), 5.15 (m, 1H, H<sup>8</sup>), 4.80, 5.08 (s, 2H, H<sup>12</sup>), 2.76 (t, 2H, H<sup>18</sup>), 2.64 (t, 2H, H<sup>13</sup>), 2.43 (d, 2H, H<sup>9</sup>), 2.22 (t, 1H, H<sup>22</sup>), 1.86 (q, 2H, H<sup>14</sup>), 1.62–1.29 (m, 9H, H<sup>19</sup>, H<sup>20</sup>, H<sup>23</sup>, H<sup>24</sup>, H<sup>31</sup>), 1.26 (m, 1H, H<sup>26</sup>), 1.06 (m, 6H, H<sup>28</sup>, H<sup>29</sup>, H<sup>30</sup>), 0.86 (q, 1H, H<sup>25</sup>), 0.85 (d, 3H, H<sup>27</sup>), 0.80 (d, 6H, H<sup>32</sup>, H<sup>33</sup>), and 0.47 (s, 3H, H<sup>34</sup>).

#### Formulation of Triiodinated Cholecalciferol Nano-Emulsions

Iodinated cholecalciferol nanoparticle emulsions were formulated using a modified method based on spontaneous nano-emulsification as previously described (29,30). Briefly, the principle, illustrated in Fig. 1 (bottom), consisted in mixing the oil phase with non-ionic surfactant and heating this mixture to ensure its homogenization. Then, this phase was

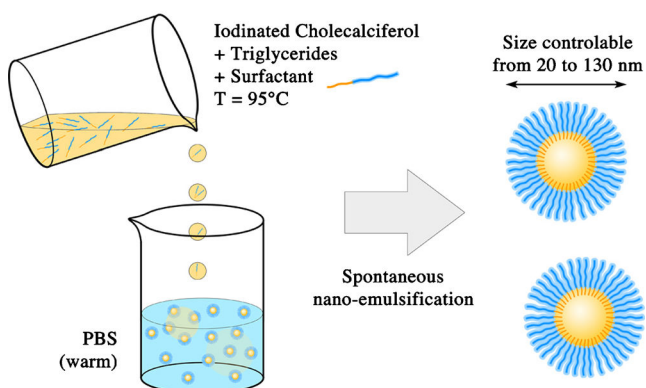
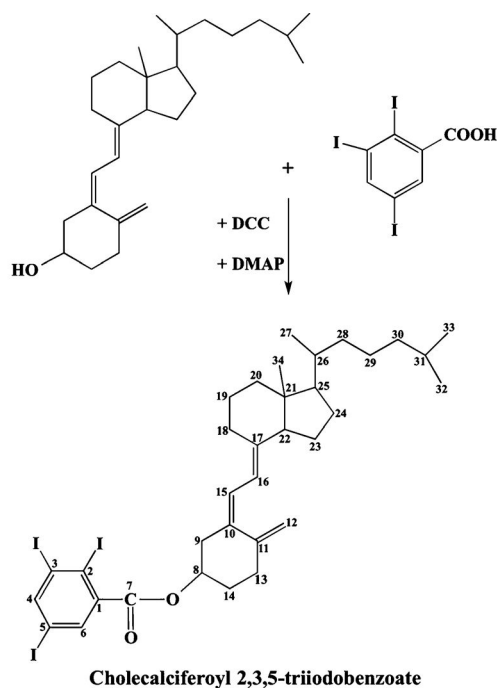


**Fig. 1** Synthesis of cholecalciferol 2,3,5-triiodobenzoate (top). Schematic illustration of the nano-emulsions formulation (bottom).

suddenly mixed with warm water, generating the stable nano-emulsions within seconds. In the case of iodinated cholecalciferol, the protocol had been adapted due to the crystalline nature of this compound. Iodinated cholecalciferol was solubilized in another oil (medium chain triglyceride, Labrafac® WL), and this mixture then was added to the non-ionic surfactant.

The nano-emulsion properties, size and size distribution were investigated in function of the formulation parameters: (i) iodinated cholecalciferol / (iodinated cholecalciferol + triglyceride) weight ratio (oil ratio, OR), (ii) surfactant / (surfactant + oil) weight ratio (SOR) and (iii) (surfactant + oil) / (surfactant + oil + water) weight ratio (SOWR). The two representative formulations exhibiting different sizes can be described as follows. The first one,  $NE_1$ , is formulated with SOR = 40 wt.%,

SOWR = 40 wt.% and OR = 66 wt.%. Triiodinated cholecalciferol (0.065 g) was firstly mixed with triglycerides (Labrafac® WL) (0.033 g), maintained at 95°C with vortex mixing followed by sonication until clear and homogenized solution was obtained. Then nonionic hydrophilic surfactant (Kolliphor ELP®) (0.065 g) was added to the previous solution, and maintained under gentle magnetic stirring alternatively with heating periodically several times. Finally, warm PBS (0.244 g) as an aqueous phase was then poured into the hot solution followed by vortex for 5 min giving rise to formation of the desired nano-emulsion with the average size of 55 nm. The second representative example,  $NE_2$ , briefly, is prepared following the same protocol with SOR = 27 wt.%, SOWR = 40 wt.% and OR = 66 wt.% (iodinated cholecalciferol: 0.0986 g, Labrafac® WL: 0.0493 g, Kolliphor ELP®: 0.055 g, PBS: 0.304 g) to give rise to the average diameter around 100 nm. In addition, owing to the fact that the nano-emulsion size is controlled by the surfactant to oil ratio, a slight excess of PBS (0.130 g) and Kolliphor ELP® (0.046 g) were added, in order to provide exactly the same concentrations in all species like for  $NE_1$ . In both cases, the value of the SOWR was kept constant at 40% throughout this study, since its influence on the nano-emulsion formation was negligible (it only influenced the droplet concentration) (31). In addition, pH and osmolality of the suspension emulsions were measured and strictly adjusted to obtain a compatibility with parenteral administration. All formulations were repeated three times. Finally, all samples were sterilized by filtration through a 0.22  $\mu$ m PVDF membrane.

#### Characterization of Nano-Emulsions by Dynamic Light Scattering (DLS)

The hydrodynamic sizes and polydispersity indices (PDI) of the particles were measured using a dynamic light scattering (DLS) device from Malvern Instruments (Malvern, Orsay, 752 France). The helium/neon laser, 4 mW, was operated at 633 nm with the scatter angle fixed at 173° and the temperature maintained at 25°C. The sizes of the nano-emulsions were determined directly after their formulation. Three different dilutions were prepared 1/1000, 10/1000, and 100/1000 before the measurement. All experiments were performed in triplicate.

#### In Vitro Studies

**Cell Culture.** Two different cell lines, namely BNL-CL2 murine hepatocytes and RAW264.7 murine macrophages were grown as monolayer cultures in DMEM medium supplemented with 10% fetal bovine serum (FBS), 100 Unit Penicillin / mL, 100  $\mu$ g Streptomycin / mL and 2 mM l-glutamine. The culture was maintained in a humidified atmosphere with 5% CO<sub>2</sub>.

**Stability of Nano-Emulsion Droplets in Serum.** Longitudinal size measurements were performed in serum, in order to investigate a potential degradation of the nano-emulsion droplets that may lead to increase or decrease of the droplet size, and potentially influence the pharmacokinetics. Nano-emulsions were incubated in serum for different periods of time.

**In Vitro Cytotoxicity (MTT-Assay).** The cytotoxicity of the iodinated cholecalciferol nano-emulsion was examined by MTT-test, which has been carried out for two cell lines (BNL-CL2 and RAW264.7 cells). The cells were seeded in 96-well plates ( $10^4$  cells per well) in 100  $\mu$ L of DMEM and then incubated overnight at 37°C under a controlled atmosphere (5% CO<sub>2</sub> and 80% H<sub>2</sub>O). Dilutions of nano-emulsions were made with sterile DMEM to get required concentrations, and then sterilized using 0.22  $\mu$ m filter. Next, the cell culture medium was replaced by the same medium containing variable concentrations of iodine encapsulated nano-emulsions (corresponding to 0.93, 0.28, 0.093, 0.028, 0.0093, 0.0028, 0.00093, 0.00028 mg I/ $10^4$  cells). After 24 h incubation, the medium was removed and the cells were washed with PBS. Then, the wells were filled with 100  $\mu$ L of cell culture medium containing MTT (0.5 mg/ml) and incubated for 4 h at 37°C. The obtained formazan crystals were dissolved by adding 100  $\mu$ L DMSO and the UV absorbance was measured at 570 nm with a microplate reader (Varioskan Flash, Thermo Scientific, USA). Experiments were carried out in triplicate and expressed as a percentage of viable cells compared to the control group.

**Cellular Uptake Experiment. Confocal Microscopy.** The cellular uptake and intracellular localization were determined in RAW264.7 cells (mouse macrophages) and BNL-CL2 (hepatocytes), using a Leica TCS SP confocal scanning system (Leica, Germany). To follow the nano-emulsion droplets, we used a modified lipophilic Nile Red dye (NR668) that was solubilized (0.1 wt.%) in the iodinated oil before formulating the nano-emulsions. NR668 synthesis was previously reported (32). The cells were cultured overnight in cell culture glass chamber slides ( $5 \times 10^4$  cells per well) before their exposition to the dye-loaded nano-emulsions in DMEM supplemented with 10% FBS at a concentration corresponding to 0.1 mg/mL, in a 5% CO<sub>2</sub> humidified atmosphere at 37°C for 30 min, 2 h, and 24 h. After incubation, the cells were stained with Calcein AM (10  $\mu$ M, 15 min of incubation in Hank's balanced salt solution, HBSS) and with Hoechst 33342 (50  $\mu$ M, 10 min of incubation in HBSS). After washing for 6 times in HBSS, in order to remove all non-penetrated nano-emulsion droplets, the cells were mounted in the fluorophore protector CC/mount and observed with a Leica confocal microscope equipped with an argon/neon laser and a 63 $\times$  oil immersion objective. The excitation wavelengths used were 360 nm for Hoechst 33342, 488 nm for Calcein AM, 543 nm for NR668

and the fluorescence signals were collected in the 380–460 nm range for Hoechst, 500–530 nm range for Calcein AM, and 560–650 nm range for Nile Red 668. The images were processed with Fiji software.

**Quantification of macrophage uptake.** Cellular uptake was quantified by fluorescence spectroscopy. Mouse macrophage RAW264.7 and hepatocyte BNL-CL2 cells were cultured as described above, except that the cells were lysed with DMSO and not mounted for microscopy analysis. The efficacy of washing and lysing was checked with fluorescence microscopy observations. The concentration of the encapsulated NR668 dye in the cell lysate was quantified by fluorimetry with an excitation wavelength of 550 nm and an emission wavelength of 630 nm (with a microplate reader Varioskan Flash, Thermo Scientific, USA). Uptake was expressed as the percentage of fluorescence associated with the cells *versus* the fluorescence in a feed solution.

### Micro-CT Imaging

The experiments were performed in agreement with the Committee of Animal Research and Ethics of the University of Lyon-1.

**In Vitro Experiments.** The X-ray attenuation properties of the iodinated nano-emulsions were evaluated at various concentrations with a micro-CT scanner (1076 Skyscan, Kartuizersweg, Belgium). Experimental parameters were as follows: X-ray, 49 keV, 129  $\mu$ A; resolution, 35 mm; pitch, 0.4°; aluminum filters, 0.5 and 632 ms. Iodine concentration of nano-emulsions was determined using a calibration curve established with a commercial hydrophilic contrast agent (Xenetix 300, namely iobitridol), correlating iodine concentration and radiopacity.

**In Vivo Experiments.** *In vivo* imaging experiments were performed with a micro-CT scanner (INVEON, Siemens, Munich, Germany). The experimental X-ray parameters were as follows: X-ray, 50 keV, 500  $\mu$ A; resolution, 111.25  $\mu$ m; pitch, 2°; aluminum filters, 0.5 and 900 ms. The acquisitions were performed on Swiss mice,  $n=3$ , for each type of nano-emulsion. Before the acquisition, mice were anesthetized with isoflurane. Then, the iodinated nano-emulsions were injected using a catheter in the tail vein, with an injection volume corresponding to 10% of the blood volume (i.e., 7.6  $\mu$ L of nano-emulsions per g of mouse weight). Scans were performed before administration, immediately after injection, and after 30 min, 1, 2, 3, 4, 6 h; 1, 2, 3, 7, 14, 21, 28 and 50 days. The micro-CT raw data were treated with OsiriX viewer to establish 2D maximum projection slices and 3D volume rendering images, and then to quantify a signal by placing a region of interest in the heart, liver, spleen, and kidney.

## RESULTS AND DISCUSSION

Spontaneous emulsification is an efficient method for generating stable aqueous suspension of oil nano-droplets. The efficiency of the process is closely dependent on the oil nature, surfactants and their own interactions, solubility in each other (31). When with classical surfactant / oil couples like non-ionic surfactant (Kolliphor ELP®) / triglycerides (Labrafac® WL) the emulsification is very efficient and allows to easily get small stable droplets, this becomes more challenging with more exotic molecules like tri-iodinated cholecalciferol. We have previously reported (11) that in the case of iodinated castor oil, or iodinated monoglycerides, grafting of the triiodobenzoic group affects the process efficiency and leads to the size increase. This phenomenon is likely due to changes in surfactant / oil interactions that may decrease with the tri-iodination. Here, we also observed a change in the emulsification efficiency before and after tri-iodination, namely an enhancement of the efficiency after tri-iodination. Figure 2 shows the effect of the surfactant amount (SOR) for different oil ratios (OR). The values of OR represent the relative percent of cholecalciferol (Fig. 2a) or tri-iodinated cholecalciferol (Fig. 2b) in the oil phase while OR=0% means that oil phase is pure triglycerides. The corresponding polydispersity indexes are reported in Table S1 (see Supplementary information section). These results clearly demonstrate that the droplet size decreased for the tri-iodinated molecules compared to the native ones. As for the non-iodinated molecules in Fig. 2a, the effect of cholecalciferol in the oil phase appears unfavorable for the lower SOR values. Even if droplet sizes decrease slightly between OR=0% and OR=50%, it dramatically grows for a further OR increase up to several orders of magnitudes for OR=75%. On the other hand, the formulations with tri-iodinated cholecalciferol, in Fig. 2b, is clearly better with smaller droplet size and good monodispersity, and actually, three cases for OR=50, 66 and 75% appear relatively similar compared to the curve without tri-iodinated cholecalciferol (OR=0%). PDI values (Table S1) are much better in this latter case, corroborating this observation.

It is noteworthy to understand that the formulations are better when increasing the surfactant concentration (through SOR), but it is to the detriment of the oil amount. In the context of the formulation of X-ray contrast agents, our interest lies in increasing the iodine amount in the droplet. It means that the best formulation should be a compromise between quality of the dispersion and iodine concentration. That is to say, the optimized formulation has the lower SOR with the best dispersion, that could be defined, for example in Fig. 2b, with  $SOR < 40\%$  and  $OR = 75\%$ . This figure also allows understanding how a fine control of the nano-emulsion size is performed, in function of the formulation parameters. Moreover, the two different sizes chosen for *in vitro* studies and *in vivo* imaging are indicated with arrows in the graph as  $NE_1$  and

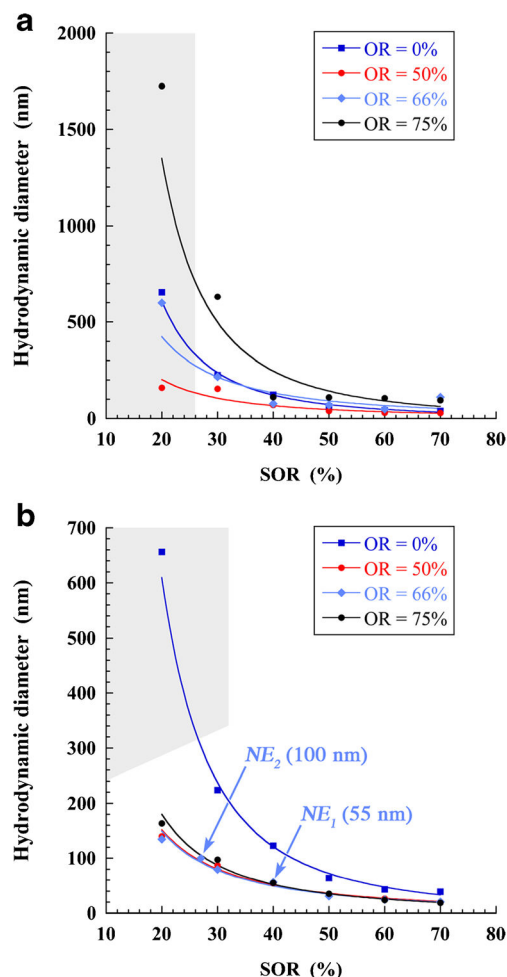


**Fig. 2** Effect of the surfactant amount ( $SOR = \text{surfactant}/(\text{surfactant} + \text{oil})$  weight ratio) on the size of the dispersion, function of the relative proportions of cholecalciferol (**a**) and tri-iodinated cholecalciferol (**b**). Grey parts indicate globally the regions where nano-emulsions do not form (either size or PDI are too high).  $NE_1$  and  $NE_2$  correspond to the formulations selected for the *in vitro* and *in vivo* studies.

$NE_2$  (for 55 and 100 nm, respectively). The corresponding size distributions obtained by DLS are presented in Fig. 3. It should be noted that they are rather well differentiated to consider them as different sized samples.

In the following we will focus on the *in vitro* evaluations of these samples, divided in two steps: (i) toxicity and stability in the serum, and (ii) cell uptake, visualization and quantification. First results have been obtained from viability studies. For this purpose, MTT-tests were performed for two cell lines, in particular macrophages and hepatocytes, and comparing as well  $NE_1$  and  $NE_2$ . Results are reported in Fig. 4, and show a clear increase in the toxicity for the bigger nano-emulsions  $NE_2$  compared to  $NE_1$ . Even if the toxicity is more marked with macrophages, this trend is conserved whatever the cell line. In the case of macrophages,  $LD_{50}$  increases of  $\Delta LD_{50} = 0.35 \text{ mg I/mL}$  (from  $LD_{50} = 0.21$  to  $0.56 \text{ mg I/mL}$  for  $NE_2$  to  $NE_1$  respectively), and it appears much important in the case

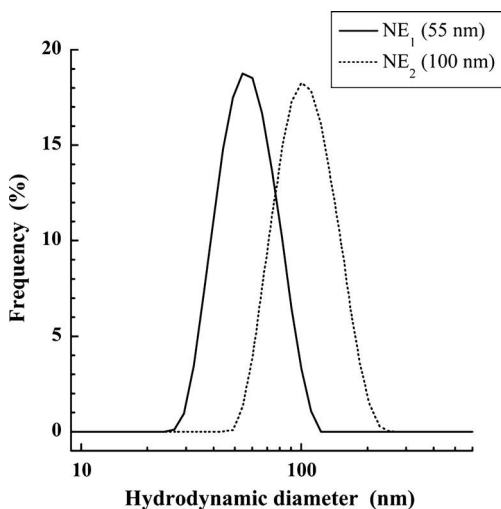


**Fig. 3** Size distribution of two nano-emulsions selected for *in vitro* and *in vivo* studies.

of hepatocytes with  $\Delta LD_{50} = 1.04$  mg I/mL (from  $LD_{50} = 0.75$  to  $1.79$  mg I/mL for  $NE_2$  to  $NE_1$  respectively). These first *in vitro* results disclose a distinct increase of the nano-emulsion toxicity in function of their size: bigger emulsions are slightly more toxic. The second aspect is that macrophages appear more sensitive to the tri-iodinated cholecalciferol than hepatocytes, possibly due to a difference in their interactions with, or uptake of the nano-emulsion droplets compared to hepatocytes.

Another important point to study before performing *in vivo* evaluation is the stability of the suspension in serum. These

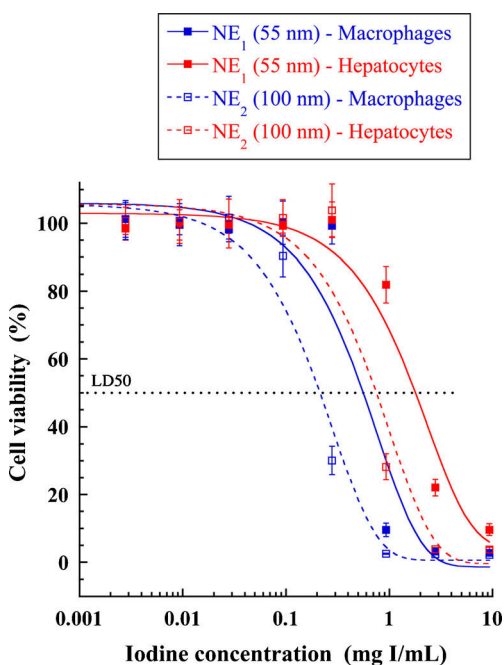


**Fig. 4** Viability of the RAW264.7 murine macrophages (blue curves) and BNL-CL2 hepatocytes (red curves) after 24 h incubation with the iodinated nano-emulsions. The nano-emulsion concentrations were expressed in iodine concentrations per mL. Filled symbols and open symbols correspond to the iodinated nano-emulsions  $NE_1$  and  $NE_2$ , respectively.

longitudinal experiments were aimed to simply show physico-chemical stability of the formulation, in order to insure that once injected, the droplets remain stable. As seen in Fig. 5, the relative stability with time whatever the dilutions, which can suggest a compatibility of the stability with the parenteral administration route. This is in the same line with those observed in case of other types of iodinated nano-emulsions (11,33).

Observations of cellular uptake of the iodinated nano-emulsions were performed by confocal microscopy, using a fluorescent probe encapsulated in the oil droplets to reveal their location. The fluorescent dye was a Nile Red lipophilic derivative, namely NR668. This particular dye was chosen owing to the absence of its leakage from the nano-emulsion droplets, ensuring their tracing even in biological media (32). The nano-emulsions were incubated with hepatocytes and macrophages for 30 min and 24 h, then washed and observed. The results are shown in Fig. 6 and disclose that: (i) 100 nm droplets are better internalized than 55 nm ones, and (ii) the uptake of macrophages was bigger than that of hepatocytes, as expected. For 55 nm droplets, we did not observe any NR668

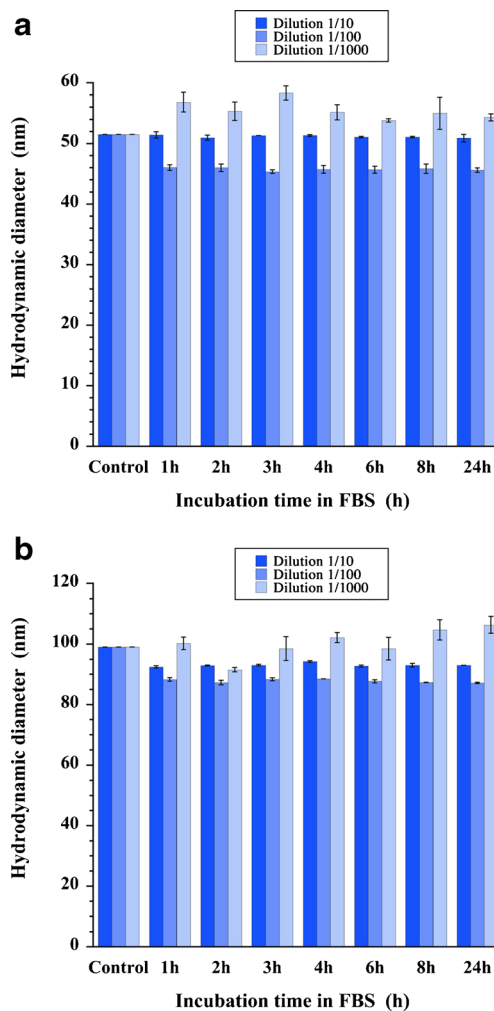


**Fig. 5** Stability of nano-emulsions in serum. Average droplet sizes were measured by DLS at different dilutions, for (a)  $NE_1$  and (b)  $NE_2$ .

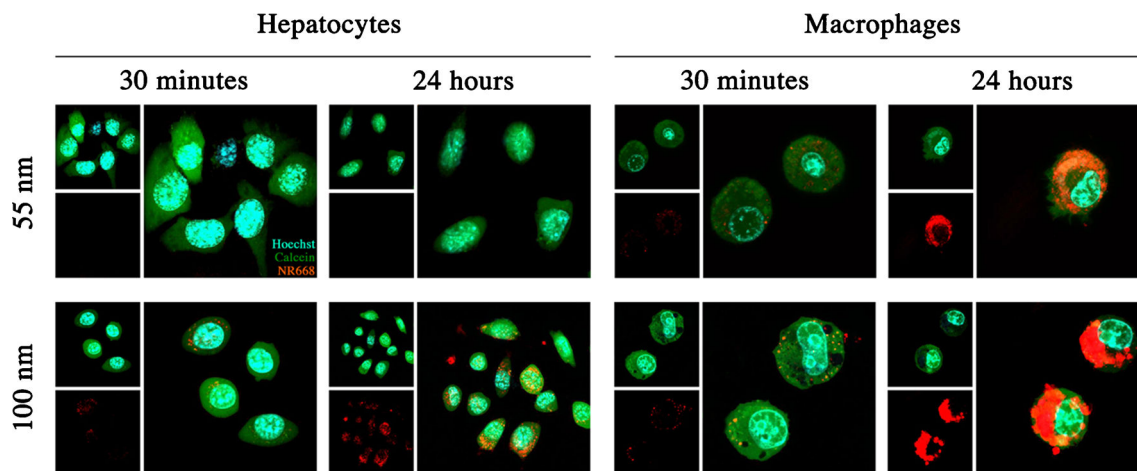


**Fig. 6** Monitoring of the uptake of NR668-loaded iodinated nano-emulsions by mouse hepatocytes (BNLCL2) and murine macrophages (RAW264.7 cells) by confocal microscopy. Nuclei were stained with Hoechst (cyan) and cells with Calcein AM (green). A lipophilic fluorescent dye NR668 was encapsulated in the nano-emulsions, which allowed observing the location of the droplets once engulfed by the cells. The cells were incubated with the nano-emulsions for 30 min and 24 h. *Top left* insets show the cells and nuclei. *Bottom left* insets show the signal and the larger right picture shows both merged.

signal of whatever the incubation time, while for 100 nm ones it was revealed already after 30 min and was clearly visible after 24 h. In the case of macrophages, a similar trend between nano-emulsions of both sizes can be noted but the signal was more pronounced. The quantification of this cell uptake is shown in Fig. 7, which confirmed these observations, and even revealed that after 24 h incubation the quantity of the droplets

that were engulfed by the cells doubled in both cases hepatocytes and macrophages. The better accumulation in macrophages of 100 nm PEGylated lipid nano-emulsions compared to the 55 nm one, was demonstrated earlier (34) and could be explained by receptor-mediated phagocytosis (35). Contrary, for the BNL-CL2 cells, which are considered as non-phagocytosis cells, smaller particles are generally better in terms of intracellular accumulation (36). However, the surface properties influence on the uptake significantly: e.g., 100 nm polymeric nanoparticles are able to take up into the non-phagocytic cells more efficiently than those with sizes of 55

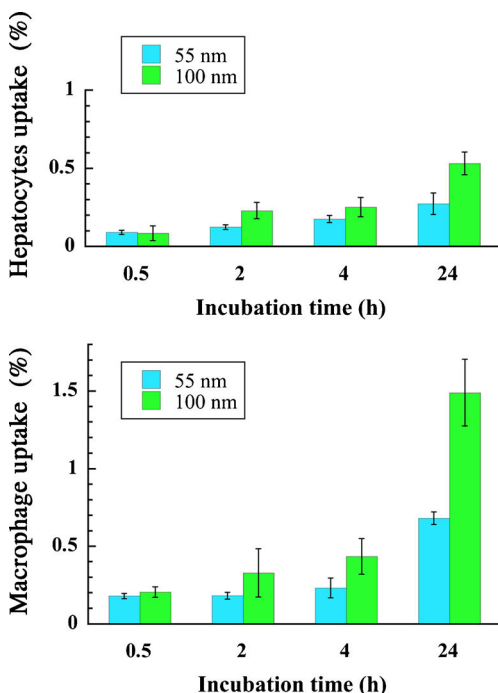


**Fig. 7** Quantification of nano-emulsion uptake by hepatocytes and macrophages as a function of the incubation time and droplet size. After incubation with the nano-emulsions loaded with NR668, the hepatocytes or macrophages were washed, lysed with DMSO, and studied by fluorometry. The uptake was expressed as a percentage of fluorescence associated with the cells versus fluorescence in a feed solution.

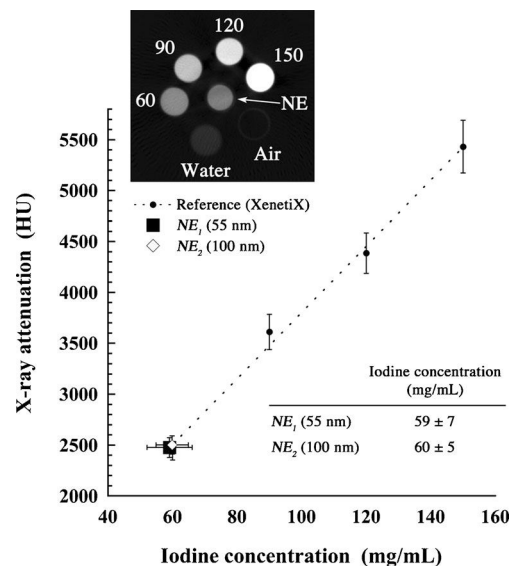
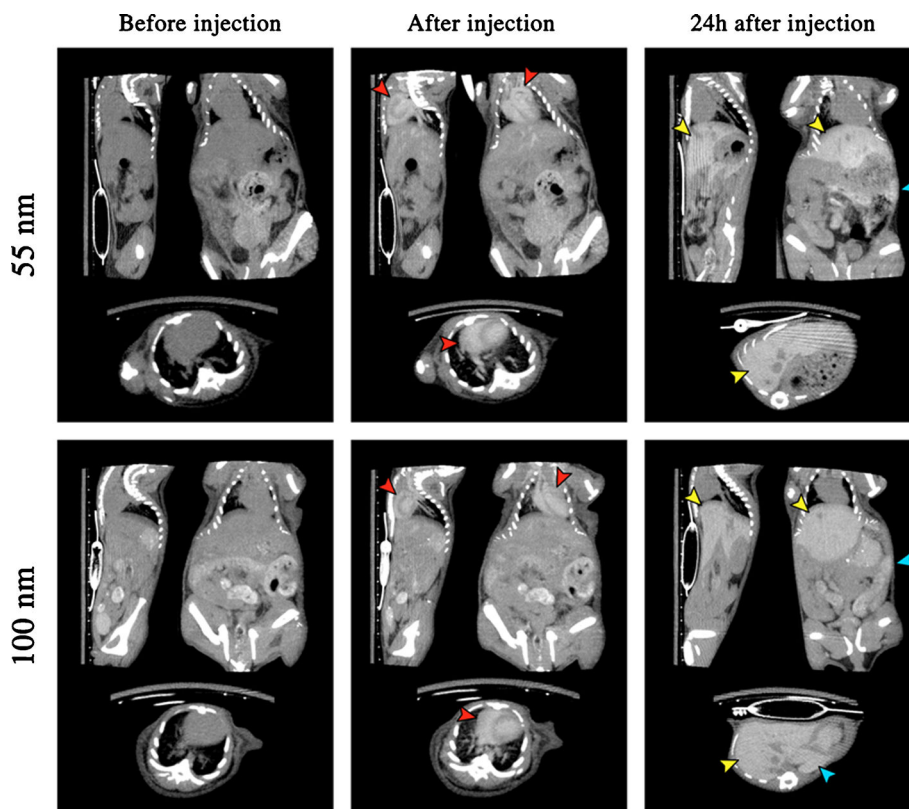


**Fig. 8** *In vitro* evaluation of the X-ray attenuation properties of NE<sub>1</sub> and NE<sub>2</sub> using a calibration curve made with iobitridol (filled circles). Inset reports the phantom of the tubes (for example one shown for NE<sub>1</sub>), with various iodine concentrations as references (expressed in mg/mL), plus water and air for normalization. The table summarizes the values obtained for the nano-emulsions.

**Fig. 9** Left: *in vivo* micro-CT imaging (maximum projection intensity) of the iodinated cholecalciferol nano-emulsions with two different sizes (55 and 100 nm) but with exactly the same composition, before, after and at 24 h after injection (representative times). Pictures show sagittal and coronal sections of the mice, as well as transverse slices through the heart, lung, and vertebra and transverse slices through the liver and spleen. Heart is indicated by red arrowheads, liver by yellow arrows, and spleen by blue arrows. 3D volume rendering is reported as Fig. S1 in *Supplementary Information*, along with two movies (movie1.mov and movie2.mov).



or higher than 200 nm (23,37). So the role of surface properties should also be mentioned, however it is not the case in the current study since the surface composition should be similar, only the size effect is studied.

This behavior arises in the same line that the results on cell viability: globally macrophages have a better interactions with the nano-emulsions and they show the highest toxicity, likewise 100 nm droplets also show highest uptake into cells, hepatocytes and macrophages, and also they show the highest toxicity compared to 55 nm ones. All these results corroborate the idea that, the uptake is linked to the toxicity, which should be enhanced with the bigger droplets. Actually, this behavior seems specific to the iodinated cholecalciferol, since with other types of iodinated oils we previously studied like iodinated castor oil or iodinated monoglyceride, droplet internalization were not related to toxicity (uptake were better macrophage and toxicity lower). Eventually, in comparison, iodinated cholecalciferol appears to present a specific toxic activity that can be more pronounced for the bigger droplets.

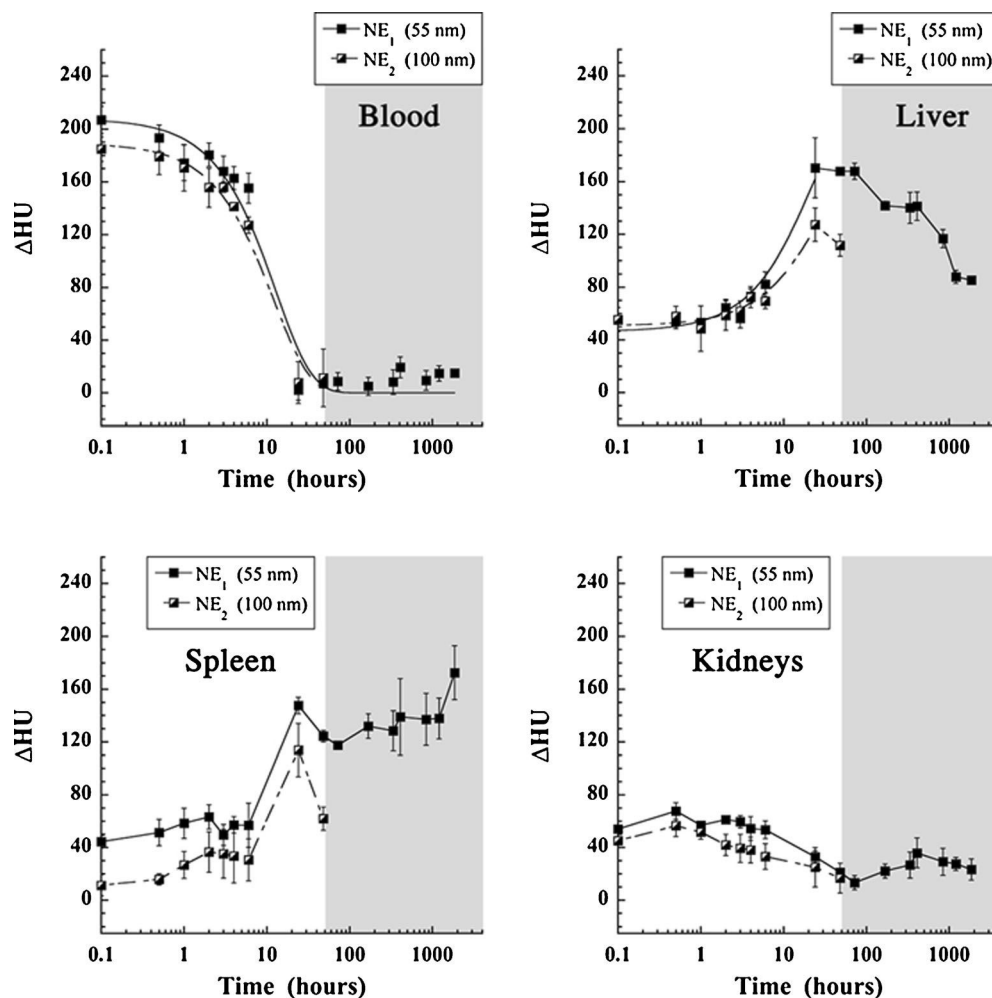
Let us focus now on the imaging properties and *in vivo* imaging of these contrast agents. The first characterization performed on the samples was the quantification of the iodine content using the X-ray scanner, compared to a commercial hydrophilic contrast agent (XenetiX®). The results, shown in Fig. 8, confirm the similar iodine concentration in both samples, which is around 60 mg/mL and is comparable with the concentrations of the best contrast agents earlier reported

(11,33). Based on these *in vitro* observations, we expect a similar contrast in blood pool once injected in mice, which is confirmed visually with the maximum intensity projections in Fig. 9 as well as quantitatively in Fig. 10.

After intravenous administration, we could clearly see the contrast agent spread over the blood compartment emphasizing the heart ventricles main venous and aorta, and even the liver irrigation. After 1 day, the contrast agent was not visible anymore in blood or heart, but has been accumulated in liver and spleen. The 3D volume rendering (see *Supplementary Information*) done on the 55 nm nano-emulsion clearly illustrates the regions containing the contrast agent after injection in blood (red), and in liver at 24 h post-injection (yellow). At first sight, all these images, presented in similar brightness/contrast conditions, seem to show similar properties for the nano-emulsions of two different sizes. However, there is a surprising and heavy difference, which is lethal in case of  $NE_2$  after 48 h post injection. When  $NE_1$  allows a follow-up of the mice during 50 days,  $NE_2$  induces systematically the mice death on the third day post-injection (with  $n=6$  in each case). The quantifications of the biodistribution and pharmacokinetics (Fig. 10) show two behaviors almost similar whether it is in blood, liver, spleen or kidney.

First observations, in line with the *in vitro* measurements of X-ray attenuation properties (Fig. 8), confirm the important contrasting properties of this product. The contrast enhancement is significant and allows a clear visualization of the

**Fig. 10** Quantitative measurements in heart, liver, spleen and kidney of the X-ray attenuation with time after i.v. administration of the iodinated cholecalciferol nano-emulsions.  $NE_1$  and  $NE_2$  refer to the nano-emulsions of the similar composition but different sizes, namely 55 and 100 nm, respectively;  $n = 6$  for each nano-emulsion. Curves were fitted with Eq. 1 for the heart (blood elimination) and Eq. 2 for the liver (accumulation). The limit between white and gray part indicates the time for which the mice injected with  $NE_2$  died, whereas the ones injected with  $NE_1$  survived.



regions and tissues where the contrast agent is accumulated, either in blood, liver or spleen. 3D volume rendering gives a more precise idea of the distribution of the contrast agent over the blood compartment, overall, right and left ventricles, liver irrigation, vena cava, hepatic portal vein, and thoracic aorta. One day after injection, arise the location of liver and spleen, indicating that most of the iodinated cholecalciferol has been accumulated in these regions. As for the quantification of the biodistribution of  $NE_1$  and  $NE_2$  over time, the contrast enhancement and kinetics appear almost superimposable for all graphs. In addition, the kinetics of blood clearance and liver accumulation can be fitted with classical mono-compartmental exponential Eqs. (1) and (2), respectively:

$$\Delta HU(t) = \Delta HU_0 \times \exp(-k_1 \cdot t) \quad (1)$$

$$\Delta HU(t) = \Delta HU_0 + \Delta HU_\infty \times (1 - \exp(-k_2 \cdot t)) \quad (2)$$

where  $\Delta HU_0$  is the initial value of the contrast enhancement after injection,  $\Delta HU_\infty$  is the contrast enhancement at the end of the accumulation process,  $k_1$  is the blood elimination rate constant and  $k_2$  is the accumulation rate constant. The obtained pharmacokinetics parameters (reported in

Table I) show a close similarity for the blood clearance between both nano-emulsions, with a similar  $t_{1/2}$  around 9 h. Moreover, a very similar behavior is observed in the following steps of accumulation / elimination of the contrast agent in liver and spleen up to 24 h post-injection. These observations are confirmed by the similar values of the accumulation rate constant for  $NE_1$  and  $NE_2$ , 0.047 and 0.036  $\text{h}^{-1}$ , respectively. However, the values of  $\Delta HU_\infty$  appear a little bit more different, in particular 174 HU and 122 HU, respectively. As

**Table I** Pharmacokinetics Parameters for the Iodinated Nano-emulsions<sup>a</sup>

	$NE_1$ (55 nm)		$NE_2$ (100 nm)	
	Blood	Liver	Blood	Liver
$\Delta HU_0$ (HU)	208	44	189	49
$k_1$ ( $\text{h}^{-1}$ )	0.077	–	0.081	–
$t_{1/2}$	9.0 h	–	8.5 h	–
$k_2$ ( $\text{h}^{-1}$ )	–	0.047	–	0.036
$\Delta HU_{\text{max}}$ (HU)	–	90	–	100

<sup>a</sup>  $\Delta HU_{\text{max}} = \Delta HU_0 + \Delta HU_\infty$

regards the accumulation in spleen, the two curves follow each other up to 24 h, and a dramatic drop of the signal arises at 48 h for  $NE_2$  before the mice death.

It is interesting to compare our product with the main commercial examples like Fenestra® (lipid nano-emulsions), AuroVist® (gold nanoparticle), eXIA 160® (aqueous colloidal iodinated dispersion) and ExiTron Nano (rare earth-based nanoparticles) which were studied on the same animal model (mice). In the present contrast agent (iodinated cholecalciferol), the initial contrast enhancement  $\Delta HU = 180\text{--}200$  HU corresponds to an increase of the contrast of 280–300% (see *Supplementary Information*), which is significantly higher than the 30% of Fenestra®, and eXIA 160® in (38), 260% of AuroVist® in (39) and 240% of ExiTron Nano 12000® in (40). In addition, the half-life of our contrast agent is optimal for CT scans (around 9 h), much longer than eXIA 160® and Fenestra LC® (38), but comparable to the ones reported for Fenestra VC® (38), AuroVist® (39) and ExiTron Nano 12000® (40).

Therefore, we can consider that the size of the nano-emulsions has not a real impact on the whole pharmacokinetics, with a significant difference that arise in the last points before mice death for  $NE_2$ , is likely linked to their lethality. On the one hand, we can conclude that the size of the nano-emulsions only slightly affects their fate *in vivo*, but on the other hand, the increase of the size has an irreversible consequence that is the lethal effect on the mice. Actually, the lethality of the iodinated nano-emulsions has never been observed, neither in all the iodinated nano-emulsions we previously synthesized and studied (10,11,33,41,42), nor in literature. This lethality is probably specific and is related to cholecalciferol. Indeed, as seen in Figs. 6 and 7,  $NE_2$  induces cellular uptake which was double higher compared to that in case of  $NE_1$ , as well as a higher toxicity (Fig. 4). These two points could orientate the explanation of the size-dependence lethality of the nano-emulsions: although accumulations in liver and spleen appear quite similar in both cases, the total toxicity of  $NE_2$  is probably increased due to a higher cellular uptake. The maximum dosage, which can be supported by the cell, is more rapidly reached with use of the nano-emulsions of the bigger size. This can induce the organ dysfunction and can be considered as an explanation of the loss of the contrast agent concentration before the death, at 48 h.

## CONCLUSION

In this study, the question of the influence of the size of the micro-CT nanoparticulate contrast agent on the fate *in vivo* is addressed. The chosen system naturally occurs in living organisms, namely cholecalciferol (or vitamin  $D_3$ ). We grafted a triiodobenzene motif with radiopaque properties. This new iodinated compound was formulated as nano-emulsions with

two different diameters, namely 55 and 100 nm, with exactly the same composition, and then studied *in vitro* and *in vivo* as X-ray contrast agent. The 100 nm nano-emulsions were found to be more toxic than 55 nm ones whatever the cell line (hepatocyte or macrophages). This was likely due to a higher cell uptake, observed by confocal microscopy, and confirmed by fluorimetric quantification. As regard the *in vivo* imaging, the total pharmacokinetics and biodistribution curves in blood, liver, spleen and kidney were quite similar. These results indicate that the nano-emulsion size has no real influence on the *in vivo* fate up to 48 h post-injection. After this time,  $NE_2$  induce the mice death, whereas with  $NE_1$  imaging can be followed up to 50 days without any trouble. This major difference could be attributed to the difference in toxicity and cell uptake related to the droplet size.

## ACKNOWLEDGMENTS AND DISCLOSURES

The authors would like to thank for grant “Attractivité IDEX 2013” within University of Strasbourg, France.

## REFERENCES

1. Patel HM. Serum opsonins and liposomes: their interaction and opsonophagocytosis. *Crit Rev Ther Drug Carrier Syst.* 1992;9: 39–90.
2. Chonn A, Semple SC, Cullis PR. Association of blood proteins with large unilamellar liposomes *in vivo*. *J Biol Chem.* 1992;267:18759–65.
3. Patil S, Gawali S, Patil S, Basu S. Synthesis, characterization and *in vitro* evaluation of novel vitamin D3 nanoparticles as a versatile platform for drug delivery in cancer therapy. *J Mater Chem B.* 2013;1:5742–50.
4. Zhang G, Yang Z, Lu W, Zhang R, Huang Q, Tian M, *et al.* Influence of anchoring ligands and particle size on the colloidal stability and *in vivo* biodistribution of polyethylene glycol-coated gold nanoparticles in tumor-xenografted mice. *Biomaterials.* 2009;30:1928–36.
5. Aggarwal P, Hall JB, McLeland CB, Dobrovolskaia MA, McNeil SE. Nanoparticle interaction with plasma proteins as it relates to particle biodistribution, biocompatibility and therapeutic efficacy. *Adv Drug Deliv Rev.* 2009;61:428–37.
6. Antonand N, Vandamme TF. Nanotechnology for computed tomography: a real potential recently disclosed. *Pharm Res.* 2014;31: 20–34.
7. Maeda H, Wu J, Sawa T, Matsumura Y, Hori K. Tumor vascular permeability and the EPR effect in macromolecular therapeutics: a review. *J Control Release.* 2000;65:271–84.
8. Hirsjärvi S, Dufort S, Bastiat G, Saulnier P, Passirani C, Coll J-L, *et al.* Surface modification of lipid nanocapsules with polysaccharides: from physicochemical characteristics to *in vivo* aspects. *Acta Biomater.* 2013;9:6686–93.
9. Hallouard F, Anton N, Choquet P, Constantinesco A, Vandamme TF. Iodinated blood pool contrast media for preclinical X-ray imaging applications – a review. *Biomaterials.* 2010;31:6249–68.
10. Li X, Anton N, Zuber G, Vandamme TF. Contrast agents for preclinical targeted X-ray imaging. *Adv Drug Deliv Rev.* 2014;76:116–33.

11. Attia MF, Anton N, Chipor M, Akasov R, Anton H, Messaddeq N, et al. Biodistribution of X-ray iodinated contrast agent in nano-emulsions is controlled by the chemical nature of the oily core. *ACS Nano*. 2014;8:10537–50.
12. Holick MF, Tian XQ, Allen M. Evolutionary importance for the membrane enhancement of the production of vitamin D3 in the skin of poikilothermic animals. *Proc Natl Acad Sci U S A*. 1995;92:3124–6.
13. MacLaughlin JA, Anderson RR, Holick MF. Spectral character of sunlight modulates photosynthesis of previtamin D3 and its photoisomers in human skin. *Science*. 1982;216:1001–3.
14. Porter CJH, Trevaskis NL, Charman WN. Lipids and lipid-based formulations: optimizing the oral delivery of lipophilic drugs. *Nat Rev Drug Discov*. 2007;6:231–48.
15. Holickand MF, Garabedian M. Vitamin D: photobiology, metabolism, mechanism of action, and clinical applications. In: Favus MJ, editor. *Primer on the metabolic bone diseases and disorders of mineral metabolism*. Washington: American Society for Bone and Mineral Research; 2006. p. 129–37.
16. Holick MF. Phylogenetic and evolutionary aspects of vitamin D from phytoplankton to humans. In: Pangand PKT, Schreibman MP, editors. *Vertebrate endocrinology: fundamentals and biomedical implications*. San Diego: Academic Press, Inc.; 1989.
17. Holick MF. Physiology, molecular biology, and clinical applications. In: Holick MF, editor. *Vitamin D and Health: evolution, biologic functions, and recommended dietary intakes for vitamin D*. Totowa: Humana Press Inc.; 2009. p. 3–35.
18. Khlebtsovand N, Dykman L. Biodistribution and toxicity of engineered gold nanoparticles: a review of in vitro and in vivo studies. *Chem Soc Rev*. 2011;40:1647–71.
19. Oberdörster G, Oberdörster E, Oberdörster J. Concepts of nanoparticle dose metric and response metric. *Environ Health Perspect*. 2007;115:A290–4.
20. Fadeelaand B, Garcia-Bennett AE. Better safe than sorry: understanding the toxicological properties of inorganic nanoparticles manufactured for biomedical applications. *Adv Drug Deliv Rev*. 2010;62:362–74.
21. Chono S, Tanino T, Seki T, Morimoto K. Uptake characteristics of liposomes by rat alveolar macrophages: influence of particle size and surface mannose modification. *J Pharm Pharmacol*. 2007;59:75–80.
22. Osaki F, Kanamori T, Sando S, Sera T, Aoyama Y. A quantum dot conjugated sugar ball and its cellular uptake. On the size effects of endocytosis in the subviral region. *J Am Chem Soc*. 2004;126:6520–1.
23. Winand KY, Feng S-S. Effects of particle size and surface coating on cellular uptake of polymeric nanoparticles for oral delivery of anticancer drugs. *Biomaterials*. 2005;26:2713–22.
24. Foged C, Brodin B, Frokjaera S, Sundblad A. Particle size and surface charge affect particle uptake by human dendritic cells in an in vitro model. *Int J Pharm*. 2005;298:315–22.
25. Chithrani BD, Ghazani AA, Chan WCW. Determining the size and shape dependence of gold nanoparticle uptake into mammalian cells. *Nano Lett*. 2006;6:662–8.
26. Lu F, Wu S-H, Hung Y, Mou C-Y. Size effect on cell uptake in well-suspended. Uniform mesoporous silica nanoparticles. *Small*. 2009;5:1408–13.
27. Lee K-D, Nir S, Papahadjopoulos D. Quantitative analysis of liposome-cell interactions in vitro: rate constants of binding and endocytosis with suspension and adherent J774 cells and human monocytes. *Biochemistry*. 1993;32:889–99.
28. Szebeni J, Muggia FM, Alving CR. Complement activation by cremophor EL as a possible contributor to hypersensitivity to paclitaxel: an in vitro study. *J Natl Cancer Inst*. 1998;90:300–6.
29. Anton N, Benoit J-P, Saulnier P. Design and production of nanoparticles formulated from nano-emulsion templates—a review. *J Control Release*. 2008;128:185–99.
30. Anton N, Gayet P, Benoit J-P, Saulnier P. Nano-emulsions and nanocapsules by the PIT method: an investigation on the role of the temperature cycling on the emulsion phase inversion. *Int J Pharm*. 2007;344:44–52.
31. Antonand N, Vandamme TF. The universality of low-energy nano-emulsification. *Int J Pharm*. 2009;377:142–7.
32. Klymchenko AS, Roger E, Anton N, Anton H, Shulov I, Vermot J, et al. Highly lipophilic fluorescent dyes in nano-emulsions: towards bright nonleaking nano-droplets. *RSC Adv*. 2012;2:11876–86.
33. Li X, Anton N, Zuber G, Zhao M, Messaddeq N, Hallouard F, et al. Iodinated  $\alpha$ -tocopherol nano-emulsions as non-toxic contrast agents for preclinical X-ray imaging. *Biomaterials*. 2013;34:481–91.
34. Vonarbourg A, Passirani C, Saulnier P, Simard P, Leroux JC, Benoit JP. Evaluation of pegylated lipid nanocapsules versus complement system activation and macrophage uptake. *J Biomed Mater Res A*. 2006;78:620–8.
35. Ohand N, Park JH. Endocytosis and exocytosis of nanoparticles in mammalian cells. *Int J Nanomedicine*. 2014;9:51–3.
36. Shang L, Nienhaus K, Nienhaus GU. Engineered nanoparticles interacting with cells: size matters. *J Nanobiotechnol*. 2014;12:1–11.
37. Xu A, Yao M, Xu G, Ying J, Ma W, Li B, et al. A physical model for the size-dependent cellular uptake of nanoparticles modified with cationic surfactants. *Int J Nanomedicine*. 2012;7:3547–54.
38. Willekens I, Lahoutte T, Buls N, Vanhove C, Deklerck R, Bossuyt A, et al. Time-course of contrast enhancement in spleen and liver with Exia 160, Fenestra LC, and VC. *Mol Imaging Biol*. 2009;11:128–35.
39. Nebuloni L, Kuhn GA, Müller R. A comparative analysis of water-soluble and blood-pool contrast agents for in vivo vascular imaging with micro-CT. *Acad Radiol*. 2013;20:1247–55.
40. Boll H, Nittka S, Doyon F, Neumaier M, Marx A, Kramer M, et al. Micro-CT based experimental liver imaging using a nanoparticulate contrast agent: a longitudinal study in mice. *PLoS ONE*. 2011;6:e25692.
41. Hallouard F, Briançon S, Anton N, Li X, Vandamme TF, Fessi H. Influence of diblock co-polymer PCL-mPEG and of various iodinated oils on the formulation by the emulsion-diffusion process of radiopaque polymeric nanoparticles. *J Pharm Sci*. 2013;102:4150–8.
42. Hallouard F, Briançon S, Anton N, Li X, Vandamme TF, Fessi H. Iodinated nano-emulsions as contrast agents for preclinical X-ray imaging, impact of the free surfactants on the pharmacokinetics. *Eur J Pharm Biopharm*. 2013;83:54–62.



---

---

# *Chapter two*

---

---

## **Chapter 2.1: Targeting agents conjugated to nano-carriers to increase drug efficiency**

This review discusses the physicochemical properties of the drugs, of the nano-carriers and the physiological characteristics of the tumor microenvironment, in order to illustrate the different strategies undertaken to deliver the active ingredient specifically to the lesion. The choice between passive targeting and active targeting will be discussed, as well as their consequences on the type of nano-carrier, properties like size, surface charge, functionalization with ligands, and type of ligands. Generally speaking this review aims to draw an overview of the concept of the drug targeting to tumors with the objective of explaining why the passive or active targeting strategy is chosen, and how they are worked out.

## 1. Introduction

Any dosage form cannot carry a therapeutic activity if the administered biologically active molecule is not able to cross the biological barriers which separate the site of administration from the site of action. The barriers to be crossed are very complex systems composed of several elements (epithelium, endothelium, cellular membrane) and several components (mechanical or physicochemical barriers and enzymatic barriers). Certain molecules are ineffective because they do not diffuse spontaneously into the cell whereas their therapeutic target is with intracellular localization.

The specific delivery of therapeutic agents to an organ, a tissue or a type of cells currently constitutes a major challenge for the treatment of the human diseases, in particular infectious, cancerous and genetic diseases.

Most of the active pharmaceutical ingredients (API) are often prone to display low bioavailability, low water solubility, biological degradation and inadvertent intrinsic side effects. To overcome such drawbacks, the design of novel drug carrier systems is of particular interest thanks to their efficient applicability through different administration routes such as oral, parenteral, dermal, topical, and pulmonary. To achieve these goals, targeted delivery of genes/drugs to specific tissues/cells has been widely investigated.

Introducing the nanotechnology into the medicine field termed as “nanomedicines” makes it possible today to present the concept of “vectorization”, also called drug targeting. Based on new physicochemical concepts and new materials, nanomedicines serve in envisage submicron systems of administration of the drugs. Nano-carriers are able to improve drug properties in various ways: by encapsulating the hydrophilic and/or hydrophobic molecules in their cores, by controlling release and distribution, by enhancing drug absorption by mucosa or cells and by protecting the drug from degradation. Such nano-carriers allowed the development of new treatments with improved specificity.

Researchers all over the world endeavor to develop submicron particles (nanoparticles, liposomes) for the transport of the drugs. After intravascular administration, the carriers are opsonized, i.e. covered with proteins and recognized by the macrophages of the liver and the spleen. This controlled biodistribution improves the targeting and the experimental treatment of pathologies such as hepatic metastasizes but also can lead to significant reduction of the drug concentrations in the undesired locations, thus decreasing the toxicity of certain anti-cancer drugs.

Although some formulations have already appeared on the market during the last decade, but there is still no universal platform suitable for the delivery of all kinds of drugs, that is to say the theory “one size fits all” does not apply. Meanwhile, current nanotechnologies have potential limitations such as:

(i) Poor drug loading that is usually less than 5% (weight % of the transported drug versus the carrier material). In consequence, either the quantity of the drug administered is not sufficient to reach a pharmacologically effective concentration in the body or the amount of the carrier material that is administered is too high, leading to adverse effects.

---

(ii) Rapid release, sometimes called “burst release”, of the encapsulated drug after administration, generally resulting from the release of a proportion of the drug fraction which is simply adsorbed (or anchored) at the surface of the nano-carrier. As a result, a significant fraction of the drug will be released before reaching the pharmacological target in the body, leading to low activity and toxicity issues.

(iii) The difficulty of designing synthetic materials which combine low toxicity, lack of immunogenicity, biodegradability and do not accumulate in cells or tissues.

Interestingly, rationally designed nanoparticles, including size, shape, surface charge and functionalization, is of great importance to overcome existing issues. Herein we will review the different types of nano-carriers which have been developed for tumor passive and active targeting. Thus we discuss the relationship between targeting mechanism and physicochemical factors of nano-carriers as well as pathophysiological characteristics of the tumor microenvironment.

## **2. Nano-carriers as drug delivery systems (DDs)**

Regarding the treatment or diagnosis of cancer, the key challenges lies in engineering drug/gene delivery systems capable of specifically targeting the diseased cells solely without affecting the normal healthy cells/tissues. This might be achievable by efficient delivery of anticancer agents into the tumor microenvironment (TME) and subsequently tumor cells [1, 2]. On the other hand, the formulated NPs must pass through several physiological and biological barriers. While their use as delivering systems imposes requirements to their size, biocompatibility, and surface chemistry for preventing unspecific interactions and introducing specific binding to their targets.

These nano-carriers must be able (i) to remain stable in the blood as long as they reach into TME, (ii) to escape from the reticuloendothelial system (RES) clearance and not to be captured by mononuclear phagocyte system (MPS). Both points have been attained by PEGylating the NPs surface, for improving their hydrophilic properties and conferring them stealth characteristics, in order to delay their recognition by immune systems and to increase the chance to target the desired tissues/cells. (iii) To accumulate in TME through irregular tumor vasculature, (iv) to penetrate into the tumor interstitial fluid of TME with high pressure, and (v) to reach the active site and interact with the targeted cells exclusively [3, 4]. Active/passive targeting is the ideal solution to promote NPs’ accumulation in the location of interest. The main factors that control the drug targeting by NPs are their surface functionalization, their physicochemical properties and the pathophysiological characteristics of the TME. These factors as will be discussed in the following sections.

Development of nano-carriers is crucial to prevent the cargos molecules from degradation or release before reaching their targets causing long-term toxicity issues. NPs are also excellent candidates for increasing the payload efficiency of the active pharmaceutical ingredients API by covalently grafting to drugs or by encapsulation. Nanoparticles can be made from a variety of materials such as lipids, compositing polymers, proteins, metals, or semiconductors. Numerous nanoparticles with well-defined shapes such as solid spheres, rods, tubes, and others have been

---

recently developed. Current nanoparticle platforms for tumors can be classified into three major categories including organic-based NPs (e.g. liposomes, dendrimers, polymeric NPs, micelles and solid lipid nanoparticles (SLNPs)), inorganic-based NPs (e.g. iron oxide nanoparticles IONPs, gold nanoparticles AuNPs, ceramic nanoparticles, semiconductor nanocrystals and carbon nanotubes CNTs) and hybrid nanoparticles. The latter are synthesized from two or more types of nanomaterials (NMs) and are generally formed with a metallic or polymeric core covered with a single or multiple lipid layers to increase the biocompatibility of the system. This type of NPs can be utilized in both diagnostic and therapeutic applications.

An alternative design of nanoparticles may also contain intrinsic thermal, electrical, optical, or magnetic properties that can be served in imaging or therapeutic purposes. Interestingly, AuNPs are used as efficient imaging agents for X-ray micro-CT thanks to their high absorption coefficient. Also, they are used in photothermal therapy (PTT) [5] as they are able to absorb photons at specific wavelength and immediately convert them into heat destroying the cancer cells. IONPs can be used for magnetic resonance imaging for potential detecting small lesions and very sensitive to image brain tumors. Meanwhile, because of their magnetic properties, they could be targeted to specific cells/tissues. After injection of IONPs, and applying external magnetic field will raise the particles temperature, a phenomenon called “hyperthermia”. Quantum dots can act as photodynamic therapeutic agents (PDT) to induce cytotoxicity by creating free oxygen radicals under light. Table 1 shows some pros and cons of such nano-carriers.

**Table 1:** Advantages and limitations of various amphiphilic-based drug delivery nanosystems

<b>Nanosystems</b>	<b>Advantages</b>	<b>Limitations</b>
<b>Micelles</b>	Easy and non-costly production	Disassembly upon dilution; too fast drug release; only suitable for lipophilic drugs
<b>Cubosomes et hexosomes</b>	Very ordered; high encapsulation efficiency; suitable for oral administration	Extremely high viscosity; short release duration
<b>Liposomes</b>	Biocompatible, biodegradable; extremely versatile; high-throughput synthesis, lyophilization; surface modifications; new generation hybrid systems	Limited shelflife (in solution); too slow drug release; hydrophilic drug leakage
<b>Lipid nanoparticles</b>	Biocompatible; high drug loading; batch-to-batch reproducibility; easy to scale-up and sterilise; long shelflife	Drug loading is limited by its solubility in lipid melt; risk of drug expulsion after polymeric transition
<b>Nano-emulsions</b>	Kinetically stable; high drug loading capacity;	High cost of industrial production

	biocompatible; slow and controlled drug release	
<b>Polymer-based self-assemblies</b>	Possible “smart” drug release (pH, temperature, redox sensitive); adaptable chemistry	Costly synthesis; safety and biodegradability concerns
<b>Macrocyclic self-assemblies</b>	Multi-dimensional hierarchical self-assemblies; novel topological structures	High cost of production; poor water solubility; low biocompatibility

### 3. Tumor-targeted drug delivery systems

Targeted drug delivery systems have several advantages including (1) protection of healthy cells from the cytotoxic compounds, (2) reduction of the dose-limiting adverse effects and (3) combating the drug-resistant cancerous cells. As matter of fact, the nucleus is ultimately the final target for many therapeutics treating various disorders including cancers, brain disorders and heart dysfunction. Because of their specific cell uptake and trafficking mechanisms, NPs allow the delivery of sensitive therapeutics to their target tissue/cell in active form and in sufficient concentration and decrease the amounts that accumulate in undesired organs/tissues. However, it has become increasingly obvious that cytosolic internalization of a drug molecule does not entail its interaction with its subcellular target and hence careful nanoparticle design and optimization is required to enable cellular/nuclear targeting.

#### 3.1. Passive targeting

It is now a well-established fact that under certain conditions (inflammation/hypoxia, which is typical for tumors), the endothelium of blood vessels becomes more permeable than in the healthy state [6]. Upon hypoxia, rapidly growing tumors recruit new vessels or engulf existing blood vessels. These newly formed leaky vessels allow selective enhanced permeation of macromolecules larger than 40 kDa and nanosystems to the tumor stroma.

Furthermore, the absence of normal lymphatic drainage in the tumor contributes to the NPs retention [7]. However, this unique feature is not applicable to small molecule drugs, which have generally short circulation time and fast wash-out from the tumor. Thus, the encapsulation of small-molecule drugs in nanosized drug carriers enhances their pharmacokinetics (prolonged systemic circulation), provides some tumor selectivity and decreases side effects. This type of tumor targeting is termed “passive”, as it relies on carrier characteristics (size, circulation time) and tumor biology (vascularity, leakiness etc.), but does not possess a ligand for specific tissue or organ binding [7, 8]. A general scheme illustrating this phenomenon along with active targeting discussed below is proposed in Fig. 1.

Since the discovery of the enhanced permeation and retention (EPR) effect in 1980s by Maeda and co-workers, [9] a lot of efforts were done to understand the significance of this phenomenon

in tumor targeting and develop appropriate drug delivery systems. Some of these nano-carriers, such as the marketed Doxil<sup>®</sup> and Caelyx<sup>®</sup>, are now successfully used in the clinics and EPR effect became a golden standard in the design of passive tumor-targeted systems [6].

However, EPR effect provides rather modest tumor specificity with 20-30% in delivery increase compared to normal organs. The EPR effect is highly dependent on the intrinsic tumor biology and in particular: (i) The degree of angiogenesis and lymphangiogenesis. (ii) The degree of perivascular tumor growth and the density of the stromal response. (iii) Intra-tumor pressure [10]. All of these factors, together with the physicochemical characteristics of nano-carriers, will determine its drug delivery efficiency.

Although the leakiness of newly formed tumor vessels influences the nanomedicine permeation, it also contributes to the high interstitial pressure, which in contrast, is able to inhibit the accumulation of drug carriers in tumor [10]. Moreover, due to the disproportion of pro- and anti-angiogenic signaling inside of different parts of the tumor, vessels are abnormal with dilated, tortuous, and saccular channels, disorganized patterns of interconnection and branching.

Due to such heterogeneous blood supply, tumor cells also grow irregularly – those that are near blood vessels proliferate faster than those that are in the tumor core and receive less nutrients and oxygen. This explains hypoxic/necrotic areas in the cores of large tumors (i.e. 1-2 cm in diameter in mice) and often impossibility for nanomedicines to reach these areas. Moreover, blood vessels in the central area of the tumors do not leak as much as one could expect due to the high interstitial pressure. Such phenomenon was observed in various kinds of murine and human tumors. High interstitial pressure not only inhibits drug delivery by convection but also compresses newly formed blood vessels. In this way, blood is conducted away from the center of the tumors towards the periphery [8, 10].

However, it is possible to modulate EPR effect chemically or mechanically to achieve vascular normalization leading to higher accumulation of nano-carriers. Among chemical EPR enhancers one could find bradykinin (kinin), nitric oxide, peroxyntirite, prostaglandins, vascular permeability factor (VPF) / vascular endothelial growth factor (VEGF) and other cytokines [7, 8]. These molecules induce hypertension or vascular normalization, which could temporary enhance tumor perfusion. Other approaches utilize ultrasound, radiation, hyperthermia or photo-immunotherapy to modulate tumors vasculature and increase nanosystems permeation. Nevertheless, all described methods have limitations and contra-indications and thus require careful consideration [8, 10, 11].

### ***3.1.1. Nano-carriers' characteristics affect passive targeting strategy***

Biodistribution, pharmacokinetics, as well as the toxicity profiles are influenced either by the physicochemical properties of the developed nano-carrier or by the pathophysiological properties of the tumor microenvironment (TME). Globally, it has been extensively demonstrated that particle size and surface charge affect the efficiency and the pathway of cellular uptake for

---

liposomes [12], quantum dots [13], polymeric NPs [14, 15], AuNPs [16], and silica NPs [17] by influencing the adhesion of the particles and their interaction with cells [18].

Another factors influencing EPR-based tumor targeting are nanomedicine size and circulation time. Size is important for the permeation and retention in the tumor and thus is limited by the fenestrations in tumor vessels (200-800 nm) [6]. On the other hand, nanomedicine diameter influences their renal excretion (less than 6 nm) or through Reticulo-Endothelial System (RES) (more than 500 nm). Thus, as already mentioned, the optimal size range is around 20-200 nm [10].

Surface chemistry and charge also play vital role in the circulation time – too hydrophobic or charged systems are rapidly opsonized by the MPS. Hence, it is preferred to make nanoparticle surface “look like water” – hydrophilic and neutral or slightly anionic. For this purpose water-soluble polymers (generally PEGs) are grafted on the nano-carrier surface [6, 19]. Moreover, PEGylation prevents nanoparticle aggregation and non-specific interactions by changing surface charge and hydration [20]. The optimal loading of PEG-modified lipids in the liposome has been shown to be around 5 - 9 mol% of classically utilized DSPE-PEG2000. At this concentration each polymer chain adopts a mushroom-like globular structure with slight overlay between distinct polymers and ensures a complete ‘stealth’ nanoparticle surface coverage [20].

However, the first injection of PEGylated liposomes was shown to induce PEGs-specific IgM and as a consequence, rapid elimination and enhanced hepatic uptake of a second dose of PEGylated liposomes. This is known as an accelerated blood clearance phenomenon and represents an important obstacle to the pharmacokinetics and pharmacodynamics of PEGylated liposomes and particles. In addition PEG corona could also be a steric hindrance preventing efficient internalization of nanosystems into tumor cells. This issue is termed in literature as “PEG dilemma” [6, 8]. Thus, in a design of a drug delivery carrier one should find an appropriate compromise between prolonged circulation time and better intracellular trafficking. The possible solutions could be shorter PEG chains (i.e.,  $M_w < 1000$ ), PEG attachment by enzyme-cleavable bound or utilization of specific tumor targeting ligands [8].

Nevertheless, PEGylation is a clinically accepted tool to control nanoparticle surface properties and produce “stealth” drug delivery carriers. Moreover, it offers a possibility to chemically bound a targeting ligand on its surface and therefore enhances intracellular uptake [20]. This so-called “active targeting” approach that will be discussed in the following section. The chemical structure of the molecules also impacts the accumulation of NPs into specific organs. As has been demonstrated by Attia *et al.* [21] in their study to develop new contrast agents based on nano-emulsion platforms, the *iv* injections of the two nano-emulsions (NEs) encapsulating different molecules revealed different accumulation sites.

### **3.2. Active targeting (Tuning surface functionality)**

It is noteworthy that the active targeting is essential for the delivery of drugs, genes, and theranostics only to the location of interest avoiding the normal tissues and thereby enhances the therapeutic efficiency and limits the side effects. Active targeting is able to significantly increase

---

the quantity of drug delivered to the target cell compared to free drug or passively targeted nanosystems.

After accumulation in the tumor region, the drug efficiency can be even increased by the so-called active targeting. This is achieved through the decoration of the nano-carrier surfaces with ligands corresponding to receptors over-expressed onto the tumor cells (illustrated in Fig. 1). This strategy will improve the affinities of the nano-carriers for the surface of cancer cell and thus enhance the drug penetration. The first evidence of this phenomenon was proposed in 1980 with antibodies grafted in the surface of liposomes [22], followed by other various kinds of ligands like for instance peptides, nucleic acids, aptamers [23, 24].

Among the classical targets, we can cite the transferrin receptors (TfR) or nicotinic acetylcholine receptors that allow the reach the environment of brain tumors. In this case, the mechanism concerns targeting of endothelial cells, *i.e.* vascular targeting. Applied to target glioma, for drug delivery and/or biomedical imaging, transferrin ligands were grafted on solid lipid nanoparticles (SLNPs) [25], micelles [26], dendrimers [27, 28], and superparamagnetic iron oxide NPs (SPIONPs) [29]. In addition, literature reports examples in which central nervous system (CNS) and glioblastoma, has been reached through the targeting of nicotinic acetylcholine with micelles [30-32].

A vast number of receptors have been recognized as well as their antibodies were successfully synthesized and investigated *in vitro* and *in vivo*. Inducing very strong ligand/receptor binding, consequently serving as potential candidates to achieve active targeting technology. It has been found that RGD peptide binds to  $\alpha_v\beta_3$  integrin. These receptors are highly present on both the glioma cells and on the vasculature of TME [33]. F3 peptide was found to bind to nucleolin receptor expressed on angiogenic endothelial cells in the TME [34]. Likewise, aminopeptidase N (CD 13) has been identified as potential receptor in the TME [35] and has been shown to be targeted by a tri-peptide (Asn-Gly-Arg (NGR) peptide) [36]. Finally among the classical examples of ligands, we can cite the folic acid (FA) that specifically binds to the folate receptor (FAR) as well present in TME. In that case different strategies have been reported, through synthesis of FA-drug conjugates, through FA-grafting onto nano-carriers promoting their endocytosis in cancer cells. Examples of commonly targeting ligands are presented in Table 2.

**Table 2:** Examples of commonly used targeting agents [20].

Class	Ligand	Targets	Advantages	Limitations
<b>Antibodies</b>	Herceptin Rituxan CD19	HER2 CD20 CD19 antigen	High affinity and strong binding ; already in clinical trials ; therapeutic potential	High production cost ; pharmacokinetics ; « binding site barrier effect » ; potential immunogenicity
<b>Peptides</b>	RGD NGR	$\alpha_v\beta_3$ integrins,	High affinity	Reduced circulation half

		Aminopeptidase N	life
<b>Proteins</b>	Transferrin LHRH	Transferrin receptor LHRH receptor	Already in clinical trials High production cost
<b>Aptamers</b>	Pegaptanib	VEGF receptor	Possible to develop for any target High production cost
<b>Small molecules</b>	Folate Galactose	Folate receptor Asialoglycoprotein receptor	Low production cost, low molecular weight ; simple chemistry Could reduce circulation time

We can summarize the active targeting of tumors can be performed by directly targeting tumor cells, targeting the vascularization of TME and targeting the tumor nucleus as described in the following sections.

### 3.2.1. Tumor cell targeting

The majority of tumor targeting is performed by the tumor cell targeting in general by nanocarriers (see Fig. 1) that improves their cell penetration.

It has been demonstrated that folic acid-conjugated to silica NPs slightly improved the tumor pressure compared to non-conjugated silica NPs [37]. Similar results were observed in FA-conjugated polymer based DDs [38]. These incoherent results oppose the rules of active targeting and this could be attributed to four possibilities: (a) not all tumor cells overexpress receptors all the time, thus receptors density on the cell surfaces are varied accordingly. The ligand/receptor interaction occurs only at the high-density receptors and meantime NPs pass by, therefore enhancing cell penetration. (b) On the other hand, it is noteworthy that surface density of ligand could have an importance on the nano-carrier specific cell binding. The higher the density, the higher the targeting efficiency [39]. On the other hand, some simulations [40] argued that ligand-functionalized NPs enhance their interactions with leaky vessels to the detriment of deeper tumor tissues. Besides, if the density is too high the opposite effect was observed and resulting of their own steric hindrance [41]. It follows therefrom that a beforehand work on whole process is necessary. (c) The third phenomenon to be taken into account is the potential increase of the nano-carrier opsonization due to the ligands [42]. (d) Finally, the specific affinity between folic acid and liver could induce a premature hepatic uptake of the FA-decorated nano-carriers, after i.v. administration [43].

To conclude, when designing ligand-functionalized targeted drug delivery systems, the essential parameters of the ligand itself should be also taken into consideration, including molecular weight (MW), targeting affinity, valence and biocompatibility. The latter is a critical parameter due to many active targeting drug delivery systems are often very efficient *in vitro* [44], while they do not always enhance drug accumulation in tumors when studied *in vivo* [45].

### 3.2.2. Vascular targeting (Endothelial cells)

Another potential alternative strategy is to target angiogenic endothelial cells, which are adjacent to tumor cells and have intimate contact with blood vessels as described in Figure 1. This will reduce blood supply to the tumor and deprive cancer cells from oxygen and nutrients with subsequent hypoxia and necrosis [46]. The integrins ( $\alpha 2\beta 3$ ,  $\alpha v\beta 3$  and  $\alpha 5\beta 1$ ) and aminopeptidase-N (CD13) are the most common targets for tumor neovasculature. They are recognized by cyclic and linear derivatives of the peptide RGD (arginylglycylaspartic acid) and NGR (asparaginyglycyl-argininic acid) respectively [47]. Unlike the EPR effect, an important advantage of vascular targeting lies in the fact that its efficiency of is not correlated to the specific blood vessel permeability or cell uptake [48, 49]. Vascular targeting is able to limit poor delivery of drugs, the drug resistance and can be more adapted to the tumor heterogeneity or to various different sorts of tumors [50].

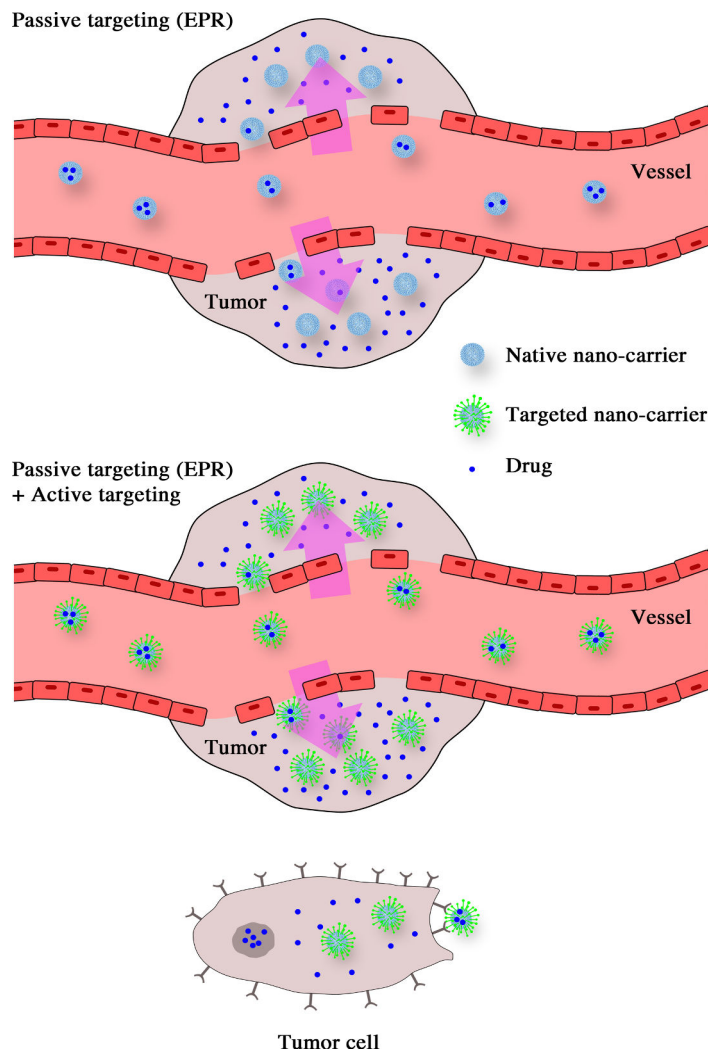


**Figure 1:** Schematic illustration of nano-carriers accumulation in tumor region through active and passive targeting

Earlier work on vascular targeting were reported in the 1920s [51] it was only in 1993 that researchers proved the real potential of this approach with a successful tumor eradication *in vivo* [52]. Then several literature reports extended the concept using ligands like vascular endothelial growth factor or RGD peptides, grafted on nanoparticles or nano-carriers like nanotubes [53], nanographene oxide [48], or QDs [54].

### **3.2.3. Targeting the mildly acidic tumor microenvironment**

In the mid-twentieth century, Otto Warburg [55] described a switch of the cancerous cellular metabolism into glycolysis with the formation of lactic acid as an endpoint to this glycolytic metabolism [56]. The lactic acid if accumulated intracellularly would lead to cell death [57]. The cancerous cells cope with this by overexpression of proton pumps and transporters to remove the protons from the cytosol to the extracellular milieu [58, 59]. This phenomenon, now known as Warburg effect, leads to the acidification of tumor extracellular environment.

Since then, considerable amount of research was carried out in order to exploit the acidic pH of the tumorous extracellular fluids [60]. *E.g.* pH sensitive liposomes were recently used to increase the therapeutic window of doxorubicin in treating breast cancer [61]. It has been shown that estrone-anchored pH-sensitive liposomes (ES-pH-sensitive-SL) were significantly more cytotoxic than free doxorubicin or non pH-sensitive estrone-anchored liposomes (ES-SL) vis-à-vis MCF-7 cell line. Furthermore, cardiotoxicity, the foremost clinical side effect of doxorubicin, of ES-pH-sensitive-SL was lower than free doxorubicin. Indeed, ES-pH-sensitive-SL displayed higher accumulation in tumor and less take up by heart, liver and kidney comparing to ES-SL or free doxorubicin. Also, ES-pH-sensitive-SL showed better inhibition of tumor growth than ES-SL and free doxorubicin when tested on breast tumor animal model [61].

### **3.2.4. Nuclear targeting**

Beside the drug delivery to the TME or more precisely to the tumor cells, some treatments needs an even more precise level which is the drug delivery at organelle level, *e.g.*, nucleus, lysosomes, mitochondria or endoplasmic reticulum. In that way, the therapeutic response will be maximized, and their toxic side effects minimized. In the case of delivery of therapeutic genes, the target is the cell nucleus to exert their effects in correcting dysfunctional or missing genes. On the other hand, cancer cell nucleus can be targeted for a destroying effect. Indeed, the mechanism of action of most anticancer drugs, *e.g.* doxorubicin, involves oxidative DNA damage and topoisomerase II inhibition within the nucleus [62]. However the effect of such anticancer drugs can be dramatically reduced if they are not specifically targeted to enter the cell as well as to the cell nucleus [62]. Nucleus targeting was investigated with different imaging probes like magnetic nanoparticles [63], AuNPs [64, 65, 66], AgNPs [67, 68] and QDs [69]. Biologically, to deliver the payload drug targeted NPs to the nucleus, they are subjected to bypass a number of barriers such as (i) the cell membrane, (ii) avoid the entrapment and degradation in endosomes/lysosomes, (iii) cytoplasmic trafficking and finally (iv) nuclear entry. Actually the nuclear targeting should

---

mostly be performed using nano-scaled carrier, that are able to cross physiological barriers and to specifically deliver active ingredient or imaging probe to intracellular regions.

Therefore, specific nucleus delivery has become a challenge task that should take into account the nano-carrier entering into the cytoplasm and then in the nucleus membrane. The nuclear pore complex (NPC) drastically controls the communication between the cytosol and nucleus.

One interesting example of nanoparticles used for nucleus targeting is the gold nanoparticles. Besides their easy synthesis, their controllable and very small size allows to reach dimension below the one of the NPC, and their chemical nature simplify their surface functionalization [70]. The NPs size is even more important since below 9 nm AuNPs present a high nucleus penetration along with a fast blood clearance. On the other hand, for higher sizes from 20 to 200 nm, it is the opposite, the blood circulation time is higher but the nucleus entering is low [71]. Drug delivery solutions to nucleus were proposed by, for instance, gold nanostars functionalized with nucleolin-specific aptamers [72]. AuNPs sizing at 30 nm, decorated with PEG (for increasing the NPs circulation in bloodstream) and peptides (RGD and nuclear targeted peptide) were shown to selectively disturb the division of cancer cells, resulting in cytokinesis arrest and resulting in apoptosis [70].

Additionally, NPs made with cationic polymers like poly(ethyleneimine) (PEI) and poly(L-lysine) were showed to be able to enter the nucleus efficiently. These polymers follow the microtubule cytoskeleton up to the nucleus [73]. Similar results are also obtained with cationic liposome-plasmid DNA complexes that successfully brought plasmid DNA into the nucleus [74]. Investigations on ligands promoting the nuclear penetration shown that nuclear location sequence (NLS) decorating NPs significantly promotes their nucleus targeting [75]. Literature provided some other examples in that sense using NLS (CGGGPKKKRKVGG)-functionalized PLGA NPs (sizing around 72 nm) and NLS- functionalized QD-conjugated PLGA NPs (168 nm), that had been shown to target and enter the nucleus of HeLa cells [76]. Transactivator of transcription (TAT) peptide (from HIV-1) has been shown efficient for the same purpose [77], especially functionalizing ultra-small mesoporous silica nanoparticles [78 , 79]. Table 3 lists different nano-carriers following active or passive targeting strategy.

**Table 3:** Selected studies have been reported showing the active or passive targeted nano-carriers bearing molecules of interest either therapeutic agents and/or contrast agent to specific cells

Carrier	Ligand (coating shell)	Active/ Passive targeting	Imaging agent and/or therapeutic agent	Application	REF.
Nanoemulsions	PEGylated hydrophilic molecules (cremophore elp)	---	Iodinated mono glyceride and iodinated castor oil	Blood pool imaging agents, accumulated particularly in Liver and/or spleen, and imaged by X-ray CT	[21]

			contrast agents		
<b>Dendrimers</b>	PEG-RGD peptide	Active	AuNPs and Gd <sup>3+</sup> chelate imaging agents	Dual-mode nanoprobe for targeted CT/MR imaging of different types of $\alpha v\beta 3$ integrin-overexpressing cancer.	[80]
<b>Dendrimers</b>	(PEG) monomethyl ether, and PEGylated Folic acid	Active	AuNPs and Gd <sup>3+</sup> complexes imaging probes	CT/MR imaging of folate receptors (FAR) of cancer cells	[81]
<b>Polyethylenimines (PEIs)</b>	(PEG), non covalent complexes with siRNA	Active	Therapeutic siRNAs	RNAi-mediated gene targeting, especially to lung	[82]
<b>Liposomes</b>	decorated by cyclic RGD peptide conjugated to tandem peptide R8 to develop a multifunctional peptide R8-RGD	Active	Paclitaxel	Targeting for brain tissues and selectively accumulated in the glioma foci	[83]
<b>Au-PEINPs</b>	PEI- PEG monomethyl ether-FA	Active	AuNPs contrast agent	FA-Au-PENPs for targeted tumor CT imaging of FAR	[84]
<b>Polymeric NPs (PLGA-PEG) NPs</b>	PEG-cyclic pentapeptide c(RGDfK)	Active	Cisplatin Pt(IV) Prodrug	Targeted to the $\alpha v\beta 3$ integrin (prostate and breast cancer epithelial cells)	[85]
<b>Polymeric Micelles NPs</b>	Transferrin-Modified PEG-phosphatidylethanolamine (Tf-mPEG-PE)	Active	R547 drug (a potent and selective ATP-competitive cyclin-dependent kinase (CDK) inhibitor)	Targeted to A2780 ovarian carcinoma cells-overexpressing transferrin receptors (TfR)	[86]
<b>Albumin NPs</b>	---	---	Tacrolimus (TAC)	TAC-loaded HSA-NPs Targets inflamed joints of rheumatoid arthritis tissues	[87]
<b>Gold NPs</b>	Anti-EGFR-PEG-AuNPs and Anti-IgG-PEG-AuNPs	Active	AuNPs imaging probes	Targeting the human squamous cell carcinoma head and neck cancer.	[88]

<b>Polymeric NPs</b>	C18PMH-PEG	---	Fe <sub>3</sub> O <sub>4</sub> contrast agent and DOX drug	Magnetically control drug delivery, and serving as a contrast agent in T2- weighted MR imaging (theranostics)	[89]
<b>Gold NPs</b>	Gum Arabic-FA	Active	Both epirubicin Drug and AuNPs contrast agent	Targeted delivery of epirubicin to A549 lung cancer cells.	[90]
<b>Quantum Dots</b>	PEGylated molecules	Active	F3 peptide and siRNA	F3/siRNA-QDs NPs produce significant knockdown of EGFP signal, and used as bioimaging probes by fluorescent imaging	[91]
<b>Lipid Nano capsules (LNCs)</b>	Polysaccharids lipochitosan (LC) and lipodextran (LD)	---	DiD fluorescent dye	Selected to HEK293( $\beta$ 3) cells-bearing mice and detected by fluorescent imaging	[92]

#### 4. Examples of targeted nano-carriers

For the delivery of nucleic acids, active targeting could be an extremely useful approach [45]. As they are large, polyanionic molecules are not able to penetrate the cells because of electrostatic repulsions from negatively charged cellular membrane. In addition, DNA and siRNA site of action is inside the cells and their unselective uptake might provoke additional side effects. In contrast, the active targeting is able to enhance nucleic acid cellular internalization and at the same time limit off-target side effects. Moreover, cationic lipids classically used for nucleic acid delivery could induce *in vivo* toxicity [93].

Recent study using double-targeted photolabile-caged cell-penetrating peptide (pcCPP) (/NGR liposomes encapsulating siRNA showed efficacy in c-myc gene silencing *in vitro* and *in vivo* [94]. pcCPP/NGR liposomes demonstrated enhanced uptake and endosomal escape in HT1080 cell line. After systemic administration in mice pcCPP/NGR liposomes were preferentially accumulated in the tumor and delayed tumor growth via RNA interference.

The first evidence of RNA interference in *humans* was shown with targeted nanoparticles [95]. On the other hand, cyclodextrin-based polymer functionalized with free PEG and PEG-transferrin conjugates. siRNA was designed to silence the expression of the M2 subunit of ribonucleotide reductase (RRM2). Systemic administration of nanoparticles revealed their dose-dependent accumulation in tumors and the decrease in RRM2 protein and corresponding mRNA. This study demonstrates that RNA interference could occur in humans after systemic administration of

siRNA in targeted nanoparticulate carrier and thus could be utilised as a gene-specific therapeutics (Table 4).

Preclinical trials and subsequent clinical translation were shown for targeted polymeric micelles encapsulated docetaxel (BIND-014) [96]. The micelles combine passive targeting via the EPR with active targeting provided by peptide derivative S,S-2-[3-[5-amino-1-carboxypentyl]-ureido]-pentanedioic acid (ACUPA), a PSMA (prostate specific membrane antigen) substrate analogue inhibitor. Administration in mice, rats and non-human primates showed prolonged circulation time (compared to free drug), minimal accumulation in the liver and controlled drug release. The same pharmacokinetics was observed in first Phase I human trials.

Antibodies (Ab) and their fragments are so far one of the most studied targeting agents in preclinical and clinical trials. For instance, HER2-targeted PEGylated liposomal doxorubicin formulation was developed to reduce unspecific cardiotoxicity of anthracyclines and enhance the drug therapeutic potential [98]. The successful results obtained in pre-clinical studies in mice and embryonic stem cells derived cardiomyocytes brought the formulation to Phase I clinical trials (MM-302) in patients with advanced breast cancer. Another immunoliposome doxorubicin formulation (MCC-465) undergoing Phase I clinical trials showed no specific cardiac toxicity and pharmacokinetics comparable to Doxil<sup>®</sup> [99]. Here a F(ab')<sub>2</sub> fragment of the human monoclonal antibody GAH (recognizes > 90% of stomach cancer tissues) was conjugated to standard PEGylated doxorubicin formulation. Other targeted nanosystems undergoing clinical trials are presented in Table 4.

Table 4: Examples of targeted nanomedicine formulations in clinical trials [47,97].

Nanoplatfrom	Drug	Ligand	Target	Cancer type	Phase
<b>Liposomes</b>	Oxaliplatin (MBP-426)	Transferrin (tr)	tr receptor	Adanced / metastatic solid tumours	I/II
<b>Liposomes</b>	Doxorubicin (MCC-465)	F(ab') <sub>2</sub> from GAH		Metastatic stomach cancer	I
<b>Liposomes</b>	p53 gene (SGT53-01)	scFv	tr receptor	Solid tumours	Ib
<b>Liposomes</b>	RB94 plasmid DNA (SGT-94)	scFv	tr receptor	Solid tumours	I
<b>Liposomes</b>	Doxorubicin (MM-302)	scFv	ErbB2 (HER2)	Advanced breast cancer	I
<b>Liposomes</b>	Melanoma Ag and IFN (Lipovaxin-MM)	Single domain Ab gragment	DC-SIGN	Melanoma vaccine	I
<b>Polymers</b>	Docetaxel	ACUPA	PSMA	Solid tumours	I

	(BIND-014)	peptide			
<b>Polymers</b>	RRM2 siRNA (CALAA-01)	tr	tr receptor	Solid tumours	I

Small natural molecules such as sugars and vitamins [20, 47] could also represent interesting alternatives to antibodies and peptides. Moreover, they are easily metabolized and should not induce toxicity or side effects. One of the successful examples in small molecule targeting are galactosylated solid lipid nanoparticles with encapsulated doxorubicin that showed enhanced cellular uptake and similar bio-distribution *in vivo* compared to non-targeted [44].

Despite the advantages that active targeting could provide and a lot of efforts that were put by the scientific community over the last 20 years for its development, clinical outcomes stay quite modest. This is often due to discrepancies between animal models and human primary tumors, tumor heterogeneity in target expression and rapid blood clearance. When designing targeted systems a careful attention should be pointed at ligand properties, target expression profile and nanoparticle surface chemistry. It is however important to point out that active targeting strategies are still highly needed for the delivery of fragile bioactive molecules such as peptides, proteins and especially nucleic acids. Thus novel targets and ligands could represent a major interest in this field.

## 5. Expert opinion

The choice between active or passive tumor targeting should firstly rely on characteristics of the tumor cells as well as of the chemical nature of the drug. For the drugs, that do not have issues with cell penetration, such as doxorubicin, the simple encapsulation in “stealth” nanosystem (that reach the target passively) is sufficient. The best efficient result will be obtained by encapsulating these drugs in stealth nano-carriers with high blood half-life, thus, increasing their chance to accumulate specifically within the tumorous tissues, and consequently decreasing the drug toxicity towards highly perfused organs like heart, kidneys and liver. On the other hand, for the therapeutic molecules that have difficulties to cross cell membrane and could induce severe damage to normal cells, active targeting should be a preferential strategy. This involves the nanocarrier decoration with ligands specific to the receptors overexpressed on the surface of cancer cells. However, even if the result is more efficient, the technology for the surface decoration with ligands can be a complex chemistry (especially for nano-emulsions), and this is why in some cases the global strategy can orientate the choice of the drug privileging only the simple EPR effect without active targeting.

Described earlier, nucleic acids are an excellent example of drugs that require the development of ligand-targeted systems. While cationic non-targeted nano-carriers could induce the interactions with cell membrane, they are non selective and toxic. On the other hand, nano-carriers decorated with ligands will stimulate receptor-mediated endocytosis and therefore the delivery of the drugs to their site of action, cytoplasm or even nucleus. This will also minimize off-target side effects and general toxicity. A combination of active or passive drug carrier with an imaging or a

diagnostic agent will generate “intelligent” theranostics system able to monitor disease progression and evaluate therapeutic efficacy of the drug in real time. The development of such systems relies on the careful consideration of tumor biology as well as on the exploration of new targets potential and original drug carriers.

## 6. References

- [1] Mussi SV, Torchilin VP. Recent trends in the use of lipidic nanoparticles as pharmaceutical carriers for cancer therapy and diagnostics. *J Mater Chem B*. 2013;1:5201-9.
  - [2] Wang M, Thanou M. Targeting nanoparticles to cancer. *Pharmacol Res* 2010;62:90-9.
  - [3] Barar J, Omidi Y. Dysregulated pH in tumor microenvironment checkmates cancer therapy. *Bioimpacts*. 2013;3:149-62.
  - [4] Omidi Y, Barar J. Targeting tumor microenvironment: crossing tumor interstitial fluid by multifunctional nanomedicines. *Bioimpacts*. 2014;4:55-67.
  - [5] Huang X, El-Sayed IH, Qian W, El-Sayed MA. Cancer cell imaging and photothermal therapy in the near-infrared region by using gold nanorods. *J Am Chem Soc*. 2006;128: 2115-20.
  - [6] Torchilin V. Tumor delivery of macromolecular drugs based on the EPR effect. *Adv Drug Deliv Rev*. 2011;63:131-5.
  - [7] Maeda H. The enhanced permeability and retention (EPR) effect in tumor vasculature: the key role of tumor-selective macromolecular drug targeting. *Adv Enzyme Regul*. 2001;41:189-207.
  - [8] Fang J, Nakamura H, Maeda H. The EPR effect: Unique features of tumor blood vessels for drug delivery, factors involved, and limitations and augmentation of the effect. *Adv Drug Deliv Rev*. 2011;63:136-51.
  - [9] Matsumura Y, Maeda H. A new concept for macromolecular therapeutics in cancer chemotherapy: mechanism of tumoritropic accumulation of proteins and the antitumor agent smancs. *Cancer Res*. 1986;46:6387-392.
  - [10] Kobayashi H, Watanabe R, Choyke PL. Improving Conventional Enhanced Permeability and Retention (EPR) Effects; What Is the Appropriate Target? *Theranostics*. 2013;4:81-9.
  - [11] Huynh E, Zheng G. Cancer nanomedicine: addressing the dark side of the enhanced permeability and retention effect. *Nanomedicine*. 2015;10:1993-5.
  - [12] Chono S, Tanino T, Seki T, Morimoto K. Uptake characteristics of liposomes by rat alveolar macrophages: influence of particle size and surface mannose modification. *J Pharm Pharmacol*. 2007;59:75-80.
  - [13] Osaki F, Kanamori T, Sando S, Sera T, Aoyama T. A quantum dot conjugated sugar ball and its cellular uptake on the size effects of endocytosis in the subviral region. *J Am Chem Soc*. 2004;126:6520-1.
  - [14] Wina KY, Feng SS. Effects of particle size and surface coating on cellular uptake of polymeric nanoparticles for oral delivery of anticancer drugs. *Biomaterials*. 2005;26:2713-22.
-

- [15] Foged C, Brodin B, Frokjaer S, Sundblad A. Particle size and surface charge affect particle uptake by human dendritic cells in an in vitro model. *Int J Pharm.* 2005;298:315-22.
- [16] Chithrani BD, Ghazani AA, Chan WCW. Determining the size and shape dependence of gold nanoparticle uptake into mammalian cells. *Nano Lett.* 2006;6:662-8.
- [17] Lu F, Wu SH, Hung Y, Mou CY. Size effect on cell uptake in well-suspended, uniform mesoporous silica nanoparticles. *Small.* 2009;5:1408-13.
- [18] Lee KD, Nir S, Papahadjopoulos D. Quantitative analysis of liposome-cell interactions in vitro: rate constants of binding and endocytosis with suspension and adherent cells and human monocytes. *Biochemistry.* 1993;32:889-99.
- [19] Immordino ML, Dosio F, Cattel L. Stealth liposomes: review of the basic science, rationale, and clinical applications, existing and potential. *Int J Nanomedicine* 2006;1:297-315.
- [20] Noble GT, Stefanick JF, Ashley JD, Kiziltepe T, Bilgicer B. Ligand-targeted liposome design: challenges and fundamental considerations. *Trends Biotechnol.* 2014;32:32-45.
- [21] Attia MF, Anton N, Chipper M, Akasov R, Anton H, Messaddeq N, et al. Biodistribution of X-Ray Iodinated Contrast Agent in Nano-Emulsions Is Controlled by the Chemical Nature of the Oily Core. *ACS Nano.* 2014;8:10537-50.
- [22] Leserman LD, Barbet J, Kourilsky F, Weinstein JN. Targeting to cells of fluorescent liposomes covalently coupled with monoclonal antibody or protein A. *Nature.* 1980;288:602-4.
- [23] Kamaly N, Xiao ZY, Valencia PM, Radovic-Moreno AF, Farokhzad OC. Targeted polymeric therapeutic nanoparticles: design, development and clinical translation. *Chem Soc Rev* 2012;41:2971-3010.
- [24] Wang X, Li S, Shi Y, Chuan X, Li J, Zhong T, et al. The development of site-specific drug delivery nanocarriers based on receptor mediation. *J Control Release.* 2014;193:139-53.
- [25] Jain A, Singhai P, Gurnany E, Updhayay S, Mody N. Transferrin-tailored solid lipid nanoparticles as vectors for site-specific delivery of temozolomide to brain. *J Nanopart Res* 2013;15:1518.
- [26] Zhang P, Hu L, Yin Q, Feng L, Li Y. Transferrin-modified c[RGDfK]-paclitaxel loaded hybrid micelle for sequential blood-brain barrier penetration and glioma targeting therapy. *Mol Pharm.* 2012;9:1590-8
- [27] He H, Li Y, Jia XR, Du J, Ying X, Lu WL, et al. PEGylated poly(amidoamine) dendrimer-based dual-targeting carrier for treating brain tumors. *Biomaterials.* 2011;32:478-87.
- [28] Li Y, He H, Jia XR, Lu WL, Lou JN, Wei Y. A dual-targeting nanocarrier based on poly(amidoamine) dendrimers conjugated with transferrin and tamoxifen for treating brain gliomas. *Biomaterials.* 2012;33:3899-908.
- [29] Jiang W, Xie H, Ghoorah D, Shang Y, Shi H, Liu F, et al. Conjugation of functionalized SPIONs with transferrin for targeting and imaging brain glial tumors in rat model. *PLoS One.* 2012;7:e37376.
- [30] Zhan C, Li B, Hu L, Wei X, Feng L, Fu W, et al. Micelle-based brain-targeted drug delivery enabled by a nicotine acetylcholine receptor ligand. *Angew Chem Int Ed Engl.* 2011;50:5482-5.
-

- [31] Zhan C, Wei X, Qian J, Feng L, Zhu J, Lu W. Co-delivery of TRAIL gene enhances the anti-glioblastoma effect of paclitaxel in vitro and in vivo. *J Control Release* 2012;160:630-6.
- [32] Zhan C, Yan Z, Xie C, Lu W. Loop 2 of Ophiophagus hannah toxin b binds with neuronal nicotinic acetylcholine receptors and enhances intracranial drug delivery. *Mol Pharm.* 2010;7:1940-7.
- [33] Bello L, Francolini M, Marthyn P, Zhang J, Carroll RS, Nikas DC, et al. Alpha(v)beta3 and alpha(v)beta5 integrin expression in glioma periphery. *Neurosurgery.* 2001;49:380-9.
- [34] Christian S, Pilch J, Akerman ME, Porkka K, Laakkonen P, Ruoslahti E. Nucleolin expressed at the cell surface is a marker of endothelial cells in angiogenic blood vessels. *J Cell Biol* 2003;163:871-8.
- [35] Pasqualini R, Koivunen E, Kain R, Lahdenranta J, Sakamoto M, Stryhn A, et al. Aminopeptidase N is a receptor for tumor-homing peptides and a target for inhibiting angiogenesis *Cancer Res.* 2000;60:722-7.
- [36] Arap W, Pasqualini R, Ruoslahti E. Cancer treatment by targeted drug delivery to tumor vasculature in a mouse model. *Science.* 1998;279: 377-80.
- [37] Lu J, Liong M, Li ZX, Zink JJ, Tamanoi F. Biocompatibility, biodistribution, and drug-delivery efficiency of mesoporous silica nanoparticles for cancer therapy in animals. *Small.* 2010;6:1794-805.
- [38] Yoo HS, Park TG. Folate receptor targeted biodegradable polymeric doxorubicin micelles. *J Control Release* 2004;96:273-83.
- [39] Tsai CP, Chen CY, Hung Y, Chang FH, Mou CY. Monoclonal antibody-functionalized mesoporous silica nanoparticles (MSN) for selective targeting breast cancer cells. *J Mater Chem.* 2009;19:5737-43.
- [40] Farokhzad OC, Langer R. Impact of nanotechnology on drug delivery. *ACS Nano.* 2009;3:16-20.
- [41] Laginha K, Mumbengegwi D, Allen T. Liposomes targeted via two different antibodies: assay, B-cell binding and cytotoxicity. *Biochim Biophys Acta.* 2005;1711:25-32.
- [42] Salvati A, Pitek AS, Monopoli MP, Prapainop K, Bombelli FB, Hristov DR, et al. Transferrin-functionalized nanoparticles lose their targeting capabilities when a biomolecule corona adsorbs on the surface. *Nat Nanotechnol.* 2013;8:137-43.
- [43] Shinoda T, Takagi A, Maeda A, Kagatani S, Konno Y, Hashida M. In vivo fate of folate-BSA in non-tumor- and tumor-bearing mice. *J Pharm Sci.* 1998;87:1521-6.
- [44] Jain A, Kesharwani P, Garg NK, Jain A, Jain SA, Jain AK, et al. Galactose engineered solid lipid nanoparticles for targeted delivery of doxorubicin. *Colloids Surf B Biointerfaces.* 2015;134:47-58.
- [45] Kunjachan S, Pola R, Gremse F, Theek B, Ehling J, Moeckel D, et al. Passive vs. Active Tumor Targeting using RGD-and NGR-modified Polymeric Nanomedicines *Nano Lett.* 2014;14:972-81.
- [46] Lammers T, Hennink WE, Storm G. Tumour-targeted nanomedicines: principles and practice *Br J Cancer.* 2008;99:392-7.
-

- [47] Jin SE, Jin HE, Hong SS. Targeted delivery system of nanobiomaterials in anticancer therapy: from cells to clinics. *Biomed Res Int.* 2014;2014:814208.
- [48] Shi S, Yang K, Hong H, Valdovinos HF, Nayak TR, Zhang Y, et al. Tumor vasculature targeting and imaging in living mice with reduced graphene oxide. *Biomaterials.* 2013;34:3002-9.
- [49] Hong H, Yang K, Zhang Y, Engle JW, Feng L, Yang Y, et al. In vivo targeting and imaging of tumor vasculature with radiolabeled, antibody-conjugated nanographene. *ACS Nano.* 2012;6:2361-70.
- [50] Seon BK, Haba A, Matsuno F, Takahashi N, Tsujie M, She X, et al. Endoglin-targeted cancer therapy. *Curr Drug Deliv.* 2011;8:135-43.
- [51] Woglom WH. A critique of tumor resistance. *J Cancer Res.* 1923;7:283-309.
- [52] Burrows FJ, Thorpe PE. Eradication of large solid tumors in mice with an immunotoxin directed against tumor vasculature. *Proc Natl Acad Sci U S A.* 1993;90:8996-9000.
- [53] Liu Z, Cai W, He L, Nakayama N, Chen K, Sun X, et al. In vivo biodistribution and highly efficient tumour targeting of carbon nanotubes in mice. *Nat Nanotechnol* 2007;2:47-52.
- [54] Cai W, Shin DW, Chen K, Gheysens O, Cao Q, Wang SX, et al. Peptide-labeled near-infrared quantum dots for imaging tumor vasculature in living subjects. *Nano Lett.* 2006;6:669-76.
- [55] O. W. On the origin of cancer cells. *Science.* 1956;123:309-14.
- [56] Xu RH, Pelicano H, Zhou Y, Carew JS, Feng L, Bhalla KN, et al. Inhibition of glycolysis in cancer cells: a novel strategy to overcome drug resistance associated with mitochondrial respiratory defect and hypoxia. *Cancer Res.* 2005;65:613-21.
- [57] Schornack PA, Gillies RJ. Contributions of cell metabolism and H<sup>+</sup> diffusion to the acidic pH of tumors. *Neoplasia.* 2003;5:135-45.
- [58] Mahon BP, Pinar MA, McKenna R. Targeting carbonic anhydrase IX activity and expression. *Molecules.* 2015;20:2323-48.
- [59] Walsh M, Fais S, Spugnini EP, Harguindey S, Abu Izneid T, Scacco L, et al. Proton pump inhibitors for the treatment of cancer in companion animals. *J Exp Clin Cancer Res.* 2015;34.
- [60] Omran Z, Rauch C. Acid-mediated Lipinski's second rule: application to drug design and targeting in cancer. *European biophysics journal : EBJ.* 2014;43:199-206.
- [61] Paliwal SR, Paliwal R, Pal HC, Saxena AK, Sharma PR, Gupta PN, et al. Estrogen-anchored pH-sensitive liposomes as nanomodule designed for site-specific delivery of doxorubicin in breast cancer therapy. *Mol Pharm.* 2012;9.
- [62] Mizutani H, Tada-Oikawa S, Hiraku Y, Kojima M, Kawanishi S. Mechanism of apoptosis induced by doxorubicin through the generation of hydrogen peroxide. *Life Sci.* 2005;76:1439-53.
- [63] Xu CJ, Xie J, Kohler N, Walsh EG, Chin YE, Sun SH. Monodisperse magnetite nanoparticles coupled with nuclear localization signal peptide for cell-nucleus targeting. *Chem Asian J* 2008;3:548-52.
- [64] Tkachenko AG, Xie H, Coleman D, Glomm W, Ryan J, Anderson MF, et al. Multifunctional gold nanoparticle-peptide complexes for nuclear targeting. *J Am Chem Soc* 2003;125:4700-1.
-

- [65] Lin SY, Chen NT, Sun SP, Chang JC, Wang YC, Yang CS, et al. The protease-mediated nucleus shuttles of subnanometer gold quantum dots for real-time monitoring of apoptotic cell death. *J Am Chem Soc.* 2010;132:8309-15.
- [66] de la Fuente JM, Berry CC. Tat peptide as an efficient molecule to translocate gold nanoparticles into the cell nucleus. *Bioconjug Chem.* 2005;16:1176-80.
- [67] Austin LA, Kang B, Yen CW, El-Sayed MA. Plasmonic imaging of human oral cancer cell communities during programmed cell death by nuclear-targeting silver nanoparticles. *J Am Chem Soc.* 2011;133:17594-7.
- [68] Austin LA, Kang B, Yen CW, El-Sayed MA. Nuclear targeted silver nanospheres perturb the cancer cell cycle differently than those of nanogold. *Bioconjug Chem.* 2011;22:2324-31.
- [69] Chen FQ, Gerion D. Fluorescent CdSe/ZnS nanocrystal-peptide conjugates for long-term, nontoxic imaging and nuclear targeting in living cells. *Nano Lett* 2004;4:1827-32.
- [70] Kang B, Mackey MA, El-Sayed MA. Nuclear targeting of gold nanoparticles in cancer cells induces DNA damage, causing cytokinesis arrest and apoptosis. *J Am Chem Soc.* 2010;132:1517-9.
- [71] Wong C, Stylianopoulos T, Cui J, Martin J, Chauhan VP, Jiang W, et al. Multistage nanoparticle delivery system for deep penetration into tumor tissue. *Proc Natl Acad Sci U S A.* 2011;108:2426-31.
- [72] Dam DH, Lee JH, Sisco PN, Co DT, Zhang M, Wasielewski MR, et al. Direct observation of nanoparticle-cancer cell nucleus interactions. *ACS Nano.* 2012;6:3318-26.
- [73] Suh J, Wirtz D, Hanes J. Efficient active transport of gene nanocarriers to the cell nucleus. *Proc Natl Acad Sci U S A* 2003;100:3878-82.
- [74] Tachibana R, Harashima H, Shinohara Y, Kiwada H. Quantitative studies on the nuclear transport of plasmid DNA and gene expression employing nonviral vectors. *Adv Drug Deliv Rev* 2001;52:219-26.
- [75] Derfus AM, Chan WCW, Bhatia SN. Intracellular delivery of quantum dots for live cell labeling and organelle tracking. *Adv Mater.* 2004;16:961-6.
- [76] Cheng FY, Wang SPH, Su C-H, Tsai TL, Wu PC, Shieh DB, et al. Stabilizer-free poly(lactide-co-glycolide) nanoparticles for multimodal biomedical probes. *Biomaterials.* 2008;29:2104-12.
- [77] Vives E, Brodin P, Lebleu B. A truncated HIV-1 Tat protein basic domain rapidly translocates through the plasma membrane and accumulates in the cell nucleus. *J Biol Chem.* 1997;272:16010-7.
- [78] Pan L, Liu J, He Q, Shi J. MSN-mediated sequential vascular-to-cell nuclear-targeted drug delivery for efficient tumor regression. *Adv Mater.* 2014;26:6742-8.
- [79] Wu M, Meng Q, Chen Y, Du Y, Zhang L, Li Y, et al. Large-pore ultrasmall mesoporous organosilica nanoparticles: micelle/precursor co-templating assembly and nuclear-targeted gene delivery. *Adv Mater.* 2015;27:215-22.
- [80] Chen Q, Wang H, Liu H, Wen S, Peng C, Shen M, et al. Multifunctional Dendrimer-Entrapped Gold Nanoparticles Modified with RGD Peptide for Targeted Computed
-

- Tomography/Magnetic Resonance Dual-Modal Imaging of Tumors. *Anal Chem.* 2015;87:3949-56.
- [81] Chen Q, Li K, Wen S, Liu H, Peng C, Cai H, et al. Targeted CT/MR dual mode imaging of tumors using multifunctional dendrimer-entrapped gold nanoparticles. *Biomaterials.* 2013;34:5200-9.
- [82] Günther M, Lipka J, Malek A, Gutsch D, Kreyling W, Aigner A. Polyethylenimines for RNAi-mediated gene targeting in vivo and siRNA delivery to the lung. *Eur J Pharm Biopharm.* 2011;77:438-49.
- [83] Liu Y, Ran R, Chen J, Kuang Q, Tang J, Mei L, et al. Paclitaxel loaded liposomes decorated with a multifunctional tandem peptide for glioma targeting. *Biomaterials.* 2014;35:4835-47.
- [84] Zhou B, Yang J, Peng C, Zhu J, Tang Y, Zhu X, et al. PEGylated polyethylenimine-entrapped gold nanoparticles modified with folic acid for targeted tumor CT imaging *Colloid Surf B-Biointerfaces.* 2016;140:489-96.
- [85] Graf N, Bielenberg DR, Kolishetti N, Muus C, Banyard J, Farokhzad OC, et al.  $\alpha V\beta 3$  Integrin-Targeted PLGA-PEG Nanoparticles for Enhanced Anti-tumor Efficacy of a Pt(IV) Prodrug. *ACS Nano.* 2012;6:4530-9.
- [86] Sawant RR, Jhaveri AM, Koshkaryev A, Zhu L, Qureshi F, Torchilin VP. Targeted Transferrin-Modified Polymeric Micelles: Enhanced Efficacy in Vitro and in Vivo in Ovarian Carcinoma *Mol Pharmaceutics.* 2014;11:375-81.
- [87] Thao IQ, Byeon HJ, Lee C, Lee S, Lee ES, Choi HG, et al. Pharmaceutical potential of tacrolimus-loaded albumin nanoparticles having targetability to rheumatoid arthritis tissues. *Int J Pharm.* 2016;497:268-76.
- [88] Reuveni T, Motiei M, Romman Z, Popovtzer A, Popovtzer R. Targeted gold nanoparticles enable molecular CT imaging of cancer: an in vivo study. *Int J Nanomed.* 2011;6:2859-64.
- [89] Wang C, Xu H, Liang C, Liu Y, Li Z, Yang G, et al. Iron Oxide @ Polypyrrole Nanoparticles as a Multifunctional Drug Carrier for Remotely Controlled Cancer Therapy with Synergistic Antitumor Effect. *ACS Nano.* 2013;7:6782-95.
- [90] Devi PR, Kumar CS, Selvamani P, Subramanian N, Ruckmani K. Synthesis and characterization of Arabic gum capped gold nanoparticles for tumor-targeted drug delivery. *Mater Lett.* 2015;139:241-4.
- [91] Derfus AM, Chen AA, Min DH, Ruoslahti E, Bhatia SN. Targeted Quantum Dot Conjugates for siRNA Delivery. *Bioconjugate Chem.* 2007;18:1391-6.
- [92] Hirsjärvi S, Dufort S, Bastiat G, Saulnier P, Passirani C, Coll JL, et al. Surface modification of lipid nanocapsules with polysaccharides: From physicochemical characteristics to in vivo aspects. *Acta Biomater.* 2013;9:6686-93.
- [93] Kral T, Leblond J, Hof M, Scherman D, Herscovici J, Mignet N. Lipopolythiourea/DNA interaction: a biophysical study. *Biophys Chem* 2010;148:68-73.
- [94] McNeeley KM, Karathanasis E, Annapragada AV, Bellamkonda RV. Masking and triggered unmasking of targeting ligands on nanocarriers to improve drug delivery to brain tumors. *Biomaterials.* 2009;30:3986-95.
-

- [95] Davis ME, Zuckerman JE, Choi CHJ, Seligson D, Tolcher A, Alabi CA, et al. Evidence of RNAi in humans from systemically administered siRNA via targeted nanoparticles. *Nature*. 2010; 464:1067-70.
- [96] Hrkach J, Von Hoff D, Mukkaram AM, Andrianova E, Auer J, Campbell T, et al. Preclinical development and clinical translation of a PSMA-targeted docetaxel nanoparticle with a differentiated pharmacological profile. *Sci Transl Med* 2012;4:128-39.
- [97] Krishnan V, Rajasekaran AK. Clinical Nanomedicine: A Solution to the Chemotherapy Conundrum in Pediatric Leukemia Therapy. *Clin Pharmacol Ther*. 2014;95:168-78.
- [98] Reynolds JG, Geretti E, Hendriks BS, Lee H, Leonard SC, Klinz SG, et al. HER2-targeted liposomal doxorubicin displays enhanced antitumorigenic effects without associated cardiotoxicity. *Toxicol Appl Pharmacol* 2012;262:1-10.
- [99] Matsumura Y, Gotoh M, Muro K, Yamada Y, Shirao K, Shimada Y, et al. Phase I and pharmacokinetic study of MCC-465, a doxorubicin (DXR) encapsulated in PEG immunoliposome, in patients with metastatic stomach cancer. *Ann Oncol*. 2004;15:517-25.



## **Chapter 2.2: Functionalizing nano-emulsions with carboxylate: impact on the biodistribution and pharmacokinetics on mice**

Herein, studying the correlation between surface charge of the nanoparticles and their biodistribution or targeting. We selected the oleic acid due to its high lipophilic properties, and design it covalent grafting with triiodobenzylalchole giving rise to triiodophenyl oleate. The synthesized molecule was elucidated by  $^1\text{HNMR}$  spectra then transformed into nano-emulsion spontaneously *via* homogenization with cremophore elp surfactant at SOR = 40 wt.% and SOWR = 40 wt.% inducing approximately zero charged nano-emulsion with around 60 nm in size. Likewise, in order to induce the surface functionalization, a lipophilic polymer (maleic anhydride-alt-1-octadecene, PMAO) was mixed to the iodinated oleate. This lipophilic polymer containing anhydride rings which opened during the nano-emulsions formulation and directly oriented to the nanodroplets surfaces functionalizing them with carboxylic groups. The size and the morphology were assessed by DLS and Cryo-TEM, in addition, zeta potential measurements showed the total difference between the neutral charged NE (-2.8 mv) and the negatively charged NE (-50 mv). Their penetration to the cells were tested against HeLa cells revealing very high internalization in case of negative NEs unlike the neutral NEs. *In vitro* experiments were followed and supported by longitudinal studied in mice giving rise to very different behave different pharmacokinetics. The supplementary part concerns with the formulation of the positive charge NEs that established by chitosan coating layer deposited on the negatively charged NEs. Unfortunately the *in vitro* cellular experiments showed completely no penetration to HeLa cells.

## Functionalizing nano-emulsions with carboxylate: impact on the biodistribution and pharmacokinetics on mice

Mohamed F. Attia,<sup>a,b,c,‡</sup> Sidy M. Dieng,<sup>a,b,‡</sup> Mayeul Collot,<sup>a,d,\*</sup> Andrey Klymchenko,<sup>a,d</sup> Caroline Bouillot,<sup>e</sup> Christophe A. Serra,<sup>f</sup> Marc Schmutz,<sup>f</sup> Meriem Er-Rafik,<sup>f</sup> Thierry F. Vandamme,<sup>a,b</sup> Nicolas Anton,<sup>a,b,\*</sup>

<sup>a</sup> University of Strasbourg, Faculty of Pharmacy, 74 route du Rhin 67401 Illkirch Cedex, France.

<sup>b</sup> CNRS UMR 7199, Laboratoire de Conception et Application de Molécules Bioactives, équipe de Pharmacie Biogalénique, 74 route du Rhin 67401 Illkirch Cedex, France.

<sup>c</sup> National Research Center, P.O. 12622, Cairo, Egypt.

<sup>d</sup> UMR CNRS 7213, Laboratoire de Biophotonique et Pharmacologie, équipe Nanochimie et Bioimagerie, 74 route du Rhin 67401 Illkirch Cedex, France.

<sup>e</sup> CERMEP Imagerie Vivant, Imaging Platform, Bron, France

<sup>f</sup> Institut Charles Sadron (ICS) – UPR 22 CNRS, Strasbourg, France

<sup>‡</sup> Co-first authors

\* To whom correspondence should be addressed:

- Dr. Nicolas Anton, University of Strasbourg, CNRS 7199, Laboratoire de Conception et Application de Molécules Bioactives, équipe de Pharmacie Biogalénique, route du Rhin No.74, F-67401 Illkirch Cedex, France.

Tel.: + 33 3 68 85 42 51, Fax: + 33 3 68 85 43 06; E-mail address: [nanton@unistra.fr](mailto:nanton@unistra.fr)

- Dr. Mayeul Collot, University of Strasbourg, CNRS 7213, Laboratoire de Biophotonique et Pharmacologie, équipe Nanochimie et Bioimagerie, 74 route du Rhin 67401 Illkirch Cedex, France.

Tel.: + 33 3 68 85 42 66, Fax: + 33 3 68 85 43 13; E-mail address: [mayeul.collot@unistra.fr](mailto:mayeul.collot@unistra.fr)

## Abstract

Efficiency of drug administration is related to the inhibition of adverse effects, and can be improved by the drug targeting. This can be performed by developing lipid nano-carriers encapsulating active ingredients, which will eventually follow their pharmacokinetics and biodistribution. Targeting technology generally goes along with the nano-carrier functionalization that can be the modification of the surface chemistry and/or ligand grafting. In this context, the great advantage of nano-emulsions is their loading capability and the possibilities offered to encapsulate several entities in a single droplet. However, since oil / water interface is a dynamic environment ruled by adsorption / desorption equilibria, the decoration of the droplets of lipid nano-emulsions with strongly anchored reactive functions is challenging. This study proposes a reliable and innovative method to functionalize lipid droplets, based on the lipophilic polymer poly(maleic anhydride-alt-1-octadecene) (PMAO), solubilized in the droplet core, and able to be hydrolyzed at the oil / water interface. The PMAO hydrolysis at oil / water interface was studied and disclosed by physico-chemical methods, surface tension and  $\zeta$  potential measurements, and quantified by a colorimetric methods originally adapted to nanoparticulate systems. *In vitro* studies revealed that the presence of carboxylates at interface has a heavy impact on the interactions with cells, as the internalization of negatively charged droplets is much higher than neutral ones. This difference was confirmed with longitudinal studies performed *in vivo* in mice after i.v. administration, followed by X-ray imaging (micro-computed tomography), the surface modification resulted in a significant difference in pharmacokinetics and biodistributions, with enhanced spleen and liver uptake. In this work we established the proof of concept of a new method for functionalizing lipid droplets, and demonstrated that surface modification can have a significant impact on their interaction with cells, pharmacokinetics and biodistribution *in vivo*.

## Keywords:

Nano-emulsions; surface functionalization; targeting; X-ray imaging; poly(maleic anhydride-alt-1-octadecene); PMAO; cell permeability.

## 1. Introduction

Generally, the main pharmacological activity of drug is potentially related to adverse effects. From the two last decades, important research efforts were precisely undertaken for reducing those effects. Increasing the benefit-to-risk ratio actually signifies improving the drug efficiency, and an important solution for this purpose is targeting the active ingredient on the disease, *e.g.* lesion, organ. Using nano-carriers is a realistic solution for performing an efficient drug targeting, and thus an accumulation of the drug specifically on the desired location and not in the healthy tissues. Drug targeting is particularly crucial in antitumor therapies, taking benefit of the particular physico-chemical properties of the tumor microenvironment for enhancing the nano-carrier accumulation [1-6]. Associating the drug with a nano-carrier will, after *in vivo* administration, modify its biodistribution, pharmacokinetics and elimination pathway in comparison with administrating the drug alone. It follows therefrom that after nano-encapsulation, the critical parameters impacting on the fate *in vivo* of the drug, will mainly be the ones of the carrier features including size, chemical composition, surface composition or charge. Finally, developing a drug targeting solution involves a deep knowledge of the interactions between the nano-carrier, the living organism, and the physiological properties of the target, what so-called “nano-bio-interactions”.

Lipid nano-droplets, so-called nano-emulsions, were shown as promising nano-carriers of liposoluble molecules [7-14]. Intrinsically, we have recently shown that, when solubilized in lipid core of droplets, active ingredients or imaging probes remains efficiently entrapped in the droplets and stay intact up to reaching the target [6]. At this point, the pathway of the drug will be the one of the lipid droplet in blood. Let us herein consider intravenous administration. Since the blood pool is the ultimate desired location for the drug, and the first one before targeting, it is the main route followed for research investigations or preclinical studies. Beyond physiological compatibilities like sterility, osmolality and pH, the size of the nanocarrier is the first important factor influencing the biodistribution [10, 15]. After injection, the nano-carrier will migrate to the heart by the vena cava, then in the lung to be back in heart by the pulmonary vena, and in the arterial circulation by the aorta. Thus a diameter higher than 5  $\mu\text{m}$  is a risk of pulmonary emboli, avoided with a size distribution centered below 200-300 nm. The blood clearance is then performed by the macrophages of the reticuloendothelial system (RES), particularly in liver and spleen. Nano-carrier uptake is mainly performed by K upfer cells in liver (25% of the liver cells and 90% of the macrophages in the body), as well as achieved by spleen. Oppositely, particles lower than 5-10 nm like micelles or small hydrophilic contrast agents undergo a renal filtration and a premature blood clearance. In fact, the circulation in bloodstream is the first crucial parameter related to the targeting efficiency: the higher the circulation time, the higher the contact with the target and potential interactions. The macrophage uptake is the consequence of the nanoparticle opsonization, by opsonin fixation onto their surface. The best conditions for inhibiting the opsonization is acknowledged as a particle size below 100 nm and a chemical surface decorated with hydrophilic polyethylene glycol polymer (PEG).

In the case of lipid nano-droplets of nano-emulsion, we have shown that the optimized conditions allowed a half-life in blood around 9h [9, 11, 16], with a complete clearance after one day. This result was obtained, for instance, with 80 nm droplets and the surface fully PEGylated [9]. Such droplets underwent the hepato-biliary expected elimination of nanoparticles through

liver and spleen. However, with the aim of targeting other organs or potentially tumor with molecules that will not cross the cell membrane (*e.g.* after passive accumulation by permeation and retention effect), active targeting strategies need to be developed. In contrast with other type of nanoparticles, the functionalization of nano-emulsions is very challenging and still not well developed. The oil / water droplet interface is a dynamic system and anchoring a ligand, even from an amphiphilic moiety would still have the risk of desorption. Surface modification of polymer or inorganic nanoparticles are very well documented [17], simply due to their chemical intrinsic predisposition, ligand bio-conjugation will be covalently grafted and highly concentrated. On the other hand, advantages of nano-emulsions over these nanoparticles are their loading capability, possibilities of co-encapsulation of different molecules with very high concentrations [11, 18, 19]. Some reports show the modification of droplet surface by post-insertion of functionalizable lipids like DSPE-PEG 2000-maleimide (1,2-distearoyl-sn-glycero-3-phosphoethanolamine-N-[maleimide (polyethylene glycol)-2000]) [20, 21], which consists of incubating a micellar solution of this DSPE-PEG 2000-maleimide with the suspension of lipid nano-droplets. As a result, a small fraction of the lipid will be inserted at the oil / water interface that allows to display around 40 functionalized sites per droplet [20, 21], which is rather low compared to the grafting efficiency obtained with polymer or inorganic nanoparticles [17]. The second pitfall of the method lies in the fact that the ligand grafting is only related to molecular adsorption at the droplet interface, that is to say considerably weaker than covalent bonding, all the more without insurance of stability after a potential ligand / receptor interaction.

The present study focused on the development of nano-carriers combining the advantages of nano-emulsions with their outstanding loading capabilities, decorated with carboxylates as reactive functions, strongly anchored onto their interface. For this purpose, poly(maleic anhydride-alt-1-octadecene) (PMAO), a cheap and commercially available polymer was used. PMAO is a lipophilic alternated polymer composed of aliphatic octadecene chains (C-18) and reactive cyclic anhydride functions. Once hydrolyzed by water, the anhydride functions provide negatively charged carboxylates leading to an amphiphilic polymer that is widely used to water-solubilize colloidal nanoparticles by wrapping [22]. Herein, PMAO was readily solubilized in the oily core of the droplet (up to 15 wt.%). After formulation of the nano-droplets, the anhydride functions quickly hydrolyzed once in contact with the water interface. As a result, negatively charged carboxylates are created and exposed to the water phase. Similarly to a rhizome network, the carboxylates are strongly anchored to the oily core of the droplet by the polymeric part of PMAO. This conjecture, schematically illustrated in Fig. 1, is the driving idea of this study. A first part of the work will concern proving the hypothesis by physicochemical methods, and a second part will investigate the impact of this surface modification on the cell uptake *in vitro* and on the pharmacokinetics and biodistribution in mice. *In vivo* longitudinal studies were performed using an iodinated oleic acid as oily droplet core, followed by X-ray imaging (micro-computed tomography).

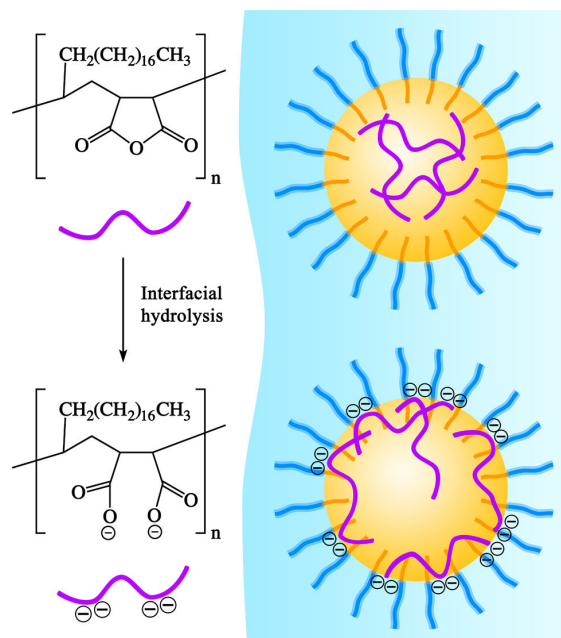


**Figure 1:** Schematic illustration of the main conjecture of the study: the PMAO, soluble in the oily core of nano-emulsion droplets hydrolyzes at interface creating carboxylates strongly anchored and available at the droplet surface.

## 2. Experimental section

### 2.1. Materials

The oil phase used in the preparation of nano-emulsions was Labrafac<sup>®</sup> WL 1349 (Gattefossé S.A., Saint-Priest, France), a mixture of capric and caprylic acid triglycerides as a model of parenteral-grade oil. For X-ray imaging, oil phase is 2,4,6-triiodophenyl oleate (TIPhO), a molecule synthesized for this study. Non-ionic surfactant (Kolliphor<sup>®</sup> ELP) is obtained from BASF (Ludwigshafen, Germany). Kolliphor<sup>®</sup> ELP (formerly named “Cremophor<sup>®</sup> ELP”) is a parenteral-grade non-ionic surfactant made by reacting ethylene oxide to castor seed oil at a molar ratio of 35. Poly (maleic anhydride-alt-1-octadecene) (PMAO), methylene blue (MB), oleic acid (OA), 2,4,6-triiodophenol (TIPh), 4-dimethylaminopyridine (DMAP), N,N'-dicyclohexylcarbodiimide (DCC), dichloromethane, ethyl acetate, cyclohexane, sodium hydrogen carbonate, sodium sulfate anhydrous, sodium chloride, Hoechst 33258, deuterated chloroform (CDCl<sub>3</sub>), were purchased from Sigma Aldrich (St. Louis, MO). WGA-488 was purchased from ThermoFisher Scientific. NR668 is a homemade modified Nile Red fluorophore [18]. Phosphate buffered saline (PBS) (for *in vivo* experiments), Dulbecco's modified Eagle medium (DMEM), Penicillin/Streptomycin solution (10.000 Units Penicillin/mL and 10 mg Streptomycin/ml) and fetal bovine serum (FBS) were obtained from PAN Biotech (Aidenbatch, Germany), and 0.22 µm syringe filters were purchased from Fisher (Germany).

### 2.2. Methods

#### 2.2.1. Axisymmetric drop shape analysis (ADSA)

Dynamic surface tension  $\gamma$  was measured with a Tracker drop tensiometer (Teclis, Longessaigne, France), according to the so-called ADSA method. A rising drop (cyclohexane) was formed at a controlled volume, and maintained in a temperature-controlled cell filled with different aqueous phase in function of the experiments (Ultrapure water, MilliQ Filtration System, or PBS at different pH: 2.4, 4.4, 5.4, 6.4, 7.4 and 9.4). The bubble shape was recorded in real-time with a video camera. As a result, its Laplacian shape gave the values of interfacial area and surface tension. All experiments were performed at 20°C, in triplicate.

### **2.2.2. Formulation of carboxylate-decorated nano-emulsions**

First, PMAO is dissolved in Labrafac<sup>®</sup> WL 1349 (0.3 g) at different concentrations from 0.5 wt.% to 15 wt.% (*i.e.* from 0.0015 g to 0.045 g). This {oil + PMAO} phase is then simultaneously homogenized at 2000 rpm and heated at 90°C (ThermoMixer C, Eppendorf) for 3 minutes. Then centrifuged 1 minute (14000 rpm, Minispin plus Microcentrifuge, Eppendorf) to avoid losing samples splashed on the tube wall. Next, Kolliphor<sup>®</sup> ELP is added to this mixture (0.2 g) again simultaneously homogenized at 2000 rpm and heated at 90°C for 5 minutes until obtaining a clear solution. Finally, 0.75 mL of warm PBS (90°C) is added to the {oil + PMAO + Kolliphor<sup>®</sup> ELP}, and homogenized (vortex) for 5 minutes to form the nano-emulsion.

### **2.2.3. Dynamic light scattering, $\zeta$ potential measurements**

Size distributions and polydispersity indices (PDI) were measured by DLS, along with  $\zeta$  potentials, with a NanoZS Malvern apparatus (Malvern, Orsay, France). The helium/neon laser, 4 mW, was operated at 633 nm, with the scatter angle fixed at 173° and the temperature maintained at 25°C. DLS data were analyzed using a cumulant-based method.  $\zeta$  potentials measurements were performed one hour after formulation. All experiments were performed in triplicate.

### **2.2.4. Cryo TEM preparations and observations**

Cryo TEM experiments were done on nano-emulsions (*i*) containing PMAO in oil (5 wt.%) and (*ii*) without PMAO, as control. Then samples were dialyzed for 24h (Spectra/Por<sup>®</sup>, Spectrum Europe B.V., Breda, the Netherlands, cutoff 12 kDa) to remove free surfactants. The vitrification of the samples was carried out in a homemade vitrification system. The chamber was held at 22°C and the relative humidity at 80%. A 5  $\mu$ L drop of the sample was deposited onto a lacey carbon film covered grid (Ted Pella) rendered hydrophilic using an ELMO glow discharge unit (Cordouan Technologies). The grid is automatically blotted to form a thin film which is plunged in liquid ethane hold at -190°C by liquid nitrogen. In that way a vitrified film is obtained in which the native structure of the objects is preserved. The grid was mounted onto a cryo holder (Gatan 626) and observed under low dose conditions in a Tecnai G2 microscope (FEI) at 200 kV. Images were acquired using an Eagle slow scan CCD camera (FEI).

### 2.2.5. Quantification of carboxylates available on the nanodroplets

Quantification of the carboxylates on the nano-droplets was performed following a colorimetric method originally adapted to colloidal systems [23]. The method based on electrostatic interaction between their negative charge, and the positive one of a hydrophilic dye (MB). As illustrated in the *Supplementary information* section, 1 mL of the suspension of nano-emulsions is placed into a dialysis tube (Spectra/Por<sup>®</sup>, Spectrum Europe B.V., Breda, the Netherlands, cutoff 12 kDa), and brought into contact with MB solution (10 mL at  $3.12 \times 10^{-6}$  mol.L<sup>-1</sup>) in the external phase (dialysate), PBS or MilliQ water. After a given and constant incubation time (fixed at 16h), a part of MB has migrated inside the dialysis tubing to stick on the charged nano-emulsion droplets. The idea is to relate the loss in MB absorbance in the dialysate (DA), to the concentration of PMAO in the droplet core. In parallel, calibration is performed with a PMAO beforehand fully hydrolyzed in aqueous phase (maintained 90°C in PBS or MilliQ water for 2h).

### 2.2.6. Synthesis and characterization of 2,4,6-triiodophenyl oleate

The iodine grafting into the oily molecule was performed *via* a simple esterification reaction. Thus 2,4,6-triiodophenol (5 g, 0.011 mol), 4-dimethylaminopyridine (0.243 g, 0.002 mol) and N,N'-dicyclohexylcarbodiimide (2.73 g, 0.013 mol) were sequentially added to a solution of oleic acid (3.7 g, 0.013 mol) in dichloromethane (250 mL) at room temperature. The reaction mixture was kept under stirring overnight at room temperature, and then dicyclohexylurea and other precipitates were removed by filtration. The organic phase was further washed twice with aqueous NaHCO<sub>3</sub> (5%), once with saturated NaCl solution and dried over anhydrous Na<sub>2</sub>SO<sub>4</sub>. The solvent was removed in vacuum and the obtained crude was then purified by gradient elution chromatography on silica gel using cyclohexane and ethyl acetate as eluents (at the ratio 9:1). The final product, 2,4,6-triiodophenyl oleate, was obtained in 47 % yield as a colorless oil. In view of the chemical structure, the theoretical iodine content should be as high as 51.7 % of the molecular weight.

### 2.2.7. NMR analysis

<sup>1</sup>H-NMR spectra were recorded with a Bruker Top Spin 3.0 operating at 400 MHz using deuterated chloroform (CDCl<sub>3</sub>) as a solvent. Chemical shifts (d) were expressed in parts per million (ppm), taking tetramethylsilane (TMS) as internal reference. The resulting <sup>1</sup>H-NMR data appear coherent with the iodine-grafted oleic acid structure by revealing another one new signal corresponds to the two CH aromatic groups at 8.12 ppm of benzene ring (see Supplementary information).

2,4,6-triiodophenyl oleate: <sup>1</sup>H-NMR (400 MHz; CDCl<sub>3</sub>): d/ppm: 8.12 (s, 2H, CH aromatic (meta)), 5.38 (m, 2H, CH=CH), 2.67 (t, *J* = 7.6 Hz, 2H, CH<sub>2</sub>-COO-), 2.05 (m, 4H, CH<sub>2</sub>-CH=CH-CH<sub>2</sub>), 1.84 (m, 2H, CH<sub>2</sub>-CH<sub>2</sub>-COO), 1.37 (m, 20H, CH<sub>3</sub>-(CH<sub>2</sub>)<sub>6</sub>-CH<sub>2</sub> and CH=CH-CH<sub>2</sub>-(CH<sub>2</sub>)<sub>4</sub>-(CH<sub>2</sub>)<sub>2</sub>-COO), 0.91 (t, *J* = 6.8 Hz, 3H, CH<sub>3</sub>).

<sup>13</sup>C NMR (101 MHz; CDCl<sub>3</sub>): δ 169.7 (CO), 151.9 (C-O), 147.0 (C-meta), 130.1 (CH=CH), 129.7 (CH=CH), 91.7 (C-ortho), 91.4 (C-para), 34.5 (CH<sub>2</sub>-CO), 31.9 (CH<sub>3</sub>-(CH<sub>2</sub>)<sub>7</sub>-CH<sub>2</sub>-CH=), 29.79 (=CH-CH<sub>2</sub>-(CH<sub>2</sub>)<sub>6</sub>-CO), 29.70 (CO-CH<sub>2</sub>-CH<sub>2</sub>), 29.54 (=CH-CH<sub>2</sub>-CH<sub>2</sub>-(CH<sub>2</sub>)<sub>5</sub>-CO), 29.35 (CO-(CH<sub>2</sub>)<sub>2</sub>-CH<sub>2</sub>), 29.33 (CO-(CH<sub>2</sub>)<sub>4</sub>-CH<sub>2</sub>), 29.15 (CO-(CH<sub>2</sub>)<sub>3</sub>-CH<sub>2</sub>), 29.13 (CH<sub>3</sub>-(CH<sub>2</sub>)<sub>5</sub>-CH<sub>2</sub>),

29.08 (CH<sub>3</sub>-(CH<sub>2</sub>)<sub>4</sub>-CH<sub>2</sub>), 27.26 (CH<sub>3</sub>-(CH<sub>2</sub>)<sub>3</sub>-CH<sub>2</sub>), 27.17 (CH<sub>3</sub>-(CH<sub>2</sub>)<sub>2</sub>-CH<sub>2</sub>), 24.6 (CH<sub>3</sub>-CH<sub>2</sub>-CH<sub>2</sub>), 22.7 (CH<sub>3</sub>-CH<sub>2</sub>), 14.2 (CH<sub>3</sub>).

### **2.2.8. Cell culture and in vitro studies**

HeLa cells (ATCC® CCL-2) were grown in Dulbecco's modified Eagle medium (DMEM, Gibco-Invitrogen), supplemented with 10% fetal bovine serum (FBS, Lonza) and 1% antibiotic solution (penicillin-streptomycin, Gibco-Invitrogen) at 37°C in humidified atmosphere containing 5% CO<sub>2</sub>. Cells were seeded onto a chambered coverglass (IBiDi) at a density of 1×10<sup>5</sup> cells/well 24h before the microscopy measurement. The cells were incubated in the presence of freshly prepared nano-droplets loaded with 0.2 wt.% NR668 (at 1000-fold dilution of the original formulation) in Opti-MEM (Gibco-Invitrogen) for 2h at 37°C. For a nuclear staining, the medium was replaced by Hoechst 33342 (conc. used 5 µg/mL) in Opti-MEM and the cells were incubated for 10 minutes at 37°C. For imaging, the medium was removed and the attached cells were washed with HBSS (ThermoFisher) three times and the cells were visualized in HBSS. Prior to imaging, the plasma membrane was stained by addition of wheat germ agglutinin-Alexa488, WGA-AlexaFluor®488 (ThermoFisher) (1 mg/mL in water) with a final concentration of 5 µg/mL. Confocal microscopy experiments were performed by using a Leica TCS SPE-II with HXC PL APO 63x/1.40 OIL CS objective. The microscope settings were: 405 nm laser for excitation of Hoechst 33342, emission was collected between 420 and 470 nm. 488 laser for excitation of WGA-AlexaFluor®488, emission was collected between 500 and 540 nm. For visualizing the nano-droplets, NR668 was excited with 561 nm laser with 570-750 nm detection range. The images were processed with the ImageJ software.

### **2.2.9. Micro-CT Imaging**

The experiments were performed in agreement with the Committee of Animal Research and Ethics of the University of Lyon-1.

#### **2.2.9.1. In vitro experiments**

The X-ray attenuation properties of the iodinated nano-emulsions were evaluated at various concentrations with a micro-CT scanner (1076 Skyscan, Kartuizersweg, Belgium). Experimental parameters were as follows: X-ray, 49 keV, 129 µA; resolution, 35 µm; pitch, 0.4°; aluminum filters, 0.5 and 632 ms. Iodine concentration of nano-emulsions was determined using a calibration curve established with a commercial hydrophilic contrast agent (XenetiX 300, namely iobitridol), correlating iodine concentration and radiopacity.

#### **2.2.9.2. In vivo experiments**

*In vivo* imaging experiments were performed with a micro-CT (micro computed tomography) scanner (INVEON, Siemens, Munich, Germany). The experimental X-ray parameters were as follows: X-ray, 50 keV, 500 µA; resolution, 111.25 µm; pitch, 2°; aluminum filters, 0.5 and 900 ms. The acquisitions were performed on Swiss mice, n = 3, for each type of nano-emulsions. Before the acquisition, mice were anesthetized with isoflurane. Then, the iodinated nano-

emulsions were injected using a catheter in the tail vein, with an injection volume corresponding to 10% of the blood volume (*i.e.*, 7.6  $\mu\text{L}$  of nano-emulsions per g of mouse weight). Scans were performed before administration, immediately after injection, and after 30 min, 1, 2, 3, 4, 6 hours and 1, 2, 3, 7, 16 and 24 days. The micro-CT raw data were treated with OsiriX viewer to establish 2D maximum projection slices, and then to quantify a signal by placing a region of interest in the heart, liver, spleen, and kidney.

### **3. Results and discussion**

#### ***3.1. Surface tension study of the PMAO at the oil / water interface***

In this surface tension study, PMAO was solubilized at 0.05 wt.% in cyclohexane as a model of organic phase compatible with ADSA experiments (suitable range of viscosities values, in the temperature of experiment). As opposed to the nano-emulsion formulation, our experiment was surfactant-free in order to focus on the effect of PMAO on the water / oil interface. The objective of this experiment was to show that PMAO migrates by diffusion at the interface and undergoes hydrolysis with water. Each anhydride function can potentially provide two negative charges (of two carboxylates) that will make a strong drop of the surface tension compared to the non-hydrolyzed anhydrides. Thus, the conjecture was ventured on the fact that, since anhydride hydrolysis reaction is catalyzed by pH of the bulk, a pH-dependent kinetics of surface tension stabilization would be driven by the hydrolysis reaction. The results are reported in Fig. 2 (a), showing a very significant evolution of the kinetics in function of the bulk pH. For the higher pH values, the surface tension stabilization is achieved within 2000 s while it is longer than  $10^4$  s for the smaller pH values. This is an actual clue of the chemical reaction of the anhydrides functions at interface.

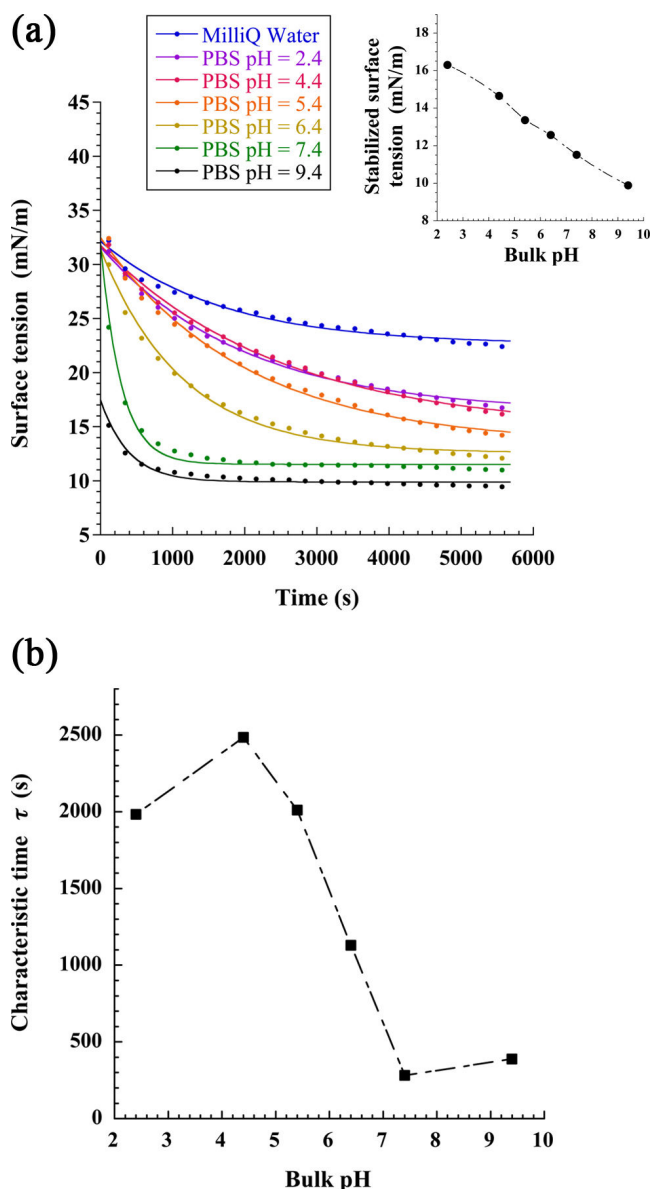


**Figure 2:** (a) Surface tension follow-up at the cyclohexane rising drop interface (containing PMAO at 0.05 wt.%) in aqueous phase of different composition and pH. Each curve was fitted with a simple mono-exponential model of Eq. 1. (a) *Inset:* values of the surface tension after stabilization in function of pH. (b) Characteristic time  $t$  (from Eq. 1) provided by the fits of (a), in function of the bulk pH.

It appears that whatever the kinetics, PMAO hydrolysis eventually occurs and the bulk high pH effectively favors the chemical reaction. Remarkably, even if the kinetics are highly different, the values of surface tension after stabilization (inset of Fig. 2 (a)) are quite close between 10 and 16 mN/m. This may be due to the change in the surface composition where the ratio carboxylates / hydroxyl will increase with the pH, visible here since the charged species have a better interfacial activity than neutral ones. Following this interpretation involves that two phenomena should impact simultaneously on the surface tension, with two different kinetics: (i) the diffusion of the PMAO towards the interface (extreme case of MilliQ water and lower pH values) and (ii) the PMAO hydrolysis giving rise to hydroxyl and carboxylates increasing the

surface activity of PMAO. The experimental curves of Fig. 2 (a) were fitted with an exponential decay reported in Eq. 1:

$$\gamma = \gamma_0 + A \left[ e^{(-t/\tau)} - 1 \right] \quad (1)$$

where  $\gamma$  is the surface tension,  $\gamma_0$  is the initial surface tension,  $\tau$  the characteristic time, and  $A$  constant parameters. Accordingly, the quantitative analysis of Fig. 2 (a) is given in Fig. 2 (b) with the values of  $\tau$  in function the bulk pH. The longer stabilization kinetics with  $\tau > 2000$  s, *i.e.* for the  $\text{pH} \leq 5.4$ , suddenly fall down to  $\tau < 500$  s with  $\text{pH} \geq 7.4$ . This variation appears very significant and we can evaluate on Fig. 2 (b) an apparent pKa around 5.9. To summarize, the hypothesis ventured on the fact that PMAO is able to migrate at the interface to be hydrolyzed seems to be correlated by this surface tension study, the optimal pH for this reaction is  $\text{pH} \geq 7.4$ .

### **3.2. Formulation of nano-emulsions with PMAO**

Formulation of nano-emulsions was performed, as described with materials compatible with the parenteral administration: triglyceride medium chains as oily core (Labrafac<sup>®</sup> WL 1349) and nonionic surfactant as stabilizer (Kolliphor<sup>®</sup> ELP). Spontaneous emulsification provided a suspension of nano-droplets sizing around 120 nm with a rather neutral  $\zeta$  potential. The same process was performed with the oil containing PMAO solubilized at different concentrations, and the corresponding droplet size and values of  $\zeta$  potentials are reported in Fig. 3 (a) and (b), respectively. The samples are measured one hour after formulation to ensure the PMAO hydrolysis is achieved in PBS ( $\text{pH} = 7.4$ ). Remarkably, the size remains rather constant with a slight decrease from 120 nm to 100 nm by increasing the polymer concentration, while the surface charge dramatically increases in absolute values, from -5 mV to around -35 mV. From the size analysis, we can say that the formulation process seems overall preserved. The slight decrease of size decrease could be likely attributed to the interfacial activity of the polymer, increasing with its concentration. On the other hand, the absolute values of  $\zeta$  potentials appear particularly high, and are related without doubt to the carboxylate functions at the interface. It is noteworthy that the values of  $\zeta$  potentials for bulk MilliQ water appears higher than bulk PBS, and it is effectively due to the difference of ionic strength of the bulk, since counter-ions of the buffer actually screen the surface charge. This also means that, theoretically, at equivalent conductivities, the two systems formulated in MilliQ water and in PBS should have extremely different  $\zeta$  potentials and surface composition (as disclosed with the tensiometry study above). Alternatively, these nano-droplets were observed by cryo TEM with 5 wt.% PMAO in oil (Fig. 3 (c)) and without PMAO as control (Fig. 3 (d)). The nano-droplets were distributed in the vitrified buffer layer, and the log-normal distribution of the population is rather visible with droplets ranging from 20 to 125 nm. In both cases, the droplets morphology appears very spherical and homogeneous. The main result lies in the fact that no real difference arose from the droplets with and without PMAO and the reason is due to the low contrast of the polymer compared to the triglycerides. The previous surface tension study and  $\zeta$  potentials values have confirmed that a part of the polymer is effectively anchored at the interface, but keeping unchanged the droplet morphology. Although these cryo TEM experiments effectively did not visually confirm the presence of PMAO at the droplet interface or even in their oily core, it demonstrated that the presence of the polymer, at concentration as high as 5 wt.% in oil, has no

---

impact on the droplet structure. We can also note that the droplets in Fig. 3 (c) seems slightly smaller than in picture (d), coherently with the DLS results of (a).

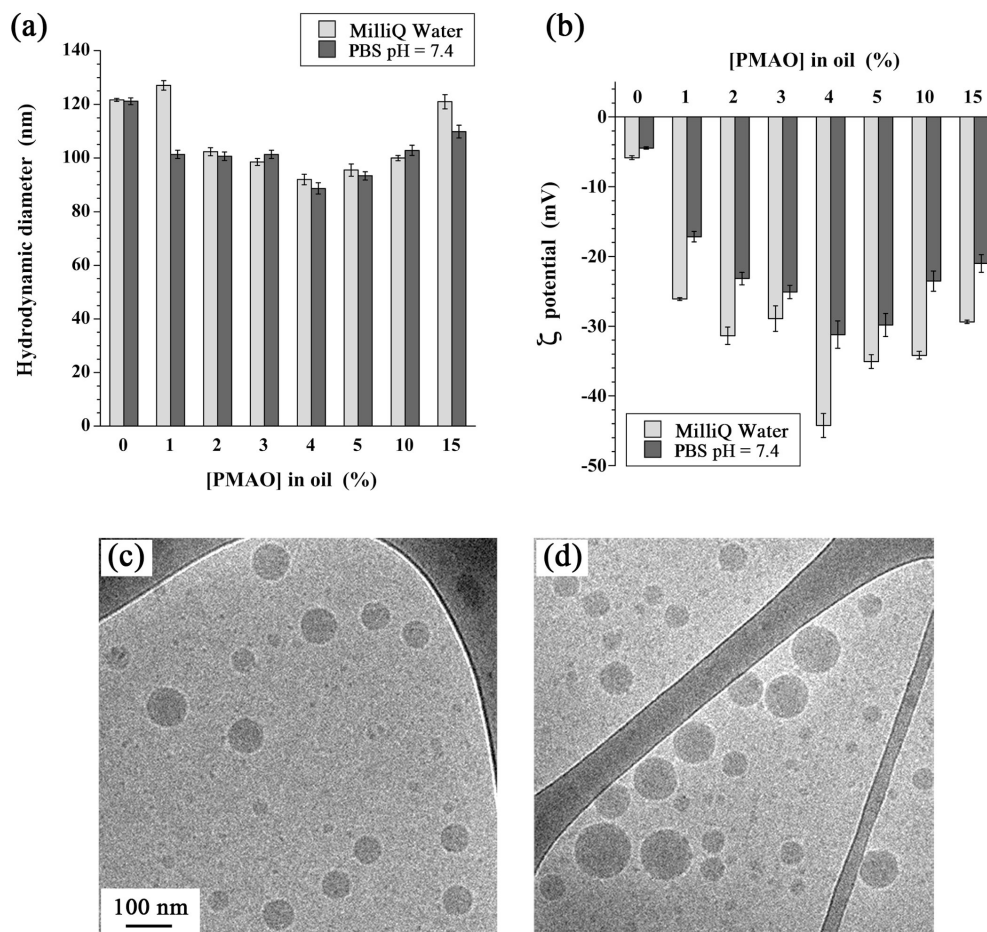


**Figure 3:** Physico-chemical characterization of nano-emulsions containing PMAO. (a) Hydrodynamic diameter and (b)  $\zeta$  potentials, in function of the polymer concentration in oil. (c,d) Cryo TEM micrographs, of (c) nano-emulsions containing 5 wt.% of PMAO in oil, and (d) nano-emulsions without PMAO in oil as control. The darkest areas are the supporting lacey film.

### 3.3. Quantification of the carboxylate at the oil / water interface of nano-emulsion droplets

The quantification of  $\text{COO}^-$  was performed according to a colorimetric method based on the electrostatic interactions between MB and the charged nano-droplet interface (described in section 2.2.5. above. The values of the MB absorbance in function of the concentration of PMAO in oil ( $[\text{PMAO}]_{\text{oil}}$ ), are reported in Fig. 4 (a), showing a gradual decrease with a steeper slope when the bulk is PBS at pH = 7.4 compared to MilliQ water, as expected. The calibration with PMAO hydrolyzed in water allowed, through the linear correlations  $\Delta A = f([\text{PMAO}]_{\text{water}})$ , to compare  $[\text{PMAO}]_{\text{water}}$  and  $[\text{PMAO}]_{\text{nano-emulsions}}$ , reported in Fig. 4 (b). For instance, in the more favorable case of pH = 7.4, this correlation let appear that to reach the same concentration of carboxylates than in water, the PMAO in nano-emulsion need to be around 33

times more concentrated. In other words, around 3.3% of the total anhydride functions of the droplets are available at the interface for an electrostatic interaction with the MB. The corresponding number of carboxylate per nano-emulsion droplet is then calculated considering the drop size (from Fig. 3 (a)) and the polymer concentration, reported in Fig. 4 (c). The colorimetric method appears efficient for evaluating the number of charged species at the interface of nanoparticles, and the number of functions disclosed is compatible with the aimed applications for potentially grafting ligands, and as well, largely exceeding the published examples of nano-emulsion functionalization, *i.e.* below 40 per droplet [20, 21]. However, it is to be noted that several studies regarding the surface functional group quantification, notably carboxylic acid, have some limitation, and only a small but constant fraction of the surface functional groups is accessible to covalent surface derivatization, independently of the total number of surface functional groups [24]. This means that the groups detected by quantification methods are actually underestimated.

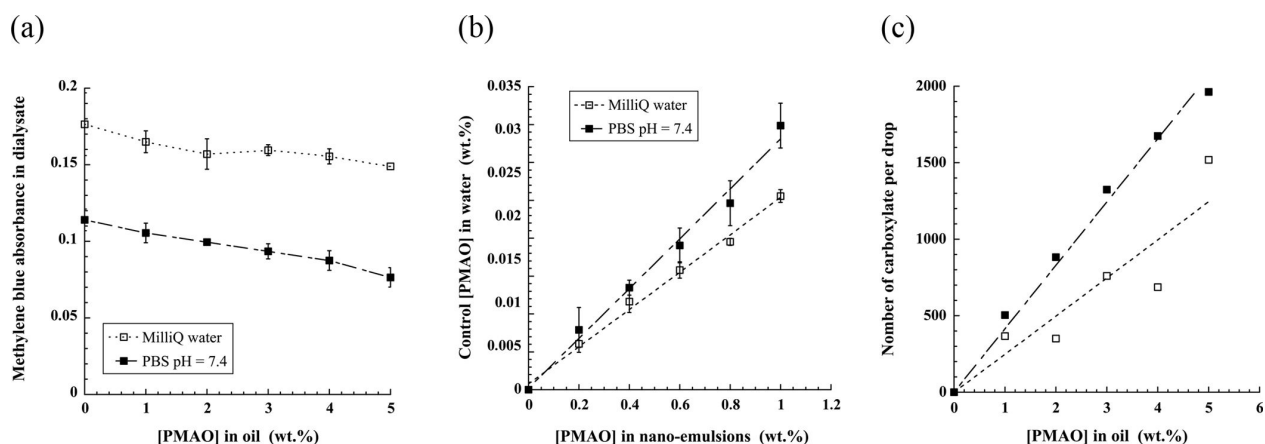


**Figure 4:** Quantification of the carboxylate functions anchored at the water / oil interface of the nano-emulsion droplets.

### 3.4. *In vitro* studies

The modification of the interfacial charge of such an extent is remarkable. The present following sections on *in vitro* cell experiments and *in vivo* imaging will focus on studying the potential impact that can induce the surface modification, on the living systems. Some studies previously conducted by our team [11, 16, 18] have shown that the interactions between nano-emulsion droplets and cells in cultures remains limited, and the cell uptake, when it arises, comes from the nature of the oily core. In the current study, three different samples were incubated with cells (HeLa as model cell line) during 2 hours, without PMAO as control, and with 0.5 and 1.0 wt.% in oil. To allow the droplet visualization under confocal microscopy, a lipophilic dye was introduced in the oily core at 0.2 wt.% in oil. This fluorophore is a modified Nile Red dye (NR668) that was proved, once encapsulated in nano-emulsion, not to leak out to the surrounding tissues or lipophilic receptors [6, 18, 19]. This tool thus ensured an efficient monitoring of the localization of the nano-emulsion droplets in fluorescence imaging. The results are reported in Fig. 5, in which the cell nucleus, plasma membrane and nano-emulsions appear in blue, green and red, respectively. The control (without PMAO) is conform to our expectations, the nano-

emulsions does definitely not enter the cells, even after 2 hours of incubation. Although cells incubated with nanodroplets containing 0.5 wt.% PMAO only displayed very dim red spots (indicated with arrows), those incubated with 1 wt.% PMAO displayed numerous bright red spots located in the cytoplasm. Due to the apparent size of these red spots (higher than the microscope resolution of 200 nm), and due to their mobility, these latter likely correspond to endosomes containing nano-emulsion droplets. It follows that the nano-emulsions droplets containing 1 wt.% PMAO and therefore displaying a high density of negative charges at their interface likely interact with the plasma membrane leading to their internalization through the endocytosis process.

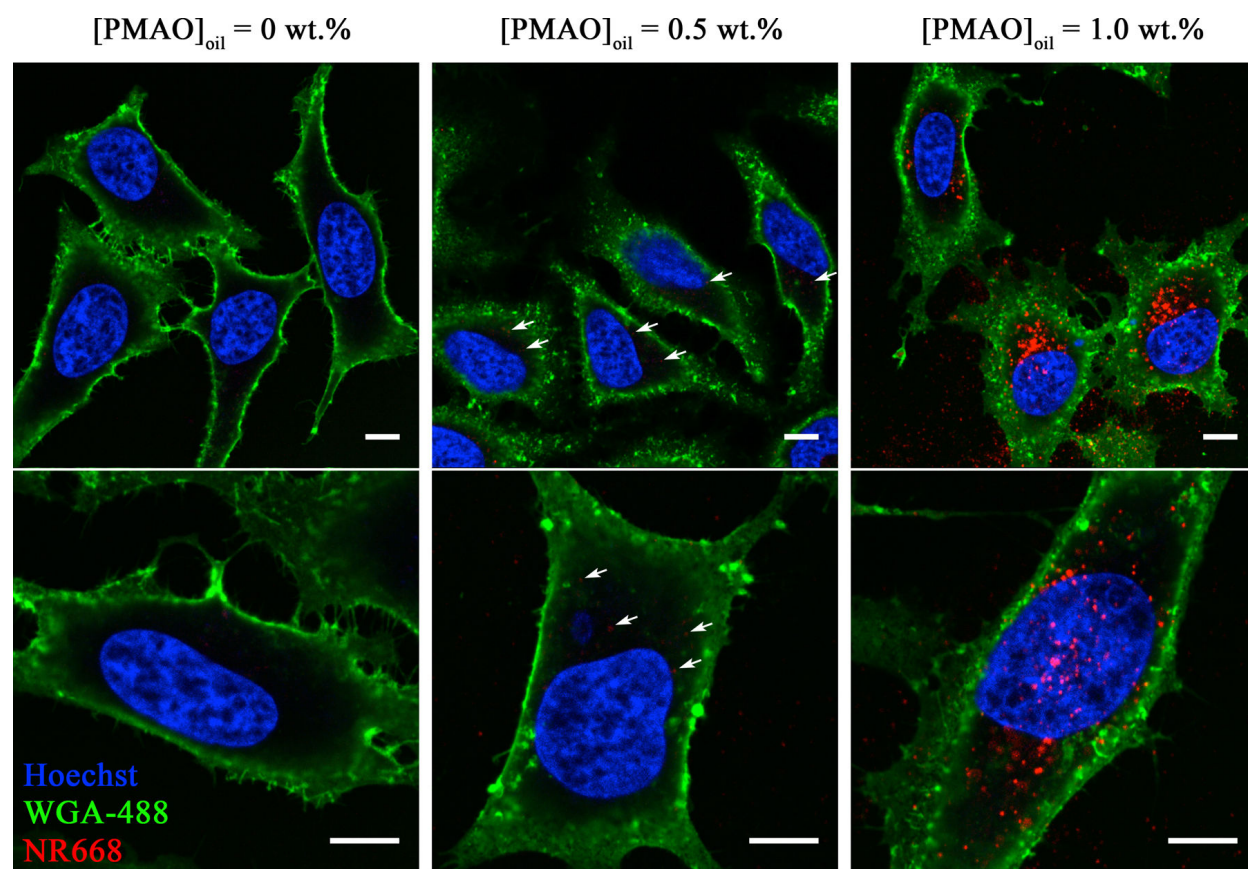


**Figure 5:** Laser scanning confocal imaging of HeLa cells incubated with NR668 doped nano-emulsion containing increasing amounts of PMAO. *In vitro* studies of the influence of PMAO in nano-emulsions on the cell uptake. HeLa cells were incubated 2h with different concentrations in PMAO in oil. Scale bars are 10  $\mu\text{m}$ .

In general, when the oily core is composed triglycerides and without surface modifications, no interactions with cells is detectable. This is attributed to the dense PEGylation of nano-droplets' surface by the nonionic surfactants which prevent the droplet from interacting with the biomolecules of the cell plasma membrane. However, up to now, such a cell uptake has never been observed with lipid droplets. It is actually a remarkable result all the more so since it is obtained with a very simple and cheap modification of the formulation. Therefore, it opens new doors for efficient drug delivery applications where the drug needs a carrier to cross the cell membrane. For example, combined to enhanced retention and permeation effect that passively

targets some tumors, these modified nano-emulsions can be an alternative to active targeting technologies (ligand / receptor based technologies) to cross the tumor cell membrane once they reach the tumor microenvironment.

### 3.5. *In vivo* imaging

This last section will investigate the impact of the surface modification on the fate of the nano-emulsion in mice after i.v. administration. This study is performed through a longitudinal study of the biodistribution. X-ray imaging is a non-invasive modality that allows a three-dimensional monitoring of the nano-carrier location in the body of the animal. This modality was chosen for this study. It involves modifying the formulation including X-ray contrast agent. For this formulation, a model lipid, oleic acid, has been modified by grafting triiodophenyl according to the novel protocol reported in Fig. 6 (a), giving rise to 2,4,6-triiodophenyl oleate (TIPhO). TIPhO is a lipophilic molecule containing the outstanding proportion of 51.7 wt.% of iodine, and replaced Labrafac<sup>®</sup> WL 1349 as oily phase in the nano-emulsification process (described above in the *Method* section), as illustrated in Fig. 6 (a). The theoretical iodine concentration in nano-emulsions, calculated from the formulation parameters reached 11.5 wt.%, which is effectively correlated by the calibration by X-ray attenuation properties reported in Fig. 6 (b), overall around 130 mg/mL. The calibration is done with a commercial iodinated contrast agent (XenetiX<sup>®</sup>), scanning the tubes in micro-CT scanner. Such an iodine concentration is largely higher than commercial products (*e.g.* 55 mg/mL for Fenestra<sup>®</sup>) and comparable with the other iodinated nano-emulsions we recently reported from triglycerides, monoglyceride, or  $\alpha$ -tocopherol [11].

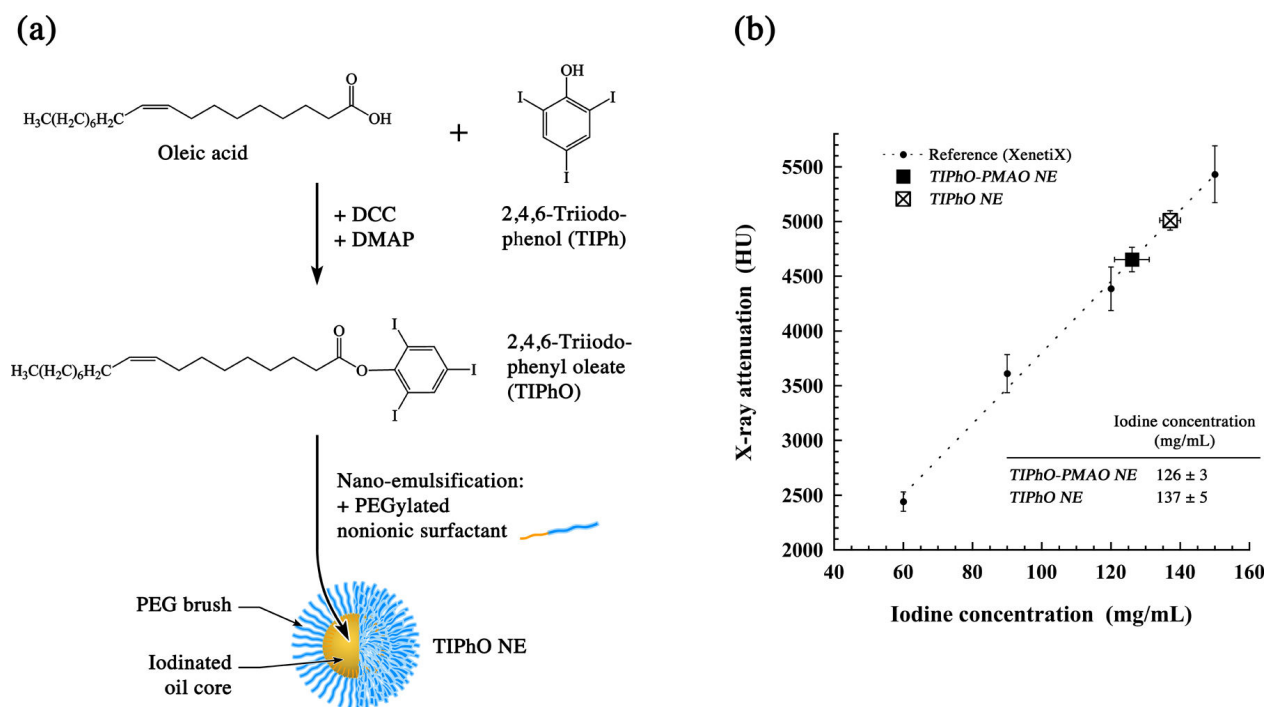


**Figure 6:** (a) Synthesis and formulation of the contrasting agent: 2,4,6-triiodophenyl oleate (TIPhO). (b) *In vitro* characterization of the X-ray contrasting properties of the nano-emulsions without PMAO (TIPhO NE), and with PMAO at 1.5 wt.% in oil (TIPhO-PMAO NE).

The next step is the surface modification of such iodinated nano-emulsions exactly as it was done up to now with Labrafac<sup>®</sup> WL 1349 nano-emulsions. The formulation was performed with PMAO at 1.5 wt.% in oil, *i.e.* at concentrations higher than the ones where cellular uptake occurs (disclosed in Fig. 5). Both TIPH<sub>O</sub> nano-emulsions (*TIPH<sub>O</sub> NE*) and TIPH<sub>O</sub>-PMAO nano-emulsions (*TIPH<sub>O</sub>-PMAO NE*) showed a size distribution centered on 50 nm, whereas, as expected, their  $\zeta$  potentials were measured at -2.5 mV and -39.7 mV, respectively. Both *TIPH<sub>O</sub> NE* and *TIPH<sub>O</sub>-PMAO NE* were intravenously administrated to mice, and regularly scanned during 24 days. Compared to the values of X-ray attenuation before injection, the contrast enhancement was followed-up in selected regions of interest (ROI): heart, liver, spleen and kidneys, *i.e.* constituting the main elimination pathway of foreign species in bloodstream, in healthy mice. The results presented in Fig. 7 overall show a behavior in the same line that the one observed for nano-emulsions: (i) a prolonged circulation in blood pool, (ii) liver and spleen uptakes, and (iii) a gradual kidneys elimination. However, a very significant difference arose between the nano-emulsions with and without PMAO.

**Figure 7:** *In vivo* micro-CT imaging, longitudinal studies of the biodistribution of O-TIB nano-emulsions after i.v. administration in mice. Nano-emulsions without PMAO (*TIPH<sub>O</sub> NE*) and with PMAO 1.5 wt.% in oil (*TIPH<sub>O</sub>-PMAO NE*) were compared; n = 3 for each type of nano-emulsion. (left) Quantitative analysis of the X-ray attenuations values, the ROIs were placed in heart, liver, spleen and kidneys. (right) Maximum intensity projection at representative times: coronal sections of mice post-injection and 6 hours after injection (showing heart and liver), and transverse sections 6 hours after injection (showing spleen). Arrows on the graphs indicate the correspondences for 6 hours.

The different experimental curves, *i.e.* blood elimination, liver/spleen accumulation, and liver/spleen elimination were fitted with the following classical mono-compartmental exponential Eq. 2, 3 and 4, respectively:

$$\Delta\text{HU}(t) = \Delta\text{HU}(t_0) \times e^{-k_1 t} \quad (2)$$

$$\Delta\text{HU}(t) = \Delta\text{HU}(t_0) + \Delta\text{HU}_\infty \times (1 - e^{-k_2 t}) \quad (3)$$

$$\Delta\text{HU}(t) = \Delta\text{HU}(t') \times e^{-k_3(t-t')} \quad (4)$$

where  $t_0$  is the initial time (injection time),  $k_1$ ,  $k_2$  and  $k_3$  are the blood elimination rate, liver / spleen accumulation rate, and liver / spleen elimination rate, respectively.  $\Delta\text{HU}_\infty$  is the contrast enhancement at the end of the accumulation process (for  $t$  trending to infinite), and  $t'$  is the time when the elimination in liver or spleen begins. The values of these parameters are reported in Table 1, where  $\Delta\text{HU}_{\text{max}} = \Delta\text{HU}(t_0) + \Delta\text{HU}_\infty$ . Maximum intensity projections are reported in Fig. 7 (left) showing mice sections (coronal and transverse) post-administration and 6 hours after injection, as representative times. Regarding the blood clearance, as observed *in vitro* (Fig. 6), it appears that the initial values of the contrast enhancement  $\Delta\text{HU}(t_0)$  slightly differ from 425 HU to 373 HU for blank and modified nano-emulsions, respectively. This difference has not a real importance for their imaging properties since both values are very high. However, the kinetics reveals the first difference between the curves, with a  $t_{1/2}$  dropping from 8.2 h to 6.0 h with the presence of PMAO. This is confirmed by the blood elimination rates  $k_1$  that are increased from  $0.084 \text{ h}^{-1}$  to  $0.116 \text{ h}^{-1}$ . On the other hand, while for the blank nano-emulsion, the liver accumulation rate  $k_2$  of the is equal to  $0.140 \text{ h}^{-1}$  and there is no accumulation in spleen, the ones corresponding to the modified nano-emulsions are much higher,  $0.520 \text{ h}^{-1}$  and  $0.523 \text{ h}^{-1}$  for liver and spleen, respectively. This corroborates the premature blood clearance seen above, and clearly discloses the impact of the droplet surface modification on the pharmacokinetics. Consequences are visible on the values of  $t'$ , when, without polymer, the maximum signal is reached in liver at 24 h, while with polymer it is 3 h in liver and 6 h in spleen. The fact that in one case the droplets accumulate in spleen and in the other case there is no accumulation is likewise an important clue on the impact of the surface charge on the behavior *in vivo*. Finally, unlike the accumulation rates in liver or spleen, the kinetics of elimination revealed by  $k_3$  is very similar whatever the organ concerned.

**Table 1:** Pharmacokinetics parameters for iodinated nano-emulsions without PMAO (*Blank NE*) and with PMAO 1.5 wt.% in oil (*Modified NE*).

	TIPhO NE			TIPhO-PMAO NE		
	Blood	Liver	Spleen	Blood	Liver	Spleen
$\Delta\text{HU}(t_0)$ (HU)	425	89	103	373	82	92
$k_1$ ( $\text{h}^{-1}$ )	0.084	–	–	0.116	–	–
$t_{1/2}$ (h)	8.2	–	–	6.0	–	–
$\Delta\text{HU}(t_{1/2})$ (HU)	213	–	–	185	–	–
$\Delta\text{HU}_{\text{max}}$ (HU)	–	215	–	–	249	197
$k_2$ ( $\text{h}^{-1}$ )	–	0.140	–	–	0.520	0.523
$t'$ (h)	–	24	–	–	3	6
$k_3$ ( $\text{h}^{-1}$ )	–	0.0083	0.0172	–	0.0080	0.0071

In the same line than the results observed above for cellular uptake, the surface modification of the droplets has a significant and important impact on both the pharmacokinetics and biodistribution. It is noteworthy that *TIPhO-PMAO NE* displayed an enhanced uptake by spleen compared to *TIPhO NE*. This difference can be attributed to different pattern of recognition towards the immune system. Such a significant difference in spleen uptake was previously reported [11] and attributed to the specific recognition by the macrophages, trapping the nano-

carriers in the spleen for elimination. In the present study, the singular difference of accumulation in spleen and liver are likely due to a similar reason, the modification of the surface composition and charge increases their recognition and allows a modification of their final destination, 4 and 8 times faster than blank nano-emulsions (values of  $t'$ ), for liver and spleen, respectively. This evidently explains the shift of the blood clearance half-lives observed. This difference is illustrated with the two-dimensional projections of the intensity (Fig. 7), where the image treatment is strictly the same between all pictures to allow a visual comparison of the X-ray attenuation. The coronal section post-injection showed in both cases an important contrast in heart, the ventricles were clearly visible along with the main veins and arteries. The contrasted points in liver were the organ vascularization. After 6 hours, the difference between neutral and negatively charged droplets was visible; the contrast in liver rose slowly in the first case while it is pronounced in the second case to the detriment of the blood. Finally, the transverse section revealed the contrast in spleen, only visible with the modified nano-emulsions.

Besides the novelty of the chemical concept for bringing to the surface of the nano-emulsion droplets a number of reacting groups, this study shows that the modification of their surface composition and/or charge lead to significant impacts on both their cellular uptake and their behavior *in vivo*. Accordingly, we pointed out a very interesting question to be addressed when surface functionalization technologies are developed: what is the impact of the surface modification itself (necessary for ligand grafting) on the biodistribution and pharmacokinetics? Addressing this problem is relatively heavy, all the more so since the fate *in vivo* can be also changed after grafting of functional groups. For example, chemical reactions involving the carboxylate groups will reduce the global number of negative charge on the surface, and potentially reduce the effect herein observed. On the other hand, it could be fundamental for a global optimization of the process, to understand the impact and compatibility of any surface modification with the aimed applications.

#### 4. Conclusion

This study proposed to study the decoration of the surface of nano-emulsions with carboxylates. Since emulsion interfaces are dynamic, the chemical modification of such a system is by definition a challenge since the adsorbed functional species or ligands can potentially desorb, according to the adsorption / desorption equilibriums. This phenomenon actually limits the possible interfacial concentration and stability of potentially grafted entities. Herein we circumvent these limitations using a lipophilic polymer, PMAO, able to hydrolyze at the interface, giving rise to a strong anchorage and decoration of the droplets with numerous carboxylates available for further functionalization. The PMAO hydrolysis at oil / water interface was studied and disclosed by physico-chemical methods, surface tension and  $\zeta$  potential measurements, and quantified by an adapted colorimetric methods. Once in contact with cells in culture, when native nano-emulsions droplets do not present interactions, the modified droplets exhibit strong interactions and, via endocytosis, end up inside the cells. This was correlated *in vivo* with the longitudinal study of the biodistribution, showing an enhanced liver and spleen uptake, up to reducing the half-life of blood clearance of two hours. In this work we establish the proof of concept of a new method for functionalizing lipid droplets, but as well, we point out that surface modification even at intermediate state without ligands, can have a significant impact on their behavior towards living systems. It is noteworthy to mention here that we overcame the

---

limitations of lipid functionalization before [X], as we successfully modified lipid nanodroplets with amino groups anchored on their surface thanks to aminosilane molecule APTES which is completely different method than the current protocol, and followed by their functionalization with dye model ligand obtaining 41% grafting efficiency.

## 5. Acknowledgments

*In vivo* imaging of this study was performed on the imaging facilities of CERMEP - Imagerie du vivant, Bron, F-69677, France, imaging facilities. The authors thank the technical staff of the platform. As we thank Ministry of Higher Education and Scientific Research of Egypt for its financial supported to Mohamed Attia.

## 6. References

- [1] Matsumura Y, Maeda H. A new concept for macromolecular therapeutics in cancer chemotherapy: Mechanism of tumor-tropic accumulation of proteins and the antitumor agent smancs. *Cancer Res.* 1986;46:6387-92.
- [2] Torchilin V. Tumor delivery of macromolecular drugs based on the EPR effect. *Adv Drug Deliv Rev.* 2011;63:131-5.
- [3] Maeda H, Sawa T, Konno T. Mechanism of tumor-targeted delivery of macromolecular drugs, including the EPR effect in solid tumor and clinical overview of the prototype polymeric drug SMANCS. *J Control Release.* 2001;74:47-61.
- [4] Jain R, Stylianopoulos T. Delivering nanomedicine to solid tumors. *Nat Rev Clin Oncol.* 2010;7:653-64.
- [5] Minko T, Kopeckova P, Pozharov V, Jensen KD, Kopecek J. The influence of cytotoxicity of macromolecules and of VEGF gene modulated vascular permeability on the enhanced permeability and retention effect in resistant solid tumors. *Pharm Res.* 2000;17:505-14.
- [6] Bouchaala R, Mercier L, Andreiuk B, Mély Y, Vandamme TF, Anton N, et al. Integrity of lipid nanocarriers in bloodstream and tumor quantified by near-infrared ratiometric FRET imaging in living mice. *J Control Release.* 2016;in press.
- [7] Anton N, Benoit J-P, Saulnier P. Design and production of nanoparticles formulated from nano-emulsion templates—A review. *J Control Release.* 2008;128:185-99.
- [8] Anton N, Vandamme TF. The universality of low-energy nano-emulsification. *Int J Pharm.* 2009;377:142-7.
- [9] Li X, Anton N, Zuber G, Zhao M, Messaddeq N, Hallouard F, et al. Iodinated  $\alpha$ -tocopherol nano-emulsions as non-toxic contrast agents for preclinical X-ray imaging. *Biomaterials.* 2013;34:481-91.
- [10] Anton N, Vandamme TF. Nanotechnology for Computed Tomography: A Real Potential Recently Disclosed. *Pharm Res.* 2014;31:20-34.
- [11] Attia MF, Anton N, Chipper M, Akasov R, Anton H, Messaddeq N, et al. Biodistribution of X-ray iodinated contrast agent in nano-emulsions is controlled by the chemical nature of the oily core. *ACS Nano.* 2014;8:10537-50.

- [12] Hallouard F, Anton N, Choquet P, Constantinesco A, Vandamme TF. Iodinated blood pool contrast media for preclinical X-ray imaging applications – A review. *Biomaterials*. 2010;31:6249-68.
- [13] Hallouard F, Briançon S, Anton N, Li X, Vandamme TF, Fessi H. Influence of diblock copolymer PCL-mPEG and of various iodinated oils on the formulation by the emulsion-diffusion process of radiopaque polymeric nanoparticles. *J Pharm Sci*. 2013;102:4150-8.
- [14] Hallouard F, Briançon S, Anton N, Li X, Vandamme TF, Fessi H. Iodinated nano-emulsions as contrast agents for preclinical X-ray imaging, impact of the free surfactants on the pharmacokinetics. *Eur J Pharm Biopharm*. 2013;83:54-62.
- [15] Li X, Anton N, Zuber G, Vandamme TF. Contrast agents for preclinical targeted X-ray imaging. *Adv Drug Deliv Rev*. 2014;76:116-33.
- [16] Attia MF, Anton N, Akasov R, Chiper M, Markvicheva E, Vandamme TF. Biodistribution and Toxicity of X-Ray Iodinated Contrast Agent in Nano-emulsions in Function of Their Size. *Pharm Res*. 2016;33:603-14.
- [17] Jakhmola A, Anton N, Vandamme TF. Inorganic nanoparticles based contrast agents for X-ray computed tomography. *Adv Healthc Mater*. 2012;1:413-31.
- [18] Klymchenko AS, Roger E, Anton N, Anton H, Shulov I, Vermot J, et al. Highly lipophilic fluorescent dyes in nano-emulsions: towards bright nonleaking nano-droplets. *RSC Adv*. 2012;2: 11876-86.
- [19] Kilin V, Anton H, Anton N, Steed E, Vermot J, Vandamme TF, et al. Counterion-enhanced cyanine dye loading into lipid nano-droplets for single-particle tracking in zebrafish. *Biomaterials*. 2014;35:4950-7.
- [20] Hirsjärvi S, Dufort S, Bastiat G, Saulnier P, Passirani C, Coll J-L, et al. Surface modification of lipid nanocapsules with polysaccharides: From physicochemical characteristics to in vivo aspects. *Acta Biomater*. 2013;9:6686-93.
- [21] Bourseau-Guilmain E, Béjaud J, Griveau A, Lautram N, Hindré F, Weyland M, et al. Development and characterization of immuno-nanocarriers targeting the cancer stem cell marker AC133. *Int J Pharm*. 2012;423:93-101.
- [22] Di Corato R, Quarta A, Piacenza P, Ragusa A, Figuerola A, Buonsanti R, et al. Water solubilization of hydrophobic nanocrystals by means of poly(maleic anhydride-alt-1-octadecene). *J Mater Chem*. 2008;18:1991-6.
- [23] Nguyen KC. Quantitative analysis of COOH-terminated alkanthiol SAMs on gold nanoparticle surface. *Adv Nat Sci:Nanosci Nanotechnol*. 2012;3:45008-13.
- [24] Hennig A, Borchering H, Jaeger C, Hatami S, Würth C, Hoffmann A, et al. Scope and limitations of surface functional group quantification methods: exploratory study with poly(acrylic acid)-grafted microand nanoparticles. *J Am Chem Soc*. 2012;134:8268-76.

# *Supplementary part*

## **1. The goal:**

This point aims to design positively charged nano-emulsions in order to study and compare them with the neutral and negative charge nanoemulsions in function their physico-chemical properties as well as *in vitro* cellular internalization experiments.

## **2. General method of preparation:**

According to the procedure described above in chapter 2.2, two negatively charged nanoemulsions were fabricated, coated by PMAO polymeric shell (0.5, 1 wt.% of PMAO) containing carboxylic groups on their surface. Different volumes of chitosan (low Mwt = 50,000-190,000 Da) of concentration (40mg/mL) then were added to the prepared NE, and homogenized by magnetic stirring for 30 minutes at room temperature. The chitosan bearing amino groups (positive charge) deposited on the carboxylic groups *via* electrostatic forces, forming finally external shell (positively charged) on the droplet surface.

## **3. Results and discussion:**

### **3.1. Hydrodynamic diameter**

Dynamic light scattering (DLS) determined the hydrodynamic diameter of the double-layered nanoemulsions. Two nano-emulsions were prepared beforehand based on the carboxylic polymer, 0.5 wt.% and 1 wt.% PMAO, and then various amounts of chitosan solution were added. The results demonstrated a significant difference of the size before and after creating the chitosan layer. Globally, both size and PDI increased as describes in Figure 1.

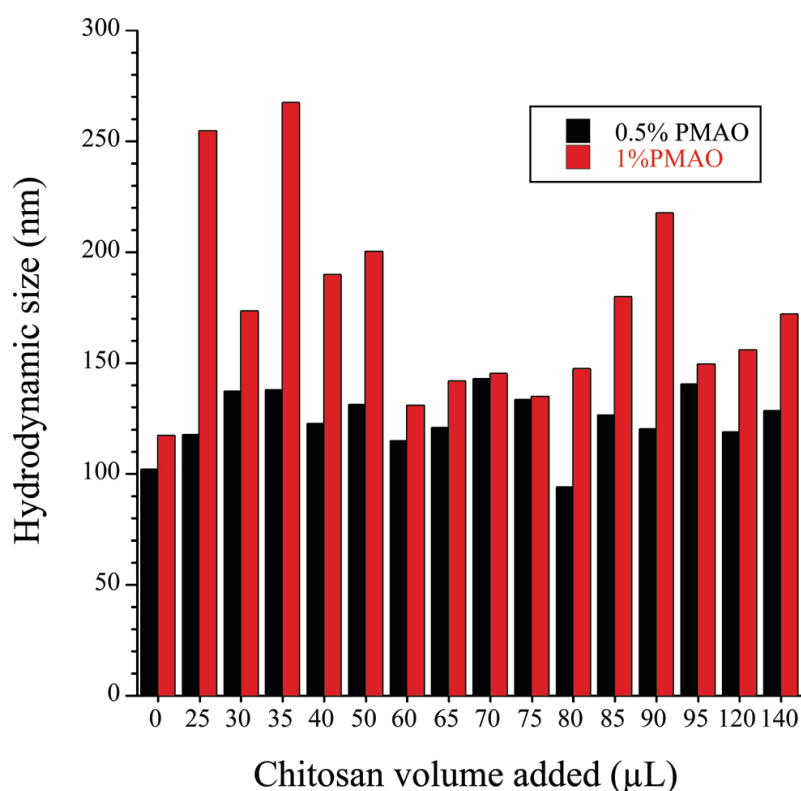


Figure 1: DLS measurements for various concentrations of chitosan deposited to NE1 of 0.5 wt.% PMAO (black column) and NE2 of 1 wt.% PMAO (red column).

### 3.2. Zeta potential

Surface charge is considered one of the important parameters affecting the biological behavior of the nanoparticles. Zeta potential (mV) of a series of the formulated nanoemulsions were determined by zetasizer instrument. The results are clearly illustrated in Figure 2 showing almost gradual increasing of the surface charge according to the amounts added of chitosan solution. Meanwhile, the two NEs of 0.5%, 1% of PMAO have comparable charge values in low concentrations of chitosan, and completely varied at higher chitosan concentrations that is to say at 1% PMAO of NE can interact with higher amount of amino groups of chitosan than 0.5% PMAO.

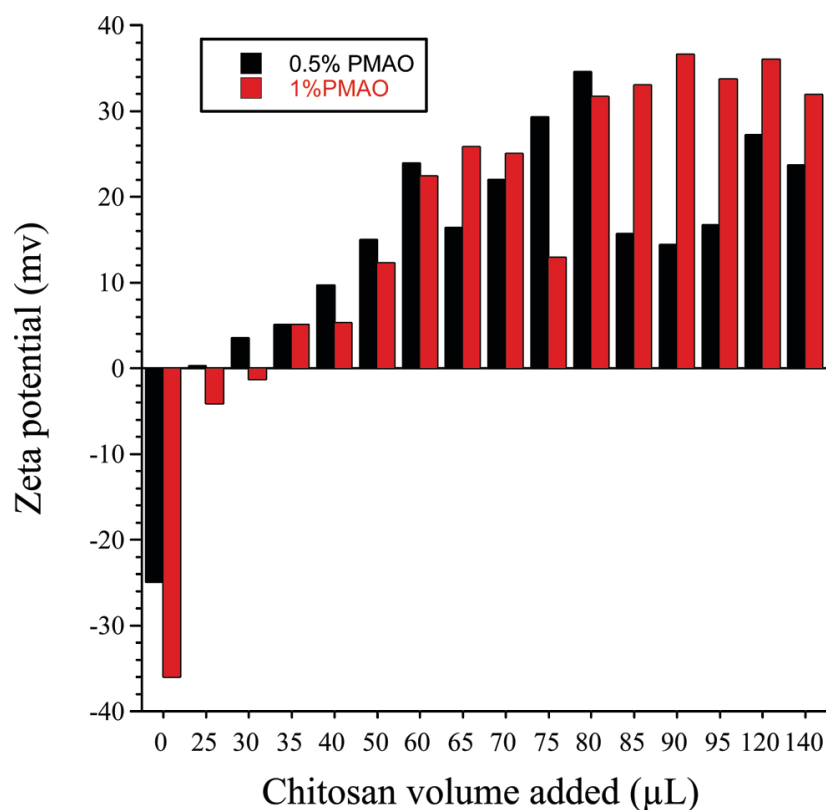


Figure 2: Measurements of zeta potentials by zetasizer to different nanoemulsions: NE1, composed of several concentrations of chitosan layer deposited to 0.5 wt.% of PMAO (black column) and NE2; corresponds to the amounts of chitosan deposited to 1wt.% of PMAO (red column).

### 3.3. Cellular uptake experiments

In order to investigate the positive charge NEs to penetrate the HeLa cell, we performed the cellular uptake study as exactly explained above in chapter 2.2. The results of the NEs coated by chitosan polymer behave a negative response towards the cell penetration. In Figure 3, the confocal microscopic images of the two NEs showed that there is no penetration of the NEs (red spots) into the nucleus or the cell membrane and still stick to the glass (black color).

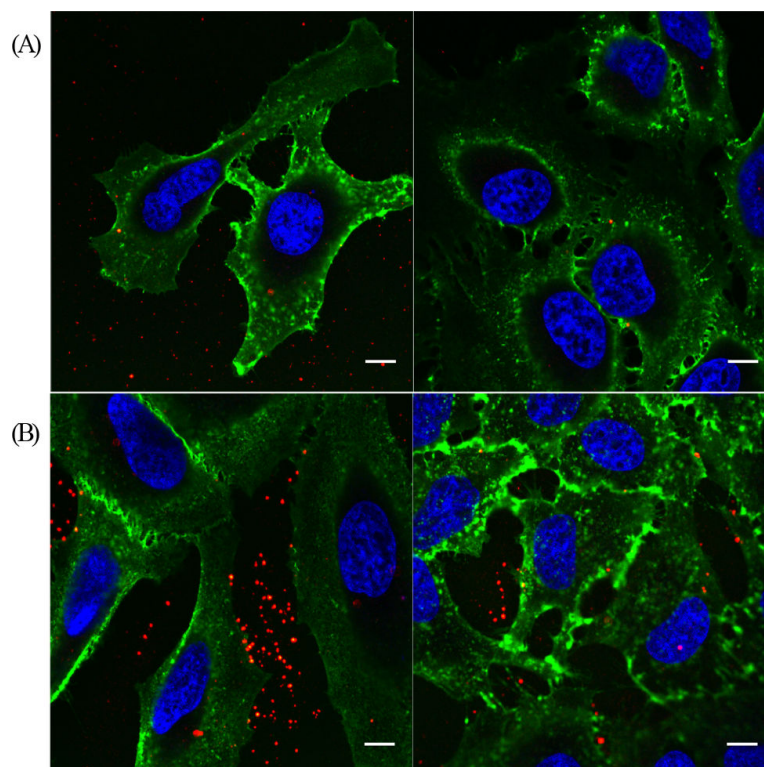


Figure 3: Confocal microscope images of *in vitro* cellular uptake experiments of the positive charge nanoemulsions against HeLa cell. (A): 0.5 wt.% of PMAO nanoemulsions coated with chitosan layer. (B): 1 wt.% of PMAO nanoemulsion coated with chitosan layer. Blue color: nucleus, green color: cell membrane, red color: nanoemulsion, and black color: glass.

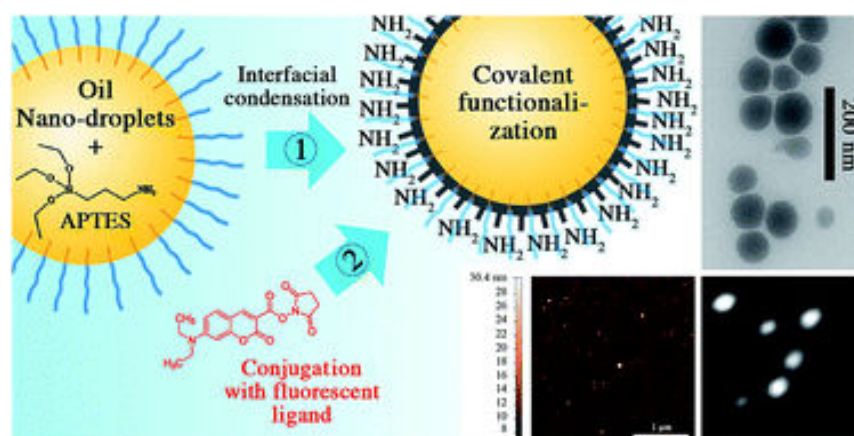
#### 4. Conclusion

To conclude, the three different nanoemulsions (positive, negative, neutral) were fabricated to examine the effect of the surface charge of the particles on the *in vitro* uptake to the cells and thus the *in vivo* biodistribution and the cytotoxicity profiles. The given results ensured that the highly negative particles internalize the cells through endocytosis, positively charged ones tend to stick to the glass, and the non charged particles do not interact with cells and glass.



## Chapter 2.3 : Functionalization of nano-emulsions with an amino-silica shell at the oil–water interface

We succeeded to functionalize the nano-emulsion droplets by silica shell terminated by active groups ( $\text{NH}_2$ ). Aiming to generate new promising candidate to conjugate with some ligands to actively target the desired lesions or cells. We proposed new strategy to formulate the nano-emulsions constitutes of medium chain triglycerides (Labrafac WL<sup>®</sup>) oil mixed well with the lipophilic silica precursor aminopropyltriethoxysilane (APTES), then homogenized with Cremophore ELP<sup>®</sup> and water. Then, APTES hydrolysis was mediated by ultrasound, inducing the silane monomer polycondensation localized on the droplets' surface forming rigid silica coating containing amino groups in the oil/water interface. DLS and TEM instruments assessed the size and the morphology of the nano-emulsion. The available amino groups that present on the surface were quantified by means of fluorescamine dye method, using spectral tools (spectrophotometry and spectrofluorometry) obtaining finally a large number of reactive sites per capsule (up to  $9 \times 10^4$ ,  $\sim 2$  amino groups per  $\text{nm}^2$ ). The last step was related to the grafting of a model ligand through reaction of an activated carboxylic acid (coumarin blue dye) on the amine functions exist onto the nanocapsule surface. The grafting efficiency was around 41% and the conjugated molecules were characterized by several spectroscopic and microscopic techniques.





CrossMark  
 click for updates

Cite this: *RSC Adv.*, 2015, 5, 74353

## Functionalization of nano-emulsions with an amino-silica shell at the oil–water interface†

Mohamed F. Attia,<sup>abc</sup> Nicolas Anton,<sup>\*ab</sup> Redouane Bouchaala,<sup>ade</sup> Pascal Didier,<sup>ad</sup> Youri Arntz,<sup>ad</sup> Nadia Messaddeq,<sup>f</sup> Andrey S. Klymchenko,<sup>ad</sup> Yves Mély<sup>ad</sup> and Thierry F. Vandamme<sup>ab</sup>

Nano-emulsions are very promising nano-carriers with high potential for loading lipophilic drugs. However, the surface of oil nano-droplets is a dynamic oil/water interface stabilized by surfactants, and its chemical modification to graft ligands is highly challenging. In this study we developed a new protocol for modification of the nano-droplets surface through a silica shell terminated by amine functions. It enabled preparation of nanocapsules of 65, 85 and 120 nm diameters with a surface coverage of ca. 2 amino groups per nm<sup>2</sup>. The nanocapsule surface was then functionalized (41% efficiency) by a model fluorescent ligand (coumarin blue) with a carboxylic function. The evidence for the successful grafting was provided by spectrofluorometry, Förster resonance energy transfer, atomic force microscopy coupled with fluorescence imaging and fluorescence correlation spectroscopy. This simple protocol for surface functionalization of the liquid/liquid interface of lipid droplets may constitute a real advance regarding potential applications that need efficient decoration of droplets with ligands.

Received 30th June 2015  
 Accepted 26th August 2015

DOI: 10.1039/c5ra12676b

[www.rsc.org/advances](http://www.rsc.org/advances)

## Introduction

Nanomedicines for therapeutics and diagnosis purposes always have a common aim: bringing the drugs to the specific target. Targets are, for instance, organs, lymph nodes, cancer tumors, and the accumulation mechanisms rely on the targets and can follow passive or active targeting. In cases of liver, spleen, or in some case tumor targeting, passive accumulation mechanisms can be sufficient to bring to the desired site a significant amount of active molecules. These passive mechanisms are driven by the uptake and metabolization of the nanoparticle systems that are undertaken by the liver and/or the spleen, depending on the chemical nature of the carrier.<sup>1</sup> In case of tumors, the passive accumulation results from the enhanced permeation and retention effect (EPR)<sup>2</sup> that is related to the

half-life of the nanomedicines in the bloodstream. On the other hand, the selective accumulation in targets can also be improved by an active mechanism, involving ligand/receptor interactions.<sup>3</sup> This approach also depends on the circulation time in blood of the nanoparticles (NPs), in order to ensure efficient ligand/receptor interactions. The higher the half-life, the better the chance of their interactions. Ligands grafted onto the NPs surface recognize the receptors and, as a result, NPs concentrate their active principles at the targeted site. Many ligands have already been proven to be effective for cancer active targeting and they can be grafted onto the surface at high concentrations. Typical examples are cyclic pentapeptides c(RGDfk) that, when grafted on the surface of polymeric PLGA-PEG NPs (poly(D,L-lactic-co-glycolic acid)-*block*-polyethylene glycol), showed increasing *in vivo* accumulation in cancer cells.<sup>4</sup> The co-encapsulation of anticancer active molecules results in specific treatment of the tumor. Other peptides like bombesin grafted onto gold NPs have shown an *in vitro* and *in vivo* cancer cell specificity allowing detection of tumors cells by X-ray imaging owing to the gold NPs accumulation.<sup>5</sup> E-selectin peptides grafted on liposome surface,<sup>6</sup> or 2-deoxy-D-glucose onto gold NPs<sup>7</sup> have also shown interesting accumulation in cancer cells due to their enhanced glucose consumption. Specific targeting of pancreatic ductal adenocarcinoma can be performed through plectin-1 targeted peptides (PTP) at the surface of hybrid iron oxide/polymeric NPs.<sup>8</sup> Another approach relies on the use of specific antibodies targeting cancer cells receptors, like anti-Her2 (ref. 9) or anti-CD4.<sup>10</sup> Different other types of ligands could also be efficient for active targeting of

<sup>a</sup>University of Strasbourg, Faculty of Pharmacy, 74 route du Rhin, 67401 Illkirch Cedex, France

<sup>b</sup>University of Strasbourg, CNRS UMR 7199, Laboratoire de Conception et Application de Molécules Bioactives, équipe de Pharmacie Biogalénique, route du Rhin No.74, F-67401 Illkirch Cedex, France. E-mail: nanton@unistra.fr; Fax: +33 3 68 85 43 06; Tel: +33 3 68 85 42 51

<sup>c</sup>National Research Center, P. O. 12622, Cairo, Egypt

<sup>d</sup>CNRS UMR 7213, Laboratoire de Biophotonique et Pharmacologie, 74 route du Rhin, 67401 Illkirch Cedex, France

<sup>e</sup>Laboratory of Photonic Systems and Nonlinear Optics, Institute of optics and fine mechanics, University of Setif 1, 19000 Algeria

<sup>f</sup>IGBMC (Institut de Génétique et de Biologie Moléculaire et Cellulaire), Inserm U964, CNRS UMR7104, Université de Strasbourg, 1 rue Laurent Fries, 67404 Illkirch, France

† Electronic supplementary information (ESI) available. See DOI: 10.1039/c5ra12676b



tumors such as folic acid for which receptors are overexpressed in gastric cancer cells<sup>11</sup> or cationic polymers that target sialic acid overexpressed on colonic malignant tissues.<sup>12</sup>

These examples clearly emphasized that specific targeting is efficient only if the surface concentration is high enough to provide a significant response or contrast *in vivo*. Active targeting is generally performed with polymeric or inorganic (particularly gold) NPs, because the surface chemistry performed on these systems is facile and efficient, providing a high number of available functional groups on the NP surface, and a high stability after ligand grafting. In the case of polymeric NPs, the functional groups (like carboxylic acids<sup>3,6,4,13</sup>) are part of the polymer constituting the NP matrix. Therefore a large number of sites are available for ligands, which after grafting are strongly anchored onto the NP surface. Functionalization of gold NPs is generally performed through strong thiol/gold interactions in order to decorate the gold NP by thiol-polyethylene glycol-COOH molecules.<sup>10,14</sup> In this case also, the reactive groups are strongly anchored to the NP core, presenting a high number of available reactive groups at the interface. Generally, the simple and efficient surface functionalization is one of the main advantages of polymeric<sup>15</sup> and inorganic NPs for active targeting strategies. In contrast, one of their main drawbacks is their limited capability in encapsulating active molecules, drugs or contrast agents, into the polymeric matrix or within the shell of inorganic NPs.

Other important family of nanomedicines is lipid nano-droplets, so-called nano-emulsions or nanocapsules. They are kinetically stable class of emulsions, in contrast to micro-emulsions that are thermodynamically stable.<sup>16</sup> Nano-emulsions can be easily formulated and they enable high loading levels of guest molecules in their core. We recently obtained<sup>17</sup> lipid nano-emulsions encapsulating in their lipid core, fluorescent probes with concentrations as high as 8 wt%, opening new possibilities for single-particle tracking *in vivo*.<sup>17b</sup> In addition, we formulated nano-emulsions as lipid reservoirs containing more than 50 wt% of iodine, and thus highly efficient for X-ray imaging.<sup>1,18</sup> In addition to iodine, we co-solubilized in the same droplets significant amounts of a fluorescent dye, which allowed monitoring their cellular uptake.<sup>1</sup> Nano-emulsions are also prospective for co-encapsulating drugs and contrast agents, and following their actual dosage in real time by imaging. In contrast, the active targeting of nano-emulsions is not presently well developed, due the technical difficulties related to the structure of the nano-emulsions. Indeed, oil droplets are stabilized by a monolayer of nonionic surfactants, so that there is no reactive groups for conjugation with ligands, and no possibilities for covalent anchoring of reactive chemical species as the liquid/liquid interface is a dynamic medium. Strategies such as post-insertion at the oil/water interface of reactive function-bearing surfactants, like DSPE-PEG 2000-maleimide (1,2-distearoyl-*sn*-glycero-3-phosphoethanolamine-*N*-[maleimide (polyethylene glycol)-2000])<sup>2b,19</sup> were developed, but the obtained surface modification is still largely below that of polymeric or inorganic NPs. The DSPE-PEG 2000-maleimide molecules are inserted in the surfactant monolayer, by incubating the lipid nano-droplets with a

micellar solution of these molecules. However, in this approach the interfacial concentration is not controlled and is significantly lower compared to polymeric or inorganic NPs. In addition, the interfacial adsorption is definitively weaker than covalent bonds, and can even be reversible leading to ligand release into the biological medium.

In the present study, we propose a new and simple method to functionalize lipid nano-droplets. The idea is first to formulate nano-emulsions, and second to build amino-silica shell at the droplet interface. As a result, covalent grafting of ligands to the lipid nanocarriers becomes possible. The silica precursor, (3-aminopropyl)triethoxysilane (APTES), beforehand solubilized in the oil core of the nano-emulsion droplets, reacted by ultrasounds with the aqueous phase at the droplets interface to generate the silica shell specifically at the interface. A significant part of the APTES' NH<sub>2</sub> groups finally appears decorating the nanocapsules, oriented towards the aqueous bulk phase. We quantified the reactive NH<sub>2</sub> groups by using the fluorescamine-based method, and further characterized the physicochemical properties of the functional nanocapsules by dynamic light scattering (DLS), transmission electron microscopy (TEM), and atomic force microscopy coupled with fluorescence microscopy (AFM-Fluo). Moreover, as a proof of concept, we grafted a fluorescent model ligand presenting activated COOH functions (coumarin blue dye) that react with the amino groups onto the capsules. Thus, we describe a robust approach to cover lipid droplets with a solid silica shell that enables their covalent functionalization.

## Experimental section

### Materials

The oil phase used in the preparation of nano-emulsions was exclusively Labrafac® WL 1349 (Gattefossé S.A., Saint-Priest, France), a mixture of capric and caprylic acid triglycerides as a model of parenteral-grade oil. Non-ionic surfactant (Kolliphor ELP®) from BASF (Ludwigshafen, Germany) was a kind gift from Laserson, Etampes, France. Kolliphor ELP (formerly named "Cremophor ELP") is a parenteral-grade non-ionic surfactant made by reacting ethylene oxide to castor seed oil at a molar ratio of 35.<sup>20</sup> 3-Aminopropyltriethoxy silane (APTES), fluorescamine, ethanolamine, 7-(diethylamino) coumarin-3-carboxylic acid *N*-succinimidyl ester (activated coumarin blue), Nile red (NIR), dry dioxane, dry dimethylformamide (DMF), and dimethylsulfoxide (DMSO) were purchased from Sigma. All chemicals used were of analytical grade and used without modification. Fetal bovine serum (FBS) was obtained from PAN Biotech (Aidenbach, Germany).

### Methods

#### Formulation of amino-decorated lipid nano-emulsions.

First, the silica monomer (APTES) is dissolved in the oil at different concentrations from 0.05 M to 0.5 M. This {oil + APTES} phase is then homogenized (vortex) 3 minutes at room temperature to obtain a transparent sample. It is then mixed with the non-ionic surfactant at different surfactant-to-oil



weight ratio, SOR = 40%, 50% and 60%, *i.e.* respectively  $\{w_{\text{surf.}} = 0.32 \text{ g}/w_{\text{oil.}} = 0.48 \text{ g}\}$ ,  $\{w_{\text{surf.}} = 0.40 \text{ g}/w_{\text{oil.}} = 0.40 \text{ g}\}$  and  $\{w_{\text{surf.}} = 0.48 \text{ g}/w_{\text{oil.}} = 0.32 \text{ g}\}$ . This mixture is homogenized (vortex) during one minute and heated at 60 °C for only one minute to avoid premature reaction of APTES. The mixture is then homogenized for 10 seconds, and finally mixed with the water phase (1.2 mL, to have 60 wt% of water in the final nano-emulsion), and homogenized (vortex) for 5 minutes. The suspension of nano-emulsion droplets is placed in a sonication bath (Thermo Scientific, T310/H) at 35 kHz during four minutes, and then homogenized (vortex) one minute, and this procedure is repeated 6 times. The result is a hydrolysis followed by a condensation of APTES, building the amino-functionalized silica capsule at the oil/water interface.

**Quantification of primary amines available on the nanocapsules.** The fluorescamine-based method is a common procedure used for the quantification of primary amines in proteins or peptides. We adapted it for the nano-emulsion system. Before reaction with primary amines, the fluorescamine is not fluorescent, but after reaction with primary amines fluorescamine appear yellow and show fluorescence properties with absorption/emission around 288 nm/490 nm, respectively. Stock solution of fluorescamine (10  $\mu\text{M}$  in anhydrous dioxane) was mixed with nano-emulsions and different APTES concentrations. The condensation reaction between fluorescamine and primary amines is very fast, being typically completed within seconds, so that the samples are mixed (vortex) for only one minute. Fluorescence intensities of the samples (diluted 30 times) were measured immediately after reaction by fluorescence spectroscopy. Each experiment was done in triplicate.

**Grafting of activated coumarin blue (7-(diethylamino) coumarin-3-carboxylic acid *N*-succinimidyl ester dye) on primary amines decorating the nanocapsules.** In this step, our aim was to show that activated coumarin blue that reacted with the available  $\text{NH}_2$  groups at the surface of the nanocapsules as well as to quantify the grafting efficiency. To this end, we used the quantification data of available  $\text{NH}_2$  groups given by the fluorescamine method described above, and we added in the bulk phase the desired amount of activated coumarin blue able to react with  $\text{NH}_2$ . Coumarin is a dye with absorption/emission at 394/473 nm, respectively. A stoichiometric ratio (1 : 1) was tested, corresponding to 25  $\mu\text{L}$  of the stock solution of activated coumarin blue (32 mM in dry dimethyl formamide) diluted in 1 mL of nano-emulsions having a concentration of available primary amines at 0.8 mM. The solution was then incubated for 24 hours under gentle stirring. Then, the sample was dialyzed through a 12 kDa membrane (Spectra/Por®, Spectrum Europe B.V., Breda, the Netherlands) for another 48 h, to ensure complete removal of excess unreacted dye (water changed three times). Finally, samples were characterized *via* fluorescence spectroscopy (see above), fluorescence correlation spectroscopy (FCS), single-particle measurement by TIRF microscopy, and atomic force microscopy coupled with fluorescence microscopy (AFM-Fluo).

#### Physicochemical characterization of nano-emulsions

**Dynamic light scattering, zeta potential measurements.** Size distributions and polydispersity indices (PDI) were measured by

DLS, along with zeta potentials, with a NanoZS Malvern apparatus (Malvern, Orsay, France). The helium/neon laser, 4 mW, was operated at 633 nm, with the scatter angle fixed at 173° and the temperature maintained at 25 °C. DLS data were analyzed using a cumulant-based method.

**Transmission electron microscopy.** The silica shell formed gives rise to a significant contrast in TEM. Therefore, samples were used without any staining agent and were diluted (1/100) with Milli-Q water. A drop of the suspension was placed on a carbon grid (carbon type-A, 300 mesh, copper, Ted Pella Inc. Redding, PA) and dried at 40 °C. Observations were carried out using a Philips Morgagni 268D electron microscope.

**Fluorescence spectroscopy.** Absorption and fluorescence spectra were recorded on a Cary 4000 spectrophotometer (Varian) and a Fluorolog (Jobin Yvon, Horiba) spectrofluorometer, respectively. Fluorescence emission spectra were recorded at room temperature with 365, 405 and 552 nm excitation wavelengths for fluorescamine-, coumarin blue-, and Nile red-loaded nanocapsules respectively. All fluorescence measurements were done using solutions with absorbance  $\leq 0.1$ . Förster resonance energy transfer (FRET) experiments were carried on nanocapsules decorated with coumarin blue as a donor. The acceptor dye Nile red was inserted into the oil core of the nanocapsules. FRET experiments were performed using the following preparation protocol: to 1 mL of MilliQ water we added 20  $\mu\text{L}$  of stock solution of Nile red (526  $\mu\text{M}$  in DMSO), and 7.5  $\mu\text{L}$  of stock solution of silica-covered nano-emulsion decorated with coumarin (after dialysis, concentration was 600  $\mu\text{M}$ ). Control measurements were done with: (i) Nile red-loaded nanocapsules with silica shell but without coumarin grafting, and (ii) nanocapsules decorated with coumarin that did not contain Nile red.

**Fluorescence correlation spectroscopy (FCS).** FCS measurements were done on a two-photon platform including an Olympus IX70 inverted microscope.<sup>21</sup> Two-photon excitation at 800 nm (15 mW laser output power) was provided by an Insight Deepsee femtosecond laser (Spectra-Physics). The measurements were performed in a 96 well plate, using a 200  $\mu\text{L}$  volume per well. The focal spot was set about 20  $\mu\text{m}$  above the bottom of the plate. Following the assumption that the NPs undergo a Gaussian diffusion in the two-photon excitation volume, the correlation function  $G(\tau)$ , calculated from the fluorescence fluctuations was fitted according to Thompson:<sup>22</sup>

$$G(\tau) = \frac{1}{N} \left(1 + \frac{\tau}{\tau_d}\right)^{-1} \left(1 + \frac{1}{s^2} \frac{\tau}{\tau_d}\right)^{-\frac{1}{2}}$$

where  $N$  is the mean number of fluorescent species within the two-photon excitation volume,  $\tau_d$  is the diffusion time and  $s$  is the ratio between the axial and lateral radii of the excitation volume. The NPs were diluted 200-fold from the originally prepared nano-emulsion. Using 6-carboxytetramethylrhodamine (TMR from Sigma-Aldrich) in water as a reference ( $D_{\text{TMR}} = 421 \mu\text{m}^2 \text{ s}^{-1}$ ),<sup>23</sup> the diffusion coefficient,  $D_{\text{exp}}$ , of the nanoparticle was calculated by:  $D_{\text{exp}} = \tau_{\text{d(capsules)}}/\tau_{\text{d(TMR)}} \times D_{\text{TMR}}$ , where  $\tau_{\text{d(capsules)}}$  and  $\tau_{\text{d(TMR)}}$  are the measured correlation times for the nanocapsules and TMR, respectively. The hydrodynamic diameter  $d$  of the nanocapsules was calculated with the Stokes-



Einstein equation:  $d = (2k_B T) / (6\pi\eta D_{\text{exp}})$ , where  $k_B$  is the Boltzmann constant,  $T$  is the absolute temperature (293 K) and  $\eta$  is the viscosity of the bulk (1 mPa s).

**Atomic force microscopy coupled with fluorescence microscopy.** The AFM/fluorescence microscope is a home-made association of an AFM composed of a SMENA Head driven by NTEGRA electronics (NT-MDT, Ru) combined with a wide-field fluorescence inverted microscope (Olympus IX-71). The fluorescence microscope is working in TIRF mode (Total Internal Reflection Fluorescence) with an oil immersion objective (NA = 1.49, 100 $\times$ ). A DPPS (cobolt) CW laser emitting at 488 nm was used to excite the NPs with a power of 3 W cm<sup>-2</sup>. Fluorescence imaging was performed using an EMCCD camera IXON 897 (ANDOR, UK). AFM images were acquired in the tapping mode, using a NSG03 (NT-MDT, RU) cantilever tip, with a spring constant of 0.9 N m<sup>-1</sup>, in liquid environment.

## Results and discussion

Nano-emulsions present many advantages such as high encapsulation efficiency,<sup>17</sup> stealth properties in the blood pool,<sup>1,18</sup> and also facile formulation.<sup>16,24</sup> Therefore, the challenge in the functionalization of oil droplets relies in the post-fabrication of a functional shell without affecting all these points. Several examples in the literature have shown the fabrication of a silica shell at the oil/water interface of emulsion droplets using TEOS (tetraethyl orthosilicate) as a silica precursor.<sup>25</sup> Here, we replaced TEOS for its derivative APTES bearing a primary amine as reactive group with the aim of building a silica shell decorated with NH<sub>2</sub> functions. As schematically illustrated in Fig. 1, APTES is introduced in the oil phase during the spontaneous nano-emulsification process, to allow its spreading over all the population of forming droplets.

In general, the condensation of a silica precursor with TEOS uses a low pH in bulk as a catalyst. However, alternative methods using ultrasounds instead of chemical catalyst have been developed,<sup>25a,26</sup> giving rise to the same TEOS interfacial condensation reaction. The advantage of the ultrasound approach is the possibility to use physiological pH and salt concentrations.

The obtained silica-treated nano-droplets, as imaged by TEM (Fig. 2(a)) appear as spherical structures with a diameter around 100–120 nm. In contrast, the control without silica (Fig. 2(b))

shows large and light oil puddles on the support, indicating that the droplets have merged during the drying process. Thus, while the sample drying on the carbon grid destroys the parent nano-droplets, the silica-treatment seems to strengthen the droplet structure. This corroborates the hypothesis that a silica framework or shell is built at the interface of the droplets. For the higher magnifications, we can note the malleability of the interface when the nanocapsules are stuck together, indicating that the nanocapsules are still deformable.

Next, we studied the size distribution, polydispersity, and zeta potential of the obtained nano-emulsions, as well as the impact of the silica concentration (APTES in oil) on these parameters. Fig. 3(a) shows a representative size distribution for the highest APTES concentration studied (0.5 M in oil). This distribution is centered at 115 nm, in line with the size range observed on the TEM micrographs, and with a polydispersity index (PDI) of 0.16. In Fig. 3(b), we show the impact of the initial APTES concentration in oil on the nano-emulsion properties. Interestingly, the silica shell has no significant influence on the size distribution and PDI. This suggests that when solubilized in oil, APTES does not interfere with the spontaneous emulsification process.

The surface charge clearly decreases with increasing APTES concentrations, from an almost neutral value without APTES (around -3 mV), up to around -20 mV above 0.25 M. This evolution of the surface properties likely reflects the density of silica at the water/oil interface, thus showing the gradual formation of the shell. These data also suggest that the shell covers the entire surface when [APTES]<sub>oil</sub>  $\geq$  0.25 M. Considering the TEM pictures (Fig. 2) and the changes in the surface potential (Fig. 3(b)), likely related to the modification of the surface composition, we can conclude that the silica shell has effectively formed at the oil-water interface. Complementary studies on stability over time of the nanocapsules in FBS were carried out and reported in ESI Fig. S1.† The results did not reveal significant changes in the size over time, but showed a slight size increase for the higher dilution (1/100 and 1/1000), which could mean a weak aggregation. However, in the conditions of usual *in vivo* administration (e.g. 1/10 for X-ray imaging<sup>1,18</sup>) no significant changes were observed.

In this study, we used APTES instead of TEOS because it bears a primary amine, in order to decorate the nanocapsules formed after the silica poly-condensation. However it is obvious

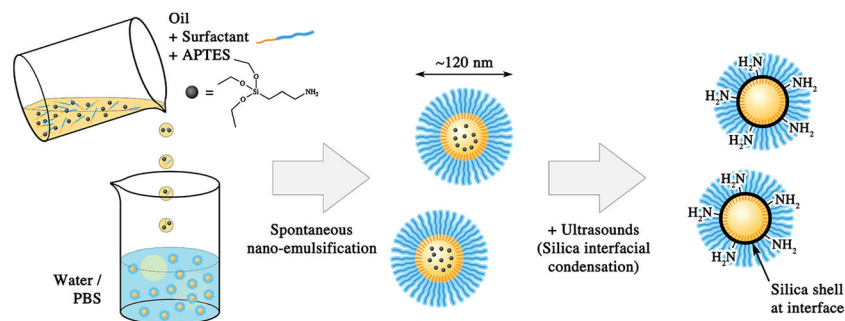


Fig. 1 General scheme describing the formulation of amino-functionalized nano-emulsion droplets.



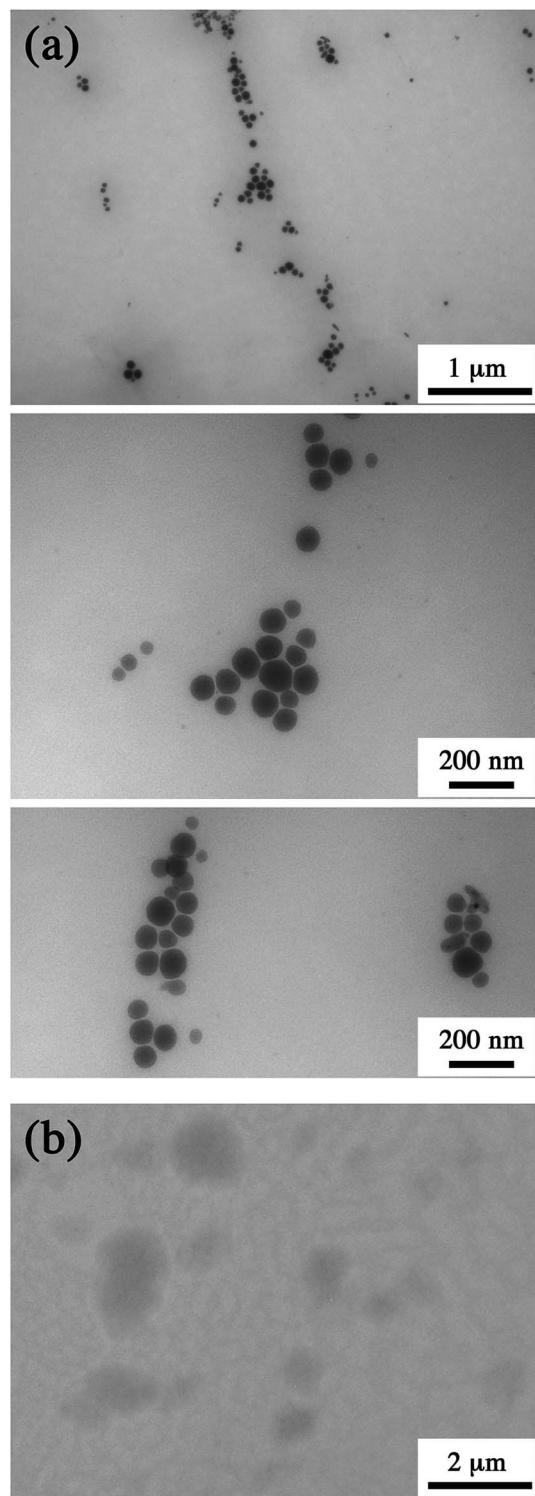


Fig. 2 (a) TEM pictures of nano-emulsion droplets after fabrication of the silica shell with  $[APTES]_{oil} = 0.5$  M. (b) Control experiment, similar nano-emulsion formulation without silica shell.

that a significant part of the  $NH_2$  of the shell will be also entrapped into the oil core. To quantify the amino groups available for reaction at the nanocapsule interface, we used a method based on fluorescamine. This dye is routinely used in

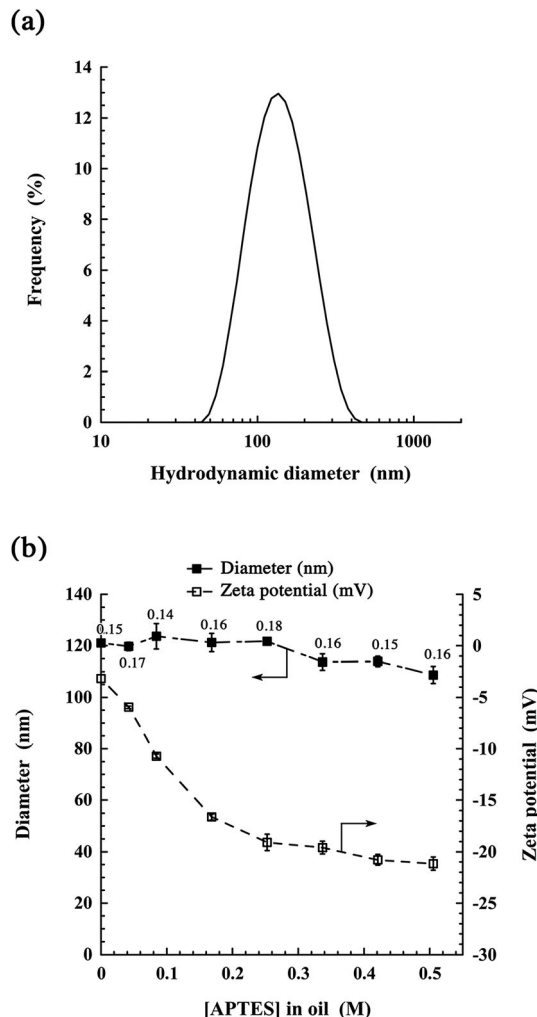


Fig. 3 Size distribution and zeta potential of silica- $NH_2$  coated nano-emulsions. (a) Representative size distribution of the silica nanocapsules suspension, for  $[APTES]_{oil} = 0.42$  M obtained by DLS. (b) Effect of the APTES concentration on the size of the nanocapsules suspension (filled squares) and on their surface charge, measured through the zeta potential (open squares).

primary amine quantification of peptides or proteins, because it becomes fluorescent only after reaction with primary amines. To elaborate the protocol to the nanocapsules, we used a model water-soluble primary amine, ethanolamine. Different ethanolamine concentrations were mixed with increasing concentrations of fluorescamine, and the fluorescence intensity was measured (see scheme in Fig. 4, top). These experiments enabled us to calibrate the fluorescamine assay with our instrumental settings (ESI section<sup>†</sup>). It was found that for a fluorescamine concentration of 500  $\mu M$ , the linearity region is obtained for ethanolamine concentrations in the range between 0 and 500  $\mu M$ .

This calibration was used to determine the apparent  $NH_2$  concentration in the suspension of  $NH_2$ -decorated nanocapsules. In order to be in the linear region, the nano-emulsions were diluted to a maximum theoretical  $NH_2$  concentration of 500  $\mu M$  and were mixed with 500  $\mu M$  fluorescamine. The



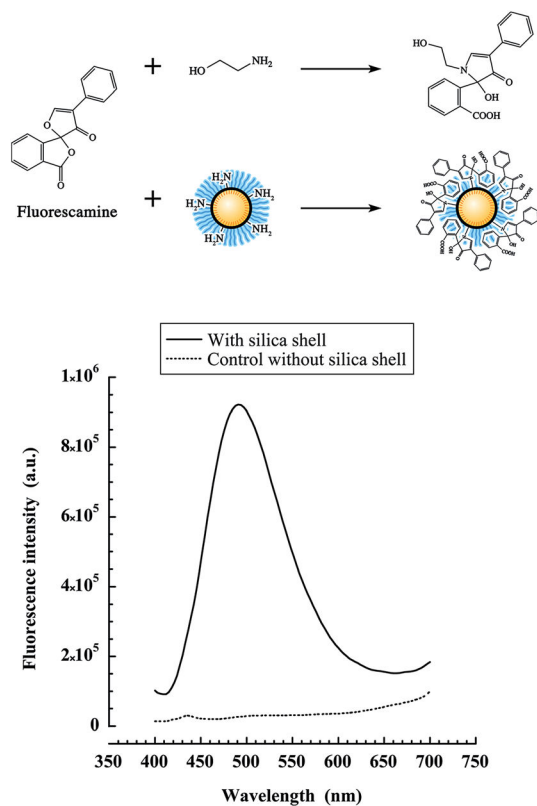


Fig. 4 (top) Schematic representation of the reaction of fluorescamine with ethanolanine and with primary amines onto the nanocapsules. (bottom) Emission spectra of fluorescamine (excited at 365 nm) mixed (full line) with  $\text{NH}_2$ -silica nano-emulsions and (dashed line) with blank nano-emulsions without silica shell.

fluorescamine reaction with the silica shell is schematically reported in Fig. 4 (top), giving rise to fluorescent nanocapsules. Nanoparticles with silica shell gave strong fluorescence, whereas no fluorescence was observed for blank nano-emulsions without silica shell (Fig. 4, bottom). This result confirmed the presence of reactive  $\text{NH}_2$  groups at the surface of the nanocapsules, as well as their accessibility for reacting with fluorescamine.

In addition, this method allowed evaluating the impact of the APTES (*i.e.* silica) concentration on the available  $\text{NH}_2$  groups at the interface, shown in Fig. 5 for 3 different nanocapsule diameters, 120, 85 and 65 nm. The surface of the nanocapsules presents a very high coverage, up to  $9 \times 10^4$  available  $\text{NH}_2$  groups per particle of 120 nm (*i.e.* 2 groups per  $\text{nm}^2$ ), prepared in the presence of 0.5 M APTES in oil. The obtained value corresponds to around 50% of the amino groups introduced with APTES in the formulation (ESI section†), indicating that half of the amine functions are entrapped in the droplets while the remaining half is available. As expected, the higher the silica concentration, the higher the number of amine functions per drop. Moreover, the larger is droplets size, the higher is the number of reactive groups. Finally, the straight lines fitting the experimental points indicate that the silica concentration at the interface is still growing and does not stabilize around

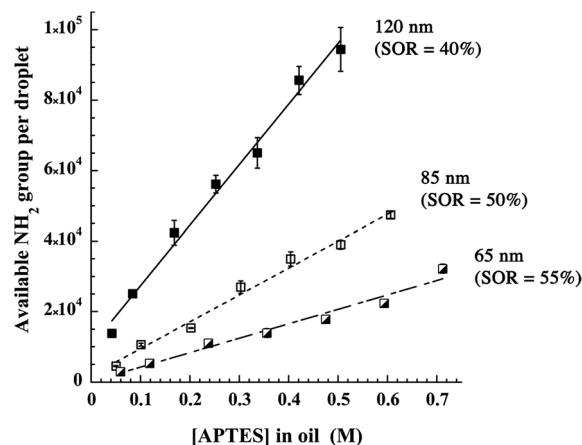


Fig. 5 Quantification, according to the fluorescamine method, of the available primary amine groups at the surface of the nanocapsules. Three different sizes of nano-emulsions were obtained by changing the SOR value as indicated.  $n = 3$ .

$[\text{APTES}]_{\text{oil}} = 0.25 \text{ M}$  as it was shown with the zeta potential (in Fig. 3). This difference is probably because the zeta potential only reflects the surface coverage by the silica and once the surface is fully covered, the zeta potential does not change. On the other hand, increasing the silica concentration could increase the thickness and/or compactness of the layer thus increasing the total amount of amino groups.

In a next step, our objective was to graft model ligands on the available  $\text{NH}_2$  functions. As a proof of concept for the grafting of ligands bearing  $\text{COOH}$  function, we selected coumarin blue that presents a *N*-hydroxysuccinimide activated acid. After reaction for 24 h, the samples are dialyzed for another 24 h to remove the free coumarin, and the emission of the samples is measured. The results reported in Fig. 6(a), show that coumarin ligands are grafted on the silica shell and not simply adsorbed on the nano-emulsion.

Surprisingly, the emission spectrum of coumarin blue is strongly red-shifted in comparison to the free dye, with a maximum emission wavelength at 554 nm *vs.* 473 nm for the free dye in water. A possible explanation is that the fluorescence properties of the dye are modified by their high local concentration once they are grafted onto the capsule surface. The light absorption measurements at the maximum of the peaks, before and after dialysis allows us evaluating the proportions of dye grafted onto the nanocapsule, giving 41.5% grafted. That is to say around  $3.7 \times 10^4$  coumarin dyes are grafted per particle. Such a huge local accumulation can modify the dye emission due to formation of ground or excited-state aggregates. To prove this hypothesis, we recorded the excitation spectra of the dye-labeled particles before dialysis (ESI†). When recorded at 554 and 465 nm, the excitation bands were both located around 400 nm, with some blue shifted maximum for the former. These spectra were close to the corresponding absorption spectrum as well as to that of free coumarin dye in water. The small blue shift of the species emitting at 554 nm suggests a ground-state aggregation of the coumarin dyes at the particle surface. These



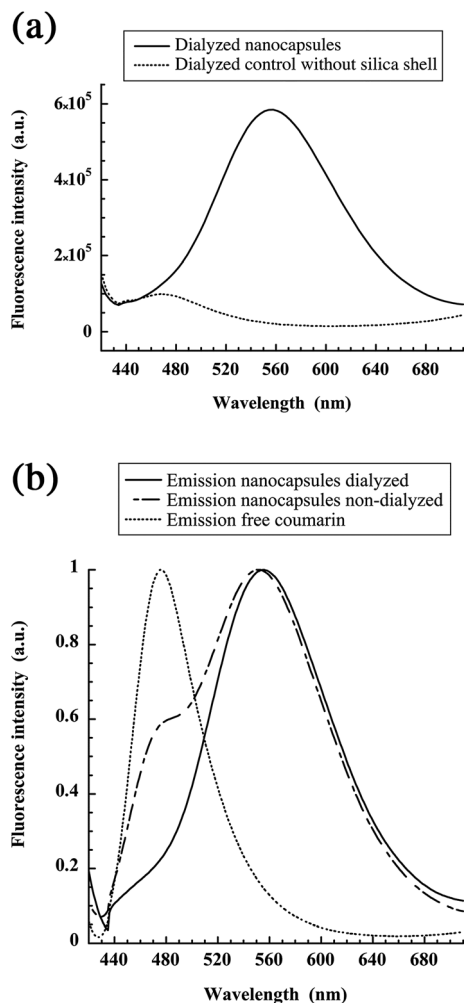


Fig. 6 (a) Emission spectra of coumarin blue (excited at 405 nm) grafted on the surface of  $\text{NH}_2$ -silica nano-emulsions with  $[\text{APTES}]_{\text{oil}} = 0.5 \text{ M}$  after 24 h dialysis (full line) and of blank nano-emulsions without silica shell (dashed line). (b) Normalized emission spectra of coumarin blue grafted onto the surface of nanocapsules, with and without dialysis, and compared to free coumarin blue. Comparison of the spectra of the dye-labeled nanocapsules before and after dialysis shows the disappearance of the shoulder of free dye around 480 nm.

aggregates may present a strongly red-shifted emission, as other dye aggregates.<sup>27</sup> In addition, quantum yields ratio between free coumarin and grafted on nanocapsules (after dialysis) has been calculated from the spectra, giving the grafted dyes 5.3 times brighter than free dye in solution. This corroborates the drastic changes in the fluorescence properties after the surface conjugation.

Then, the dialyzed suspensions of nanocapsules decorated with coumarin, in which we have loaded the oil core with Nile red were studied with Förster Resonance Energy Transfer (FRET) experiments. Since the Nile red is homogeneously distributed in all the nanocapsules, our aim here was to study by FRET the co-localization of the two dyes in order to show that coumarin is grafted to all the nanocapsules. The control experiment with only coumarin gives a significant fluorescence peak. In the presence of Nile red as FRET acceptor, the

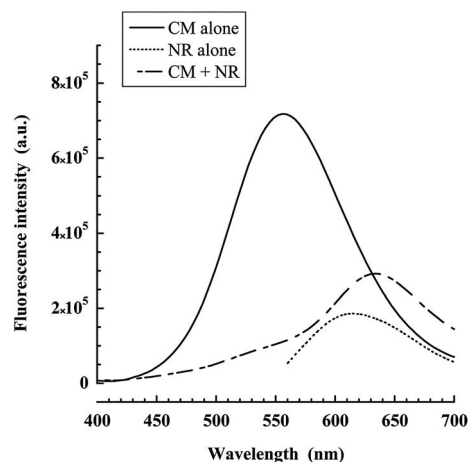


Fig. 7 Emission spectra for FRET experiments and controls. The studied systems are either nanocapsules only decorated with coumarin blue (CM alone), or nanocapsules only loaded with Nile red (NR alone), or finally nanocapsules decorated with coumarin blue and loaded with Nile red (CM + NR);  $[\text{APTES}]_{\text{oil}} = 0.5 \text{ M}$ .

fluorescence of coumarin is strongly inhibited giving rise to the fluorescence of the acceptor. Thus, the distance from coumarin to the closest Nile red molecules in the oil phase appears to be well below the Förster radius ( $\sim 5 \text{ nm}$ ).

Moreover, another physical method, combined AFM and fluorescence microscopy, shows the co-localization of the particles and the fluorescence signal of coumarin (Fig. 8). Indeed, the nanocapsules detected by AFM could be observed in the fluorescence images as bright spots, indicating that these nanostructures were labeled with the dye. However, the fluorescence spots appeared much larger due to diffraction limited resolution of fluorescence microscopy. The AFM micrographs

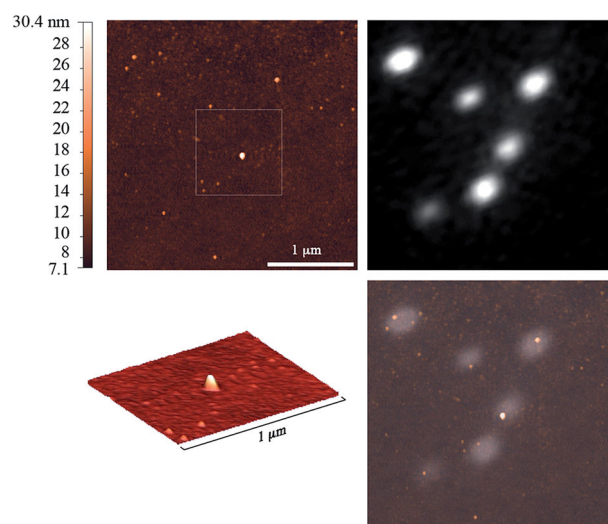


Fig. 8 Combined AFM and fluorescence microscopy of nanocapsules decorated with coumarin blue ( $[\text{APTES}]_{\text{oil}} = 0.5 \text{ M}$ ). Left: AFM micrograph with a 3D representation of the nanocapsules. Right: corresponding fluorescence acquisition showing the match between AFM and Fluorescence.



**Table 1** FCS data for coumarin blue-coated nanocapsules. Control refers to nano-emulsions without silica-shell and coated refers to nanocapsules with NH<sub>2</sub>-silica shell ([APTES]<sub>oil</sub> = 0.5 M). *N* is the average number of particles in the focal volume,  $\tau_c$  is the correlation time, and Br the brightness, is the ratio of photon count rate per capsule with respect to TMR. Br/Br(TMR) is the brightness over the one of TMR

	TMR (5 mW)	NC + dye (5 mW)	TMR (10 mW)	Free dye (10 mW)
<i>N</i>	21.0	0.24	23.36	54.9
$\tau_c$	0.048	4.79	0.040	0.022
Br	2.27	38.72	7.54	0.20
Br/Br(TMR)	1	17.1	1	0.027

evidence the spherical shape of the particles, in line with the TEM image (Fig. 2). The fluorescent dots correspond well to the particles seen by AFM. Thus, AFM-Fluo further confirms that dialyzed samples show significant fluorescence originated from the nanocapsules.

To further confirm the successful surface modification of the nanocapsules, we studied by fluorescence correlation spectroscopy (FCS) the silica coated and non-coated nanocapsules after treatment with coumarin blue. FCS is a powerful technique to study fluorescent nanoparticles because it can provide simultaneously multiple parameters such as the correlation time, the number of particle per volume and the photon count rate, which provide access to the particle size, concentration and brightness, respectively. Corresponding values are reported in Table 1. Two powers of laser were adopted to compare nanocapsules with grafted dyes and free dyes, since on the one hand free dye is not sensitive enough at 5 mW (does not correlate) and on the other hand, we observed a strong bleaching at the grafted ones at 10 mW. It can be seen that the grafted particles have a significantly higher correlation time than free species, TMR of free dyes. This indicates a bigger size calculated at 100.1 nm, in agreement with DLS and TEM data. The same trend is observed with brightness, and to be comparable we consider the value of the brightness over the one of TMR as reference (Br/Br(TMR)), giving the grafted ones around 633 times higher than free dye.

## Conclusion

To summarize, the aim of this study was to propose a new method for functionalizing nano-emulsion droplets, after their formulation. Lipophilic silica precursor (APTES) was added to the oil before the formulation, and turned into silica shell after nano-droplet fabrication by sonochemistry that avoids addition of catalyst in the bulk phase. In comparison with existing methods to functionalize nano-droplets like post-insertion of functionalized lipids, this novel procedure brings real advantages: covalent grafting of functional groups at the nano-droplet surface *i.e.* strongly anchored on the silica nanocapsules, as well as a large number of reactive sites per capsule (up to  $9 \times 10^4$ ,  $\sim 2$  amino groups per nm<sup>2</sup>). The functional silica shell fabrication is

simple, quick, and affects neither the formulation process nor the droplets size. Amino-group quantification allowed understanding the impact of formulation parameters, like the droplet size or APTES concentration, on the number of reactive NH<sub>2</sub> groups decorating the resulting nanocapsules. Finally, the last part of the study was focused on the grafting of a model ligand though the reaction of an activated carboxylic acid (coumarin blue) on the amine functions available onto the nanocapsule surface. We achieved a grafting efficiency of around 41% and characterized the conjugate by various spectroscopic and microscopic methods, proving the concept of this new original protocol for functionalizing oil droplets. Nano-emulsions are a particularly interesting type of nano-carriers, able to solubilize a large range of active molecules or contrast agents, and their simple surface functionalization is a real step forward regarding potential applications like active targeting *in vivo*.

## References

- M. F. Attia, N. Anton, M. Chiper, R. Akasov, H. Anton, N. Messaddeq, S. Fournel, A. S. Klymchenko, Y. Mély and T. F. Vandamme, *ACS Nano*, 2014, **8**, 10537.
- (a) H. Maeda, J. Wu, T. Sawa, Y. Matsumura and K. Hori, *J. Controlled Release*, 2000, **65**, 271; (b) S. Hirsjärvi, S. Dufort, G. Bastiat, P. Saulnier, C. Passirani, J. L. Coll and J. P. Benoît, *Acta Biomater.*, 2013, **9**, 6686.
- (a) J. Tomasina, L. Poulain, E. Abeilard, F. Giffard, E. Brotin, L. Carduner, F. Carreiras, P. Gauduchon, S. Rault and A. Malzert-Fréon, *Int. J. Pharm.*, 2013, **458**, 197; (b) N. R. Jana, N. Erathodiyil, J. Jiang and J. Y. Ying, *Langmuir*, 2010, **26**, 6503; (c) M. Soster, R. Juris, S. Bonacchi, D. Genovese, M. Montalti, E. Rampazzo, N. Zaccheroni, P. Garagnani, F. Bussolino, L. Prodi and S. Marchiò, *Int. J. Nanomed.*, 2012, **7**, 4797.
- N. Graf, D. R. Bielenberg, N. Kolishetti, C. Muus, J. Banyard, O. C. Farokhzad and S. J. Lippard, *ACS Nano*, 2012, **6**, 4530.
- N. Chanda, V. Kattumuri, R. Shukla, A. Zambre, K. Katti, A. Upendran, R. R. Kulkarni, P. Kan, G. M. Fent, S. W. Casteel, C. J. Smith, E. Boote, J. D. Robertson, C. Cutler, J. R. Lever, K. V. Katti and R. Kannan, *Proc. Natl. Acad. Sci. U. S. A.*, 2010, **107**, 8760.
- C. Wyss, S. C. Schaefer, L. Juillerat-Jeanneret, L. Lagopoulos, H. A. Lehr, C. D. Becker and X. Montet, *Eur. J. Radiol.*, 2009, **19**, 2487.
- B. Aydogan, J. Li, T. Rajh, A. Chaudhary, S. J. Chmura, C. Pelizzari, C. Wietholt, M. Kurtoglu and P. Redmond, *Mol. Imag. Biol.*, 2010, **12**, 463.
- K. A. Kelly, N. Bardeesy, R. Anbazhagan, S. Gurumurthy, J. Berger, H. Alencar, R. A. Depinho, U. Mahmood and R. Weissleder, *PLoS Med.*, 2008, **15**, e85.
- J. F. Hainfeld, M. J. O'Connor, F. A. Dilmanian, D. N. Slatkin, D. J. Adams and H. M. Smilowitz, *Br. J. Radiol.*, 2011, **84**, 526.
- W. Eck, A. I. Nicholson, H. Zentgraf, W. Semmler and S. Bartling, *Nano Lett.*, 2010, **10**, 2318.
- (a) X. Shi, S. Wang, S. Meshinchi, M. E. van Antwerp, X. Bi, I. Lee and J. R. J. Baker, *Small*, 2007, **3**, 1245; (b) S. D. Weitman, R. H. Lark, L. R. Coney, D. W. Fort,



- V. Frasca, V. R. J. Zurawski and B. A. Kamen, *Cancer Res.*, 1992, **52**, 3396; (c) J. F. Ross, P. K. Chaudhuri and M. Ratnam, *Cancer*, 1994, **73**, 2432.
- 12 A. K. Azab, J. Kleinstern, M. Srebnik and A. Rubinstein, *Pharm. Res.*, 2008, **25**, 379.
- 13 (a) E. Rampazzo, R. Voltan, L. Petrizza, N. Zaccheroni, L. Prodi, F. Casciano, G. Zauli and P. Secchiero, *Nanoscale*, 2013, **5**, 7897; (b) M. Helle, E. Rampazzo, M. Monchanin, F. Marchal, F. Guillemin, S. Bonacchi, F. Salis, L. Prodi and L. Bezdetnaya, *ACS Nano*, 2013, **7**, 8645.
- 14 J. Zhu, C. Waengler, R. B. Lennox and R. Schirrmacher, *Langmuir*, 2012, **28**, 5508.
- 15 B. J. Kim, J. Bang, C. J. Hawker, J. J. Chiu, D. J. Pine, S. G. Jang, S. M. Yang and E. J. Kramer, *Langmuir*, 2007, **23**, 12693.
- 16 N. Anton and T. F. Vandamme, *Pharm. Res.*, 2011, **28**, 978.
- 17 (a) A. Klymchenko, E. Roger, N. Anton, H. Anton, I. Shulov, J. Vermot, Y. Mely and T. F. Vandamme, *RSC Adv.*, 2012, **2**, 11876; (b) V. Kilin, H. Anton, N. Anton, E. Steed, J. Vermot, T. F. Vandamme, Y. Mely and A. S. Klymchenko, *Biomaterials*, 2014, **35**, 4950.
- 18 X. Li, N. Anton, G. Zuber, M. Zhao, N. Messaddeq, F. Hallouard, H. Fessi and T. F. Vandamme, *Biomaterials*, 2013, **34**, 481.
- 19 E. Bourseau-Guilmain, J. Béjaud, A. Griveau, N. Lautram, F. Hindré, M. Weyland, J. P. Benoit and E. Garcion, *Int. J. Pharm.*, 2012, **423**, 93.
- 20 J. Szebeni, F. M. Muggia and C. R. Alving, *J. Natl. Cancer Inst.*, 1998, **90**, 300.
- 21 J. P. Clamme, J. Azoulay and Y. Mély, *Biophys. J.*, 2003, **84**, 1960.
- 22 N. L. Thompson, Fluorescence correlation spectroscopy, in *Topics in Fluorescence Spectroscopy Techniques*, ed. J. R. Lakowicz, Plenum Press, New York, 1991, vol. 1, p. 337.
- 23 P. Didier, J. Godet and Y. Mély, *J. Fluoresc.*, 2009, **19**, 561.
- 24 N. Anton and T. F. Vandamme, *Int. J. Pharm.*, 2009, **377**, 142.
- 25 (a) S. H. Wu, Y. Hung and C. Y. Mou, *Chem. Mater.*, 2013, **25**, 352; (b) L. Spornath and S. Magdassi, *Micro Nano Lett.*, 2009, **5**, 28.
- 26 J. Ocotlan-Flores and J. M. Saniger, *J. Sol-Gel Sci. Technol.*, 2006, **39**, 235.
- 27 F. Würthner, T. E. Kaiser and C. R. Saha-Möller, *Angew. Chem., Int. Ed.*, 2011, **50**, 3376.





---

---

# *Chapter three*

---

---

## **Chapter 3.1: Inorganic nanoparticles for micro CT imaging**

This review provides a state-of-the-art overview of an important application for inorganic nanoparticles in biomedical imaging. We focused mainly on X-ray imaging, but included a short comparison to magnetic and fluorescent modalities. X-ray imaging, which forms the basis for computer tomography, presents many advantages over other imaging modalities, in terms of structural and functional imaging, as well as the potential to target specific tissues. The general principles of the imaging techniques are reviewed, and the impact of the formulation processes of nanoparticles, their structures, chemical nature, and surface functionalization, as well as *in vitro* and *in vivo* behaviors are reviewed and discussed. This chapter summarizes all the latest technologies for targeting nanoparticles designed to improve imaging techniques and advance therapeutic efficacy.

## 1. Introduction

This chapter presents a general overview of various inorganic nanomaterials, and their uses in biomedical imaging. The current state of all aspects of inorganic nanoparticles (NPs), especially for X-ray computer tomography (CT) imaging, their synthesis, the surface chemistry functionalization for receptor targeting, as well as *in vitro* and *in vivo* biomedical applications, will be reviewed in this chapter. We will first provide a general description of the entire diagnostic process that occurs through the combination of imaging modalities and contrast agents (CA) in order to eventually obtain the ideal visualization of the area of interest.

A schematic representation (Figure 1) illustrates the principle of a microCT scanner. In brief, the idea of using tomography as a diagnostic tool in medicine was adopted soon after the discovery of X-rays by W. C. Roentgen in 1895. The first successful CT imaging device was built in 1972 by G.N. Hounsfield, who shared the Nobel Prize in medicine with A.M. Cormack in 1979 for the development of X-ray CT imaging and diagnostics.

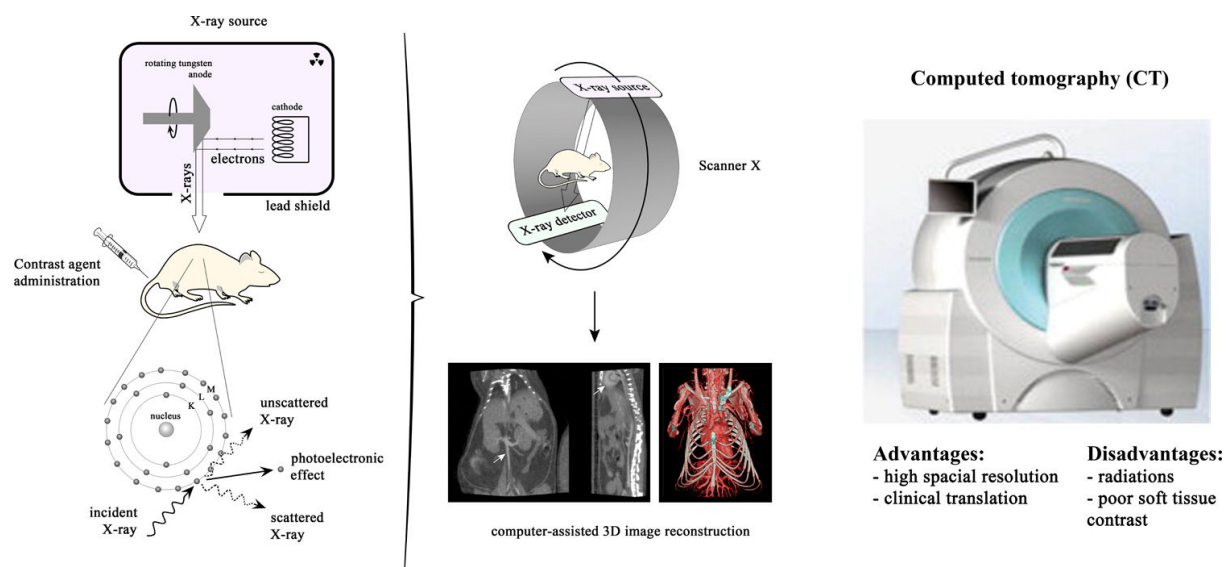


Figure 1: Schematic diagram of basic principles of computed assisted tomography. Reproduced with permission from (1), copyright 2012, Wiley, and with permission from (2), copyright 2012, Elsevier.

X-rays are generated by means of electron beams accelerated by a high voltage within a vacuum tube, which collide with a heavy metal anode. The beams pass through the subject and undergo interactions with various molecules. In the pathway of the beam, as it passes through crossed fibers and tissues, some of the X-ray energy is absorbed, reflected, or scattered in different directions. The net quantity of X-rays, expressed by attenuation degree, relies on the thickness of the object, the density of the particular organs, and the number of electrons per atom of the element (atomic number). That is why the final beam is less intense than the incident electron beam and can be recorded *via* a detector. This affords non-destructive 3D imaging of a variety of tissue types and organ systems, such as the gastrointestinal tract (GI), cardiovascular system, renal tract, lungs, cartilage, liver, bone, tumorous tissue, and others. Although X-ray attenuation is directly and qualitatively

visualized on CT images, quantitative information can also be extracted from them. To obtain such data, the attenuation coefficient is measured and expressed as Hounsfield units (HU). In order to compare different experiments, the attenuation values must be normalized. This is performed by imposing the values corresponding to air and water, *i.e.*, -1000 HU and 0 HU, respectively. In contrast, mineralized tissues, such as bones, present an attenuation around 1000 HU, but most soft tissues fall within 30-100 HU. CT scanners are calibrated with a reference to water. For a material with a linear X-ray attenuation coefficient ( $\mu$ ), the corresponding HU value is calculated by Equation 1:

$$HU = [(\mu - \mu_{water}) / (\mu_{water})] \times 1000 \text{ (eq. 1)}$$

where ( $\mu_{water}$ ) is the linear X-ray attenuation coefficient of water.

## 2. General nanoparticulate systems for imaging purposes

During the past several decades, inorganic nanomaterials, including gold NPs (AuNPs), silver NPs (AgNPs), iron oxide NPs (IONPs), semiconductor quantum dots NPs (Qds), and others, have been developed as contrast-enhancer nanoprobe, commonly called nanoparticulate contrast agents (CA). These molecular imaging tools enable high-resolution scanning of bone structures due to a difference in the electron densities, but are very limited in imaging specific molecules. Using contrast materials is thus crucial for visualizing soft tissues and internal structures or organs. X-ray micro-computed tomography (microCT) (3) is one of many emerging imaging modalities used for medical diagnostic radiology in which contrast is enhanced through the administration of heavy-atom CA (e.g., AuNPs, AgNPs, iodine NPs) (4). Other imaging techniques, such as magnetic resonance imaging (MRI) (5, 6) commonly uses gadolinium chelates ( $Gd^{3+}$  chelates) and IONPs, which have been approved as contrast media since the mid-1990s (7). In the case of fluorescent imaging, contrast efficiency is improved by organic dyes and QD CAs. Each technique is based on the principle that an emission signal is induced by an excitation source (*i.e.*, beam of light, magnetic field, radiofrequency) to tissues or organs. The administration of CA changes the emission characteristics of a biological compartment due to their specific contrast properties or their specific interactions with their biological environment. Eventually, all interactions are recorded and processed to reconstruct 2D or 3D images.

Despite the fact that MRI has revolutionized medical imaging in recent times, X-ray imaging is still one of the most employed techniques, accounting for over 80% of all diagnostic tests. It is needless to say that CAs are thus an essential part of radiology. Currently, two types of X-ray CAs are generally employed in medicine (8). These are based upon the use of orally administrated barium sulfate suspensions (predominantly used for GI imaging) and iodinated organic compounds (9-13) administered either orally or intravenously. At present, most available organic X-ray CAs involve the use of a single triiodobenzene moiety or two aromatic rings that are connected to each other by a covalent spacer (13-16).

Historically, the first trial for scanning the body in the presence of contrast media based on iodine used lithium iodide and sodium iodide. These were among the first water-soluble imaging agents. However, due to the associated toxicity of the iodine concentrations

necessary for imaging, they are now considered unsuitable for most clinical applications. Small hydrophilic iodinated molecules are another type of iodinated-based CAs and were synthesized to have a low molecular weight (< 2000 Da) and iodinated aromatics to provide a higher stability that would lower toxicity, compared to iodinated aliphatic molecules. These small hydrophilic molecules are generally ionic molecules, and are mostly a negatively charged species. Even though they are widely used in the clinic, they exhibit numerous inherent disadvantages (17) due to their higher tendency to interact with biological structures, as well as because of their high intrinsic osmolality in aqueous formulations, which leads to renal toxicity and other physiological problems, such as bradycardia, vasodilation, and pulmonary hypertension. To overcome these limitations, non-ionic imaging media, such as iohexol, iopromide, iodixanol, ioxaglate iothamate, and iopamidol, etc., are used (17, 18). It is assumed that they possess a lower osmolality and exhibit a lower incidence of adverse health effects (19, 20). Two novel, low-osmolality, two-ring iodinated CAs are osimenol and GE-145. Experimental results indicate an improvement in physical and pharmacological properties compared to current clinically approved CA(21-25). An additional class of iodinated CA are (1,2,3-trialkyl-2,4,6-triiodobenzene), used to image the GI tract, whereas phosphonate/peptide conjugated benzene derivatives are potentially suitable for targeted imaging agents(26, 27). Many research groups are examining ionic CA to provide qualitative and quantitative information on the functional state of the tissue, the extent of pathogens, or structural damage. For instance, anionic  $\text{Ca}^{2+}$  chelating CA are used to assess bone microdamage (28-30) and ( $\text{CA}^{4+}$ ) are employed as a cationic CA for cartilage tissue imaging (31-33).

Overall, different kinds of nanoparticulate systems, mostly based on liposomes, nano-emulsions, polymeric NPs dendrimers (DEs), inorganic NPs, and others, have been formulated for many reasons, such as their tunable morphology (size, shape) and their biocompatible properties. This is why nanocarriers are now widely used in medicinal applications, especially in the field known as nanomedicine (34). Their key advantages lie in their ability to carry a high payload of contrast-generating material, but they also have long blood circulation half-lives depending on the coating material. Multiple properties/components can be integrated into NPs with relative ease and can be easily modified in various ways to include targeting moieties, such as antibodies, proteins, peptides, or aptamers (35-38). However, new alternative inorganic NP-based X-ray contrast agents have been developed to improve contrast enhancement while mitigating the drawbacks of current CA. Due to the fascinating properties found in these inorganic NPs, such as the facile method of preparation, various protocols have been applied to control size and shape, which have a substantial impact on contrast, as well as targeting through surface functionalization. Inorganic NPs are promising candidates for potential use in the clinic to improve the diagnostic process. The intrinsic X-ray absorption coefficient of inorganic NPs (e.g., gold, silver, bismuth, platinum, gadolinium) surpasses most iodine-based CAs, giving rise to greater contrast and thereby reducing the radiation dose. This can make them more compatible and applicable to patients for whom conventional iodinated contrast media are contraindicated, because, for instance, of renal insufficiency or allergic responses (39).

---

### 3. Stringent requirements for ideal imaging probes

In general, to generate an efficient end product that is potentially applicable in a clinical setting, several factors must be taken into account, notably related to validation in the laboratory (*i.e.*, small animal testing), as well as industrial production (e.g., production scale-up). The desirable properties of CAs are summarized in Table 1.

**Table 1:** Marketing needs vs laboratory scale for CA commercialization and production

Properties that support product marketing	Characteristics needed during synthesis in the laboratory
1. Safety for the patient	Biocompatibility: <ul style="list-style-type: none"> <li>• Non-toxicity and (if possible) biodegradability of the materials used in the CA formulation.</li> <li>• It is recommended that the molecules be coated with biocompatible polymers, such as a PEGylated shell, carbohydrates, etc., conferring stealth properties by avoiding NPs' interactions with plasma proteins (opsonins) in order to delay their recognition by the reticuloendothelial system (RES), and thus, prolonging their circulation time in the bloodstream (boosting their half life time, <math>t_{1/2}</math>). As a consequence, the anti-fooling (Jeff, "anti-fooling" correct?) corona shell prevents rapid clearance and gives sufficient time for NPs to bind with specific targets.</li> <li>• Appropriate pH, osmolality and viscosity.</li> </ul>
2. High efficacy	Which is strongly dependent on <ul style="list-style-type: none"> <li>• High water solubility</li> <li>• High concentration of the X-ray CA and/or active principle ingredient (API).</li> <li>• The pathway mechanism to inhibit degradation or release prior to reaching active sites.</li> <li>• Long blood circulation times, <i>i.e.</i>, "blood-pool agents."</li> <li>• Minimum amount of molecules to provide high efficiency.</li> <li>• Size (passive targeting <i>versus</i> the enhanced permeation retention (EPR) process or accumulation in specific tissues). NPs size are important in terms of excretion time—less than 20 nm (rapid renal elimination), and 50-200 nm (delay elimination time).</li> <li>• Selectivity of surface-ligand functionalization by active targeting mechanism (ligand-receptor binding).</li> </ul>
3. Patient compliance (high dosing)	<ul style="list-style-type: none"> <li>• Decreased dose gives the same effect (e.g., once per day or once per week is better than three times <i>daily</i>) and this basically depends on the high concentration of the molecules of interest.</li> <li>• High "per dose" concentration is required.</li> </ul>
4. No side effects found	Depends on <ul style="list-style-type: none"> <li>• Biocompatibility</li> <li>• Biodegradability</li> <li>• Biodistribution</li> <li>• Complete removal from the body after function achieved.</li> </ul>

	<ul style="list-style-type: none"> <li>No interactions between NPs and other biomacromolecules and/or NPs metabolites or biodegraded products.</li> </ul>
5. No drug-drug interactions	<ul style="list-style-type: none"> <li>Stable and inert toward combinations or interaction with other biomolecules (non-ionic molecules are favored over ionic molecules).</li> </ul>
6. Combination therapies	<ul style="list-style-type: none"> <li>Formulation aimed at diagnostic imaging, medical treatment, or both (theranostics), by encapsulating more than one molecule of interest in the same NPs for multi-function purposes.</li> </ul>
7. Essence of natural molecules over synthetic molecules in toxicity	<ul style="list-style-type: none"> <li>It is well established that natural biomolecules are more biocompatible and have high biological acceptability due to the homogeneity and the similarities in biological and physiological behaviors in biological systems.</li> </ul>
8. Affordability to the patient (cost-effectiveness)	<p>This is a result of</p> <ul style="list-style-type: none"> <li>The ease of synthesis and preparation (in a few steps).</li> <li>Eco-friendly reactions (solvent-less, green chemistry).</li> <li>Using water as a solvent in chemical reactions.</li> <li>Carrying out reactions at room temperature.</li> </ul>

To sum up a few key specifications required for the development of CAs:

- Size of NPs
- Biocompatibility and safety of NPs
- Toxicity and injectability (chemical nature, pH, osmolality, viscosity)
- Targeting (passive and/or active)
- Stability (the interactions toward biomolecules, blood circulation time)
- Surface ligand functionalization
- Efficacy (concentration of CT CA and/or of active principles)
- Few synthesis steps

To fulfill these requirements, various materials and CA designs are currently being proposed and assessed in both the clinical and laboratory settings. In the following parts of this review, we summarize the literature and developments in the field of CA research over the past ten years. Specifically, we focus on advances in the fields of metal-based imaging agents, including those in the form of NPs. Before going into details about those inorganic nanoproboscopes, it is necessary to understand how such systems are formed and how their designs might affect their *in vivo* fate in biomedical applications.

#### 4. Biodistribution and pharmacokinetics of the developed CAs

The most important aspects, which should be taken into account, are the physicochemical factors that largely affect the biodistribution and toxicity of NPs (40-42). It has been extensively demonstrated that particle size and surface charge affect the efficiency and the pathway of cellular uptake for liposomes (43), quantum dots (44), polymeric NPs (45, 46), AuNPs (47), and silica NPs (48) by influencing the adhesion of the particles and their interaction with cells (49). The first key parameter is size. Particularly because size can range from 10-200 nm, NPs are primarily accumulated in organs of the mononuclear phagocyte

system (MPS), especially the liver and spleen (50-52), while particles smaller than 10 nm are rapidly excreted through the kidneys (53, 54).

The second major characteristic is the surface charge of the NPs, which is determined by the conjugated ligands on the NPs surface. For example, AuNPs coated with positively charged molecules, such as cetyl trimethylammonium bromide (CTAB) (55), show a high accumulation in all organs and exhibit severe cytotoxic effects (56, 57). However, AuNPs with negatively charged capping molecules, such as citrate (58), are prone to opsonization and accumulate in MPS organs, but they are much less toxic compared to positively charged AuNPs (56, 57). Neutral molecules, such as PEG (59), help to decrease opsonization by creating a charge-shielding layer, as well as steric hindrance to minimize adsorption of serum proteins (60, 61). The third aspect is the shape or morphology of the NPs, which affects largely *in vitro* cellular uptake and their *in vivo* journey (47, 62).

Another factor is the composition of NPs, such as PLGA/mPEG copolymers, that affect colloidal stability, and thus, biodistribution. It has been proven that a high PEG/PLGA ratio induces long blood circulation times of PLGA–mPEG NPs (63). Surface ligand properties control the pharmacokinetics through ligand-receptor interactions (64-66). The chemical nature of the molecules also influences the accumulation of NPs into specific organs (67) through the EPR effect (passive targeting mechanism). Furthermore, free surfactant in the NPs suspensions has been shown (68) to play a significant role in tolerance and biodistribution.

## 5. General steps in the formation of inorganic NPs

Inorganic NPs can actually exhibit very specific properties, such as optical, magnetic, or electronic properties based on their composition, shape, and nanometric size. However, obtaining NPs remains quite complicated because so many parameters related to synthesis conditions, such as temperature, the nature of precursors, as well as concentration, pH, and stabilizers, are combined and affect the mechanism of NPs formation (Figure 2). LaMer (69) proposed the first mechanism of NP synthesis based on a three-step formation, including (i) a supersaturation of monomer in the bulk solution leading to (ii) a burst of nucleation providing seeds or nuclei, which then (iii) grow following Fick's law of diffusion. Basically, after step (ii), monomers diffuse from the bulk solution to the nuclear surface and use the surface as a template in order to generate NPs. An initial model of these mechanisms was developed by Reiss and then by Lifshitz, Slyozov, and Wagner (LSW theory). A new approach was proposed by Finke and Watsky, which suggested that nucleation and growth were simultaneous processes. Nucleation was introduced as a slow step leading to an autocatalytic surface growth step. Regarding the size distribution, it should be pointed out that even tight control over the above-mentioned parameters cannot ensure the formation of monodisperse NPs due to a lack of understanding of the impact of each reactional condition. Furthermore, Ostwald ripening, digestive ripening, or coalescence and orientated attachment may occur and yield polydisperse or/and anisotropic NPs(70, 71). Most colloidal NPs are based on nucleation and growth steps, such as copper, metal oxides, or even semiconductor nanocrystals, but also

---

inorganic NPs for X-ray (XR) imaging, like gold and silver, which were widely studied by Rothenberg (70).

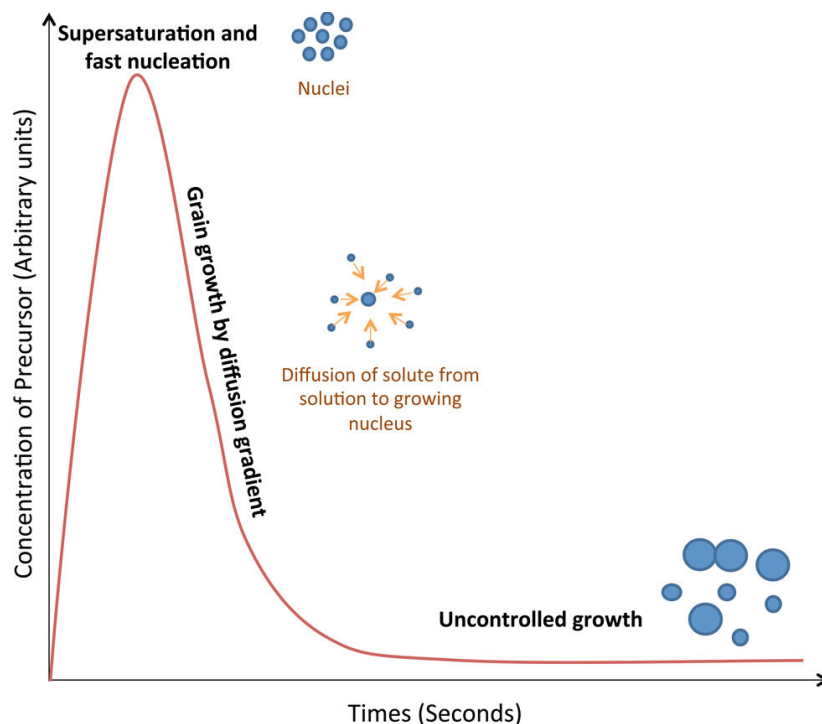


**Figure 2:** General overview of the formation of inorganic NPs over the time of the reaction.

## 6. AuNPs as a CT CA

AuNPs are the most commonly used NPs-based agents for CT imaging. AuNPs have promising applications in many fields, ranging from bioconjugated probes, optics, and electronics to sensors for photon-thermal energy converters and catalysis. AuNPs have been especially promising for myriad pioneering biomedical applications (72), such as photoacoustic imaging, photothermal ablation, and DNA detection (73, 74), as well as drug delivery systems (DDS) (75-77). They are generally regarded as biocompatible and are undergoing evaluation as therapeutic agents in a number of clinical trials.

To present the key advantages of AuNPs for imaging purposes, it is necessary to study their interaction with the X-ray beam. Generally, materials attenuate the X-ray beam *via* the photoelectric effect, *i.e.*, the generated X-ray photon collides with and transfers its energy to a K-shell electron, typically. The electron is then ejected from its shell and travels a short distance prior to losing its energy. For a given photon energy, the photoelectric effect scales with  $Z^3$  ( $Z$  being the atomic number, Figure 3). Interestingly, the photoelectric effect is highly influenced not only by the atomic number of elements, but also by the energy of both the electron shells and the generated X-ray photon. If the energy of the X-ray photon is less than that of the electron shell, a photoelectric interaction cannot take place. The X-ray energy must be higher than that of the electron shell. The K-edge of iodine ( $Z = 53$ ) is 33.2 keV, thus iodine gives stronger contrast when scanned at 80 keV than 120 kV. However, the K-edge for gold ( $Z = 79$ ) is 80.7 keV, *i.e.*, it absorbs X-rays strongly in the 80–120 keV region, reducing

interference from bone and soft tissue absorption. Consequently, the gold molecule provides stronger contrast when scanned at 120 keV than a 80 keV mass X-ray absorption coefficient. This yields a higher mass X-ray absorption coefficient ( $5.16 \text{ cm}^2\text{g}^{-1}$  at 100 KeV) than iodine, for example (78). This means that gold provides about 2.7 times greater X-ray contrast per unit weight than iodine.

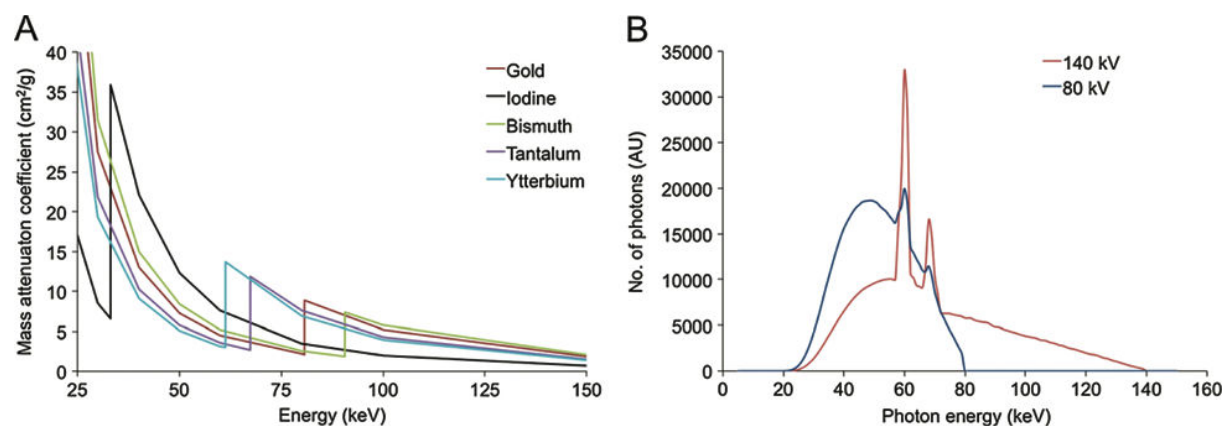


**Figure 3:** (A) Mass attenuation coefficients of a variety of elements. (B) Photon energy distribution generated from the X-ray tube of a CT scanner run at 80 or 140 keV. Reproduced with permission from Ref. (79), copyright 2014, Wiley.

Thus, evaluating the imaging performance in terms of signal-to-noise ratio (SNR) and contrast-to-noise ratio (CNR) allows an estimate of the minimum gold concentration required to obtain sufficient X-ray attenuation by human tissue in spectral CT imaging (80). These good attenuation properties enable the use of low doses of gold CA injection and therefore reduce the potential side effects for patients. Furthermore, the potential to functionalize their surfaces by simple chemical reactions offer many possibilities to translate these biocompatible AuNPs into an efficient, actively-targeted CA.

### 6.1 Synthesis of AuNPs

Nanotechnology is an interesting field, based on the formation of nanosized assemblies of organic and/or inorganic components using numerous methods of preparation to obtain the desired physical and chemical properties. All materials tend to be found in a stable state. For these nanomaterials to yield a metastable state, two successive processes are required: i) a reduction to form the NPs; and ii) stabilization using capping agents or surfactants in order to prevent the particles from agglomerating. This provides a sufficient electrostatic repulsion and/or steric barrier by adsorption on the surface of inorganic NPs.

The general synthesis of AuNPs has been achieved by several methods that are mostly based on the reduction of the gold precursor, such as  $\text{HAuCl}_4$  with different kinds of reducers and/or stabilizers. The reducers can be either strong reducers, such as sodium borohydride, aldehydes, and amines, or mild reducers, including alcohol, trisodium citrate, and ascorbic acid. The size and the shape of the resulting AuNPs are significantly influenced by various parameters, such as the method (*i.e.*, chemical or physical), the reagent concentrations (the

precursor and/or capping agent), the reaction temperature, the reaction time, the solvent, and the addition rate of reactants. The wide variety in AuNPs shape (*i.e.*, rods, clusters, stars, triangles, cubes, cuboids, cages, spheres) offers opportunities to yield novel optical properties and uncover mechanisms that control the growth step, which can produce anisotropic gold nano-structures (Figure 4). This variety of synthesis opportunities stimulates researchers to further investigate AuNPs.

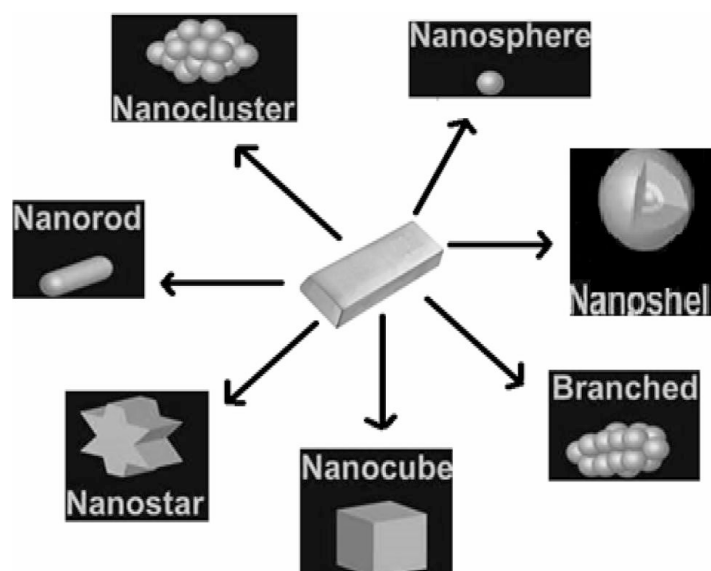


**Figure 4:** An overview of AuNPs shapes. Copied from Ref. (81), copyright 2014 (open access).

There are three main methods to synthesize AuNPs: physical, chemical, and biological, using top-down approaches. The physical method utilizes dispersion techniques to directly shatter large gold particles into AuNPs and involves microwave irradiation (82), ultra-violet irradiation (8), sonochemical methods (83), laser ablation (84), photochemical and radical-induced methods (85, 86), and thermolytic processes (87). The biological method uses fungi or bacteria as nanofactories (88, 89).

Synthetic approaches for AuNPs are well developed, in terms of control over their size, morphology, and surface chemistry, based on established chemical methods (bottom-up methods). They have some advantages, such as superior uniformity and adjustability of particle diameter, and ability to control the shape. The chemical reduction method is a common technique employed to produce AuNPs for X-ray CT imaging using many reducing agents. Several synthetic pathways involving a chemical reduction have been proposed toward this end, such as:

- (i) Citrate reduction method (carried out in the aqueous phase), using either citrate salts as both a reducing and stabilizing agent (90) or citrate tannic acid as a stabilizer to control the size range within 7.5-8 pH and a temperature of 60 °C. This allows the production of spherical AuNPs with a monodisperse size ranging from 3 to 17 nm (91, 92).
- (ii) Synthesis in an organic medium, such as toluene with sodium borohydride ( $\text{NaBH}_4$ ) in the presence of tetraoctylammonium bromide (TOAB) as a phase transfer reagent (93).
- (iii) Thiol compound-based AuNPs. This includes alkanethiolates in presence of  $\text{NaBH}_4$

which has been executed by Brust and Schiffrin to form alkanethiolate-protected AuNPs with a core size ranging from 2 to 5 nm (93).

(iv) Amine compound-based NPs, Gomez *et al.* reported that Au (I) complexes could undergo decomposition with alkylamines and form amine-protected AuNPs (94). Osterloh *et al.* synthesized monodisperse amine-protected AuNPs and AgNPs using oleylamine ligand (95). The difference between amine chemistry-based synthesis *vs.* thiols is that amine ligands can serve as both reducing agents and capping ligands for NPs (this means amine-based AuNPs synthesis can often be described as a single-phase-reaction system), whereas, in the thiol chemistry-based synthesis, an additional reducing agent other than thiol ligands, usually  $\text{NaBH}_4$ , needs to be added to the reaction. Since sodium borohydride is soluble in a polar solvent, such as water, and most thiol ligands are soluble in nonpolar organic solvents, such as toluene, thiol chemistry-based nanoparticle syntheses are thus conducted using a two-phase reaction system. Figure 5 illustrates the investigations of Lui *et al.* on the thermodynamic follow-up, the growth kinetics, and the mechanism of formation of  $\sim 10$  nm spherical oleylamine-stabilized AuNPs and how to control their size, in terms of time, during the nucleation process *via* uv-visible spectrophotometric measures (96).

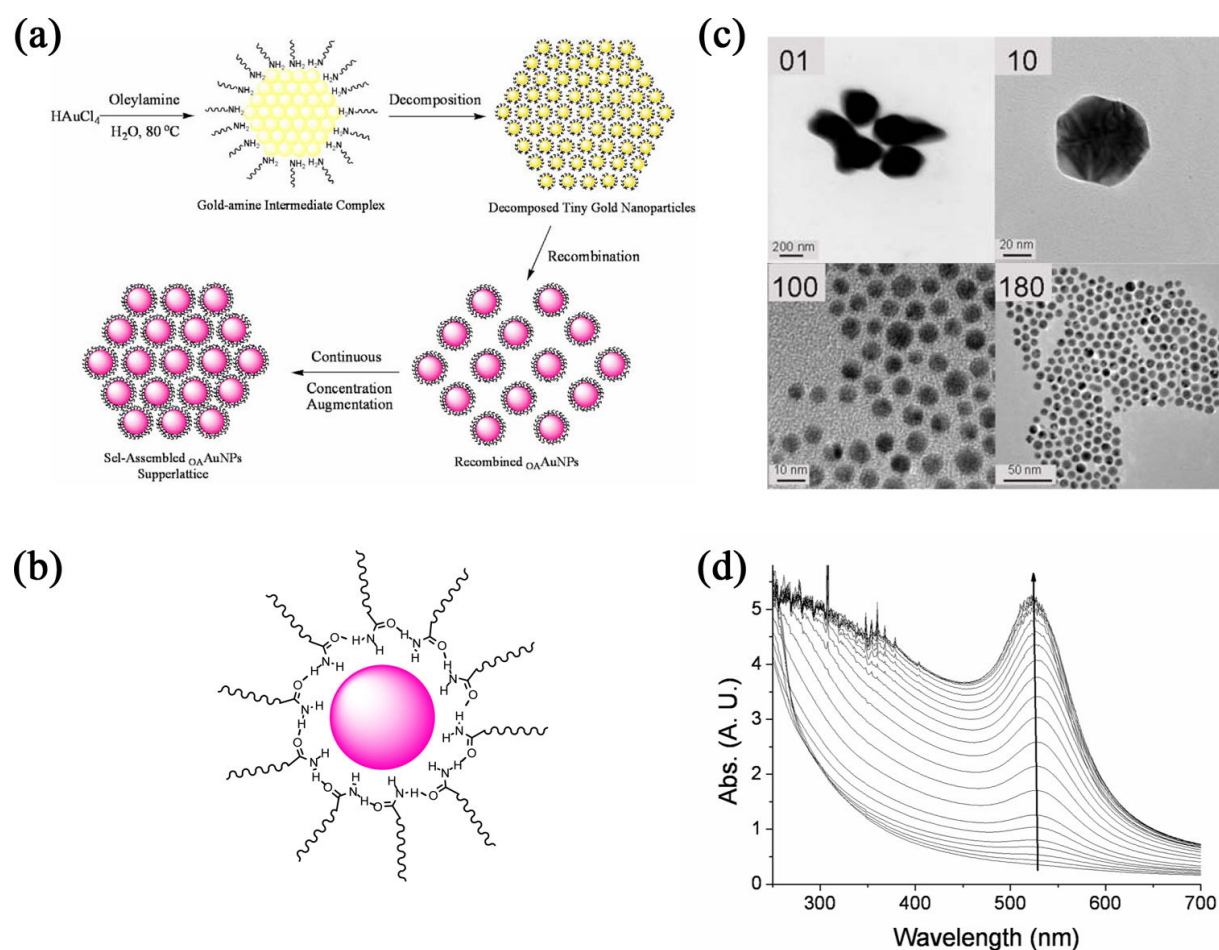


**Figure 5:** (a) An illustration of the AuNPs formation process using oleylamine as both a reducing and capping agent, (b) The composition of AuNPs formed, (c) TEM images of the intermediate product of gold nanoparticle growth collected at different reaction times (1, 10, 100, 180 min), (d) UV-visible spectra of the gold seeds solution measured between 32-212 minutes during the chemical reaction. Adapted from Liu Xiong *et al.* (96),

copyright 2007, American Scientific Publishers (ASP).

(v) L-tryptophan as a reducing agent for ionic gold and polyethylene glycol was used to produce  $\text{AuCl}_4^-$  ions to provide high stability and uniformity in size, shape, and particle distribution (97).

(vi) “Green chemistry“ using either the methanol extract of medicinal plants (98) or amino acid derivatives of serrapeptase as reducing agents provides stable environment-friendly AuNPs (99).

## **6.2 Chemical and biochemical properties**

### **6.2.1 Surface engineering of AuNPs, coating, and functionalization with ligands for active targeting**

Due to the inertness of AuNPs, in terms of reactivity, and their unique physical and chemical stability, they can be exploited in biomedicine as advanced tunable nanoplatfroms. It is well known that NPs generally need to be coated, embedded, chelated, or encapsulated to be protected from the external environment, and driven to a selected zone, by organic or inorganic capping layers or within nanocarrier cores. Bifunctional ligands are mainly used to i) stabilize the NPs by bonding to their surface through coordination bonds between pairs of electrons of ligands to the metal ions and ii) highlight a chemical function capable of selectively interacting with the receptors of the cells of interest to the surrounding environment. The need to target specific biomolecules through active targeting is essential for delivering DNA, peptides, and proteins into desired locations. This leads us to briefly discuss the modification or functionalization of nanocarriers. Nano-emulsions or liposomes are hardly subject to further chemical conjugation on their surfaces due to their aqueous formulations. However, the stabilizing agent or the coating shell that decorates the inorganic NPs enhances the chemistry of their surfaces.

The major reasons to modify AuNPs are i) to enhance the stability and water dispersion in order to prevent AuNPs from agglomeration and sedimentation during storage and usage, ii) to prolong vascular circulation (*i.e.*, reduce their capture by the reticuloendothelial organs such as the liver, kidney, and spleen) so that the AuNPs can effectively reach the imaging target, and iii) to facilitate targeting characteristics by attaching targeting molecules, such as antibodies and folic acids (commonly overexpressed by cancerous cells) onto the surface of AuNPs to increase their accumulation at the lesion location. A greater accumulation at the target improves imaging by increasing the HU value. It is anticipated that the targeted delivery of AuNPs might significantly reduce the dosage of AuNPs with better specificity, enhance efficacy, and avoid adverse side effects and toxicity issues. Furthermore, the biomedical applications involving functionalized AuNPs (*f*-AuNPs) are used to formulate, for example, bioassays to detect human IgG in serum samples, chitosan-AuNPs for quantitative detection of glucose, the detection of *E.coli* *via f*-AuNPs with antibodies, or enzyme immobilization.

The main challenge currently is to detect the location of tumors along with solutions for treatments (theranostics). Cancer cells overexpress specific biomolecules (hormones or receptors) on their surfaces. For instance, epidermal growth factor receptor (EGFR) helps in

---

the proliferation and survival of cancer cells, and the objective of *f*-AuNPs is to block these receptors, leading to cell death. Accordingly, several siRNA were used to block the expression of various genes: VEGF; UBB; and Hepatitis B Virus Surface Antigen (HBsAg). For VEGF, the AuNP-siVEGF was used against PC-3 cancer cells. A549 cells were used to validate the interference in UBB gene expression with AuNP-siUBB. In case of hepatitis B, HepG2.2.15 cells were treated with AuNP- siHBsAg. These results indicated that *f*-AuNPs are good candidates for DDS-based RNA delivery in anticancer or vaccine strategies, with reduced cytotoxicity when compared to classical PEI constructs, and exhibit good endosomal escape properties.

The impact of surface functionalization on the toxicity of AuNPs is directly linked to the altered biodistribution of *f*-AuNPs compared to non-functionalized AuNPs. The majority of AuNPs administered *in vivo* accumulate in the liver due to a non-specific bioaccumulation that results from a passive targeting strategy. The active targeting process thus aims to reduce the accumulation of AuNPs in non-targeted organs. However, this goal has not been realized as yet, especially for the targeted delivery of AuNPs. Indeed, the highly concentrated doses of *f*-AuNPs saturate the active receptors or targeted substrate, with the excess amounts being spontaneously directed to the non-targeted organs.—Therefore, dosing studies are critical for determining the minimum dose required to enhance contrast without inducing cytotoxicity in a given application and model. Basic research must be performed to understand this process. The modification of AuNPs can be achieved by covalent conjugation of biomolecules (e.g., glycosides, antibodies, peptides, and oligonucleotides) using carbodiimide coupling, Michael addition, cycloaddition, and hydrazone ligation, etc., whereas, non-covalent interactions include electrostatic conjugation, metal-affinity coordination, and biotin–avidin interaction (Figure 6). Alternatively, encapsulation of the prepared AuNPs can be achieved in lipid nanodroplets (liposomes or DEs), decorated by silica coating or biopolymer coatings (Figure 7).

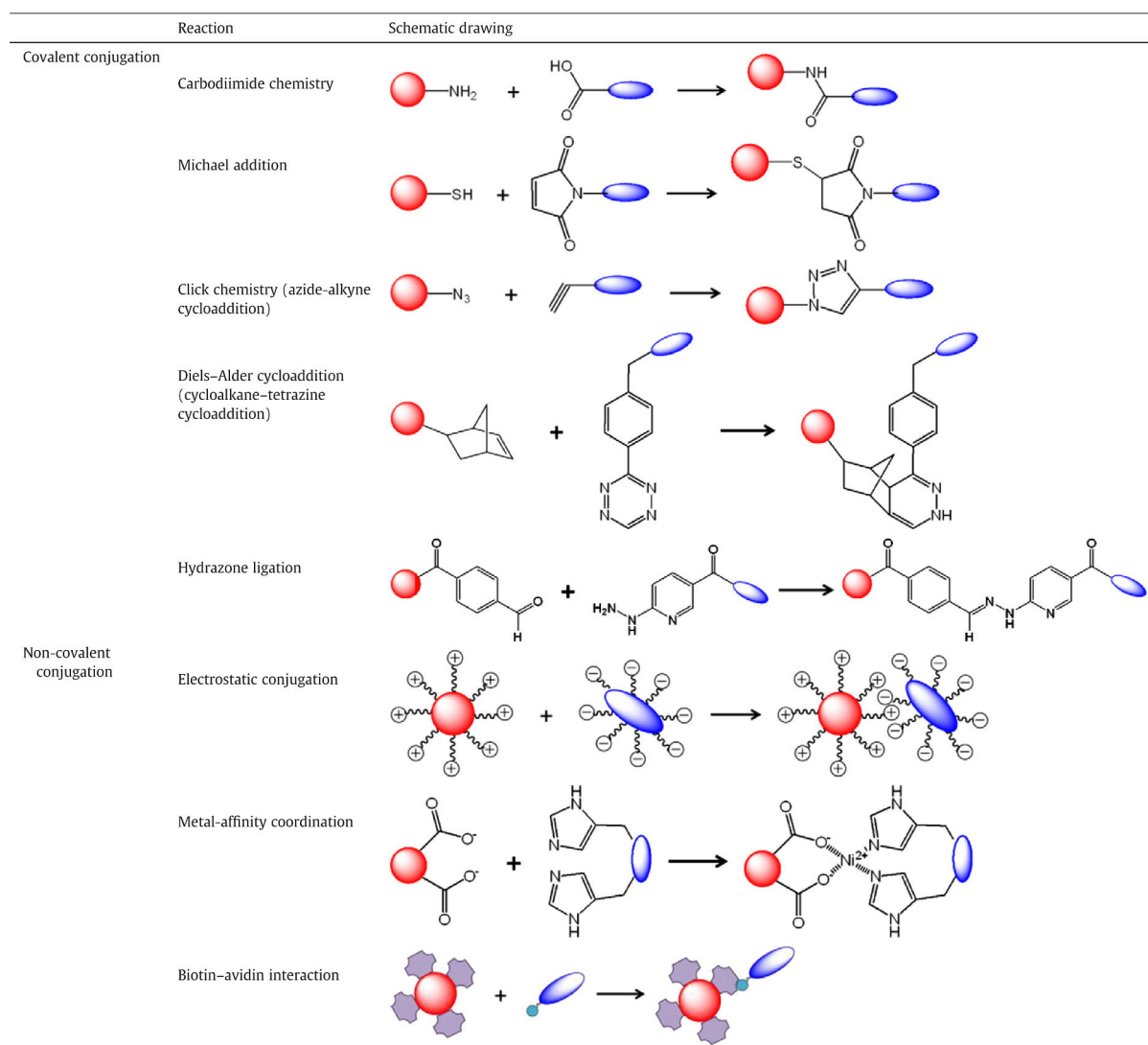


**Figure 6:** Different chemical reactions on the surface of AuNPs. Reproduced with permission from Ref. (100), copyright 2013, Elsevier.

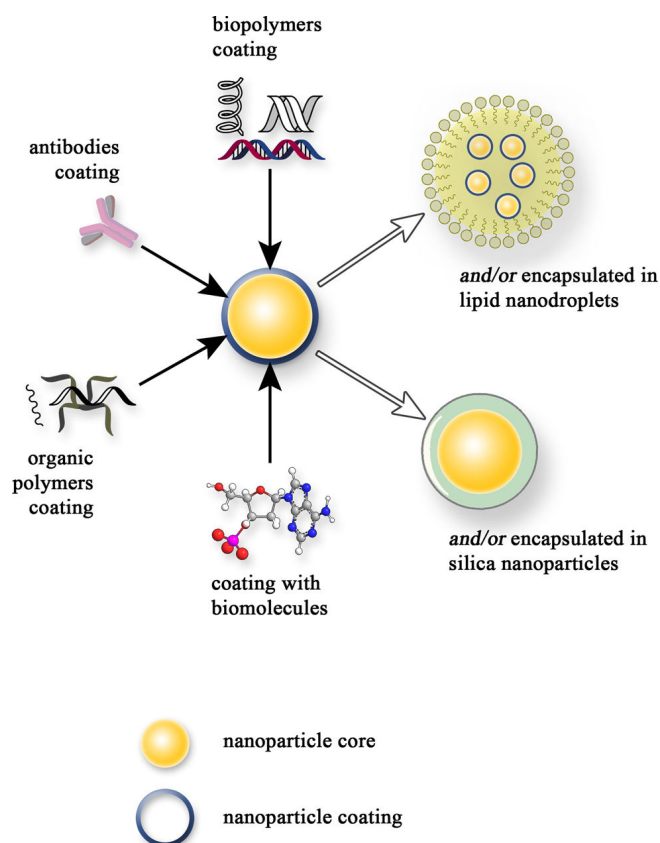


**Figure 7:** Several coating agents or ligands for AuNPs surface functionalizations. Reproduced with permission from (1), copyright 2012, Wiley.

### 6.3 *In vitro* and *in vivo* studies (targeting):

AuNPs can easily penetrate cell membranes, enter cells, and localize inside organelles, such as the endoplasmic reticulum and Golgi apparatus. The importance of such chemical and physical properties has been investigated to determine the pharmacokinetics, tumor uptake, toxicity, and biodistribution of the AuNPs. In Figure 8, selected studies illustrate the main differences in both *in vitro* experiments and *in vivo* testing of AuNPs.

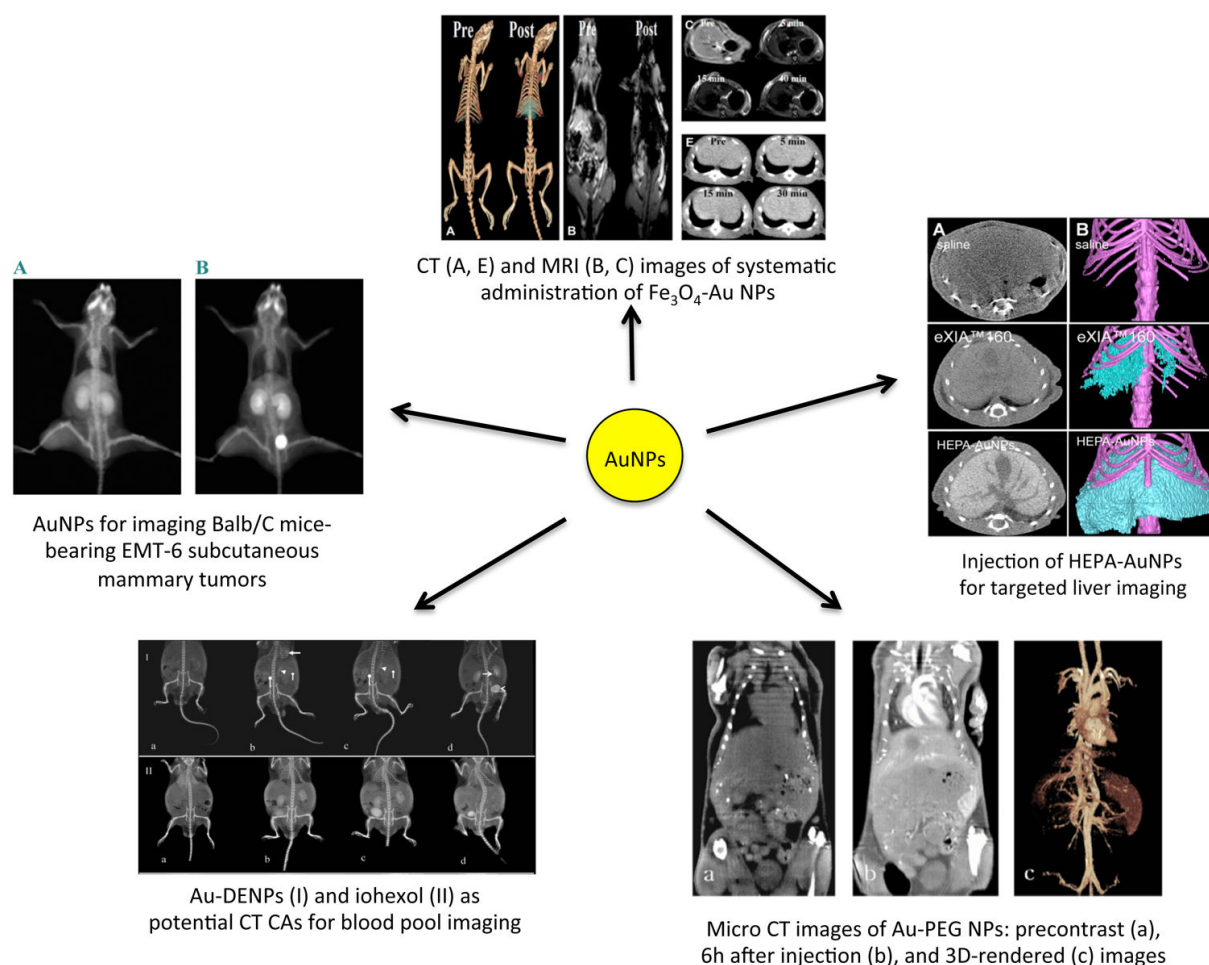


**Figure 8:** Selected examples for *in vivo* micro CT imaging of AuNPs. (Upper middle) Reproduced with permission from (101), copyright 2015, Elsevier. (Upper right) Reproduced with permission from (102), copyright 2009, Wiley. (Bottom right) Reproduced with permission from (103), copyright 2012, Royal Society of Chemistry (RSC). (Bottom left) Reproduced with permission from (104), copyright 2012, Springer. (Upper left) Reproduced with permission from (105), copyright 2015, Wiley.

### Size effects

AuNPs less than 3 nm in size are highly toxic due to irreversible binding to biomolecules (106). However, a size greater than 3 nm reveals low toxicity *in vitro* and *in vivo* (40, 107). A size of 10-20 nm exhibits the broadest biodistribution, helps to deliver a higher mass concentration with a lower number of particles, and improves contrast enhancement. HU values therefore depend on the mass concentration, but not on the number of AuNPs. A size greater than 6 nm is preferred to avoid renal filtration and toxicity. This is also less than the diameter of transvascular pores (~100 nm) that undergo passive or active tumor targeting.

Biodistribution studies suggest a size-dependent tissue infiltration (108). It has been reported that 4 nm and 13 nm of AuNPs were detected in the blood for 24 hours, but cleared by seven days. In contrast, 100 nm AuNPs were completely removed after 24 hours. Smaller sizes were observed in lymph nodes, with a slow elimination rate, unlike the larger size AuNP, which were rapidly taken up by the liver, spleen, and lymph nodes and leading to a faster elimination rate. Another study showed that AuNPs of 15 nm in diameter pass the blood brain barrier

(BBB) and localized in the brain (109). For much larger NPs (200 nm), biodistribution is completely different, with AuNPs distributed in the blood, stomach, and pancreas.

#### *Shape effects*

An *in vivo* study indicated that shape is a significant factor that may determine the AuNPs bio-fate (110). PEGylated gold nanorods (NRs) and nanospheres were synthesized and showed a high accumulation in the liver and spleen in mice bearing an ovarian tumor. However, NRs were found to accumulate more than nanospheres in other organs. Also, NRs had a longer circulation time compared to nanospheres.

#### *Surface charge effects*

It should be noted that AuNPs with a cationic surface charge present a much higher toxicity than those with an anionic surface coating. This is due to the *in vivo* interaction with biomolecules that are almost negatively charged species. Therefore, the cellular uptake affects the toxicity, the biodistribution, and the elimination rate as well.

#### *Functionalized ligands effects*

It has been suggested that CTAB-AuNPs or biological molecules, such as lecithin (111), could significantly reduce cytotoxicity, as lecithin did not show significant toxicity (112, 113). An *in vivo* study has also revealed a strong relationship between the nature of the AuNPs coating agent and their pharmacokinetics. For example, maltose-stabilized AuNPs were distributed in the lungs, whereas gum Arabic-stabilized AuNPs were distributed in the liver (114).

#### *Molecular weight of coating shell*

PEG-AuNPs designed with different PEG molecular weights indicated that high MW-PEG (long chains) stabilized the AuNPs and screened the surface charge better than low MW-PEG (short chains) (115). Decoration of AuNPs with PEGylated molecules enables conjugation with ligands and prevents the NPs from agglomeration. Moreover, the biodistribution of AuNPs is correlated to the polyethylene glycol used for functionalization and the injected dose (89).

#### *Concentration of administered AuNPs*

The concentration should be optimized to be less than the lethal dose and sufficiently high to induce a high X-ray absorption coefficient.

#### *Surface functionalization (f-AuNPs)*

Facile synthesis and molecular surface functionalization promote colloidal stability and make active targeting a significant advantage of AuNPs compared to other NPs. A variety of molecules can be conjugated to the surface of AuNPs, with thiol, disulfide, amine, carboxylate, and phosphine ligands commonly used to form linkages with AuNP surfaces. Therefore, it is useful for biolabeling, bioassay, clinical diagnosis, and therapy.

## 7 Gold-hybrid NPs

As we mentioned earlier, improving the contrast enhancement basically relies on the delivery of the largest mass to the site of interest. However, large doses of exogenous contrast media may cause adverse side effects *in vivo*, including toxicity. Therefore, an appropriate dose must be determined in order to enhance contrast without inducing cytotoxicity. One of the main limitations of CT compared to other imaging modalities is the relatively high mass concentration of CA required for contrast-enhanced imaging. Millimolar concentrations are required for CT, while an optimum concentration for MRI CA is in the micromolar range (116, 117).

The synthesis of multifunctional nanomaterials for biomedical applications is one of the most challenging issues. There is actually a real need to design AuNPs associated with other imaging agents, thus forming new hybrid NPs that can be valid not only for CT, but also for MRI and/or optical imaging. It is thought that dual- or multi-modal imaging techniques will improve imaging characteristics, which will overcome the drawbacks of low resolution and low sensitivity and the lack of molecular CT imaging compared to PET and MRI.

Multimodal imaging facilitates the performance of pharmacokinetics studies, helps elucidate complex mechanisms of drug uptake, gives insight into processes that affect and influence tumor growth and behavior, and thus, allows clinicians to obtain comprehensive morphological and molecular profiles of the imaged tissues. This information will improve the accuracy of clinical diagnostics by combining the advantages of each single imaging technique. A variety of CT/MRI, CT/MRI/optical imaging, CT/SPECT, CT/SERS, and CT/MRI/fluorescent multimodal imaging agents have been reported in recent papers. Other types of multimodal CAs are also in development: SPECT/fluorescence (118); PET/NIRF used with ICG (119); QDs (120); PET/MRI (121, 122); and even four modalities incorporating MRI/PET/BREFT/ fluorescence (123).

### 7.1 Gold-iron hybrid NPs

Of particular interest is the combination of gold and magnetic NPs, especially IONPs, which confers on the resultant hybrid nanocomposites (NCs) a surface plasmon property for optical and X-ray attenuation properties on CT imaging due to the gold element and dark contrast for MRI imaging due to the IONPs.

The rationale for the design of AuNPs associated with supraparamagnetic IONPs as a  $\text{Fe}_3\text{O}_4@Au$  core/shell NCs is shown in Figure 9. Constructing nanoparticles with more than two moieties is not only used for biomedical imaging, but also for photothermal therapy, controlled DDS, biosensors, protein separation, DNA detection, and immunoassays (124-130).

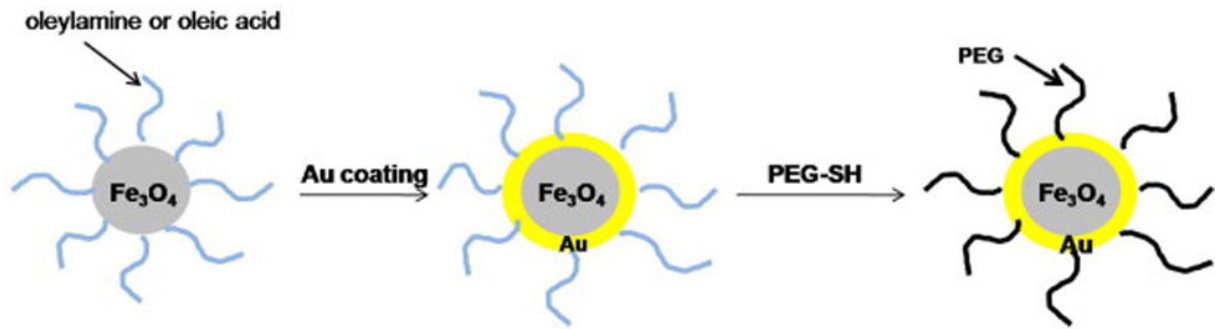


**Figure 9:** Synthetic scheme for the preparation of PEG-coated  $\text{Fe}_3\text{O}_4@Au$  core/shell NCs. Reproduced with permission from (2), copyright 2012, Elsevier.

The key advantage of using these NPs is to minimize patient exposure time to radiation and to produce very high resolution of soft tissues and biological compartments. One of the characteristics of the  $\text{Fe}_3\text{O}_4@Au$  core/shell NCs is that they can follow active targeting mechanisms by functionalizing the surface of the gold shell, undergoing the passive targeting, or following magnetic targeted drug delivery (MTD), by applying an external magnetic field on the location of interest to promote the IONPs NPs attraction near or within the desired target. Although the disadvantage of the formed NCs is the low water solubility, this can be improved either by NPs bioconjugation or by their entrapment in a coating layer, such as nanoemulsions, dendrimers (DE), or polymers (PEGylated chains for cytocompatibility).

Fabrication of the  $\text{Fe}_3\text{O}_4@Au$  core/shell structure is achieved by initial synthesis of the core IONPs, which can be achieved through several processes, including co-precipitation, thermal decomposition, the reversed micelle technique, and the solvothermal method. Two standard types of  $\text{Fe}_3\text{O}_4@Au$  NCs were designed: i) a bi-layer based on a magnetic core and gold shell; or ii) a multi-layer composite structure consisting of a magnetic core, glue material (silica (131), polymers (132, 133) and others (134) and gold shell (Figure 10). The most common protocol for their synthesis is the formation of a gold shell directly onto the magnetic surface, which is prepared beforehand, and subsequently incorporating the IONPs into an  $\text{HAuCl}_4$  solution, followed by adding a sodium citrate reducing agent for Au shell formation due to the ligand exchange of the iron by the coated gold layer. (Jeff, this whole paragraph is really confusing...really terrible)

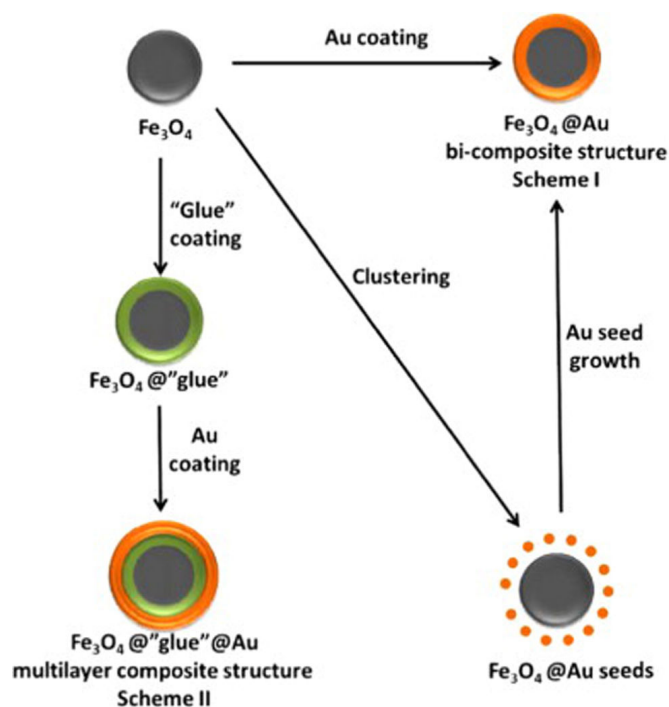


**Figure 10:** Schematic representation of different approaches for the synthesis of Fe<sub>3</sub>O<sub>4</sub>@Au core/shell NPs. Reproduced with permission from (135), copyright 2015, Elsevier.

Recently, Jingchao Li and coworkers (129) reported a facile one-pot synthesis of gold/iron NCs coated with a monomethylether of polyethylene glycol-modified polyethyleneimine polymer (*m*PEG-PEI-NH<sub>2</sub>) using NaBH<sub>4</sub> as a reducing agent to obtain *m*PEG-PEI-NH<sub>2</sub> AuNPs, mixing all with iron (II) precursor to yield Fe<sub>3</sub>O<sub>4</sub>@Au-*m*PEG-PEI-NH<sub>2</sub> NPs that showed hematocompatibility and non-toxicity *in vitro*. Such an assembly exhibited relatively high  $r_2$  relaxivity (146.07 mM<sup>-1</sup> s<sup>-1</sup>) and good X-ray attenuation properties as well, which enables their utilization for the *in vivo* MR imaging of mouse liver and the *in vivo* CT imaging of rat liver and aorta.

A similar study published by Hongdong Cai *et al.* (136) reported a unique folic acid (FA)-modified DE-assisted approach to create Fe<sub>3</sub>O<sub>4</sub>/Au-FA NC particles with a tunable molar ratio of Au:Fe<sub>3</sub>O<sub>4</sub> (2.02), which displays a relatively high  $r_2$  relaxivity (92.67 mM<sup>-1</sup> s<sup>-1</sup>) and good X-ray attenuation value and provides biocompatibility and low toxicity in the given concentration range. Interestingly, the Fe<sub>3</sub>O<sub>4</sub>/Au-FA NCs are specifically taken up by cancer cells that overexpress FA receptors *via* active targeting in order to be an efficient nanoprobe for targeted dual mode (CT/MRI) imaging of a xenograft tumor model.

A further study developed a Au/Fe/Au plasmonic NPs loading methotrexate (MTX), a drug (137) that can be used for magnetic targeted chemo-photothermal treatment of arthritis. Their intravenous injection into CIA mice revealed MR images of NPs accumulation in the inflamed paws of mice after attraction to the targeted zone by external magnetic fields. NIR irradiation increased the temperature of the exposed area and accelerated the release rate of the drug from the NPs, allowing the chemo-photothermal treatment. Moreover, the combination of consecutive NIR irradiation and external magnetic field applications gave rise to higher therapeutic efficacy against conventional treatment.

## 7.2 Gold-gadolinium hybrid NPs

Similarly, the formation of new hybrid nanosystems based on gadolinium is an essential for providing dual-function CA for CT/MR imaging modalities. Basically, gadolinium (III), which has seven unpaired electrons and a large magnetic moment, can significantly influence the water proton relaxation and so exhibits excellent MRI contrast.  $Gd^{3+}$  chelate-based NPs are of great interest due to their adapted biodistribution and passive uptake in the tumor as a result of the EPR process. Moreover, they can act as effective radiosensitizers under different types of irradiation (radiotherapy, neutron therapy, or hadron therapy).

Various procedures have been followed to formulate gold-grafted gadolinium (Au-g-Gd) to be exploited either as a bimodal diagnostic agent and/or as a drug carrier.  $Gd^{3+}$  chelates are synthesized based on attaching such ligands to gadolinium metal *via* coordination bonds and donation of the lone pair of electrons from the ligand to the metal ion. Basically, many ligands might be used in  $Gd^{3+}$  chelates, *i.e.*, alkyne-derived diethylenetriamine (DTTA), dithiolated diethylenetriamine-pentaacetic acid (DTDTPA), ethylenediaminetetra acid (EDTA), 1,4,7,10-tetraazacyclododecane- 1,4,7,10-tetraacetic acid (DOTA), modified-polyacrylic acid (m-PAA), etc. Two well-known strategies have been reported for yielding Gd/Au NCs: The first relies on Gd-coated Au (138), since the particles were obtained by encapsulating gold cores within a multilayered organic shell composed of  $Gd^{3+}$  chelates bonded to each other through disulfide bonds (S-S linkage), as presented in Figure 11.

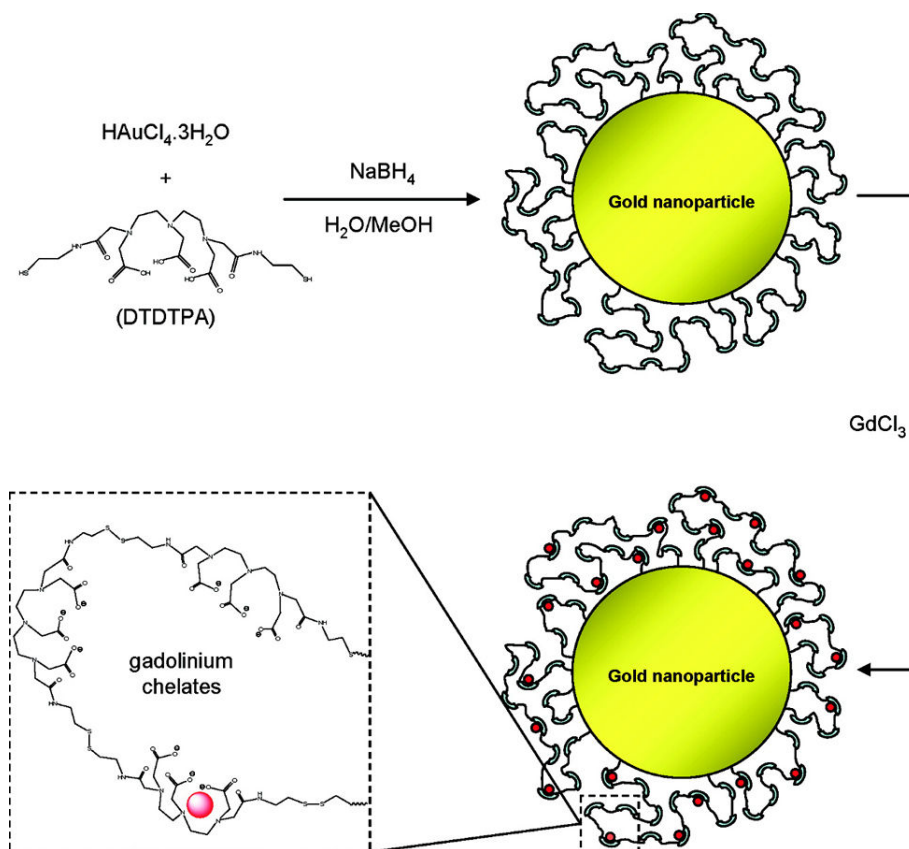


**Figure 11:** Synthetic pathway of Au-g-Gd NPs. Reproduced with permission from (138), copyright 2008, the American Chemical Society (ACS).

The contrast enhancement in MRI stems from the presence of the entrapped gadolinium ions in the organic shell, whereas the gold core provides a strong X-ray absorption. The second approach is Au-coated Gd, which has been reported by Wang *et al.* (139, 140), and forms the Gd<sup>3+</sup> chelate template decorated by AuNPs seeds that combine the advantages of each element in bioimaging applications.

A synthetic approach (141) was reported for the development of novel NCs with high relaxivities and a lower mass gold content, which is often distinct from the gold cluster compounds that contain a large amount of gold. The idea is to deposit the Gd-based macromolecular complex layer on AuNPs for stabilization and to improve the gold functionalization. These colloids exhibit high relaxivity and contrast enhancement when using 0.15 wt.%, yielding an efficient dual modal CA for CT/MR imaging techniques.

Xiangyang Shi's research group (142) also synthesized FA-modified Au-dendrimeric NPs (FA-modified Au-DENPs) loaded with Gd<sup>3+</sup> chelates instead of IONPs for dual-imaging purposes. The resultant Gd-Au DENPs-FA probes presented comparable results that displayed high X-ray attenuation intensity and reasonable  $r_1$  relaxivity. In addition, the relaxivity  $r_2$  of Gd-Au DENPs-FA was (87.892 mM<sup>-1</sup>s<sup>-1</sup>), which is 1.22 times higher than that of G5-Gd-FA (72.264 mM<sup>-1</sup>s<sup>-1</sup>), ensuring added value to the dual-function CAs. These properties made them ideally suited for CT/MR imaging of cancer cells *in vitro* and a xenograft tumor model *in vivo* via the FA receptor-mediated active targeting pathway. Accordingly, they succeeded in another study (143) in designing the Gd-Au DENPs-RGD by simply conjugating the terminated NH<sub>2</sub> group of the DE with an RGD peptide. The *in vitro* results proved the negligible toxicity at an Au concentration up to 100 μM. With the displayed X-ray attenuation property, the  $r_1$  was (2.643 mM<sup>-1</sup>s<sup>-1</sup>) and showed hemocompatibility, and this was also suited for targeted dual-modality CT/MR imaging of a xenograft tumor model overexpressing the  $\alpha_v\beta_3$  integrin *in vivo*.

Lijun Wang *et al.* (139) have emphasized that a Gd-doped, layered, double hydroxide (LDH)/Au NCs platform can be used as both an anticancer DDS and as a diagnostic agent. The LDH-Gd/Au NCs demonstrated high DOX loading capacity (264 mg drug/g of NCs) with an interesting pH-responsive release feature. Meanwhile, the NCs have been found to be better CT and MRI CAs during *in vitro* evaluation than the commercial CT agent, iobitridol, and the MRI agent, Magnevist. *In vitro* experiments showed negligible toxicity vs Hela cells and L929 cells. *In vivo* results revealed that NCs are taken up more by the spleen than the liver. In the same study, these investigators functionalized the NCs by coating them with heparin, resulting in outstanding CT/MRI contrast, and were used to image mice bearing tumors *in vivo*.

### 7.2.1 Gold-silica nanosystems and other hybrids

The element silicon (Si) is the second most abundant element in the earth's crust. It has been found in the general form of silicon oxides or silicates, such as SiO<sub>2</sub>, TEOS, APTES, and their derivatives. It is highly reactive due to its tetravalent state.

Among inorganic NPs, silica NPs (SiNPs) are one of the most biocompatible nanoparticles approved by the FDA. They offer numerous advantages over inorganic NPs, such as well-defined, tunable structures in shape and size. As demonstrated by our research group, forming an amino silica shell coating for nanodroplet nanoemulsions resulted in a tunable spherical shape against the non-coated silica shell, which was clearly demonstrated on TEM micrographs (144). These coatings can be easily prepared from inexpensive materials and simple functionalization due to the chemistry of siloxanes, or can even be loaded onto other materials. Silica nanostructures have high chemical stability, including resistance against enzymatic degradation (145, 146). Moreover, they do not interfere with magnetic radiation. The fluorescent silica NPs, known as “Cornell Dots,” were approved for the first time in 2011 by the FDA, in a human clinical trial, as imaging agents for a human melanoma model (147). SiNPs were successfully applied for diagnostic and therapeutic purposes. The synthetic approaches successfully generated silica as a core (148), a shell (149), or in the interface between multilayered NCs (149, 150), depending on the characteristics needed and the specific applications.

Several investigations have been performed to introduce silica-based NCs for *in vivo* and *in vitro* studies. L. Marques and co-workers (148) have synthesized new hybrid particles, poly (allylhydrochloride)/silica/gold (PHA/SiO<sub>2</sub>/AuNPs) functionalized with biotin as a biosensor for detecting streptavidin protein (SV). The generated 300 nm silica cores were decorated with AuNPs seeds on their surface. The key advantage of the proposed NCs is that it is easily tailored by changing ligands to allow the targeting of clinically relevant protein compounds. However, Kuo-Wei Hu *et al.* (150) presented hybrid NPs based on three moieties: Gd<sub>2</sub>O(CO<sub>3</sub>)<sub>2</sub>.H<sub>2</sub>O/silica/Au particles. Initially forming a Gd<sup>3+</sup> chelate core shielded by a silica layer due to the condensation of the precursor TEOS and the reaction of APTES, the nanoconstruct was finally conjugated to the AuNPs, eventually obtaining the Gd/Si/Au NPs. The thickness of the formed Au shell substantially affected the MRI performance and the photothermal destruction of cancer cells. Decreasing the Au thickness (concentration) spontaneously induces higher MRI values, giving the optimum photothermal cancer destruction and *vice versa*. This is simply because the MRI effect is dependent on the Gd<sup>3+</sup> chelate concentration, whereas the photothermal process is influenced by the Au concentration.

## 8 Miscellaneous multifunctional CAs

The importance of multifunctional CAs is to reduce procedural steps by gathering more than one type of information from a single NP. Therefore, organic fluorescent dyes, Qds, and other precursors might be incorporated into hybrid nanosystems and thereby impart additional properties to the material. Herein, we show such examples to explain this process. For instance, Wenjie Dong *et al.* (149) have developed a bimodal imaging agent, Au/Si/QDs, using a reverse microemulsion method to prepare Au@SiO<sub>2</sub>, followed by the formation of CdSe-ZS QDs on the surface and then coating again with modified silica (SiO<sub>2</sub>-PVP). This resulted in Au@SiO<sub>2</sub>-QDs/SiO<sub>2</sub>-PVP NCs that displayed high fluorescence intensity and good

---

X-ray absorption to be suitable as a bimodal imaging probe for CT/fluorescent imaging techniques.

Another study (151) showed a simple route for the preparation of trimodal CA, called  $\text{Fe}_3\text{O}_4$ @dye-hybrid@Au NCs, as described in Figure 12. The *in vitro* cytotoxicity measurements of the NPs were assayed against different cell lines, including breast cancer MCF-7 and mouse fibroblast L929 cells, and low toxicity and high biocompatibility were observed. However, the evaluation of the PEG- $\text{Fe}_3\text{O}_4$ @dye-hybrid@Au resulted in both high HU values and induced MRI contrast, allowing visualization of the location of tumors with both CT and MRI *in vivo*.

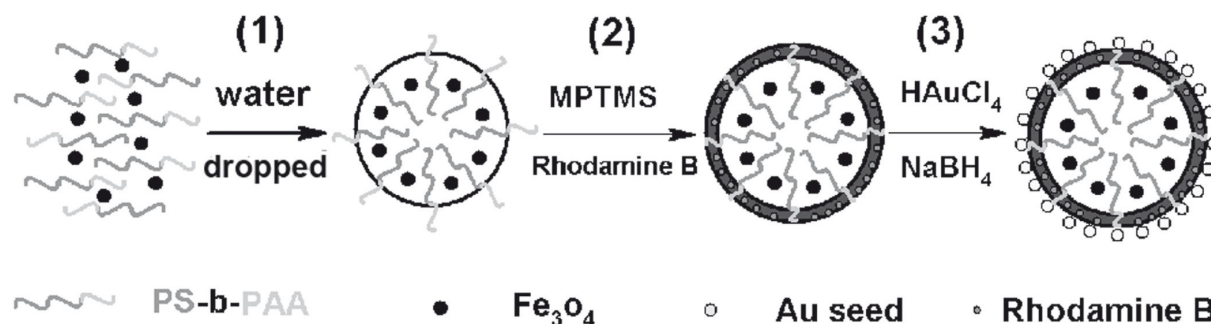


**Figure 12:** Schematic diagram of formulation process of  $\text{Fe}_3\text{O}_4$ @dye-hybrid@Au NPs. Reprinted with permission from (151), copyright 2013, Wiley.

A green and facile method (152) was designed to synthesize a multifunctional nanosystem ( $\text{Fe}_3\text{O}_4$ @C@Ag) of 200 nm diameter as a bimodal imaging probe and DOX-loaded  $\text{Fe}_3\text{O}_4$ @C@Ag as a DDS. The loading content was 997 mg/g. The *in vitro* cell viability tests revealed good biocompatibility. The obtained NCs were used in dual-mode imaging—two-photon fluorescence (TPF) imaging and MRI due to the magnetism of  $\text{Fe}_3\text{O}_4$  and the (SPR) of AgNPs.

Constructing an optical bi-probe with both plasmonic and fluorescent components has been achieved by Wu *et al.* (153) via synthesis of AuNPs with a silica coating decorated with high brilliant CdSe/CdS/ZnS QDs. The silica layer was imbedded to minimize the spectral overlapping and to avoid FRET between AuNPs and QDs. The resulting NCs as (AuNRs@Si@QD@Si) were then modified with a PEG shell and transferrin conjugation (PEG-AuNR-QD-Tf), which provided low toxicity and efficient cancer cell targeting on A549 cells *in vitro*. Both fluorescent and dark-field co-localization was achieved with high contrast. The last example is the combination of the trivalent lanthanide ions, which have luminescence and magnetic resonance imaging signal outputs with a tunable size, allowing the formulation of tailored nanoprobe ideally suited to the investigation of biological systems. In accordance with the aforementioned protocol of Gd/Au hybrid nanosystem synthesis, other lanthanide ions were incorporated with gold, which provided many new hybrid nanoplatforms. S. Bohic *et al.* (154) have developed four different nanosystems, including Au@Eu, Au@Ce, Pt@Eu, and Pt@Ce. Other nanoplatforms, such as Au@Eu<sup>3+</sup>/Tb<sup>3+</sup>, have been fabricated by Thomas and co-workers (155), as shown in Figure 13.

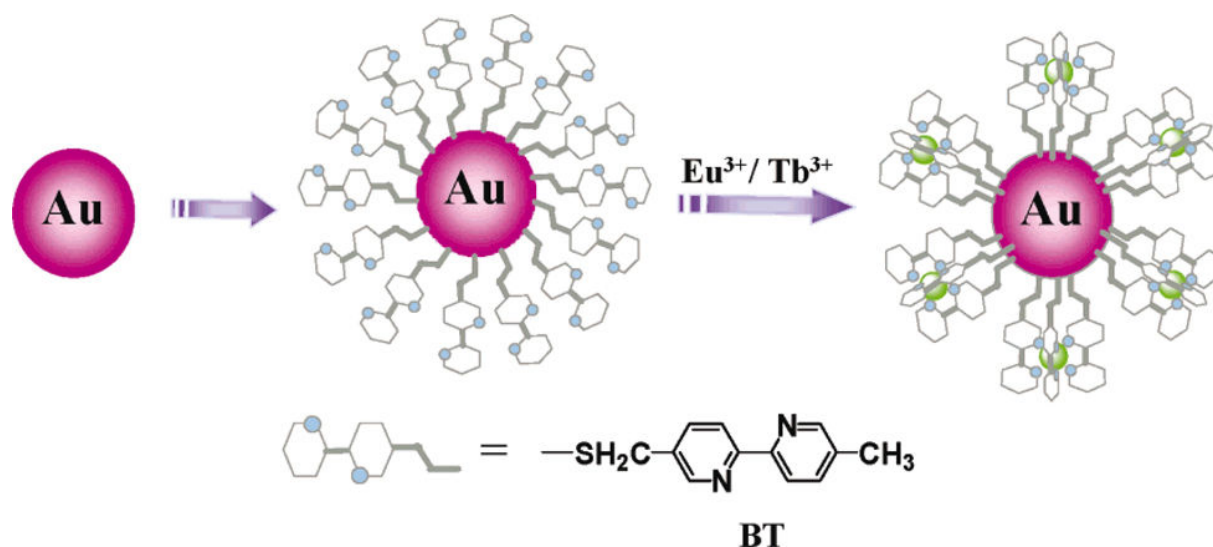


**Figure 13:** Design strategy for luminescence nanomaterials (Au/Eu<sup>3+</sup>/Tb<sup>3+</sup>) NPs. Reproduced with permission from Ref. (155), copyright 2006, the American Chemical Society (ACS).

## 9 Silver-based CA

In 1905, Collargol (a colloidal silver preparation) was used in urinary tract radiography (156). Later, other silver compounds, such as AgI and Ag<sub>2</sub>O, were used as contrast materials in retrograde pyelography (157). This procedure was quite useful in the diagnosis of dilation, kinking, and displacement of the renal pelvis and ureter, as well as in the detection of renal malformations and renal tumors. As recently as 1979, a silver iodide colloid was used as a model compound in an animal study in order to determine the suitability of metal NPs as hepatobiliary CAs for CT (158). However, the use of these silver agents was discontinued due to severe side effects and significant toxicity (159). AgNPs also showed excellent behavior in surface-enhanced Raman scattering for advanced Raman spectroscopy, which has the potential for a broad range of applications in clinical molecular imaging (160). Moreover, AgNPs displayed strong activities in anti-bacterial, anti-fungal, and anti-viral studies (161-165). Various synthetic routes are currently used to develop stable AgNPs, including diagnostic biomedical optical imaging and other biomedical applications (166). AgNPs were fabricated in a HEPES buffer and exhibited potent cytoprotective and postinfection anti-HIV-1 activities toward Hut/CCR5 cells (167). New synthetic protocols have been reported elsewhere (168-171).

Recently, Zou *et al.* (172) have employed AgNPs as a CA for micro CT visualization of the middle and inner ear of the rat and the transportation pathway after transtympanic injection. They prepared AgNPs in various concentrations (1.85, 37.1, and 370.7 mM) before administration to rat middle ear cadaver heads. These were imaged using micro CT at several time points. The minimum concentration of AgNPs that gave reasonable contrast was 37.1 mM, which was visible in the middle ear at 7 d post-administration. AgNPs at 370.7 mM generated signals in the middle ear, ossicular chain, round window membrane, oval window, scala tympani, and Eustachian tube at both four-hour and 24-hour time points, providing the

imaging evidence that AgNPs are able to access the inner ear in a dose-dependent manner after intratympanic administration. A study was performed by Adrian Chrastina and Jan E. Schnitzer (173) to investigate the biodistribution of AgNPs. They have developed a rapid method for radiolabeling of AgNPs with iodine-125 in order to track the *in vivo* tissue uptake of AgNPs after systemic administration using biodistribution analysis and (SPECT) imaging, and demonstrating uptake in the liver and spleen. Many studies indicated that AgNPs alone or associated with other inorganic metals, such as Gd or Au, are efficient delivery systems for both imaging agents and therapeutics (174-176).

## 10 Bismuth-Based Agents

Bismuth is also an appealing element upon which to base CT CAs. It is used as a viable alternative to AuNPs due to numerous advantages: i) a high atomic number ( $Z = 83$ ), which results in good X-ray-attenuating properties (absorption K-edges = 91); ii) approximately 1000-fold less expensive than gold elements; and iii) one of the most biocompatible elements among the heavy elements. However, its ionic form is toxic at 0.2 M (177). It is well known that metallothioneine, a cysteine-rich protein abundant in the kidneys, exhibits a preferential affinity for Bi(III) species, and thus, enhances the clearance and urinary excretion of Bi(III) complexes (178). Moreover, Bi(III) complexes could be exploited as DDS, biosensors, injectable CT CAs, and even as photothermal therapy (PTT) agents in the biomedical area. Few challenges face the bismuth NPs with regard to size, morphology, or surface chemistry, compared to AuNPs.

Several approaches for synthesizing BiNPs as CT CA have been reported, for instance, using the precursor bismuth nitrate pentahydrate, which is the source of the Bi(III) cation, to produce stable bismuth glyconanoparticles (BiGNPs) using an aerobic method in the presence of sodium borohydride ( $\text{NaBH}_4$ ) for reduction. Rabin *et al.* were the first to report bismuth NPs as CT CAs (179). They prepared bismuth sulfide NPs by co-precipitation of bismuth citrate and sodium sulfide in the presence of 3-mercaptopropionic acid, acting as a surfactant. The NPs were further coated with polyvinylpyrrolidone (PVP), resulting in plate-shaped NPs and showing negligible toxicity when tested on hepatocytes and macrophages below 20 mM of Bi. *In vivo* CT imaging was performed on mice, giving rise to a blood pool agent ( $t_{1/2} = 140$  min) with a maximum enhancement of 557 HU.

In recent years, bismuth-based nanomaterials, such as  $\text{Bi}_2\text{S}_3$  NPs,  $\text{Bi}_2\text{S}_3$  NRs,  $\text{Bi}_2\text{Se}_3$  nanoplates, and  $\text{Bi}_2\text{S}_3$  nanodots, conveniently integrate a broad range of clinically relevant functionalities. A general protocol has been applied to synthesize oleic acid-coated bismuth sulfide NPs ((OA- $\text{Bi}_2\text{O}_3$ ) NPs). Subsequently, the hydrophobic oleate surface coating can be dispersed in organic solvents to facilitate their surface modification using a hydrophilic coating shell *via* a ligand exchange reaction like tween-20 (180), polyvinyl pyrrolidone (PVP), D- $\alpha$ -Tocopherol Polyethylene Glycol 1000 Succinate (TPGS) (181), or PEG<sub>5000</sub>-DSPE.

In 2015, Yuliang Zhao and coworkers published two studies focusing on the establishment of  $\text{Bi}_2\text{S}_3$  NRs in nanomedicine. The first study (180) was about precision cancer nanomedicine

based on  $\text{Bi}_2\text{S}_3$  NPs. These authors successfully designed  $\text{Bi}_2\text{S}_3$  NRs for multispectral optoacoustic tomography (MSOT)/X-ray CT-guided photothermal therapy (PTT). These characteristics made  $\text{Bi}_2\text{S}_3$  NPs simultaneously act as “satellite” and “precision targeted weapon” for a visual guide to destroy tumors *in vivo*. A cell viability assay was carried out on 4T1 cells, indicating biocompatible NPs with “no dead cells up to 300  $\mu\text{g}/\text{ml}$ .” *In vitro* photothermal effects were tested on 4T1 cells with different concentrations of the  $\text{Bi}_2\text{O}_3$  NRs, kept for 24 hours, and irradiated for eight minutes using an 808 nm laser. This afforded a high efficient destruction of tumor cells. *In vivo* X-ray imaging applied to mice bearing 4T1 tumors showed the difference before and after injection, highlighting all the vascular structures because of the good X-ray absorption (182) of  $\text{Bi}_2\text{S}_3$  NRs. Finally, *in vivo* photothermal therapy was achieved by *i.v* injection of 20 mg  $\text{kg}^{-1}$  under 808 nm laser irradiation. The average weights of tumors were collected from the mice at the end of photothermal therapy, and revealed no obvious metastases in the  $\text{Bi}_2\text{S}_3$  NRs + laser group by HE staining. A complete investigation was undertaken on BiNRs from the synthesis and finalized by the *in vivo* treatment of tumors, as described in Figure 14.

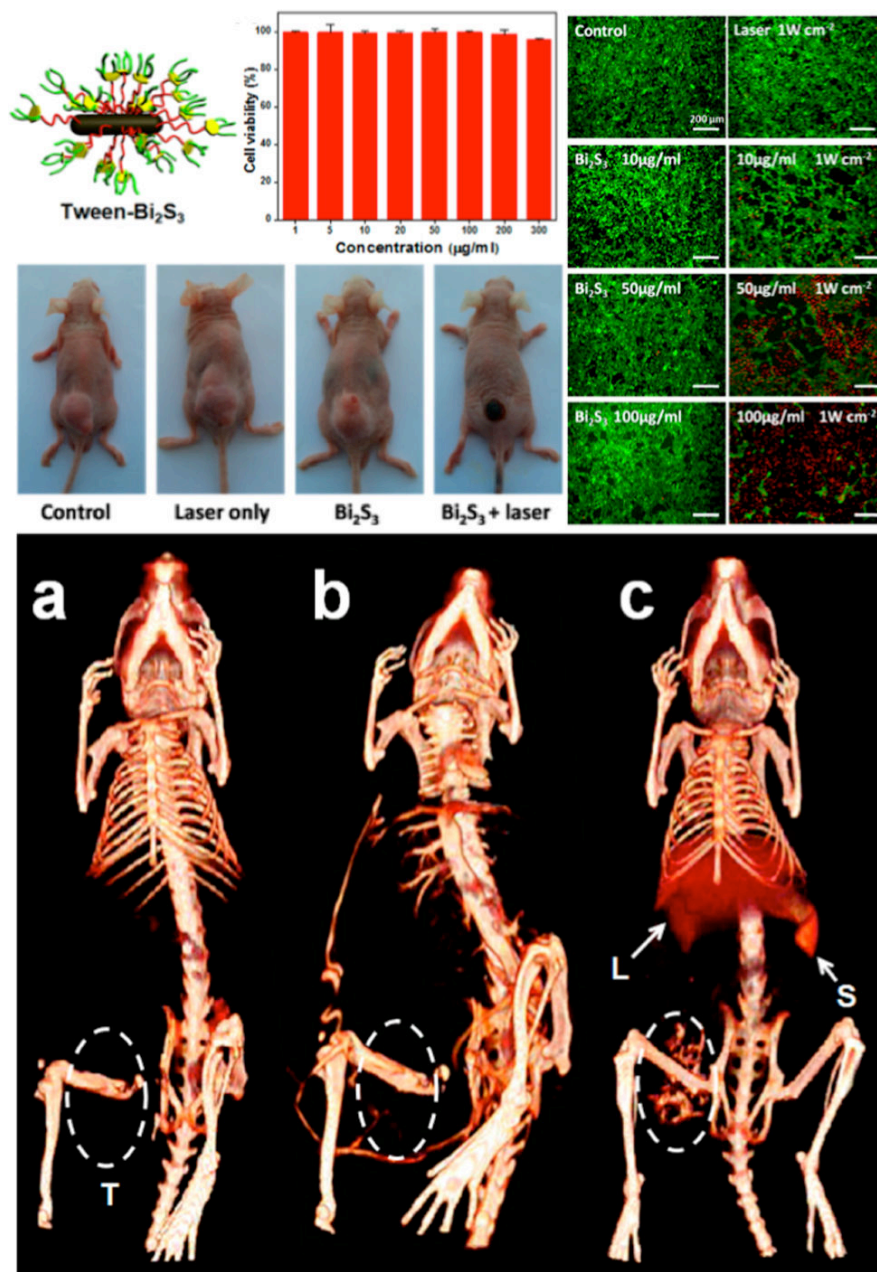


**Figure 14:** A) Schematic depiction of the structure of a Bi<sub>2</sub>O<sub>3</sub>-Tween20 NRs. (B) Cell viability of 4T1 cells after cultured with various concentrations of Bi<sub>2</sub>S<sub>3</sub> NRs for 24 h. (C) *In vitro* photothermal effect. Live-dead staining of 4T1 cells. 4T1 cells were incubated with different concentrations of Bi<sub>2</sub>S<sub>3</sub> NRs for 24 h and irradiated for eight minutes using an 808 nm laser (1W cm<sup>-2</sup>). (D) Representative photos of mice after different treatments 14 days after treatment. (E) *In vivo* X-ray CT imaging in 4T1 tumor-bearing mice. CT images of mice before injection (a), five minutes post *i.v.* injection (b), and three hours post *i.v.* injection (c) with Bi<sub>2</sub>S<sub>3</sub> NRs. Liver (L), spleen (S), and tumor (T). Figure adapted with permission from Jing Liu *et al.* (169), copyright 2015, the American Chemical Society (ACS).

The second study (181) demonstrated the development of multimodal CA based on Bi<sub>2</sub>S<sub>3</sub>@SiO<sub>2</sub> NRs for the non-invasive visualization of the GI tract. Simple synthesis of Bi<sub>2</sub>S<sub>3</sub> was performed by the solvothermal method, followed by a functionalization step through D- $\alpha$ -Tocopherol Polyethylene Glycol 1000 Succinate (TPGS), inducing TPGS-Bi<sub>2</sub>S<sub>3</sub> NRs. Coating with a thin silica layer improved biocompatibility, dispersion, and stability in the

harsh environment of the GI. The coating also reduced concern about the release of Bi ions. *In vitro* cytotoxicity studies performed on 16 HBE cells showed low toxicity and high biocompatibility. An *in vitro* evaluation of both CT and PAT demonstrated significant values. *In vivo* X-ray CT imaging of the GI in BALB/c nude mice after oral administration of  $\text{Bi}_2\text{S}_3@\text{SiO}_2$  NRs was obtained and the small intestine was clearly observed, as depicted in Figure 15.

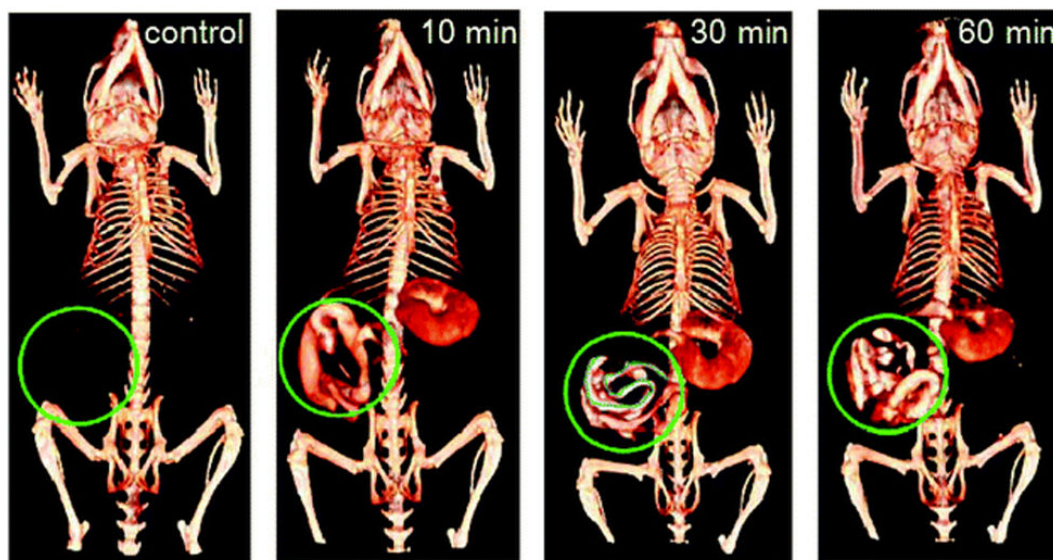


**Figure 15:** CT imaging of the GI *in vivo*. *In vivo* X-ray CT imaging of the GI in BALB/c nude mice at different intervals after oral administration of  $\text{Bi}_2\text{S}_3@\text{SiO}_2$  NRs. Reprinted with permission from (170), copyright 2015, Royal Society of Chemistry (RSC).

Recently, S Veintemillas-Verdaguer *et al.* (183) have developed a bismuth-labeled magnetic colloid through the combination of iron and bismuth in one entity, which could overcome the shortcomings of two imaging modalities and leverage the advantages of both, providing improved precision, feasibility, and efficacy of diagnosis. The resulting core/shell nanocrystals ( $\text{SPIO}@\text{Bi}$ ) were created and a coating of m-PEG Silane was used as a stabilizer to form a highly crystalline 8 nm core of maghemite with a 1 nm shell of bismuth atoms. Cytotoxicity measurements were tested on Hela cells, and showed low toxicity. These NPs are used for CT and MRI.

An example of the synthesis of the DE-stabilized bismuth sulfide NPs ( $\text{Bi}_2\text{S}_3$  DESNPs) was reported by Yi Fang *et al.* (184), who proposed the formation of stable  $\text{Bi}_2\text{S}_3$  DESNPs with an average size range of 5.2–5.7 nm. Their X-ray absorption coefficient measurements showed that the attenuation values were much higher than that of iodine-based CT CA at the same molar concentration of the active element (Bi against iodine). MTT and hemolysis assays for  $\text{Bi}_2\text{S}_3$  DESNPs possessed good cytocompatibility and a low hemolysis effect in a given concentration. Furthermore, it has been assumed that these NPs might have great potential as a highly efficient and unique CA due to the chemistry of DEs and their capability for further chemical coupling with various biological molecules.

One of the fundamental criteria for the BiNPs are that it can serve as DDs, particularly for the

delivery of anticancer drugs to tumors, as being studied by Kathrin Bogusz *et al.* (185). These authors synthesized, for the first time, a theranostic system for the  $\alpha$ - $\text{Bi}_2\text{O}_3$  NPs that was covalently bound with MTX as a chemotherapeutic drug, which can target cancer cells through (3-aminopropyl) trimethoxysilane (APTMS) *via* a precipitation and coating method. The  $\alpha$ - $\text{Bi}_2\text{O}_3$ -APTMS-MTX conjugate was of 50 nm in diameter, possessed efficient biocompatible particles, and showed excellent *in vitro* and *in vivo* results for imaging and improved 9L cancer cell internalization.

## 11 Platinum-based NPs

The element platinum (Pt) has good contrast due to its high atomic number, ( $Z \geq 78$ ), but, to date, only a few studies have been done. Recently, Liang *et al.* (186) synthesized water-soluble l-cysteine-coated FePt NPs (FePt-Cys NPs) as a dual MRI/CT imaging agent for the diagnosis of malignant gliomas through a co-reduction route. The MRI and CT imaging ability of FePt-Cys NPs was evaluated using different glioma cells (C6, SGH44, U251). CT/MR imaging was more sensitive than that of the commonly used iohexol, even if the  $r_2$  value of FePt-Cys NPs was lower than that of FePt NPs coated with  $\text{Fe}_2\text{O}_3$  and  $\text{SiO}_2$ .

The biocompatibility of the NPs was further evaluated using three different cell lines (ECV304, L929, and HEK293), and displayed excellent biocompatibility. Thus, these NPs are promising as a dual MRI/CT CA for the diagnosis of malignant brain gliomas. The key advantage of cysteine as a coating agent is that it prevents damage to brain tissues. Such modifications reduce the toxicity of dendrimer-entrapped metal NPs and suggest further biofunctionalization to produce multifunctional metal NPs for a range of biological sensing and therapeutics applications. These fabricated enzyme field-effect transistors, produced with dendrimer-encapsulated platinum NPs, provide a linear range of 0.25–2.0 mM, with a detection limit of  $\sim 0.15$  mM as a glucose biosensor (187). Platinum compounds are one of the more prominent examples of inorganic NPs used for therapeutic applications (e.g., cisplatin, carboplatin, oxaliplatin, etc.) in the treatment of cancer (188).

## 12 MRI and optical imaging and their current inorganic NP-based CAs

### 12.1 Inorganic NPs for MRI

#### *Basic principle of MRI devices*

It is well-known that magnetic fields can cross human tissues without causing any harmful adverse effects for subjects with no magnetizable materials (189, 190). The use of a magnetic field has been extended to biomedical applications, such as diagnostic and therapeutic domains (drug and gene delivery, hyperthermia cancer therapy, magnetic separation, etc.) (189-192). MRI is one of most developed techniques for diagnostic purposes. MR imaging is a non-invasive and non-ionizing imaging technique that provides 3D images of deep and soft tissues with high resolution, and is mostly used for the detection of tumors and metastases,

---

observation of the brain and the nervous system, or for the evaluation of cardiovascular functions (189, 190, 193, 194). Basically, the concept of MRI relies on the protons from water, proteins, or lipid membranes of human body tissues to respond to a magnetic field ( $B_0 > 2$  T) and a radiofrequency sequence (rf-pulses (5-100 MHz)) (Figure 16). According to the proton NMR principle, applying a magnetic field  $B_0$  leads magnetic moments or spins of protons to align along the  $B_0$  axis (z-axis). Then, rf-pulses are introduced to proton nuclei, which absorb the energy and make the net magnetization of each spin switch from the z-axis to the xy-plane. When rf-pulses are finally stopped, magnetic moments relax and precess at the Larmor frequency to re-align along  $B_0$  (189, 190, 192, 194). Relaxations are thus measured, and then submitted to a Fourier transform to provide the reconstruction of 3D images (190).

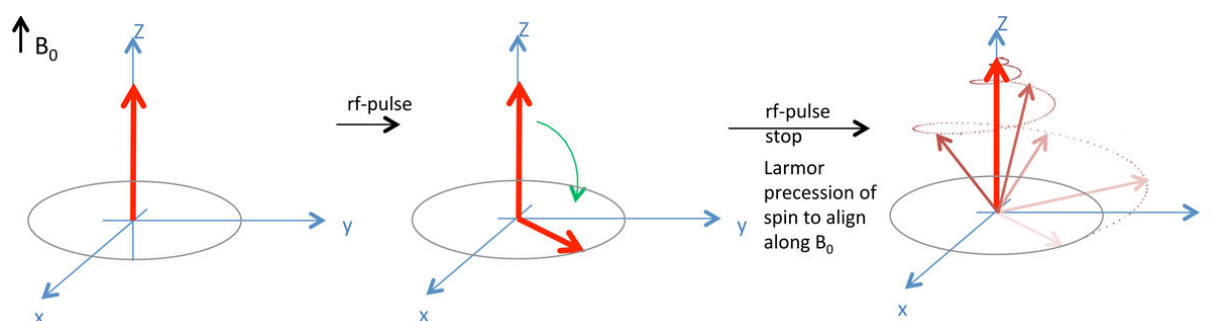


Figure 16: Main steps involved during MRI at spin-scale (from alignment to  $B_0$ , rf-pulses session to spin relaxation).

### *Origin of MRI contrasts*

Relaxation is actually based on two phenomena: i) the longitudinal relaxation, commonly called T1 relaxation or T1-recovery, and “spin-lattice” relaxation due to the dissipation of the absorbed energy from rf-pulses to the surrounding tissues; and ii) the transversal relaxation, generally named T2 relaxation or T2-decay and “spin-spin” relaxation because of the loss of phase coherence by spin-spin interactions during spin precession. As implied, longitudinal and transversal relaxations are characterized by the times of relaxation, i.e., T1 and T2 (189, 190, 192, 194, 195). T1 corresponds to the time to release 63% of longitudinal magnetization from spins to the surrounding media, generally as energy-like heat, (Jeff, “energy-like heat?”) whereas T2 is the time that transverse magnetization needs to decrease 37% (190). Furthermore, longitudinal and transversal relaxations are two parallel magnetic phenomena, and thus, provide their own type of contrast: T1-recovery and T2-decay have brightening (positive contrast) and darkening (negative contrast) effects, respectively (193). Regardless of the differences in contrast effects from T1-recovery and T2-delay, it should be noted that the MRI contrast is only related to the magnetic behavior of one element type (protons). However, T1 and T2 varies between organs. Indeed, because of differences between one tissue and another, the spins will not relax at the same time, since each tissue type is subject to different interactions. Moreover, many experimental parameters can also influence the proton relaxation rates (189, 194).

### ***Contrast enhancement nanosystems***

Although contrast naturally occurs through T1- and T2-relaxations, the differentiation between tissues might need to be enhanced in order to increase the accuracy of diagnosis. By injecting a CA, a difference in the signal between two adjacent regions will be more easily detected and lead to a better understanding of images *via* a clearer visualization of tissues (190, 194). Currently, nanoparticulate CAs are used to alter the relaxation time of protons by reducing T1 and T2 (190, 192). MRI is highly sensitive and does not require a high dose of contrast media (few mmol/L or  $\mu\text{mol/L}$  of CA) to provide an efficient clarification of images without saturation. Generally, the efficiency of an MRI CA is expressed through longitudinal and transversal relaxivity, i.e.,  $r_1$  and  $r_2$ , respectively ( $\text{mM}^{-1}\text{s}^{-1}$ ) (191, 194, 196). Such parameters are clearly defined as the increment of the relaxation rate of water protons for 1 mmol/L of CA. Since MRI images rely on both T1 and T2 relaxations, two groups of CA are available for T1- and T2-weighted imaging. To determine whether a CA is more suitable for T1- or T2-weighted imaging, the  $r_2/r_1$  ratio has to be evaluated. The higher the  $r_2/r_1$  ( $>1-10$ ), the more contrast in T2-imaging (194, 196). Both types of contrast involve magnetic NPs, which can accumulate in limited areas due to their nanometer scale (189). The most widely clinically used T1-contrast agent is based on the paramagnetic heavy metal ions,  $\text{Gd}^{3+}$  chelates. T2-contrast agents, conversely, have mostly relied on superparamagnetic IONPs, and, for two decades, have provided the best candidates for nanoparticulate and inorganic material that produces a negative MRI contrast (Jeff, this sentence doesn't make sense...) (190, 194, 197). Nanoparticulate CA are formulated as a core-shell composed of three parts: i) the inner core (MRI signal); ii) the hydrophilic shell or nanocarrier for the biocompatibility and stability of the core; and iii) the targeting moieties attached to the coating (194).

### ***$\text{Gd}^{3+}$ chelates***

Gadolinium-based T1-weighted CAs are paramagnetic NPs made of  $\text{Gd}^{3+}$  ions anchored into nanocarriers, such as liposomes, inorganic nanomaterials, carbon nanotubes, micelles, lipoproteins, perfluorocarbons, dendrimers, or microemulsions. Basically, to ensure the safe use of  $\text{Gd}^{3+}$ , nanocarriers must provide enough anchoring sites to chelate these toxic heavy metal ions by stabilizing them kinetically and thermodynamically (190, 193, 194, 196). It has been assumed that  $\text{Gd}^{3+}$  leakage or release might provoke harmful adverse effects on humans. However, toxicity issues with  $\text{Gd}^{3+}$ , such as macrophage death and replacement of calcium ions within the human body, have been noticed for many years, as  $\text{Gd}^{3+}$  complexes were the first generation of CA based on a nanoparticulate system for intravascular injection (190). Currently,  $\text{Gd}^{3+}$  chelates involved in clinical applications are based on gadolinium oxides ( $\text{Gd}_2\text{O}_3$ ), gadolinium fluoride ( $\text{GdF}_3$ ), and gadolinium phosphate ( $\text{GdPO}_4$ ). Elements other than lanthanides may also provide good candidates, notably the transition metal elements ( $\text{Mn}^{2+}$ ,  $\text{Fe}^{3+}$ ,  $\text{Cu}^{2+}$ ...) or metal alloy NPs due to their large number of unpaired electrons, which provide paramagnetic ions suitable for T1-weighted MRI (194). Introduced at doses near 0.1 mmol/kg of body mass,  $\text{Gd}^{3+}$  chelates have a non-selective extracellular biodistribution and are mainly used to improve the contrast of interstitial and intravascular body spaces, such as fluid compartments or lesions, before being excreted through renal

clearance. In addition, they easily interact with blood compartment cells, which make them unsuitable for long-term experiments like cell-tracking (190, 194). Contrary to  $Gd^{3+}$  chelates, the next generation of T1 CA, for instance, manganese oxide (MnO) NPs (such as Teslacan,® a commercial T1-weighted contrast agent), might be taken up by cells and can cross natural barriers for brain, kidney, and liver imaging (194). To conclude, some requirements must be fulfilled to use  $Gd^{3+}$  chelate NPs as a stable biocompatible T1-weighted CA (194). Specifically,  $Gd^{3+}$  chelate NPs must i) exhibit a low  $r_2/r_1$  ratio ( $\leq 1$  or 2) (and also a high  $r_1/r_2$ ) to provide positive contrast, ii) be incorporated into a hydrophilic nanocarrier bearing bioactive materials for targeting purposes with an overall size smaller than 100 nm in order to iii) form stable  $Gd^{3+}$  chelates to reduce potential side effects, and iv) have a favorable pharmacokinetic profile (good biodistribution and bioaccumulation). A remaining challenge is cell uptake with medium- to long-term accumulation. Such behavior remains unresolved and prevents  $Gd^{3+}$  chelate NPs from use in experiments that require long-term positive contrast.

### ***Superparamagnetic IONPs (SPIONs)***

The first use of SPION for imaging purposes was for liver disease because of the selective and spontaneous uptake by Kupffer cells and a passive bioaccumulation within RES cells (192-194). For biomedical applications based on magnetic devices, the most widely used SPION nanocrystals are made of magnetite ( $Fe_3O_4$ ) and maghemite ( $\gamma-Fe_2O_3$ ) due to their high magnetism (189, 192, 194). They are both synthesized by two main pathways: the coprecipitation corresponding to the reduction of iron salt in alkaline aqueous solutions in the presence of ligands (macromolecules) to control the growth of NPs, and thermal decomposition depending on the high temperature decomposition of an organometallic complex in the presence of surfactant, leading to a lipophilic SPIONs. Although the latter method provides hydrophobic SPIONs, nanocrystals have high crystallinity and monodispersity, which leads to a homogeneous and strongly magnetic property. Otherwise, ligand exchange procedures can be carried out to turn a lipophilic surface into both hydrophilic and tailored. Indeed, SPIONs smaller than 50 nm, called ultra-small SPIONs, are not sequestered by RES and extravasate through the capillary system to reach small access areas such as lymph nodes. Consequently, the *in vivo* biodistribution and bioaccumulation of decorated SPIONs rely not only on surface chemistry, but are also size-dependent (196, 198). Magnetism is also size-dependent with bigger SPIONs and produces stronger effects. The major challenge of SPIONs for MRI is to find a compromise between the design of physicochemical properties (overall size, neutral or charged surface, stealthiness, type of shell, and/or bioactive ligand), magnetic properties, and pharmacokinetics to obtain a long-circulating colloidal, biocompatible, and stealthy T2-weighted CA. To conclude, some requirements are required for translation from the bench to animal models and into clinical studies, Specifically, SPIONs must i) be produced in uniform and controllable range sizes with a high degree of crystallinity to ensure good magnetism for MRI, ii) form a stable and biocompatible colloidal dispersion, iii) have a predictable *in vivo* fate by focusing on the targeting strategy, and iv) show a low toxicity after intravenous injection and biodegradation (providing iron ions).

---

## 12.2 Quantum dots for optical imaging

Quantum dots (Qds) are single inorganic nanocrystals ranging from 2 to 10 nm, and composed of semiconductor materials introduced in 1998 as nanodevices for cell labeling. However, quantum dots are currently used for fluorescent-based biomedical applications as diverse as molecular and cellular imaging, sensing, drug delivery, and targeting (199-203). Biomedical applications that rely on fluorescent phenomena generally involve nanomaterials (Qds) or substances (dyes, fluorophores) capable of absorbing energy from light radiation and to re-emitting a ray with a lower wavelength.

To produce fluorescent phenomena using semiconductors, electrons must be excited by external radiation to pass through a small band gap from valence to conductive bands. A hole is thus created and forms an electron-hole pair linked by Coulombic force across the band gap. Then, light is emitted and corresponds to a fluorescent emission rather than producing heat to relax the excited electron and fill the created hole. In the specific case of Qds, absorption and emission are obviously composition- and size-dependent, since those two parameters affect fluorescence properties and semi-conductor-like behavior (199, 200, 202). First, the composition of Qds confers semiconductor properties based on the elements involved in its construction and their ability to form electron-hole pairs. Second, Qds are nanometer-scale devices and are commonly compared to an “artificial atom” or hydrogen-like system because their radius ranges around Bohr’s model atom radius. However, the comparison depends not only on the size factor, but also more precisely on its consequence for the spectroscopic aspects. It should be noted that in the Bohr model, the energy of the electronic level is quantized because of the nanosize and also confers a quantum confinement effect due to the closeness of electrons within the Bohr atom. The quantum confinement effect in Qds causes the emission of light from the electron-hole pair (called excitation) with a narrow and well-defined wavelength from the ultraviolet region of the spectrum (200, 203, 204). Semiconductor nanocrystal-based Qds act as an atom with regard to the quantum confinement effect, but they have a crystalline nanostructure. Consequently, due to the confined nanospace within a semiconductor nanocrystal, colloidal Qds can exhibit tunable fluorescent properties by a change of size and/or composition. This double dependence renders Qds an innovative compact nanoprobe for fluorescent imaging.

Although the nanosize is an asset for the optical and electronic properties, it also has a huge impact on biodistribution and bioaccumulation. Consequently, a compromise between the design that provides good physicochemical properties for biomedical applications and the overall size lead to a quantum confinement effect that must be investigated. *In vivo* and *in vitro* biomedical applications imply the use of water-soluble Qds with high biocompatibility and stealth properties to be stable in physiological media and to have a residence time within the blood-stream long enough to let the fluorescent colloids achieve their tasks. The fate of Qds in a biological environment is basically dictated by the nanosize and surface state (charge, zeta potential, and functionalization) (202). As a result, ligands, such as pegylated polymers, zwitterionic molecules, thiolated, or amino- bifunctional ligands with polar end-of-chain groups, render Qds transferable into an aqueous phase, but are generally attached in

---

order to stabilize and to extend the lifetime of Qds in biological conditions. Such organic shells are basically formed *in situ*, *i.e.*, during the Qds synthesis, and can be linked to the quantum core by covalent bond, electrostatic bond, chelation, or adsorption. As for all nanoparticulate systems involved in *in vivo* biomedical applications, the stealth property is the key skill that Qds must exhibit. Indeed, to target the RES and tumors, a passive targeting strategy can simply be used because Qds will (i) be detected as foreign entities and will be taken-up by the liver, the spleen, and the lymph nodes, or (ii) extravasate through the leaky vascular system of the tumor (199, 201, 202). A specific biorecognition or active targeting is often needed in fields, such as molecular and cellular sensing, local imaging, and DDS, to enhance the selectivity of nanoprobes. The dose can be decreased through optimization of the fluorescent materials' accumulation in a local and targeted area. By applying recognition strategies, bioconjugated Qds are able to selectively interact with biological structures at the cellular and molecular levels. The versatility of the Qds surface is basically improved and developed because of the high surface-to-volume ratio, which provides an incredible number of sites for the attachment of ligands and turning the Qds into biocompatible and multivalent fluorescent nanoprobes (200).

However, tailoring the surface of Qds may lead to an increase in size. Indeed, but using a nanocarrier such as beads and copolymeric micelles based on surfactant or phospholipids, would provide much larger nanodevices, thus compromising the biodistribution of the final construct. The resulting final assembly may not be able to gain access to some size-limited areas, whereas the non-modified Qd may be capable of passively targeting these areas. Nanocarriers offer efficient protection for Qds' fluorescent properties, a versatile surface for further vectorization purposes, and a dense structure onto which plasma proteins are not absorbed. In addition, changing the overall hydrodynamic diameter of assembling would drastically affect the biodistribution and the bioaccumulation. It is preferable that decorated fluorescent nanoprobes be as small as possible, not only for because they are subject to the quantum confinement effect, but also in order to cross natural barriers and penetrate deep tissues and organs. Contrary to fluorophore molecules, this point remains also one of the major challenges in the design of Qds because of their compact or rigid structure. In fact, fluorophores are basically in solution and may thus pass through vessel and/or extravasate more easily through tissues. Even though the chemistry of surface modification has been developed to improve vectorization and biocompatibility, investigations must find a balance with regard to the size and the surface of the functionalization of Qds to prevent them from fast excretion *via* renal clearance after opsonization, and enhance their permeation through tissues to reach their target.

Apart from the biodistribution, the bioaccumulation and optimal time of residence within the blood stream or organs and cells must also be considered for biomedical applications that require entrapment of Qds. At some point, Qds must be excreted. Indeed, it seems that long-term accumulation may provoke some adverse effects due to the unstable structure of Qds, such as the impairment of cellular functions and the intracellular oxidation of the Qds, which then cause a leakage of free semiconductor compounds, which means metal ions and free radicals. To date, the pharmacokinetics and toxicity of Qds and their metabolites remain

---

unclear. For this reason, colloidal semiconductor nanocrystals are still prohibited from clinical applications. Most Qds are made with elements from groups III-V, II-VI, and IV-VI of the periodic table, such as cadmium sulfide (CdS), cadmium selenide (CdSe), indium arsenide (InAs), or lead-based elements (Pb) or zinc (Zn). However, the current trend for Qds is to generate new types of semiconductor nanocrystals based on less toxic and more stable metallic assembling to be able to extend the use of Qds from *in vitro* to *in vivo* assays. For example, graphene, silicon, gold, or even diamonds Qds, have been proposed as innovative and adverse-effect-free nanomaterials. Some new types of Qds have also emerged with emissions in near infrared or a reduction in the need for external radiation, commonly called self-illuminated Qds. Basically, synthesis relies on a thermal decomposition in the non-polar organic phase of a metallic precursor, in the presence of stabilizers, to control the growth of crystals. Despite the reactional conditions, the size and the emission spectrum are variable, but Qds are generally monodispersed through this method. Aqueous phase preparation is also possible and provides water-soluble Qds without any further surface modifications, unlike the previous method, which requires a ligand exchange procedure to make the Qds surface suitable for biological media. Although attaching ligands aims to create an organic shell to stabilize and tailor Qds, an inorganic coating is a potential solution to overcome stability and toxicity issues. For instance, capping the Qd core with a silica, gold, or metal shell (quantum shell) prevents the Qds core from corrosion, leakage of toxic free metal ions, and free radicals, causing oxidative stress, and an intermittent fluorescence mostly caused by defects on their surface. When Qds are overcoated with an inorganic layer, ligands are grafted onto this overcapping through the same type of bond-forming nanocomposites on a quantum dot core in an inorganic-organic shield that protects the unstable and potentially harmful Qd core.

Despite a lack of knowledge and understanding about the potential damage to biological entities, Qds keep providing an outstanding nanodevice for fluorescent imaging. For instance, in comparison to organic molecule-based fluorescent probes, Qds possess a well-defined and narrow window of emission spectra tunable by a change of crystal size, a large absorption spectra (allowing the excitation of several fluorescent colors), and a high photostability (resistance to light radiation), all of which renders them more efficient and suitable than dyes for biomedical applications. However, before reaching clinical translation, some issues must still be addressed: (i) a lack of understanding of the pharmacokinetics of Qds; (ii) insufficient knowledge about the adverse effects and toxicity of free compounds and/or of metabolites released by biodegradation; and (iii) the compromise between the size and physicochemical surface properties of the Qd core and also of the final core-shell assembly.

## **13 Lesser known elements and derivatives-based inorganic nanoparticulate CAs**

### ***13.1 Thorium: a well-known efficient, but carcinogenic, colloidal X-ray CA***

During the 1920s, thorium became the most popular heavy metal element for X-ray imaging. First introduced as a ThO<sub>2</sub> emulsion design to be given as an oral CA for GI, ThO<sub>2</sub> was used as an intravenous injectable suspension for imaging a wide range of organs,, such as liver and

---

spleen, for RES angiography, brain for cerebral arteriography, bladder and urethra for pyelography, and finally, for the placenta in the obstetric field. Commercially sold as Thorostat CA, it has been injected in about 10 millions patients in 30 years until the 1950s. Because of a lack of complete excretion, which caused long-term bioaccumulation in RES organs, patients who had been injected were exposed to Th radioactivity. Many cases of liver disease, like cirrhosis and malign tumors, were reported. Additional studies pointed out later the acute toxicity and lethal effects of Thorostat. ThO<sub>2</sub> was classified as a contraindicated CA and eventually no longer used (1, 11).

### ***13.2 Tantalum-based nanoparticulate and radiopaque CA***

Tantalum is a transition metal as efficient as gold, bismuth, barium, or iodinated compounds for X-ray imaging, but has been proven to be safer than other nanoparticulate CAs. Basically used in a pentoxide tantalum Ta<sub>2</sub>O<sub>5</sub> form, studies assumed that this nanoparticulate metal oxide was biocompatible, water-soluble, and chemically stable. Although the design of those NPs still needs improvement with regard to efficient targeting properties, the lymph nodes and liver were imaged by passive targeting, which exhibited good selectivity toward the RES with good X-ray attenuation, as shown by Oh *et al.* (205). Cartilage was also imaged by active targeting applied through a charge-surface modification method that involved quarternary ammonium ligands, as shown by Freedman *et al.* (1, 105, 206, 207). However, Ta powder has also been used as a pure powder. Indeed, its good radiopaque properties enabled the use of tantalum powder for tracheobronchial imaging *via* trachea airway administration in the 1970s. The main advantage of Ta powder is its high density, which produces images with small amounts of tantalum. Nevertheless, this route of administration promoted the incomplete cleaning of tantalum by coughing from the lower respiratory tract, and some TA powder was retained in the bronchioles. Some cases of pneumonia were indeed observed after Tantalum-based CA administration, which limited clinical development through the airway administration route. Intravenous and oral administrations were then developed to reach the liver, spleen, and GI organs for X-ray imaging, with an aqueous suspension of Ta powder for contrast enhancement (1, 11).

### **13.3 Europium chelate-based NPs for magnetic and optical bioimaging**

Gd<sup>3+</sup>, Europium, or Eu<sup>III</sup> belong to the lanthanide elements and exhibit paramagnetic properties. Based on their properties, Eu<sup>III</sup> chelates formed a new class of MRI CAs called paramagnetic CEST (PARACEST) CAs. These CAs provide information about not only tissues, but also about the chemical structure of the molecules that comprise those tissues and organs. This advanced category of paramagnetic complexes is actually a useful tool in NMR to study complex molecular structures and their proton interactions (208). Although Gd<sup>3+</sup> must be chelated for safety reasons, Eu<sup>III</sup> is basically chelated to enhance its properties as a CA. Eu<sup>III</sup> complexes can also be used for optical imaging, as they are photon-sensitive because they emit red-light after being exposed to a 400 nm photon. Ligands involved in the complex structure are mostly chromophore molecules able to transfer photon energy to the

---

entrapped paramagnetic core. Decades ago, there was great interest in nanoparticulate  $\text{Eu}^{\text{III}}$  chelates. Three main advantages render Europium NPs substantially more attractive than “free” lanthanide complexes, for several reasons. i) A high payload of complexes can be encapsulated within the nanoparticulate matrix, which ii) photostabilizes the complex and enhances the luminescence effect because of confinement and high concentration, and iii) provides a high surface-to-volume ratio available for functionalization and bonding with biomolecules (active targeting) (209). Two synthesis pathways have been reported in the literature: precipitation and copolymerization in microemulsion systems. For instance, Ye *et al.* (210) prepared a 29 to 37 nm optical contrast nano-labeled probes to depict the hepatitis B antigen based on  $\text{Eu}^{\text{III}}$  chelates anchored within a silica matrix obtained by hydrolysis of tetraethylorthosilicate (TEOS) in the presence of  $\text{Eu}^{3+}$  chelates and streptavidin as a labeling agent in microemulsion media. Wang *et al.* (211) also introduced a 200 nm  $\text{Eu}^{3+}$  complex synthesis by precipitation of  $\text{EuCl}_3$  as an  $\text{Eu}^{3+}$  precursor in buffer aqueous solution and stabilizing ligands for luminescent purposes. In 2010, Peng *et al.* (212) proposed an innovative nanosensor based on europium chelates for fluorescent imaging. Meanwhile, Winter *et al.* (213) synthesized an  $\text{Eu}^{3+}$ -based PARACEST CA in perfluorocarbon NPs by microfluidic polymerization for fibrin detection in the diagnosis of cardiovascular disease.

### **13.4 Ytterbium lanthanide element for X-ray, optical imaging, and MRI**

Ytterbium lanthanide and its hybrid and/or doped forms have been introduced in the literature as promising inorganic NPs compared to other lanthanide or rare earth elements. Mostly applied for optical imaging, ytterbium provides good radiopacity for *in vivo* X-ray imaging of the heart, liver, spleen, lymph nodes, and vessels, and can offer even more contrast by incorporating doping agents, such as erbium, gadolinium, or barium to ytterbium oxide ( $\text{Yb}_2\text{O}_3$ ) or fluorine ytterbium ( $\text{YbF}_3$ ). Generally, ytterbium oxides, hybrids, and doped forms are created by alkaline homogeneous precipitation or by thermal decomposition with fatty acid ligands (105, 207, 214). Multimodal imaging couples X-ray and optical modalities, as in Tian *et al.* (215). This concept quite often involves ytterbium, a rare earth element that, due to an upconversion effect, renders it suitable for fluorescent imaging. (Jeff, as meant?) For example, photon excitation of Yb initiates a fluorescent element, such as  $\text{Eu}^{3+}$ , to emit light in the NIR region by exciting photon light energy much lower than  $\text{Eu}^{3+}$  probes usually need. In case of biological assays, this proves to be an asset, since it reduces cell and DNA damage. Many authors base bioimaging on that effect, and therefore, combine fluorescent probes with Yb (182, 216). Ytterbium element-based CA has also been reported to be efficient as a PARACEST CA, such as in case of cell labeling and cell tracking.

## **14 Conclusion**

X-ray computed tomography (CT), with its many advantages, has become a low-cost, frequently used technology. Indeed, these inherent advantages have led to X-ray CT being the most widely used and available diagnostic imaging tool. However, there are still more potential applications, as its use is currently limited due to the rapid clearance and toxicity of available contrast agents that are currently mostly based on small iodinated molecules. In this

context, the next generation of contrast agents will offer great innovations with materials that possess targeting properties, long retention times, and multimodal characteristics. This review summarized the latest advances that fulfill these new objectives through flexible platforms constructed with different inorganic materials, and functionalizable with a large panel of targeting moieties. There is, as yet, no ideal contrast agent, but the large variety of inorganic nanoparticulate systems described highlights the challenge in balancing the inherent advantages and drawbacks when designing these novel compounds. Inorganic nanoparticles are still in the development phase and remain mostly limited to *in vitro* experiments or preliminary animal studies that aim to establish *in vivo* feasibility. Toxicological studies remain the mainstay in the development of inorganic nanoparticles. However, it is realistic to predict that careful studies of surface functionalization will result in efficient solutions to address this major remaining hurdle and thus provide exciting solutions for novel diagnostic and theranostic probes.

## 15 References

1. Jakhmola A, Anton N, Vandamme TF. Inorganic nanoparticles based contrast agents for X-ray computed tomography. *Adv Healthc Mater.* 2012;1(4):413-31.
2. Kim D, Jon S. Gold nanoparticles in image- guided cancer therapy. *Inorg Chim Acta.* 2012;393:154-64.
3. Hallouard F, Anton N, Choquet P, Constantinescu A, Vandamme T. Iodinated blood pool contrast media for preclinical X-ray imaging applications--a review. *Biomaterials.* 2010;31(24):6249-68.
4. Reichard P. Nobel Lectures: Physiology or Medicine 1971–1980. Lindsten J, editor. Singapore: World Scientific Publishing Co.; 1992.
5. Jun Y, Lee J, Cheon J. Chemical Design of Nanoparticle Probes for High-Performance Magnetic Resonance Imaging. *Angew Chem-Int Edit.* 2008;47(28):5122–35.
6. Niu DC, Li YS, Ma Z, Diao H, Gu JL, Chen HR, et al. Preparation of Uniform, Water-Soluble, and Multifunctional Nanocomposites with Tunable Sizes. *Adv Funct Mater.* 2010;20(5):773-80.
7. Corot C, Robert P, Idee J-M, Port M. Recent advances in iron oxide nanocrystal technology for medical imaging. *Adv Drug Deliv Rev.* 2006;58(14):1471-504.
8. Abyaneh M, Paramanik D, Varma S, Gosavi S, Kulkarni S. Formation of gold nanoparticles in polymethylmethacrylate by UV irradiation. *J Phys D: Appl Phys.* 2007;40(12):3771-9.
9. Krause W. Contrast Agents II Optical, Ultrasound, X-Ray and Radiopharmaceutical Imag in Volume. Krause W, editor. *Top. Curr. Chem.*: springer; 2002.
10. Krause W, Schneider PW. Contrast Agents II Optical, Ultrasound, X-Ray and Radiopharmaceutical Imag in Volume. Krause W, editor. *Top. Curr. Chem.*: springer; 2002.
11. Yu S-B, Watson AD. Metal based X-ray contrast media. *Chem Rev.* 1999;99:2353-77.
12. Hoey GB, Weight P, Ranks RD. Radiocontrast Agents. Knoefel PK, editor 1971.

13. Haavaldsen J, Nordal V, Kelly M. X-ray contrast agents. I. Synthesis of some derivatives of 5-amino-2,4,6-triiodoisophthalamide. *Acta Pharm Suec.* 1983;20(3):219-32.
14. McClennan BL. Adverse reactions to contrast media: Recognition and Response. *Invest Radiol.* 1994;29:S46-S50.
15. Hoey GB, Smith KR. Chemistry of X-ray contrast media. In: Sovak M, editor. *Radiocontrast agents*; New York: Springer-Verlag; 1984. p. 23-125.
16. Krause W, Niehues D. Biochemical characterisation of X-ray contrast media. *Invest Radiol.* 1996;31:30-42.
17. Aspelin P. Why choice of contrast medium matters. *Eur Radiol Suppl.* 2006;16:D22-D7.
18. Christiansen C. X-ray contrast media--an overview. *Toxicology.* 2005;209(2):185-7.
19. McClennan BL. Ionic and non-ionic iodinated contrast media : evolution and strategies for use. *Am J Roentgenol.* 1990;155:225-33.
20. Katayama H, Yamaguchi K, Kozuka T, Takashima T, Seez P, Matsuura K. Adverse reactions to ionic and nonionic contrast media. *Radiology.* 1990;175:621-8.
21. Riefke B, Gonzalez L, Carretero J, Gonzalez C, Jimenez I, Alguacil LF, et al. The effect of glucose and copper on the stability of diatrizoic acid. *Acad Radiol.* 2002;9(Suppl 1):S178-81.
22. Sovak M, Terry R, Abramjuk C, Faberova V, Fiserova M, Laznicek M, et al. Iosimenol, a low-viscosity nonionic dimer: preclinical physicochemistry, pharmacology, and pharmacokinetics. *Invest Radiol.* 2004;39(3):171-81.
23. Chai CM, Rasmussen H, Eriksen M, Hvoslef AM, Evans P, Newton BB, et al. Predicting cardiotoxicity propensity of the novel iodinated contrast medium GE-145: Ventricular fibrillation during left coronary arteriography in pigs. *Acta Radiol.* 2010;51(9):1007-13.
24. Wistrand LG, Rogstad A, Hagelin G, Roed L, Oulie I, Gram A, et al. GE-145, a new low-osmolar dimeric radiographic contrast medium. *Acta Radiol.* 2010;51(9):1014-20.
25. Fernandez Cabezudo MJ, Petroianu G, Al-Ramadi B, Langer RD. Iosimenol, a new non-ionic dimeric contrast medium, does not induce immunoreactivity in the popliteal lymph node assay. *Br J Radiol.* 2007;80(957):713-8.
26. Estep KG, Josef KA, Bacon ER, Illig CR, Toner JL, Mishra D, et al. 1,3,5-Trialkyl-2,4,6-triiodobenzenes: novel X-ray contrast agents for gastrointestinal imaging. *J Med Chem.* 2000;43(10):1940-8.
27. Shalem H, Shatzmiller S, Feit BA. Synthesis of model compounds for potential contrast agents containing phosphonate and peptide moieties. *J Chem Soc, Perkin Trans.* 2000;1:2831-7.
28. Lee TC, Mohsin S, Taylor D, Parkesh R, Gunnlaugsson T, O'Brien FJ, et al. Detecting microdamage in bone. *J Anat.* 2003;203(2):161-72.
29. Parkesh R, Gowin W, Lee TC, Gunnlaugsson T. Synthesis and evaluation of potential CT (computer tomography) contrast agents for bone structure and microdamage analysis. *Org Biomol Chem.* 2006;4(19):3611-7.
30. Parkesh R, Lee TC, Gunnlaugsson T, Gowin W. Microdamage in bone: surface analysis and radiological detection. *J Biomech.* 2006;39(8):1552-6.

31. Bansal PN, Joshi NS, Entezari V, Grinstaff MW, Snyder BD. Contrast Enhanced Computed Tomography can predict the glycosaminoglycan content and biomechanical properties of articular cartilage. *Osteoarthritis Cartilage*. 2010;18(2):184-91.
32. Joshi NS, Bansal PN, Stewart RC, Snyder BD, Grinstaff MW. Effect of contrast agent charge on visualization of articular cartilage using computed tomography: exploiting electrostatic interactions for improved sensitivity. *J Am Chem Soc*. 2009; 131(37): 13234-5.
33. Hayward LN, de BCM, Lusic H, Gerstenfeld LC, Grinstaff MW, Morgan EF. MRT letter: Contrast-enhanced computed tomographic imaging of soft callus formation in fracture healing. *Microsc Res Tech*. 2012;75(1):7-14.
34. Kim BYS, Rutka JT, Chan WCW. Nanomedicine. *New Eng J Med*. 2010;363(25):2434-43.
35. Javier DJ, Nitin N, Levy M, Ellington A, Richards-Kortum R. Aptamer-targeted gold nanoparticles as molecular-specific contrast agents for reflectance imaging. *Bioconjugate Chem*. 2008;19(6):1309-12.
36. Van Tilborg G, Vucic E, Strijkers G, Cormode D, Mani V, Skajaa T, et al. Annexin A5-functionalized bimodal nanoparticles for MRI and fluorescence imaging of atherosclerotic plaques. *Bioconjugate Chem*. 2010;21(10):1794-803.
37. Nahrendorf M, Jaffer F, Kelly K, Sosnovik D, Aikawa E, Libby P, et al. Noninvasive vascular cell adhesion molecule-1 imaging identifies inflammatory activation of cells in atherosclerosis. *Circulation*. 2006;114:1504-11.
38. Pan D, Roessl E, Schlomka J-P, Caruthers S, Senpan A, Scott M, et al. Computed tomography in color: nanoK-enhanced spectral CT molecular imaging. *Angew Chem-Int Edit*. 2010;49:9635-9.
39. Stacul F, van der Molen AJ, Reimer P, Webb JAW, Thomsen HS, Morcos SK, et al. Contrast induced nephropathy: updated ESUR Contrast Media Safety Committee guidelines. *Eur Radiol*. 2011;21(12):2527-41.
40. Khlebtsov N, Dykman L. Biodistribution and toxicity of engineered gold nanoparticles: a review of in vitro and in vivo studies. *Chem Soc Rev* 2011;40:1647-71.
41. Oberdorster G, Oberdorster E, Oberdorster J. Concepts of nanoparticle dose metric and response metric. *Environ Health Perspect*. 2007;115(6):A290-A4.
42. Fadeel B, Garcia-Bennett A. Better safe than sorry: understanding the toxicological properties of inorganic nanoparticles manufactured for biomedical applications. *Adv Drug Deliv Rev*. 2010;62(3):362-74.
43. Chono S, Tanino T, Seki T, Morimoto K. Uptake characteristics of liposomes by rat alveolar macrophages: influence of particle size and surface mannose modification. *J Pharm Pharmacol*. 2007;59(1):75-80.
44. Osaki F, Kanamori T, Sando S, Sera T, Aoyama T. A quantum dot conjugated sugar ball and its cellular uptake on the size effects of endocytosis in the subviral region *J Am Chem Soc*. 2004;126(21):6520-1.
45. Wina KY, Feng SS. Effects of particle size and surface coating on cellular uptake of polymeric nanoparticles for oral delivery of anticancer drugs. *Biomaterials*. 2005;26(15):2713-22.

46. Foged C, Brodin B, Frokjaer S, Sundblad A. Particle size and surface charge affect particle uptake by human dendritic cells in an in vitro model. *Int J Pharm.* 2005;298(2):315-22.
47. Chithrani BD, Ghazani AA, Chan WCW. Determining the size and shape dependence of gold nanoparticle uptake into mammalian cells. *Nano Lett* 2006;6(4):662-8.
48. Lu F, Wu SH, Hung Y, Mou CY. Size effect on cell uptake in well-suspended, uniform mesoporous silica nanoparticles. *Small.* 2009;5(12):1408-13.
49. Lee KD, Nir S, Papahadjopoulos D. Quantitative analysis of liposome-cell interactions in vitro: rate constants of binding and endocytosis with suspension and adherent cells and human monocytes. *Biochemistry.* 1993;32(3):889-99.
50. Bergen JM, Von Recum HA, Goodman TT, Massey AP, Pun SH. Gold nanoparticles as a versatile platform for optimizing physicochemical parameters for targeted drug delivery. *Macromol Biosci.* 2006;6(7):506-16.
51. Diagaradjane P, Shetty A, Wang JC, Elliott AM, Schwartz J, Shentu S, et al. Modulation of in vivo tumor radiation response via gold nanoshell-mediated vascular-focused hyperthermia: characterizing an integrated antihypoxic and localized vascular disrupting targeting strategy *Nano Lett.* 2008;8(5):1492-500.
52. Sadauskas E, Wallin H, Stoltenberg M, Vogel U, Doering P, Larsen A, et al. Kupffer cells are central in the removal of nanoparticles from the organism. *Part Fibre Toxicol* 2007;4:10-7.
53. Semmler-Behnke M, Kreyling WG, Lipka J, Fertsch S, Wenk A, Takenaka S, et al. Biodistribution of 1.4- and 18-nm gold particles in rats. *Small.* 2008;4(12):2108-11.
54. Hillyer JF, Albrecht RM. Gastrointestinal persorption and tissue distribution of differently sized colloidal gold nanoparticles *J Pharm Sci.* 2001;90(12):1927-36.
55. Parab HJ, Chen HM, Lai T-C, Huang JH, Chen PH, Liu R-S, et al. Biosensing, cytotoxicity, and cellular uptake studies of surface-modified gold nanorods. *J Phys Chem C.* 2009;113(18):7574-8.
56. Arvizo RR, Miranda OR, Moyano DF, Walden CA, Giri K, Bhattacharya R, et al. Modulating pharmacokinetics, tumor uptake and biodistribution by engineered nanoparticles. *PLoS One.* 2011;6(9):e24374.
57. Hirn S, Semmler-Behnke M, Schleh C, Wenk A, Lipka J, Schäffler M, et al. Particle size-dependent and surface charge-dependent biodistribution of gold nanoparticles after intravenous administration. *Eur J Pharm Biopharm.* 2011;77(3):407-16.
58. Jensen SA, Day ES, Ko CH, Hurley LA, Luciano JP, Kouri FM, et al. Spherical nucleic acid nanoparticle conjugates as an RNAi-based therapy for glioblastoma. *Sci Transl Med* 2013;5(209):209-20.
59. Niidome T, Yamagata M, Okamoto Y, Akiyama Y, Takahashi H, Kawano T, et al. PEG-modified gold nanorods with a stealth character for in vivo applications. *J Control Release.* 2006;114(3):343-7.
60. Alkilany AM, Shatanawi A, Kurtz T, Caldwell RB, Caldwell RW. Toxicity and cellular uptake of gold nanorods in vascular endothelium and smooth muscles of isolated rat blood vessel: importance of surface modification. *Small.* 2012;8(8):1270-8.

61. Qhattal HS, Hye T, Alali A, Liu X. Hyaluronan polymer length, grafting density, and surface poly(ethylene glycol) coating influence in vivo circulation and tumor targeting of hyaluronan-grafted liposomes. *ACS Nano*. 2014;8(6):5423-40.
62. Albanese A, Tang PS, Chan WCW. The effect of nanoparticle size, shape, and surface chemistry on biological systems. *Annu Rev Biomed Eng*. 2012;14:1-16.
63. Avgoustakis K, Beletsi A, Panagi Z, Klepetsanis P, Livaniou E, Evangelatos G, et al. Effect of copolymer composition on the physicochemical characteristics, in vitro stability, and biodistribution of PLGA–mPEG nanoparticles. *Int J Pharm*. 2003;259(1-2):115-27.
64. Melancon MP, Lu W, Yang Z, Zhang R, Cheng Z, Elliot AM, et al. In vitro and in vivo targeting of hollow gold nanoshells directed at epidermal growth factor receptor for photothermal ablation therapy. *Mol Cancer Ther*. 2008;7(6):1730-9.
65. Qian X, Peng X-H, Ansari DO, Yin-Goen Q, Chen GZ, Shin DM, et al. In vivo tumor targeting and spectroscopic detection with surface-enhanced Raman nanoparticle tags. *Nat Biotechnol*. 2008;26(1):83-90.
66. Goel R, Shah N, Visaria R, Paciotti GF, Bischof JC. Biodistribution of TNF-alpha-coated gold nanoparticles in an in vivo model system. *Nanomedicine*. 2009;4(4):401-10.
67. Attia MF, Anton N, Chipor M, Akasov R, Anton H, Messaddeq N, et al. Biodistribution of X-Ray Iodinated Contrast Agent in Nano-Emulsions Is Controlled by the Chemical Nature of the Oily Core. *ACS Nano*. 2014;8(10):10537-50.
68. Hallouard F, Briançon S, Anton N, Li X, Vandamme T, Fessi H. Iodinated nano-emulsions as contrast agents for preclinical X-ray imaging: Impact of the free surfactants on the pharmacokinetics. *Eur J Pharm Biopharm*. 2013;83(1):54-62.
69. LaMer VK, Dinegar RH. Theory, production and mechanism of formation of monodispersed hydrosols. *J Am Chem Soc*. 1950;72(11):4847-54.
70. Thanh NTK, Maclean N, Mahiddine S. Mechanisms of nucleation and growth of nanoparticles in solution. *Chem Rev*. 2014;114(15):7610-30.
71. Yin Y, Alivisatos P. Colloidal nanocrystal synthesis and the organic-inorganic interface. *Nature*. 2005;437:664-70.
72. Mieszawska AJM, Willem JM, Fayad ZA, Cormode DP. Multifunctional gold nanoparticles for diagnosis and therapy of disease. *Mol Pharm*. 2013;10(3):831-47.
73. Lytton-Jean AK, Han MS, Mirkin CA. Microarray detection of duplex and triplex DNA binders with DNA-modified gold nanoparticles *Anal Chem*. 2007;79(15):6037-41.
74. Agarwal A, Huang SW, O'Donnell M, Day KC, Day M, Kotov N, et al. Targeted gold nanorod contrast agent for prostate cancer detection by photoacoustic imaging. *J Appl Phys*. 2007;102(6):064701-4.
75. Jain S, Hirst DG, O'Sullivan JM. Gold nanoparticles as novel agents for cancer therapy. *Br J Radiol*. 2012;85(1010):101-13.
76. Dreaden EC, Alkilany AM, Huang XH, Murphy CJ, El-Sayed MA. The golden age: gold nanoparticles for biomedicine. *Chem Soc Rev*. 2012;41(7):2740-79.
77. Alkilany AM, Thompson LB, Boulos SP, Sisco PN, Murphy CJ. Gold nanorods: their potential for photothermal therapeutics and drug delivery, tempered by the complexity of their biological interactions. *Adv Drug Deliv Rev*. 2012;64(2):190-9.

78. Hainfeld JF, Slatkin DN, Focella TM, Smilowitz HM. Gold nanoparticles: A new X-ray contrast agent. *Br J Radiol.* 2006;79(939):248-53.
79. Cormode DP, Naha PC, Fayad ZA. Nanoparticle contrast agents for computed tomography: a focus on micelles. *Contrast Media Mol Imaging.* 2013;9(1):37-52.
80. Müllner M, Schlattl H, Hoeschen C, Dietrich O. Feasibility of spectral CT imaging for the detection of liver lesions with gold-based contrast agents - A simulation study. *Physica Medica.* 2015;XXX:1-7.
81. Khan AK, Rashid R, Murtaza G, Zahra A. Gold Nanoparticles: Synthesis and Applications in Drug Delivery. *Trop J Pharm Res.* 2014;13(7):1169-77.
82. Tuval T, Gedanken A. A microwave-assisted polyol method for the deposition of silver nanoparticles on silica spheres. *Nanotechnology.* 2007;18(25):255601-8.
83. Jin Y, Wang P, Yin D, Liu J, Qin L, Yu N, et al. Gold nanoparticles prepared by sonochemical method in thiol- functionalized ionic liquid. *Colloid Surf A: Physicochem Eng Aspects.* 2007;302(1-3):366-70.
84. Giorgetti E, Giusti A, Laza S, Marsili P, Giammanco F. Production of colloidal gold nanoparticles by picosecond laser ablation in liquid. *Phys Status Solidi.* 2007;204(6):1693-8.
85. Mandal T, Fleming M, Walt D. Preparation of polymer coated gold nanoparticles by surface-confined living radical polymerization at ambient temperature. *Nano Lett* 2002;2(1):3-7.
86. Warren SC, Jackson AC, Cater-Cyker ZD, DiSalvo FJ, Wiesner U. Nanoparticle synthesis via the photochemical polythiol process. *J Am Chem Soc.* 2007;129(33):10072-3.
87. Nakamoto M, Yamamoto M, Fukusumi M. Thermolysis of gold(I) thiolate complexes producing novel gold nanoparticles passivated by alkyl groups. *Chem Commun.* 2002;15:1622-3.
88. Katz E, Willner I. Integrated nanoparticle-biomolecule hybrid systems: synthesis, properties, and applications. *Angew Chem-Int Edit.* 2004;43(45):6042-108.
89. Alivisatos P. The use of nanocrystals in biological detection. *Nat Biotechnol* 2004;22(1):47-52.
90. Connor EE, Mwamuka J, Gole A, Murphy CJ, Wyatt MD. Gold nanoparticles are taken up by human cells but do not cause acute cytotoxicity. *Small.* 2005;1(3):325-7.
91. Slot JW, H.J. G. A new method of preparing gold probes for multiple-labeling cytochemistry. *Eur J Cell Biol.* 1985;38(1):87-93.
92. Habrioux A, Hebie S, Napporn T, Rousseau J, Servat K, K.B. K. One-Step Synthesis of Clean and Size-Controlled Gold Electrocatalysts: Modeling by Taguchi Design of Experiments. *Electrocatalysis.* 2011;2(4):279-84.
93. Brust M, Walker M, Bethell D, Schiffrin DJ, Whyman RJ. Synthesis of thiol derivatized gold nanoparticles in a two phase liquid-liquid system. *J Chem Soc Chem Commun.* 1994(7):801-2.
94. Gomez S, Philippot K, Collière V, Chaudret B, Senocqb F, Lecantec V. Gold nanoparticles from self-assembled gold(I) amine precursors *Chem Commun.* 2000(19):1945-6.

95. Hiramatsu H, Osterloh FE. A Simple Large-Scale Synthesis of Nearly Monodisperse Gold and Silver Nanoparticles with Adjustable Sizes and with Exchangeable Surfactants. *Chem Mater*. 2004;16(13):2509-11.
96. Liu X, Atwater M, Wang J, Dai Q, Zou J, Brennan JP, et al. A Study on Gold Nanoparticle Synthesis Using Oleylamine as Both Reducing Agent and Protecting Ligand. *J Nanosci Nanotechnol*. 2007;7(9):3126-33.
97. Akbarzadeh A, Zare D, Farhangi A, Mehrabi MR, Norouzian D, Tangestaninejad S, et al. Synthesis and characterization of gold nanoparticles by tryptophane. *Am J Appl Sci*. 2009;6(4):691-5.
98. Ramezani N, Ehsanfar N, Shamsa F, Amin G, Shahverdi HR, Esfahani HM, et al. Screening of medicinal plant methanol extracts for the synthesis of gold nanoparticles by their reducing potential. *Z Naturforsch*. 2008;63b(7):903-8.
99. Ravindra P. Protein-mediated synthesis of gold nanoparticles. *Mater Sci Eng B*. 2009;163:93-8.
100. Nam J, Won N, Bang J, Jin H, Park J, Jung S, et al. Surface engineering of inorganic nanoparticles for imaging and therapy. *Adv Drug Deliv Rev*. 2013;65(5):622-48.
101. Zhao HY, Liu S, He J, Pan CC, Li H, Zhou ZY, et al. Synthesis and application of strawberry-like Fe<sub>3</sub>O<sub>4</sub>-Au nanoparticles as CT-MR dual-modality contrast agents in accurate detection of the progressive liver disease. *Biomaterials*. 2015;51:194-207.
102. Sun I-C, Eun D-K, Na JH, Lee S, Kim I-J, Youn I-C, et al. Heparin-Coated Gold Nanoparticles for Liver-Specific CT Imaging. *Chemistry*. 2009;15:13341-7.
103. Xi D, Dong S, Meng X, Lu Q, Meng L, Yec J. Gold nanoparticles as computerized tomography (CT) contrast agents. *RSC Adv*. 2012;2:12515-24.
104. Wang H, Zheng L, Guo R, Peng C, Shen M, Shi X, et al. Dendrimer-entrapped gold nanoparticles as potential CT contrast agents for blood pool imaging. *Nanoscale Res Lett*. 2012;7(1):190-8.
105. De La Vega JC, Häfeli UO. Utilization of nanoparticles as X-ray contrast agents for diagnostic imaging applications. *Contrast Media Mol Imaging*. 2015;10(2):81-95.
106. Tsoli M, Kuhn H, Brandau W, Esche H, Schmid G. Cellular uptake and toxicity of Au<sub>55</sub> clusters. *Small*. 2005;1(18):841-4.
107. Alkilany AM, Murphy CJ. Toxicity and cellular uptake of gold nanoparticles: what we have learned so far? *J Nanopart Res*. 2010;12(7):2313-33.
108. Cho WS, Cho M, Jeong J, Choi M, Han BS, Shin HS, et al. Size-dependent tissue kinetics of PEG-coated gold nanoparticles. *Toxicol Appl Pharmacol*. 2010;245(1):116-23.
109. Sonavane G, Tomoda K, Makino K. Biodistribution of colloidal gold nanoparticles after intravenous administration: Effect of particle size. *Colloids Surf B Biointerfaces*. 2008;66(2):274-80.
110. Arnida, Janát-Amsbury MM, Ray A, Peterson CM, Ghandehari H. Geometry and surface characteristics of gold nanoparticles influence their biodistribution and uptake by macrophages. *Eur J Pharm Biopharm*. 2011;77(3):417-23.
111. Boisselier E, Astruc D. Gold nanoparticles in nanomedicine: preparations, imaging, diagnostics, therapies and toxicity. *Chem Soc Rev*. 2009;38(6):1759-82.

112. Giljohann DA, Seferos DS, Daniel WL, Massich MD, Patel PC, Mirkin CA. Gold Nanoparticles for Biology and Medicine. *Angew Chem-Int Edit.* 2010;49(19):3280-94.
113. Giljohann DA, Seferos DS, Patel PC, Millstone JE, Rosi NL, Mirkin CA. Oligonucleotide loading determines cellular uptake of DNA-modified gold nanoparticles. *Nano Lett.* 2007;7(12):3818-21.
114. Fent GM, Casteel SW, Kim DY, Kannan R, Katti K, Chanda N, et al. Biodistribution of maltose and gum arabic hybrid gold nanoparticles after intravenous injection in juvenile swine. *Nanomedicine.* 2009;5(2):128-35.
115. Thomas T, Mascarenhas RJ, D'Souza OJ, Martis P, Dalhalla J, Swamy BEK. Multi-walled carbon nanotube modified carbon paste electrode as a sensor for the amperometric detection of L-tryptophan in biological samples. *J Colloid Interface Sci.* 2013;402:223-9.
116. Lee N, Choi SH, Hyeon T. Nano-sized CT contrast agents. *Adv Mater.* 2013;25(19):2641-60.
117. Willmann JK, Van Bruggen N, Dinkelborg LM, Gambhir SS. Molecular imaging in drug development. *Nat Rev Drug Discov.* 2008;7(7):591-607.
118. Jennings LE, Long NJ. 'two is better than one'—probes for dual-modality molecular imaging. *Chem Commun.* 2009(24):3511-24.
119. Chung D, Kang K, Jeon Y, Kim Y, Alothman ZA, Ahmed AYH, et al., inventors Fluorescent silica nanoparticle with radioactive tag and the detecting method of PET and fluorescent dual imaging using thereof 2010.
120. Chen K, Li Z-B, Wang H, Cai W, Chen X. Dual- modality optical and positron emission tomography imaging of vascular endothelial growth factor receptor on tumor vasculature using quantum dots. *Eur J Nucl Med Mol Imaging.* 2008;35(12):2235-44.
121. Lee HY, Li Z, Chen K, Hsu AR, Xu CJ, Xie J, et al. PET/MRI dual-modality tumor imaging using arginine-glycine-aspartic (RGD)-conjugated radiolabeled iron oxide nanoparticles. *J Nucl Med.* 2008;49(8):1371-9.
122. Lewin M, Carlesso N, Tung CH, Tang XW, Cory D, Scadden DT, et al. Tat peptide-derivatized magnetic nanoparticles allow in vivo tracking and recovery of progenitor cells. *Nat Biotechnol.* 2000;18(4):410-4.
123. Hwang DW, Ko HY, Kim S-K, Kim D, Lee DS, Kim S. Development of a quadruple imaging modality by using nano-particles. *Chemistry.* 2009;15(37):9387-93.
124. Park HY, Schadt MJ, Wang L, Lim II, Njoki PN, Kim SH, et al. Fabrication of magnetic core@shell Fe oxide@Au nanoparticles for interfacial bioactivity and bio-separation. *Langmuir.* 2007;23(17):9050-6.
125. Fortina P, Kricka LJ, Graves DJ, Park J, Hyslop T, Tam F, et al. Applications of nanoparticles to diagnostics and therapeutics in colorectal cancer. *Trends Biotechnol.* 2007;25(4):145-52.
126. Kogan MJ, Olmedo I, Hosta L, Guerrero AR, Cruz LJ, Albericio F. Peptides and metallic nanoparticles for biomedical applications. *Nanomedicine.* 2007;2(3): 287-306.
127. Grubisha DS, Lipert DS, Park HY, Driskell J, Porter MD. Femtomolar detection of prostate-specific antigen: an immunoassay based on surface-enhanced Raman scattering and immunogold labels. *Anal Chem.* 2003;75(21):5936-43.

128. Zhou J, Ralston J, Sedev R, Beattie DA. Functionalized gold nanoparticles: synthesis, structure and colloid stability. *J Colloid Interface Sci.* 2009;331(2):251-62.
129. Li J, Zheng L, Cai H, Sun W, Shen M, Zhang G, et al. Facile one-pot synthesis of Fe<sub>3</sub>O<sub>4</sub>@Au composite nanoparticles for dual-mode MR/CT imaging applications *ACS Appl Mater Interfaces.* 2013;5(20):10357-66.
130. Elbially NS, Fathy MM, Khalil WM. Preparation and characterization of magnetic gold nanoparticles to be used as doxorubicin nanocarriers. *Phys Medica.* 2014;30(7):843-8.
131. Salgueirino-Maceira V, Duarte MC, Farle M, Quintela AL, Sieradzki K, R. D. Bifunctional gold-coated magnetic silica spheres. *Chem Mater* 2006;18(11):2701-6.
132. Hu Y, Meng L, Niu L, Q. L. Facile synthesis of superparamagnetic Fe<sub>3</sub>O<sub>4</sub>@polyphosphazene@Au shells for magnetic resonance imaging and photo-thermal therapy. *ACS Appl Mater Interfaces.* 2013;5(11):4586-91.
133. Goon IY, Lai LMH, Lim M, Munroe P, Gooding JJ, R. A. Fabrication and dispersion of gold-shell-protected magnetite nanoparticles: systematic control using polyethyleneimine. *Chem Mater.* 2009;21(4):673-81.
134. Zhuo Y, Yuan PX, Yuan R, Chai YQ, Hong CL. Bionzyme functionalized three-layer composite magnetic nanoparticles for electrochemical immunosensors. *Biomaterials.* 2009;30(12):2284-90.
135. Salihov SV, Ivanenkov YA, Krechetov SP, Veselov MS, Sviridenkova NV, Savchenko AG, et al. Recent advances in the synthesis of Fe<sub>3</sub>O<sub>4</sub>@AU core/shell nanoparticles. *J Magn Magn Mater.* 2015;394:173-8.
136. Cai H, Li K, Li J, Wen S, Chen Q, Shen M, et al. Dendrimer-Assisted formation of Fe<sub>3</sub>O<sub>4</sub>/Au nanocomposite particles for targeted dual mode CT/MRI imaging of tumors. *Small.* 2015;11(35):4584-93.
137. Kim HJ, Lee S-M, Park K-H, Mun CH, Park Y-B, Yoo K-H. Drug-loaded gold/iron/gold plasmonic nanoparticles for magnetic targeted chemo-photothermal treatment of rheumatoid arthritis. *Biomaterials.* 2015;61:95-102.
138. Alric C, Taleb J, Duc GL, Mandon C, Billotey C, Meur-Herland AL, et al. Gadolinium Chelate Coated Gold Nanoparticles As Contrast Agents for Both X-ray Computed Tomography and Magnetic Resonance Imaging. *J AM CHEM SOC.* 2008;130(18):5908-15.
139. Wang L, Xing H, Zhang S, Ren Q, Pan L, Zhang K, et al. A Gd-doped Mg-Al-LDH/Au nanocomposite for CT/MR bimodal imagings and simultaneous drug delivery. *Biomaterials.* 2013;34(13):3390-401.
140. Tian C, Zhu L, Lin F, Boyes SG. Poly(acrylic acid) Bridged Gadolinium Metal-Organic Framework– Gold Nanoparticle Composites as Contrast Agents for Computed Tomography and Magnetic Resonance Bimodal Imaging. *ACS Appl Mater Interfaces.* 2015;7(32):17765-75.
141. Zeng C, Shi X, Wu B, Zhang D, W. Z. Colloids containing gadolinium-capped gold nanoparticles as high relaxivity dual-modality contrast agents for CT and MRI. *Colloids Surf B: Biointerfaces.* 2014;123:130-5.
142. Chen Q, Li K, Wen S, Liu H, Peng C, Cai H, et al. Targeted CT/MR dual mode imaging of tumors using multifunctional dendrimer-entrapped gold nanoparticles. *Biomaterials.* 2013;34(21):5200-9.

143. Chen Q, Wang H, Liu H, Wen S, Peng C, Shen M, et al. Multifunctional Dendrimer-Entrapped Gold Nanoparticles Modified with RGD Peptide for Targeted Computed Tomography/Magnetic Resonance Dual-Modal Imaging of Tumors. *Anal Chem.* 2015;87(7):3949-56.
144. Attia MF, Anton N, Bouchaal R, Didier P, Arntz Y, Messaddeq N, et al. Functionalization of nano-emulsions with an amino-silica shell at the oil-water interface. *RSC Adv.* 2015;5:74353-61.
145. Rosenholm JM, Sahlgren C, Lindén M. Towards multifunctional, targeted drug delivery systems using mesoporous silica nanoparticles – opportunities & challenges. *Nanoscale.* 2010;2(10):1870-83.
146. Ambrogio MW, Thomas CR, Zhao YL, Zink JISJF. Mechanized silica nanoparticles: a new frontier in theranostic nanomedicine. *Acc Chem Res.* 2011;44(10): 903-13
147. Benezra M, Penate-Medina O, Zanzonico PB, Schaer DO, H. , Burns A, DeStanchina E, et al. Multimodal silica nanoparticles are effective cancer-targeted probes in a model of human melanoma. *J Clin Invest.* 2011;121(7):2768-80.
148. Marques L, Hernandez FU, James SW, Morgan SP, Clark M, Tatam RP, et al. Highly sensitive optical fibre long period grating biosensor anchored with silica core gold shell nanoparticles. *Biosens Bioelectron.* 2016;75:222-31.
149. Song J-T, Yang X-Q, Zhang X-S, Yan D-M, Yao M-H, Qin M-Y, et al. Composite silica coated gold nanosphere and quantum dots nanoparticles for X-ray CT and fluorescence bimodal imaging. *Dalton Trans.* 2015;44(25):11314-20.
150. Hu K-W, Jhang F-Y, Su C-H, C-S. Y. Fabrication of Gd<sub>2</sub>O(CO<sub>3</sub>)<sub>2</sub>.H<sub>2</sub>O/silica/gold hybrid particles as a bifunctional agent for MR imaging and photothermal destruction of cancer cells. *J Mater Chem.* 2009;19(15):2147-53.
151. Dong W, Li Y, Niu D, Ma Z, Liu X, Gu J, et al. A Simple Route to Prepare Monodisperse AuNP-Decorated, Dye-doped, Superparamagnetic Nanocomposites for Optical, MR, and CT Trimodal imaging. *Small.* 2013;9(15):2500-8.
152. Chen J, Guo Z, Wang H-B, Gong M, Kong X-K, Xia P, et al. Multifunctional Fe<sub>3</sub>O<sub>4</sub>@C@Ag hybrid nanoparticles as dual modal imaging probes and near-infrared light-responsive drug delivery platform. *Biomaterials.* 2013;34(2):571-81.
153. Wu Q, Chen L, Huang L, Wang J, Liu J, Hu C, et al. Quantum Dots Decorated Gold Nanorod as Fluorescent-Plasmonic Dual- Modal Contrasts Agent for Cancer Imaging. *Biosens Bioelectron.* 2015;74:16-23.
154. Bohic S, Cotte M, Salomé M, Fayard B, Kuehbacher M, Cloetens P, et al. Biomedical applications of the ESRF synchrotron-based microspectroscopy platform. *J Struct Biol.* 2012;177(2):248-58.
155. Ipe BI, Yoosaf K, G. TK. Functionalized gold nanoparticles as phosphorescent nanomaterials and sensors. *J Am Chem Soc* 2006;128(6):1907-13.
156. Voelcker F, Von Lichtenberg A. Pyelographie Rontgenographie des Nirenbeckens nach Kollargol-fulling. *Muench Med Wochenschr.* 1906;53(105).
157. Uhle AA, Pfahler GE, MacKinney WH, Miller AG. XIII. Combined Cystoscopic and Röntgenographic Examination of the Kidneys and Ureter. *Ann Surg.* 1910;51(4):546-51.

158. Seltzer SE, Adams DF, Davis MA, Hessel SJH, A. , Havron A, Hollenberg NK. Development of selective hepatic contrast agents for CT scanning. *Invest Radiol.* 1979;14:356.
159. Eisenberg RL. *Radiology, An Illustrated History.* St. Louis: Mosby-Year Book; 1992.
160. Zhang C, Wang K, Han D, Pang Q. Surface enhanced Raman scattering (SERS) spectra of trinitrotoluene in silver colloids prepared by microwave heating method. *Spectrochim Acta A Mol Biomol Spectrosc* 2014;122:387-91.
161. Martinez-Gutierrez F, Boegli L, Agostinho A, Sánchez EM, Bach H, Ruiz F, et al. Antibiofilm activity of silver nanoparticles against different microorganisms. *Biofouling.* 2013;29(6):651-60.
162. Doudi M, Naghsh N, Setorki M. Comparison of the effects of silver nanoparticles on pathogenic bacteria resistant to beta-lactam antibiotics (ESBLs) as a prokaryote model and Wistar rats as a eukaryote model. *Med Sci Monit Basic Res.* 2013;19:103-10.
163. Xiang D, Zheng Y, Duan W, Li X, Yin J, Shigdar S, et al. Inhibition of A/Human/Hubei/3/2005 (H3N2) influenza virus infection by silver nanoparticles in vitro and in vivo. *Int J Nanomedicine.* 2013;8:4103-13.
164. Pinto RJ, Almeida A, Fernandes SC, Freire CS, Silvestre AJ, Neto CP, et al. Antifungal activity of transparent nanocomposite thin films of pullulan and silver against *Aspergillus niger*. *Colloids Surf B: Biointerfaces.* 2013;103:143-8.
165. Lu Z, Rong K, Li J, Yang H, Chen R. Size-dependent antibacterial activities of silver nanoparticles against oral anaerobic pathogenic bacteria. *J Mater Sci Mater Med.* 2013;24(6):1465-71.
166. Willems, Wildenberg VD. Roadmaps at 2015 on nanotechnology application in the sectors of: materials, health & medical systems, energy. November 2015.
167. Müller S. Magnetic fluid hyperthermia therapy for malignant brain tumors - an ethical discussion. *Nanomed: Nanotech Biol Med.* 2009;5:387-93.
168. El-Kheshen AA, Gad El-Rab SF. Effect of reducing and protecting agents on size of silver nanoparticles and their anti-bacterial activity. *Der Pharma Chemica.* 2012;4(1):53-65.
169. Fribourg-blanc E, Dang DTM, Le TTT, Trinh CD, Thanh TTN, Dang CM. Investigation of shape controlled silver nanoplates by simple chemical reduction method. *NANO: Brief Reports and Reviews.* 2013;8(3): 1350030- 40.
170. Attia MF, Azib T, Salmi Z, Singh A, Decorse P, Battaglini N, et al. One-step UV-induced modification of cellulose fabrics by polypyrrole/silver nanocomposite films. *J Colloid Interface Sci.* 2013;393:130-7
171. Çınar S, Gündüz G, Mavis B, Çolak Ü. Synthesis of Silver Nanoparticles by Oleylamine-Oleic Acid Reduction and Its Use in Making Nanocable by Coaxial Electrospinning. *J Nanosci Nanotechnol.* 2011;11:3669-79.
172. Zou J, Hannula M, Misra S, Feng H, Labrador RH, Aula AS, et al. Micro CT visualization of silver nanoparticles in the middle and inner ear of rat and transportation pathway after transtympanic injection. *Journal of Nanobiotechnology* 2015;13:5.
173. Chrastina A, Schnitzer JE. Iodine-125 radiolabeling of silver nanoparticles for in vivo SPECT imaging. *Int J Nanomedicine.* 2010;5:653-9.

174. Liu H, Wang H, Guo R, Cao X, Zhao J, Luo Y, et al. Size-controlled synthesis of dendrimer-stabilized silver nanoparticles for X-ray computed tomography imaging applications. *Polym Chem.* 2010;1:1677-83.
175. Liu H, Shen M, Zhao J, Zhu J, Xiao T, Cao X, et al. Facile formation of folic acid-modified dendrimer-stabilized gold-silver alloy nanoparticles for potential cellular computed tomography imaging applications. *Analyst.* 2013;138:1979-87.
176. Li J, You J, Dai Y, Shi M, Han C, K. X. Gadolinium Oxide Nanoparticles and Aptamer-Functionalized Silver Nanoclusters-Based Multimodal Molecular Imaging Nanoprobe for Optical/Magnetic Resonance Cancer Cell Imaging. *Anal Chem.* 2014;86:11306-11.
177. Luo Y, Wang CM, Qiao Y, Hossain M, Ma LY, Su M. In vitro cytotoxicity of surface modified bismuth nanoparticles. *J Mater Sci Mater Med.* 2012;23(10):2563-73.
178. Sun H, Li H, Harvey H, Sadler PJ. Interactions of bismuth complexes with metallothionein(II). *J Biol Chem.* 1999;274(41):29094-101.
179. Rabin O, Perez JM, Grimm J, Wojtkiewicz G, Weissleder R. An X-ray computed tomography imaging agent based on long-circulating bismuth sulphide nanoparticles *Nat Mater.* 2006;5:118-22.
180. Liu J, Zheng X, Yan L, Zhou L, Tian G, Yin W, et al. Bismuth Sulfide Nanorods as a Precision Nanomedicine for in Vivo Multimodal Imaging-Guided Photothermal Therapy of Tumor *ACS Nano.* 2015;9(1):696-707.
181. Zheng X, Shi J, Bu Y, Tian C, Zhang X, Yin W, et al. Silica-coated bismuth sulfide nanorods as multimodal contrast agents for a non-invasive visualization of the gastrointestinal tract. *Nanoscale.* 2015;7(29):12581-91.
182. García-Sevillano J, Cantelar E, Cussó F, Ocaña M. Up-conversion in Er<sup>3+</sup>/Yb<sup>3+</sup> co-doped LaPO<sub>4</sub> submicron-sized spheres. *Opt Mater.* 2015;41:104-7.
183. Veintemillas-Verdaguer S, Luengo Y, Serna CJ, Andrés-Vergés M, Varela M, Calero M, et al. Bismuth labeling for the CT assessment of local administration of magnetic nanoparticles. *Nanotechnology* 2015 26(13):135101.
184. Fang Y, Peng C, Guo R, Zheng L, Qin J, Zhou B, et al. Dendrimer-stabilized bismuth sulfide nanoparticles: synthesis, characterization, and potential computed tomography imaging applications. *Analyst.* 2013;138(11):3172-80.
185. Bogusz K, Tehei M, Stewart C, McDonald M, Cardillo D, Lerch M, et al. Synthesis of potential theranostic system consisting of methotrexate-immobilized (3-aminopropyl)trimethoxysilane coated  $\alpha$ -Bi<sub>2</sub>O<sub>3</sub> nanoparticles for cancer treatment. *RSC Adv.* 2014;4(46):24412-9.
186. liang S, Zhou QW, M., Zhu Y, Wu Q, Yang X. Water-soluble l-cysteine-coated FePt nanoparticles as dual MRI/CT imaging contrast agent for glioma. *Int J Nanomedicine.* 2015;10:2325-33.
187. Cormode DP, Skajaa T, Van Schooneveld MM, Koole R, Jarzyna P, Lobatto ME, et al. Nanocrystal core high-density lipoproteins: A multimodality contrast agent platform. *Nano Lett* 2008;8(11):3715-23.
188. Harper BW, Krause-Heuer AM, Grant MP, Manohar M, Garbutcheon-Singh KB, Aldrich-Wright JR. Advances in platinum chemotherapeutics. *Chemistry.* 2010;16(24):7064-77.

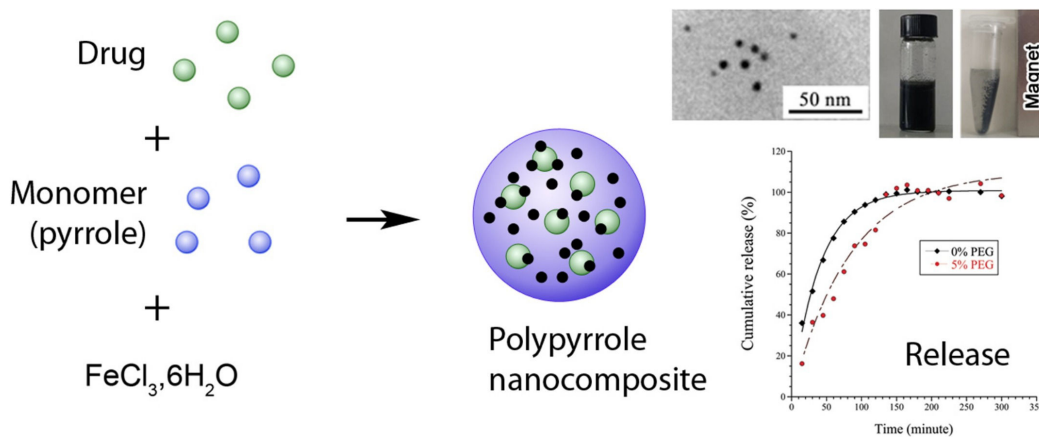
189. Sun C, Lee JSH, Zhang M. Magnetic nanoparticles in MR imaging and drug delivery. *Adv Drug Deliv Rev* 2008;60(11):1252-65.
190. Mornet S, Vasseur S, Grasset F, Duguet E. Magnetic nanoparticle design for medical diagnosis and therapy. *J Mater Chem*. 2004;14:2161-75.
191. Laurent S, Forge D, Port M, Roch A, Robic C, Vander EL, et al. Magnetic iron oxide nanoparticles: Synthesis, stabilization, vectorization, physicochemical characterizations and biological applications. *Chem Rev*. 2008;108(6):2064-110.
192. Pankhurst QA, Connolly J, Jones SK, Dobson J. Applications of magnetic nanoparticles in biomedicine. *J Phys D: Appl Phys*. 2003;36(18):R167-R81.
193. Hahn M, Singh AK, Sharma P, Brown SC, Moudgil BM. Nanoparticles as contrast agents for in-vivo bioimaging: Current status and future perspectives. *Anal Bioanal Chem*. 2011;399(1):3-27.
194. Na HB, Song IC, Hyeon T. Inorganic nanoparticles for MRI contrast agents. *Adv Mater*. 2009;21(21):2133-48.
195. Key J, Leary JF. Nanoparticles for multimodal in vivo imaging in nanomedicine. *Int J Nanomedicine*. 2014;9:711-26.
196. Chen W, Cormode DP, Fayad ZA, Mulder WJM. Nanoparticles as magnetic resonance imaging contrast agents for vascular and cardiac diseases. *Wiley Interdiscip Rev Nanomed Nanobiotechnol* 2011;3(2):146-61.
197. Cormode DP, Skajaa T, Fayad ZA, Mulder WJM. Nanotechnology in medical imaging: probe design and applications. *Arterioscler Thromb Vasc Biol*. 2009;29(7):992-1000.
198. Lodhia J, Mandarano G, Ferris NJ, Eu P, Cowell SF. Development and use of iron oxide nanoparticles (Part 1): Synthesis of iron oxide nanoparticles for MRI. *Biomed Imaging Interv J*. 2010;6(2):e12.
199. He X, Ma N. An overview of recent advance of quantum dots for biomedical applications. *Colloid Surf B-Biointerfaces*. 2014;124:118-31.
200. Michalet X, Pinaud FF, Bentolila LA, Tsay JM, Doose S, Li J, et al. Quantum Dots for Live Cell, in vivo Imaging, and Diagnostics. *Science*. 2005;307(5709):538-44.
201. Hardman R. A toxicologic review of quantum dots: Toxicity depends on physicochemical and environmental factors. *Environ Health Perspect*. 2006;114(2):165-72.
202. Volkov Y. Nanomedicine: Focus on Quantum Dots. Quantum dots in nanomedicine: recent trends, advances and unresolved issues. *Biochem Biophys Res Commun* 2015;XXX:1-9.
203. Murphy CJ. Peer Reviewed: Optical Sensing with Quantum Dots. *Anal Chem*. 2002;74(19):520A-6A.
204. Vasudevan D, Gaddam RR, Trinchi A, Cole I. Core-Shell Quantum Dots: Properties and Applications. *J Alloy Compd*. 2015;636:395-404.
205. Oh MH, Lee N, Kim H, Park SP, Piao Y, Lee J, et al. Large-scale synthesis of bioinert tantalum oxide nanoparticles for X-ray computed tomography imaging and bimodal image-guided sentinel lymph node mapping. *J Am Chem Soc* 2011;133(14):5508-15.
206. Freedman JD, Lusic H, Snyder BD, Grinstaff MW. Synthesis of Tantalum Oxide Nanoparticles for Imaging Articular Cartilage Using X-Ray Computed Tomography:

- Visualization of Ex vivo/In vivo Murine Tibia and Ex vivo Human Index Finger Cartilage *Angew Chem-Int Edit.* 2013;18(9):1199-216.
207. He W, Ai K, Lu L. Nanoparticulate X-ray CT contrast agents. *Sci China.* 2015;58(5):753-60.
208. Woods M, Woessner DE, Sherry D. Paramagnetic lanthanide complexes as PARACEST agents for medical imaging. *Chem Soc Rev.* 2006;35(6):500-11.
209. Ma Y, Wang Y. Recent advances in the sensitized luminescence of organic europium complexes. *Coord Chem Rev.* 2010;254(9-10):972-90.
210. Ye Z, Tan M, Wang G, Yuan J. Novel fluorescent europium chelate-doped silica nanoparticles: preparation, characterization and time-resolved fluorometric application. *J Mater Chem.* 2004;14(5):851-6.
211. Wang D, Cao W, Fan J. Synthesis and luminescence properties of the europium quaternary complexes nanoparticles. *Sci China Chem* 2014;57(6):791-6
212. Peng HS, Huang SH, Wolfbeis OS. Ratiometric fluorescent nanoparticles for sensing temperature. *J Nanoparticle Res.* 2010;12(8):2729-33.
213. Winter PM, Cai K, Chen J, Adair CR, Kiefer GE, Athey PS, et al. Targeted PARACEST nanoparticle contrast agent for the detection of fibrin. *Magn Reson Med.* 2006;56(6):1384-8.
214. Li X, Anton N, Zuber G, Vandamme T. Contrast agents for preclinical targeted X-ray imaging. *Adv Drug Deliv Rev.* 2014;76:116-33.
215. Tian G, Zheng X, Zhang X, Yin W, Yu J, Wang D, et al. TPGS-stabilized NaYbF<sub>4</sub>:Er upconversion nanoparticles for dual-modal fluorescent/CT imaging and anticancer drug delivery to overcome multi-drug resistance. *Biomaterials.* 2015;40(107-116).
216. Chatterjee DK, Rufaihah AJ, Zhang Y. Upconversion fluorescence imaging of cells and small animals using lanthanide doped nanocrystals. *Biomaterials.* 2008;29(7):937-43.



## Chapter 3.2 : One-step synthesis of iron oxide polypyrrole nanoparticles encapsulating ketoprofen as model of hydrophobic drug

We reported one-pot synthesis of a novel multifunction nanocomposite (NC) composed of polypyrrole/iron oxide NPs and incorporating the ketoprofen as hydrophobic model drug, all coated with PEGylated shell. This has been achieved by *in situ* chemical oxidative polymerization method aiming to impart the resulting nanocarrier real advantages like increasing the encapsulation efficiency of the ketoprofen, improving the drug water solubility thanks to the PEG chains of the Solutol HS15<sup>®</sup> (surfactant) and conferring them a magnetic properties that came from the iron oxide particles. Potential physicochemical characterization was done on the constructed NCs such as FTIR, TGA, TEM and SEM to investigate the chemical structure, the size and the morphological shape. Three concentrations of the drug encapsulated 5, 10, and 20 wt.%, which resulted in high encapsulation efficiencies 75%, 95%, and 98% respectively. *In vitro* release studies were evaluated for different concentration giving rise to complete drug release after approximately 2 hours. Magnetic relaxometry studies confirmed their possible applications as potential contrast agent in the field of magnetic resonance imaging (MRI). This schematic representation describes the proposed study.





## One-step synthesis of iron oxide polypyrrole nanoparticles encapsulating ketoprofen as model of hydrophobic drug



Mohamed F. Attia<sup>a,b,c</sup>, Nicolas Anton<sup>a,b,\*</sup>, Ikram Ullah Khan<sup>a,d,e</sup>, Christophe A. Serra<sup>d</sup>, Nadia Messaddeq<sup>f</sup>, Anshuman Jakhmola<sup>g</sup>, Raffaele Vecchione<sup>g</sup>, Thierry Vandamme<sup>a,b</sup>

<sup>a</sup> University of Strasbourg, Faculty of Pharmacy, 74 route du Rhin 67401 Illkirch Cedex, France

<sup>b</sup> CNRS UMR 7199, Laboratoire de Conception et Application de Molécules Bioactives, équipe de Pharmacie Biogalénique, University of Strasbourg, route du Rhin No. 74, F-67401 Illkirch Cedex, France

<sup>c</sup> National Research Center, P.O. 12622, Cairo, Egypt

<sup>d</sup> Institut Charles Sadron (ICS)–UPR 22CNRS, Strasbourg, France

<sup>e</sup> Department of Pharmaceutics, Faculty of Pharmaceutical Sciences, Government College University, Faisalabad, Pakistan

<sup>f</sup> IGBMC (Institut de Génétique et de Biologie Moléculaire et Cellulaire), Inserm U964, CNRS UMR7104, Université de Strasbourg, 1 rue Laurent Fries, 67404 Illkirch, France

<sup>g</sup> Istituto Italiano di Tecnologia, IIT@CRIB, Largo Barsanti e Matteucci, 53 80125 Napoli, Italy

### ARTICLE INFO

#### Article history:

Received 18 March 2016

Received in revised form 26 April 2016

Accepted 28 April 2016

Available online 7 May 2016

#### Keywords:

Ketoprofen

Nanomedicine

Encapsulation

PEGylated shell

Drug delivery system

Polypyrrole

MRI contrasting agents

### ABSTRACT

This study reports a novel one-step synthesis of hybrid iron oxide/polypyrrole multifunctional nanoparticles encapsulating hydrophobic drug and decorated with polyethylene glycol. The overall process is based on the *in situ* chemical oxidative polymerization of pyrrole along with the reduction of ferric chloride (FeCl<sub>3</sub>) in the presence of ketoprofen as model drug and PEGylated surfactants. The final product is a nanocomposite composed of polypyrrole and a mixture of FeO/Fe<sub>2</sub>O<sub>3</sub>. Different concentrations of ketoprofen were encapsulated in the nanocomposite, and were characterized by Fourier transform infrared spectroscopy (FTIR) and differential scanning calorimetry (DSC). Encapsulation efficiency of the final product was measured by absorption, which can reach up to 98%. The release experiments confirmed complete drug release after about 3 h in PBS solution. Morphological characterization of the nanocomposites was performed by electron microscopy (scanning and transmission electron microscopy) which confirmed the spherical geometry and opaque nature of nanoparticles with average particle size well below 50 nm. The final product is multifunctional system, which could act both as a nanocarrier for drug molecules as well as a contrasting agent. Magnetic relaxometry studies confirmed their possible applications as potential contrast agent in the field of magnetic resonance imaging (MRI).

© 2016 Elsevier B.V. All rights reserved.

### 1. Introduction

Nanotechnology involves manipulating properties and structures at the nanoscale level offering many advantages and properties which otherwise are not possible at macroscopic level. One such area is the combination of nanotechnology with medical applications that has led to the emergence of a new field called nanomedicine. Important tools for the development of nanomedicine are the nano-carriers, which have received a special

attention over the past few years. These systems have opened new ways to modify the biodistribution and pharmacokinetics of active principle ingredients (API) by improving their bioavailability and/or targeting specific sites at high concentrations while minimizing the side effects. Polymeric nanoparticles are one such organic strategy for nanomedicine which have high potential to revolutionize modern medicine (Nasongkla et al., 2006; Khemtong et al., 2009; Feng et al., 2010), liposomes (Ewesuedo and Ratain, 2003; Petros et al., 2008; Ferrara et al., 2009), dendrimers (Medina and El-Sayed, 2009) and inorganic NPs (Liong et al., 2008; Morgan et al., 2008; Kim et al., 2009) because of their numerous advantages like their possible biocompatibility, biodegradability, non-immunogenic properties, and their potential applications for controlled drug release into targeted cancer cells or tumor tissues (Haag and Kratz 2006). Some specific systems like polymer-drug

\* Corresponding author at: University of Strasbourg, CNRS 7199, Laboratoire de Conception et Application de Molécules Bioactives, équipe de Pharmacie Biogalénique, route du Rhin No.74, F-67401 Illkirch Cedex, France.

E-mail address: [nanton@unistra.fr](mailto:nanton@unistra.fr) (N. Anton).

conjugates can even increase the drug payloads, reduce the systemic toxicity, prolong drug circulation time, and improve drug solubility and targeting (Godwin et al., 2001; Ye et al., 2006). There are many synthesis protocols for the preparation of polymer based NPs, which can be broadly divided-up to (i) monomers polymerization in the form of nanoparticles, and (ii) nanoprecipitation of preformed polymers. Polymeric nanoparticles based on intrinsic conductive polymers (ICPs) such as polypyrrole, polyaniline, polythiophene are often prepared by polymerization of their monomers. Among these, polypyrrole possess many interesting properties like good conductivity, bio-degradability, biocompatibility and possess no threat to the environment which makes it a promising candidate for a wide range of applications. (Skotheim, 1986; Stupnisek-Lisac et al., 1992; Tarcha et al., 1992; Pope et al., 1996; Faverolle et al., 1998; Skotheim et al., 1998; Leclerc, 1999; Jager et al., 2001; Iroh and Su, 2002; Kros et al., 2002; An et al., 2004; Kros et al., 2004; Wang et al., 2004; White and Slade, 2004; Ramanathan et al., 2005; Reece et al., 2005; Sides and Martin, 2005; Wadhwa et al., 2006; Esrafilzadeh et al., 2013; Maity et al., 2014). Another advantage lies in their facile synthesis through various polymerization routes, e.g. from photosynthesis polymerization process (Yang and Lu, 2005; Hodko et al., 2009; Attia et al., 2013), electrochemical polymerization pathway (Ashraf et al., 1996; Li et al., 2005) to *in situ* chemical oxidative polymerization reaction (Fujii et al., 2007; Müllera et al., 2011; Wang et al., 2013; Ghadim et al., 2014) in the presence ferric chloride (FeCl<sub>3</sub>), ferric nitrate (Fe(NO<sub>3</sub>)<sub>2</sub>), ammonium persulfate (NH<sub>4</sub>S<sub>2</sub>O<sub>8</sub>), sodium persulfate (Na<sub>2</sub>S<sub>2</sub>O<sub>8</sub>) as oxidizing agents. These reactions involve polymeric stabilizers or surfactants like polyvinylpyrrolidone (PVP), polyvinylalcohol (PVA), sodium dodecyl sulfate (SDS), cetyltrimmonium bromide (CTAB).

The properties of polypyrrole NPs can be further enhanced by making hybrid particles especially using the polymer for encapsulation of metal or inorganic particles e.g. gold, silver, copper, and iron inside the polymer core (Gangopadhyay and De, 2000; Martins et al., 2006). Such hybrid nanocomposites have found a broad range of applications as they often exhibit many new properties as well as improved physical and chemical properties over their single-component counterparts. Unfortunately, such hybrid materials are often met with some limitations like difficulty in process design, PPy mechanical performance, and poor water solubility, which limit their applications in biomedical fields and also potential industrial scaling-up. In order to overcome these limitations, many techniques have been developed based on the dispersion of ICPs in a matrix composed of an insulation polymer, which improves the process design and mechanical performance along with the electrical, magnetic and optical properties of ICPs (Wang and Fernandez, 1992; Vicentini et al., 2007).

In the present study we have proposed a novel nanocarrier system based on polypyrrole nanocomposite, capable of encapsulating ketoprofen as model drug. These nanoparticles were synthesized by a one-step *in situ* polymerization reaction, coated with a PEG chains, and are designed to show electromagnetic properties. The PEG layer not only controlled the *in vivo* behavior such as blood clearance (Soppimath et al., 2001) but also allow a precise control on the final size and monodispersity feature of the nanocarrier. This morphology of the nanoparticles as well as their ability to encapsulate a model drug, and their release profile have also been thoroughly investigated. Our main objectives in this study are focused on the design, characterization and physico-chemical evaluation of a new nanoparticulate system. The main advantage is the simple one-pot synthesis protocol for the preparation of multifunctional polymeric nanoparticles. In addition, the materials herein used have already been used in biological application showing their biocompatibility (Alizadeh and Shamaeli 2014). The final material has been thoroughly characterized

to confirm the size, change in morphology with composition, magnetic properties, as well as encapsulation and release profile of a model lipophilic drug (ketoprofen).

## 2. Experimental part

### 2.1. Reagents and materials

Prior to synthesis pyrrole (Aldrich) was distilled twice under reduced pressure, and was refrigerated in dark at low temperature in an inert environment. Iron (III) chloride hexahydrate (FeCl<sub>3</sub>·6H<sub>2</sub>O, Aldrich) was used as an oxidant/dopant species and was employed without further purification. Ketoprofen as a hydrophobic drug model was purchased from Sigma–Aldrich. Kolliphor<sup>®</sup> HS 15 is a mixture of free PEG 660 and PEG 660 hydroxystearate (PEG 660 12-hydroxystearate, MW 870 Da) (BASF, Ludwigshafen, Germany). Distilled water and methanol were used as solvents, stock solution of phosphate buffer saline (PBS) pH 7.4 prepared by using double distilled water. Dialysis tubing (12,000–14,000 molecular weight cutoff) were obtained from Sigma Aldrich, USA. 0.45 μm syringe filters were purchased from Fisher (Germany).

### 2.2. Preparation of ketoprofen doped iron/PPy-PEG nanocomposites as drug delivery system

The drug-loaded nanocomposites (NCs) were synthesized according to the concept of *in situ* chemical oxidative polymerization, based on a modified reported method (Škodová et al., 2013). As illustrated in Fig. 1, FeCl<sub>3</sub>·6H<sub>2</sub>O was used as an oxidant to initiate the polymerization process, and the ferric ion(+III) was reduced during the chemical reaction (redox reaction) forming FeO and Fe<sub>2</sub>O<sub>3</sub> in nanometric sizes that were embedded in the polymer matrix (Zong et al., 2015). Nonionic hydrophilic PEGylated surfactant (Kolliphor<sup>®</sup> HS 15) was introduced during the synthesis as emulsifier and stabilizer. In a typical procedure, an aqueous and organic phase have been prepared separately, (i) The surfactant (Kolliphor<sup>®</sup> HS 15) was added in the 55 mL aqueous phase (milliQ water) corresponding to 0, 5, 10, 20, 30, 40, 50 wt.% of the total amount of NCs under vigorous stirring. This was followed by addition of (2.8 mmoles, 1 equiv.) of ferric chloride. (ii) The organic phase (methanol) was prepared by dissolving pyrrole monomer (11.2 mmoles, 4 equiv.), in 3 mL of methanol followed by addition of different amounts of ketoprofen (K) (5, 10, 20 wt.% of Ket/total NC ratio). After complete homogenization, the organic phase was added drop wise into the aqueous phase under vigorous stirring at 1000 rpm. The complete polymerization took about 12 h at room temperature, gradually getting converted into nanocomposites displaying a black aspect. The particles was then collected by centrifugation and the resulting nanoparticles were thoroughly washed three times with deionized water to remove any hydrophilic remnants, one time with ethanol, and finally with acetone to remove excess of free ketoprofen and free pyrrole monomer. The precipitate was finally dried under vacuum for 24 h.

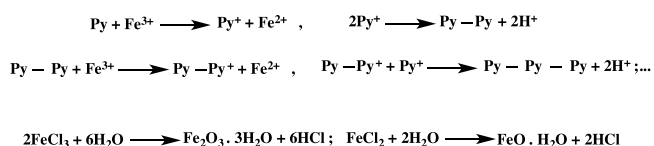


Fig. 1. Chemical equations for oxidation–reduction process during the polymerization of polypyrrole inducing iron oxide NPs imbedded into the NCs.

### 2.3. Infrared spectroscopy (IR)

FTIR is an important technique which is used to identify the various vibrational modes of the groups present in the molecules, their properties and their relationship with the molecular structure through the vibrational, transitional, and rotational motions of the atoms revealing characteristic frequencies, leading to frequency shifts and splitting in absorption peaks that corresponding to specific function groups *via* (Nicolet 380 FT-IR Spectrometer). The spectra were recorded for pure ketoprofen, drug-free nanocomposite and drug-loaded nanoparticles and sixty-four scans were signal-averaged in the range from 4000 to 500  $\text{cm}^{-1}$  at a resolution of 4  $\text{cm}^{-1}$  (Lee et al., 2003; Ranjha et al., 2009).

### 2.4. Differential scanning calorimetry (DSC)

Differential scanning calorimetry (DSC) was conducted on TA DSC Q200. The samples were equilibrated at 20 °C for 30 min. Indium standard was used to calibrate the DSC temperature and enthalpy scale. The powder samples were hermetically sealed in aluminum pans and heated at a constant rate of 10 °C/min, over a temperature range of 20–170 °C. Inert atmosphere was maintained by purging nitrogen at the flow rate of 15.8 mL/min, linear velocity 35 cm/sec and pressure 24.7 kPa.

### 2.5. Transmission electron microscopy (TEM)

The morphology and the particle diameter of the nanoparticles were characterized by transmission electron microscopy. The drug-nanocomposite gives significant contrast in TEM which was due to high opacity of the polypyrrole polymer, and therefore no staining agents were required. Dispersion solution was prepared (1 mg NPs/mL), and then diluted by 10 with Milli-Q water. A drop of the suspension was placed on carbon-coated copper grid (carbon type-A, 300 mesh, copper, Ted Pella Inc. Redding, PA) on an underlying tissue paper, leaving behind a thin colloidal film and dried at 40 °C for 20 min. Results were obtained using a Philips Morgagni 268D electron microscope.

### 2.6. Scanning electron microscopy (SEM)

The surface morphologies of the ketoprofen-loaded PPy/Iron nanocomposites were observed by scanning electron microscopy (SEM – AIS –2100) with an accelerating voltage of approximate 1.5–20 kV. Gold coating was performed to prevent charge-up of sample.

### 2.7. UV–vis absorption spectroscopy

UV–vis absorption spectra of the nanoparticle products were recorded on sample solution using a Cary 4 spectrophotometer (Varian) with a scan range of 200–500 nm at scanning rate 600 nm/min and a 1 nm resolution. Sample cell used in the study was a 1 cm quartz cuvette. All experimental data were corrected for PBS and ethanol background absorption. In order to determine the concentration of ketoprofen which revealed maximum absorption band at 260 nm wavelengths.

### 2.8. Encapsulation efficiency (EE%)

20 mg of ketoprofen-loaded nanocomposite were incubated in 10 mL of phosphate buffer saline solution (PBS) of pH 7.4 for complete extraction of the drug from nanoparticles into the solution. Then, the solution was filtered through 0.45  $\mu\text{m}$  syringe filter. Filtrate was analyzed by spectrophotometry at 260 (UV-

2101PC SHIMADZU) for ketoprofen. Encapsulation efficiency of respective drug was calculated by using the following equation

$$\% \text{ Encapsulation Efficiency} = (\text{encapsulated drug amount} / \text{total drug amount}) \times 100$$

### 2.9. In vitro release study

The required amount of drug-loaded nanocomposite was taken in a dialysis (MWCO: 12,000–14,000 g/mol). The dialysis tube, containing 25 mg of ketoprofen-loaded polypyrrole nanocomposites in 10 mL of PBS, then solution was introduced into the *in vitro* release medium containing 100 mL of phosphate buffer saline (pH 7.4). The whole assemblies were kept at fixed temperature ( $37 \pm 1$ ) °C measured in the dialysis tubes and constant pH value (pH = 7.4) during release and gently stirred magnetically. Sink conditions were maintained by replacing 5 mL of the release medium with fresh media at each sampling point. The amount of drug released was estimated from the measurement of the residual drug in the NPs at each sampling point by spectrophotometry measurements at  $\lambda_{\text{max}} = 260$  nm of an aliquot taken inside the dialysis bag. The drug concentration could be directly calculated from the measured absorbance. The amount of drug released was calculated from the amount of drug initially present in the NPs and the amount of drug retained in the NPs at each sampling point. Each experiment was carried out in triplicate, and average values plotted.

### 2.10. MRI experiments

$T_1$  and  $T_2$  relaxation times were measured with Bruker NMR analyzer equipped with mq60 Minispec v. 2.71 Rev.09/NT software (Billerica, MA, USA) operating at 1.41 T (60 MHz) and 37 °C.  $T_1$  relaxation times were measured using an inversion recovery pulse sequence (t1\_ir\_mb) with the following parameters: 8 scans per point 20 data items for fitting, single-exponential curve fitting, phase cycling, 5 ms first pulse separation, and a recycle delay and final pulse separation  $\geq 5T_1$ .  $T_2$  relaxation times were measured using a Carr-Purcell-Meiboom-Gill (CPMG) pulse sequence (t2\_cp\_mb) with the following parameters: 8 scans per item, bi exponential curve fitting, Phase cycling, 5 ms pulse separation first, 15 s recycle delay, 1 ms 90–180° pulse separation ( $\tau$ ), 200 data items for fitting. Relaxivities were determined by taking the slope of a plot of  $1/T_1(\text{s}^{-1})$  or  $1/T_2(\text{s}^{-1})$  vs. iron oxide concentration (mM).

## 3. Results and discussion

The advantages of polypyrrole as described before motivated us to investigate the potential of polypyrrole nanocomposite as an efficient drug delivery carrier system. Ketoprofen was selected as a model of hydrophobic drug, which displayed an efficient solubility in the pyrrole monomer, we expect significant encapsulation efficiency. The whole fabrication is schematically presented in Fig. 2.

The stoichiometric ratio between the pyrrole monomer and  $\text{FeCl}_3$  was thoroughly optimized and was around 4:1, which produced particles of uniform morphology (Wang et al., 2013). PEGylated surfactant was then introduced which acted as an emulsifier and stabilizing agent by forming a coating layer around nanoparticles. In this study, four nanocomposite platforms were synthesized and studied: (i) pristine non-PEGylated PPy NPs, (ii) PPy-PEGylated NPs, (iii) ketoprofen-loaded PPy NCs, and (iv) ketoprofen-loaded PPy-PEGylated NCs. The basic idea was to exploit the attractive electrostatic interactions between polypyrrole polymer (positive) and ketoprofen (negative) (as illustrated in

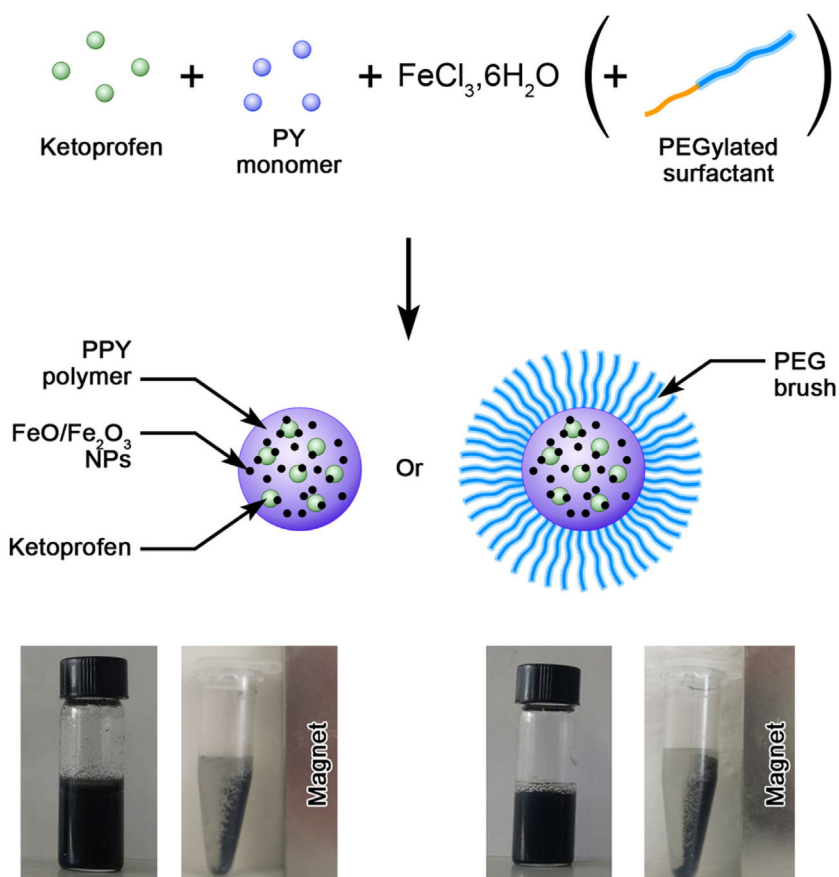


**Fig. 2.** Schematic representation of the fabrication process and of the structures of the PPY nanocomposites, with and without nonionic surfactant as stabilizer. Bottom picture show the macroscopic aspect of the respective suspensions, and general behavior when in close contact with a magnet.

**Fig. 3**), which should improve the drug encapsulation properties. On the other hand, the PEGylated surfactants will stabilize the developing nanoparticles through a simple homogeneous adsorption, and other kinds of bonds as drawn in Supplementary information.

### 3.1. FTIR analysis

For a drug delivery system, it is very important to rule out any possible strong interactions between polymer and drug and also the influence of processing parameters on integrity of active ingredients. FTIR is an excellent technique to detect spectral

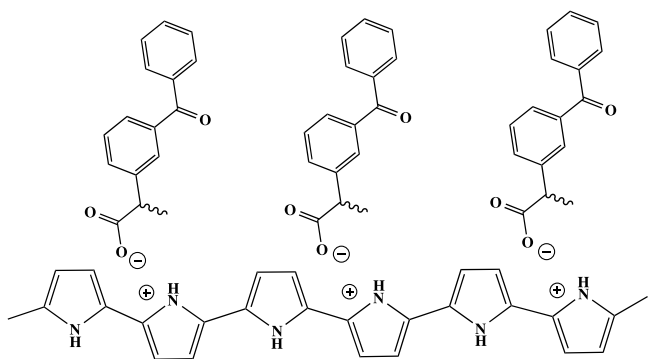


**Fig. 3.** Schematic representation shows the possible ionic forces between the ketoprofen drug and polypyrrole polymer.

changes that arise due to alteration in bonds. FTIR spectra (**Fig. 4**) were recorded in the mid-infrared region ( $400\text{--}4500\text{ cm}^{-1}$ ) where functional groups give characteristic IR absorption at specific narrow frequency range. In current study FTIR spectra of pure ketoprofen showed dimeric carboxylic acid carbonyl group stretching peak at  $1692\text{ cm}^{-1}$  and ketonic carbonyl stretching peak at  $1652\text{ cm}^{-1}$  (**Khan et al., 2013**). In control sample (b) bands appearing at  $1520$  and  $1434\text{ cm}^{-1}$  may be assigned to typical polypyrrole ring vibrations. The peak appearing at  $1126\text{ cm}^{-1}$  is assigned to the N—C stretching vibration and the bands at  $833$ ,  $963\text{ cm}^{-1}$  confirms the presence of polymerized pyrrole (**Xu et al., 2011**). Ketoprofen characteristic peaks were observed in all formulations except one containing 5% ketoprofen, which we believe was due to low loading of ketoprofen and limitations of the instrument to detect. Due to absence of any new peaks it was clear that there was no chemical interaction between ketoprofen or crystalline form of drug with polypyrrole as the C=O stretching of the dimeric ketoprofen was clearly visible. This fact was also evident from the literature (**Banchero et al., 2013**).

### 3.2. DSC characterization

We next performed DSC analysis for the sample. This technique is a useful tool to analyze and predict compatibility between active ingredients and excipients by rapidly evaluating appearance, disappearance or shift of endothermic and exothermic peaks (**Mura et al., 1995**). As shown in **Fig. 5**, DSC curve of pure ketoprofen displays endothermic peak around  $97^\circ\text{C}$ , which corresponds to melting point of drug as indicated in literature (**Banchero et al.,**

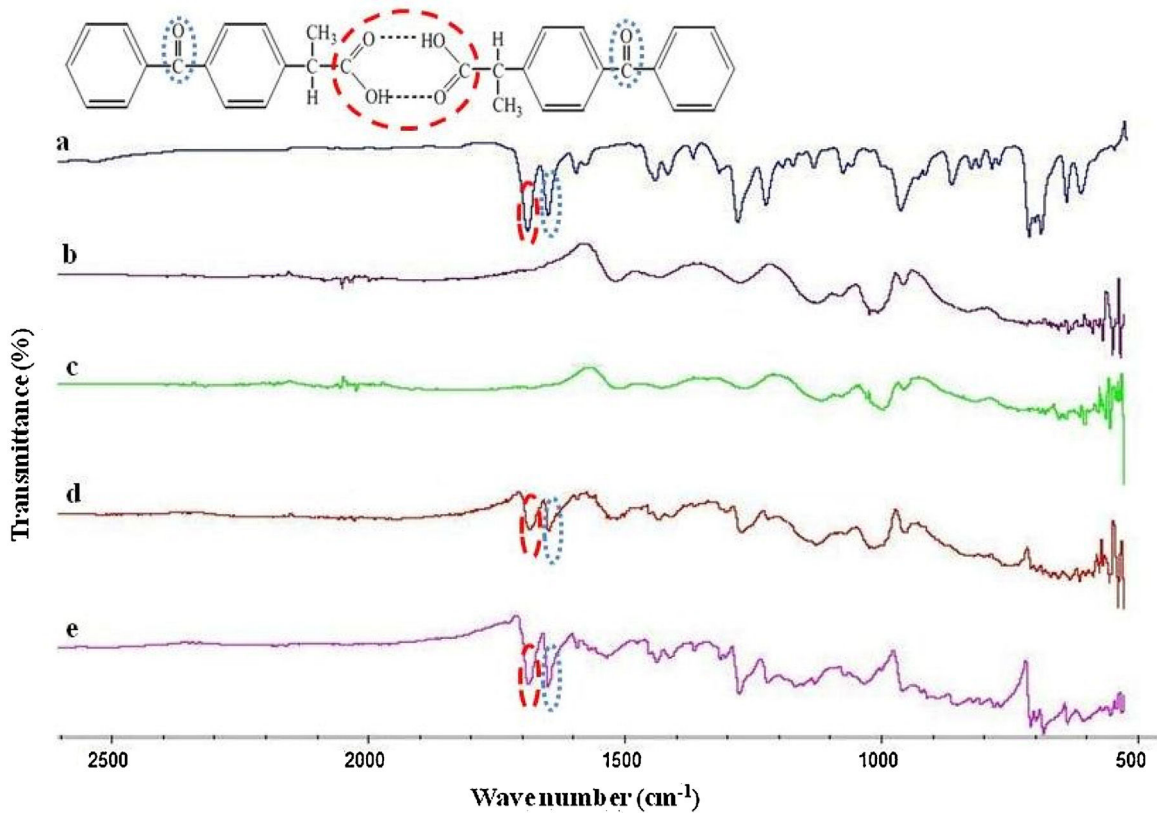


**Fig. 4.** FTIR spectra of free nanocomposite, free ketoprofen and ketoprofen-loaded nanoparticles: Ketoprofen alone (a), NCs as a control sample (0% ketoprofen) (b), 5 wt.% ketoprofen/NCs (c), 10 wt.% ketoprofen/NCs (d), and 20 wt.% ketoprofen/NCs (e).

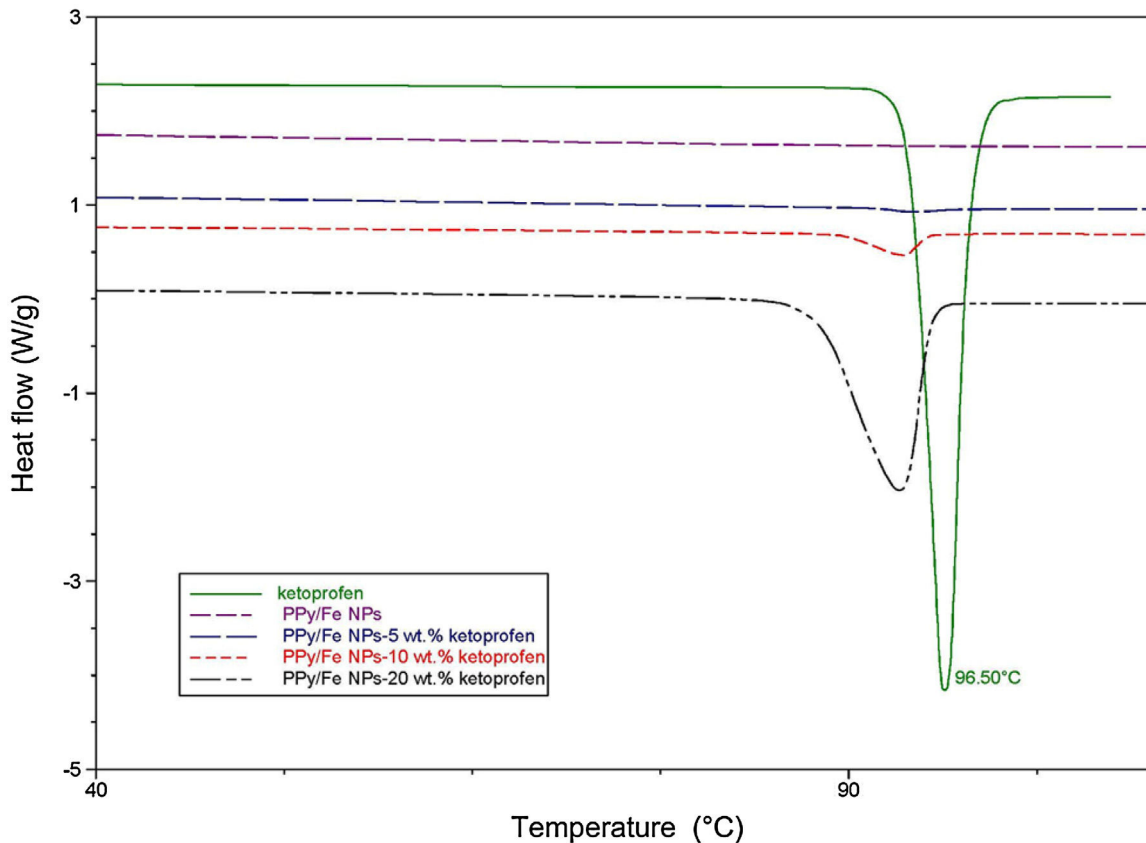


**Fig. 5.** DSC analysis of free drug, nanocomposites, drug-loaded nanocomposites in different ratios.

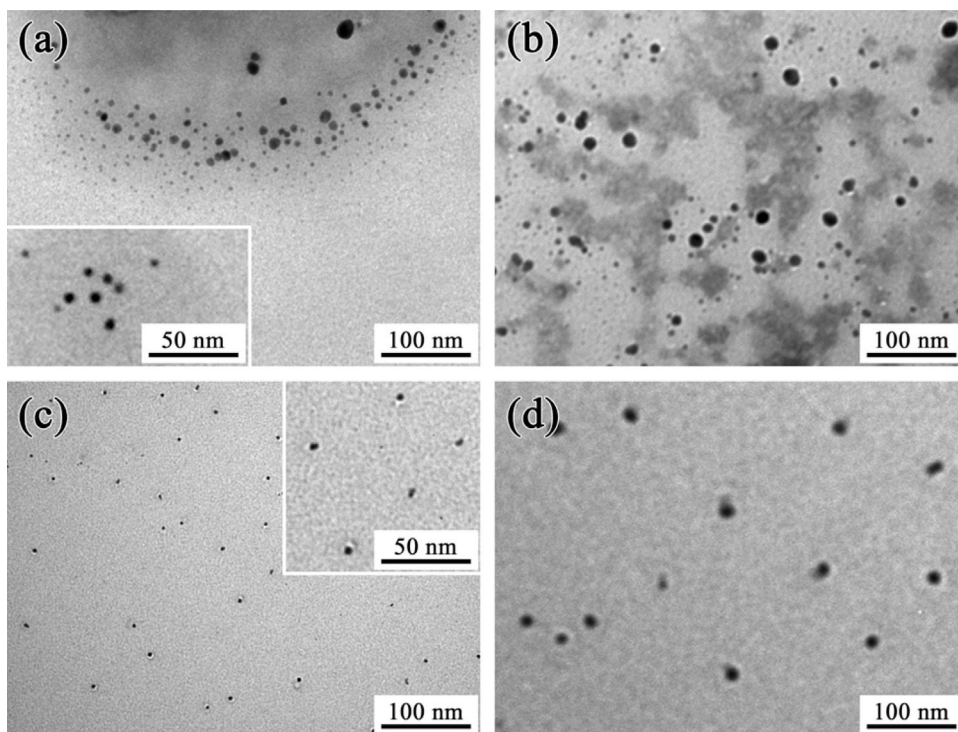


**Fig. 6.** TEM micrographs of the NCs of various compositions: (a) 10 wt.% ketoprofen, (b) 20 wt.% ketoprofen, (c) 5 wt.% PEGylated surfactant, (d) 40 wt.% PEGylated surfactant.

2013; Khan et al., 2013). In all formulations of drug loaded particles we observed the similar endothermic peak of ketoprofen. This suggests that overall process of nanoparticle formation did not affect the integrity of ketoprofen and is still in its crystalline form. Moreover, it further confirms the results of FTIR that there is no chemical interaction between drug and polymer.

### 3.3. Determination of the particle size and morphology of the NCs

The morphology of the system was thoroughly analyzed both by TEM and SEM.

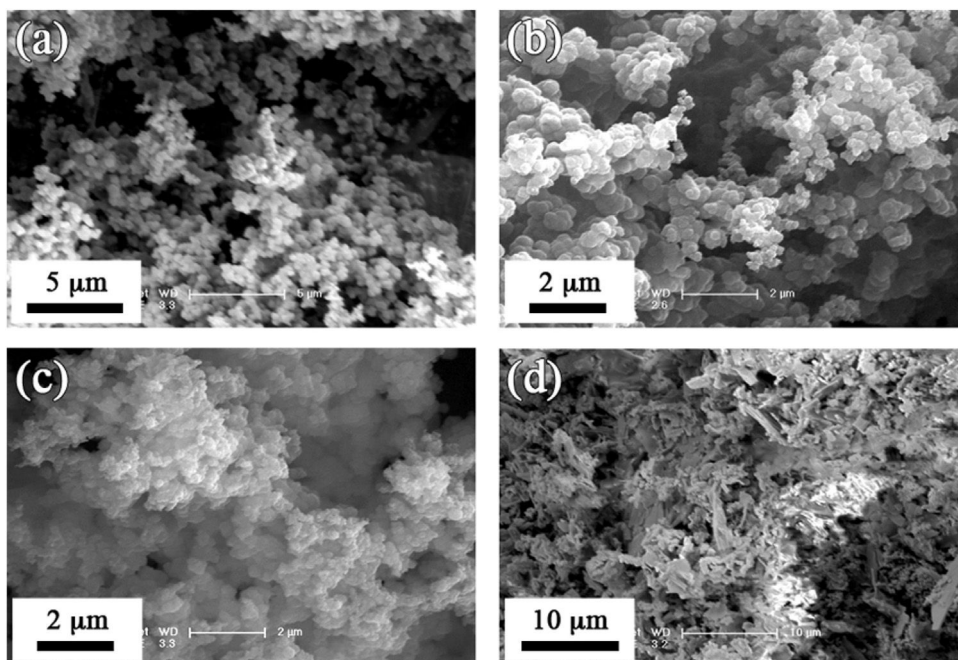


**Fig. 7.** SEM micrographs of the NCs of amounts of ketoprofen: (a) blank without ketoprofen, (b) 5 wt.% ketoprofen, (c) 10 wt.% ketoprofen, (d) 20 wt.% ketoprofen.

### 3.3.1. TEM characterization

The optimized particles synthesized at PPy/FeCl<sub>3</sub> stoichiometric ratio at (4:1) was selected as they displayed best uniformity in the size distribution and aspect. In addition, the PPy nanocomposites are dense and do not require any specific staining agent. Particles with different loadings of ketoprofen (10 wt.% and 20 wt.%) were analyzed and are compared, in Fig. 6(a) and (b), respectively. The micrographs display dark particles spherical in shape. For higher drug loadings second light-gray layer like a fractal crystalline network could also be observed which was, likely due to excess ketoprofen, which crystallized under vacuum. Overall the amount of drug loading does impact the NCs size, and were in close ranges below 50 nm. On the other hand, the effect of PEGylated surfactants have a significant influence on the size, giving the smallest nanoparticles for 5 wt.% (c) and much larger for 40 wt.% (d). In the synthesis of inorganic nanoparticles, surfactant is generally used for controlling the growth and overall morphology of particles. In our case also surfactant plays such a similar role due

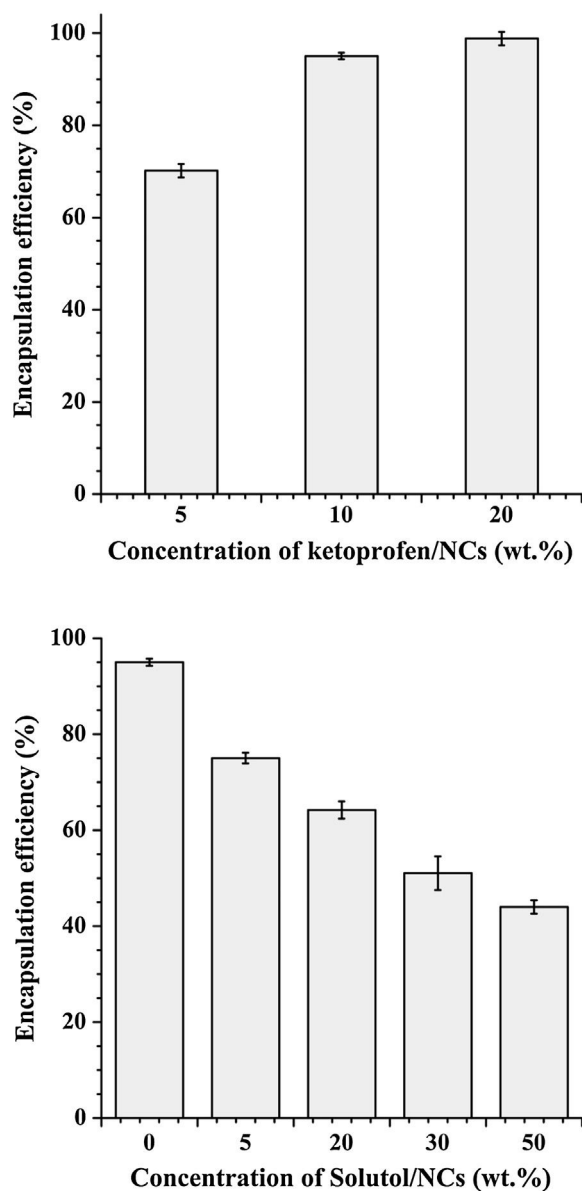


**Fig. 8.** Encapsulation efficiencies for drug loading composite particles. Three concentrations of ketoprofen loaded at 0 wt.% of solutol (non-PEGylated NCs) (up). Different concentrations of solutol (PEGylated surfactant) at constant drug/Pyrrrole 23 wt.% (bottom) (n=3).

to specific interactions with the growing polymer, and thus reducing the NCs size (Fig. 6(a) and (b)). However at higher concentrations of surfactants the nanoparticle size surprisingly increased as can be seen in picture (d), which could be due to interferences between the polymers and surfactant at such high surfactant amount.

### 3.3.2. SEM images

The surface characteristics of PPy NPs were further analyzed by SEM, as reported in Fig. 7. The micrographs revealed the granular nature of the particles compatible with the TEM observations. The particle size was not affected by the drug amount (for 5 wt.% and 10 wt.%), but was larger than blank particles. For high amount of ketoprofen (20 wt.%) (Fig. 7(d)) we can see the recrystallization of the free drug as observed in TEM above. This also proved that the

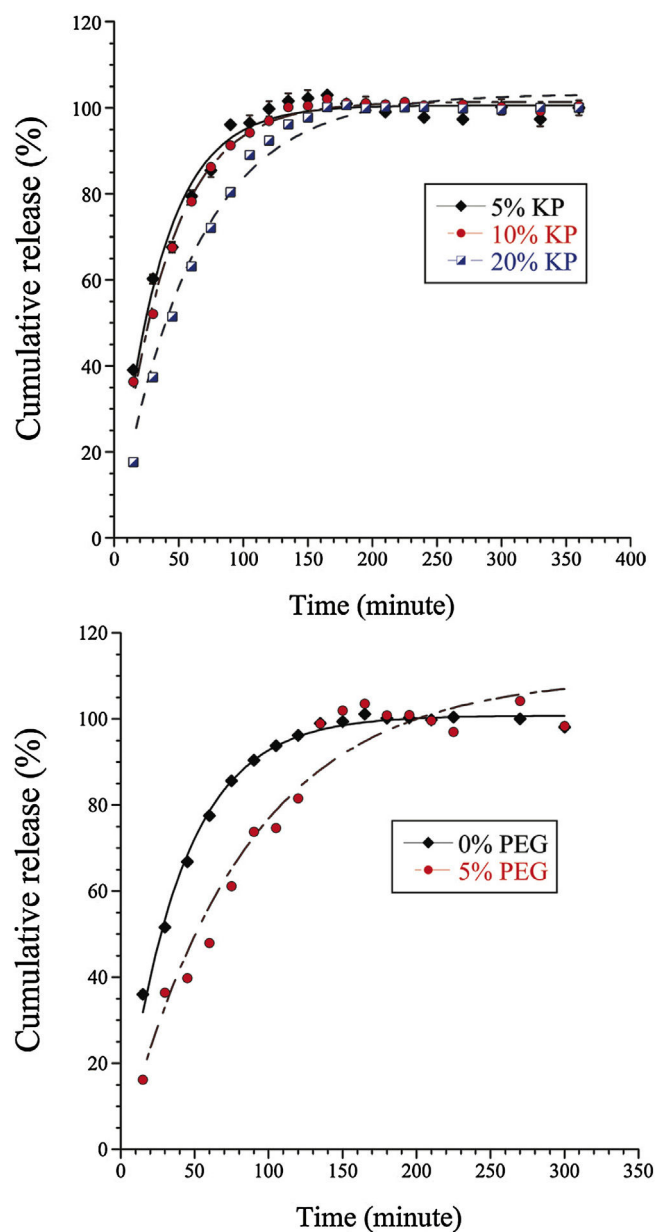


**Fig. 9.** *In vitro* release profiles of three different formulations of non-PEGylated NCs loading drug: 5 wt.%, 10 wt.%, 20 wt.% ketoprofen-loaded NPs (up). 0 wt.%, 5 wt.% PEGylated surfactant at 10% ketoprofen (bottom). Measurements were carried out in triplicates.

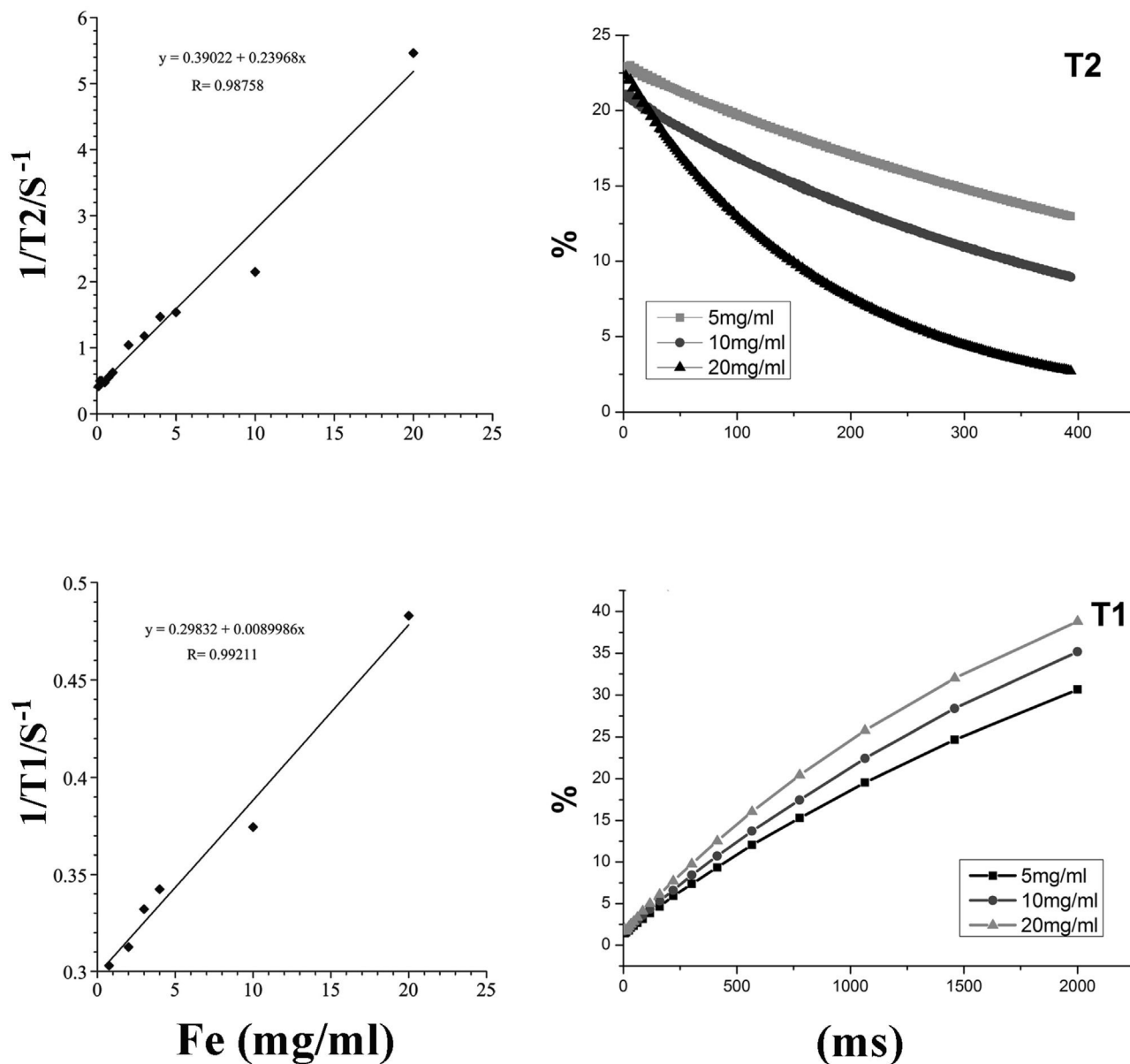


**Fig. 10.** (Top) Plot of the spin-spin transversal relaxation rate ( $1/T_2/S^{-1}$ ) against concentration of iron oxide, and the variation of T2 signal with the amount of iron oxide nanoparticles in the core. (Bottom) Plot of the spin-spin longitudinal relaxation rate ( $1/T_1/S^{-1}$ ) against concentration of iron oxide and the variation of T1 relaxation time with the amount of iron oxide nanoparticles in the core.

NCs can efficiently encapsulate to a maximum of 10 wt.% of ketoprofen.

### 3.4. Encapsulation efficiency of ketoprofen (EE)

The percent of the encapsulated drug into the NPs is considered one of the critical parameters in the drug delivery system. Different concentrations of ketoprofen and of PEGylated surfactants were selected to prepare nanocomposites, and to study the optimal drug EE. The results, reported in Fig. 8 (up) report the ketoprofen encapsulation efficiency of non-PEGylated nanoparticles containing 5 wt.%, 10 wt.% and 20 wt.% of drug. Values of EE rapidly increase up to close to 100% for 20 wt.% ketoprofen, meaning that electrostatic interactions gradually predominate over counter-ions as the drug concentration is sufficiently high. We also focused on the effect of surfactants on the encapsulation efficiency, Ketoprofen amount was fixed at 23% of the pyrrole monomer to ensure a maximum drug encapsulation, and the amount of PEGylated

surfactant was increased up to 50 wt.% respective to the whole mass of NCs (the corresponding absorption spectra are reported in Supplementary information section Fig. S2). The results, reported in Fig. 8 (bottom) disclose a clear drop of the EE values up to 44% for 50 wt.% of surfactants. This observation can be explained by two phenomena, (i) by a substantial interaction of the surfactants with the polymer as explained in Supplementary information Fig. S1, maybe a competition between hydrophobic and electrostatic interactions, (ii) by a premature drug release in surfactant micelles at the higher concentrations.

### 3.5. In vitro release study

As discussed before that drug release depends on several key factors such as the size of the particles *i.e.* the surface area. Both PEGylated and non-PEGylated NCs were studied. We first tested non-PEGylated NPs with different amount of drug loadings (5 wt.%, 10 wt.% and 20 wt.% of the total NPs weight) as reported in Fig. 9

top. The release profile of drug could be fitted by exponential curve. It can be seen from the curves that the release of drug was practically independent of drug loadings and displayed characteristic times of the exponential fits of 35.0 min, 39.4 min and 60.1 min for 5%, 10% and 20%, respectively. The very slight shift of the 20% curve may be simply explained by the constant diffusion coefficient of the drug that delays the time to reach 100% cumulative release when the global concentration is increased. On the other hand, the influence of the PEGylated surfactant displayed difference in kinetics (Fig. 9 bottom), with characteristic times of the exponential fits of 39.6 min and 83.4 min for 0% and 5% PEG, respectively. This difference was probably due to change in size as observed in TEM images; the higher the PEG concentration, the larger the NCs and hence less overall surface area thus lowering the drug release. The simple one-pot synthesis of these nanocomposites was due to the polymerization of pyrrole monomer in presence of ferric chloride. This results in formation of nanoparticles with intrinsic magnetic properties due to formation of iron oxides. The magnetic particles have a wide variety of applications in the field of nanomedicine for example the release profile of a magnetic nanocarrier system can be modified by applying magnetic field (Uva et al., 2014). Further the magnetic properties can also be exploited for MRI imaging. Iron oxide is an important MRI contrasting agents which can be helpful in tracking the drugs if administrated intravenously. However *in vivo* analysis is required to study this aspect completely.

In addition, it is noteworthy to mention that ketoprofen is partially soluble in PBS and globally induces a release within two hours proving that a lipophilic drug cannot only be encapsulated and confined within the nanocarrier system but is also completely released. All these features are needed for an efficient drug delivery system. The results were also consistent with similar types of drug delivery systems reported in literature (Alizadeh and Shamaeli, 2014).

### 3.6. Property of encapsulated iron oxide nanoparticles for MRI contrast agents

These experiments were based on the nano-confinement capabilities of the polymeric particles. As discussed earlier these particles could be easily loaded with drug molecules; however, it was also possible to encapsulate small nanoparticles of few nanometers inside the nanocarrier system. The polypyrrole polymer was preloaded with iron oxide ( $\text{FeO}/\text{Fe}_2\text{O}_3$ ) nanoparticles together with drug molecules as previously confirmed in TEM and SEM micrographs. Iron oxide nanoparticles are often called  $T_2$  agents as they possess inherent magnetic properties, which shorten the relaxation times of the surrounding protons (Morales et al., 2009). Both  $T_1$  and  $T_2$  relaxation times were measured for samples loaded with different amounts of iron oxide nanoparticles see results in Fig. 10. Relaxivities  $r_1$  and  $r_2$  were calculated from the slopes of the plot of  $1/T_2(\text{s}^{-1})$ ,  $1/T_1(\text{s}^{-1})$  vs. concentration of iron oxide and were found to be 0.009 and 0.24 respectively. The ratio  $r_2/r_1$  was calculated which indicates the relaxometric properties of the contrasting agent. In general, for paramagnetic materials  $r_2/r_1$  varies between 1 and 2 while for the superparamagnetic colloids it can be as large as 50 (Hatakeyama et al., 2011). In our case  $r_2/r_1$  was fairly high and was calculated to be 26.6. The ratio  $r_2/r_1$  indicates the effectiveness of the contrast, and was similar to the value reported for the iron oxide nanoparticles synthesized by other methods. This high value of the ratio  $r_2/r_1$  can be also considered as an indicator of the clustering between particles. It is to be noted that the magnetic properties in the nanocarrier system were developed due to formation of iron oxides during the polymerization reaction. The model drug ketoprofen had no effect on the magnetic properties or any other applications. Ketoprofen was only

chosen as model lipophilic drug to study the encapsulation and release profile and was not aimed for a systemic effect. Moreover it is worth mentioning that the targeting properties depend only on the nanocarrier system and not on the encapsulated drugs. In fact the presence of iron oxides in the nanocarrier system was an added advantage, as the particles became MRI active.

## 4. Conclusion

In summary, this study proposes a one-step synthesis of a novel multifunction drug nanocarrier system based on iron/polypyrrole nanocomposites decorated by PEGylated coating. A hydrophobic drug model, ketoprofen, was encapsulated along with the *in situ* chemical oxidative polymerization of pyrrole monomer by using ferric chloride hexahydrate as an oxidizing agent, and partially dopant species. For non-PEGylated NPs the drug-loading efficiencies reaches up to 98% for 20 wt.% ketoprofen. The PPy, polymer which is widely used for tissue engineering applications, (George et al., 2005; Fonner et al., 2008; Oh et al., 2010; Yang et al., 2012) also offers a number of additional functionalities, for example its hydrophobic structure with delocalized  $\pi$ -electrons, allows binding with aromatic drug molecules such as ketoprofen (ionic interaction) and giving rise to high payload capacity of the drug. This process opens new insights for surface modification of polypyrrole nanocomposites by PEGylated molecules terminated with active function groups that can modulate the surface charge or further bio-conjugation.

## Acknowledgement

The authors want to thanks Prof. Paolo Netti for making available the equipment used for MRI measurements.

## Appendix A. Supplementary data

Supplementary data associated with this article can be found, in the online version, at <http://dx.doi.org/10.1016/j.ijpharm.2016.04.073>.

## References

- Škodová, J., Kopecký, D., Vrnata, M., Varga, M., Prokeš, J., Cieslar, M., Bober, P., Stejskal, J., 2013. Polypyrrole–silver composites prepared by the reduction of silver ions with polypyrrole nanotubes. *Polym. Chem.* 4, 3610–3616.
- Alizadeh, N., Shamaeli, E., 2014. Electrochemically controlled release of anticancer drug methotrexate using nanostructured polypyrrole modified with cetylpyridinium: release kinetics investigation. *Electrochim. Acta* 130, 488–496.
- An, K.H., Jeong, S.Y., Hwang, H.R., Lee, Y.H., 2004. Enhanced sensitivity of a gas sensor incorporating single-walled carbon nanotube–polypyrrole nanocomposites. *Adv. Mater.* 16, 1005–1009.
- Ashraf, S.A., Chen, F., Too, C.O., Wallace, G.G., 1996. Bulk electropolymerization of alkylpyrroles. *Polymer* 37 (13), 2811–2819.
- Attia, M.F., Azib, T., Salmi, Z., Singh, A., Decorse, P., Battaglini, N., Lecoq, H., Omastová, M., Higazy, A.A., Elshafei, A.M., Hashem, M.M., Chehimi, M.M., 2013. One-step UV-induced modification of cellulose fabrics by polypyrrole/silver nanocomposite films. *J. Colloid Interface Sci.* 393, 130–137.
- Banchero, M., Ronchetti, S., Manna, L., 2013. Characterization of ketoprofen/methylmastová. In: Higazy, A.A., Elshafei, A.M., Hashem, M.M., Chehimi, M.M. (Eds.), *One-Step UVtry*, 2013, pp. 1–8.
- Esfarilzadeh, D., Razal, J.M., Moulton, S.E., Stewart, E.M., Wallace, G.G., 2013. Multifunctional conducting fibres with electrically controlled release of ciprofloxacin. *J. Control. Release* 169, 313–320.
- Ewesuedo, R., Ratain, M., 2003. *Principles of Cancer Therapeutics*. Springer, Secaucus, NJ.
- Faverolle, F., Attias, A.J., Bloch, B., 1998. Highly conducting and strongly adhering polypyrrole coating layers deposited on glass substrates by a chemical process. *Chem. Mater.* 10 (3), 740–752.
- Feng, X., Lv, F., Liu, L., Tang, H., Xing, C., Yang, Q., Wang, S., 2010. Conjugated polymer nanoparticles for drug delivery and imaging. *ACS Appl. Mater. Interfaces* 2 (8), 2429–2435.
- Ferrara, K.W., Borden, M.A., Zhang, H., 2009. Lipid-shelled vehicles: engineering for ultrasound molecular imaging and drug delivery. *Acc. Chem. Res.* 42 (7), 881–892.

- Fonner, J.M., Forciniti, L., Nguyen, H., Byrne, J.D., Kou, Y.F., Syeda-Nawaz, J., Schmidt, C.E., 2008. Biocompatibility implications of polypyrrole synthesis techniques. *Biomed. Mater.* 3 (3), 034124.
- Fujii, S., Aichi, A., Akamatsu, K., Nawafune, H., Nakamura, Y., 2007. One-step synthesis of polypyrrole-coated silver nanocomposite particles and their application as a coloured particulate emulsifier. *J. Mater. Chem.* 17 (36), 3777–3779.
- Gangopadhyay, R., De, A., 2000. Conducting polymer nanocomposites: a brief overview. *Chem. Mater.* 12 (3), 608–622.
- George, P.M., Lyckman, A.W., LaVan, D.A., Hegde, A., Leung, Y., Avasare, R., Testa, C., Alexander, P.M., Langer, R., Sur, M., 2005. Fabrication and biocompatibility of polypyrrole implants suitable for neural prosthetics. *Biomaterials* 26, 3511–3519.
- Ghadim, M.F., Imani, A., Farzi, G., 2014. Synthesis of PPy–silver nanocomposites via in situ oxidative polymerization. *J. Nanostruct. Chem.* 4, 101.
- Godwin, A., Bolina, K., Clochard, M., Dinand, E., Rankin, S., Simic, S., Brocchini, S., 2001. New strategies for polymer development in pharmaceutical science – a short review. *J. Pharm. Pharmacol.* 53 (9), 1175–1184.
- Haag, R., Kratz, F., 2006. Polymer therapeutics: concepts and applications. *Angew. Chem. Int. Edit.* 45, 1198–1215.
- Hatakeyama, W., Sanchez, T.J., Rowe, M.D., Serkova, N.J., Liberatore, M.W., Boyes, S. G., 2011. Synthesis of gadolinium nanoscale metal organic framework with hydrotropes: manipulation of particle size and magnetic resonance imaging capability. *ACS Appl. Mater. Interfaces* 3, 1502–1510.
- Hodko, D., Gamboa-Aldeco, M., Murphy, O.J., 2009. Photopolymerized silver-containing conducting polymer films: part I. An electronic conductivity and cyclic voltammetric investigation. *J. Solid State Electrochem.* 13, 1063–1075.
- Iroh, J., Su, W., 2002. Adhesion of electrochemically formed polypyrrole coatings to low carbon steel. *J. Appl. Polym. Sci.* 85 (13), 2757–2763.
- Jager, E.W.H., Inganäs, O., Lundström, I., 2001. Perpendicular actuation with individually controlled polymer microactuators. *Adv. Mater.* 13 (1), 76–79.
- Khan, I.U., Serra, C.A., Anton, N., Vandamme, T., 2013. Continuous-flow encapsulation of ketoprofen in copolymer microbeads via co-axial microfluidic device: influence of operating and material parameters on drug carrier properties. *Int. J. Pharm.* 441 (1–2), 809–817.
- Khemtong, C., Kessinger, C.W., Gao, J., 2009. Polymeric nanomedicine for cancer MR imaging and drug delivery. *Chem. Commun.* 24, 3497–3510.
- Kim, J., Piao, Y., Hyeon, Y., 2009. Multifunctional nanostructured materials for multimodal imaging, and simultaneous imaging and therapy. *Chem. Soc. Rev.* 38, 372–390.
- Kros, A., Nolte, R.J.M., Sommerdijk, N.A.J.M., 2002. Conducting polymers with confined dimensions: track-Etch membranes for amperometric biosensor applications. *Adv. Mater.* 14 (23), 1779–1782.
- Kros, A., Linhardt, J., Bowman, H., Tirrell, D., 2004. From giant vesicles to filaments and wires: templates for conducting polymers. *Adv. Mater.* 16, 723–727.
- Leclerc, M., 1999. Optical and electrochemical transducers based on functionalized conjugated polymers. *Adv. Mater.* 11 (18), 1491–1498.
- Lee, T.Y., Roper, T.M., Jonsson, E.S., Kudyakov, I., Viswanathan, K., Nason, C., 2003. The kinetics of vinyl acrylate photopolymerization. *Polymer* 44, 2859–2865.
- Li, C.M., Sun, C.Q., Chen, W., Pan, L., 2005. Electrochemical thin film deposition of polypyrrole on different substrates. *Surf. Coat. Technol.* 198, 474–477.
- Liong, M., Lu, J., Kovichich, M., Xia, T., Ruehm, S.G., Nel, A.E., Tamaroi, F., Zink, Jeffrey I., 2008. Multifunctional inorganic nanoparticles for imaging, targeting, and drug delivery. *ACS Nano* 5 (2), 889–896.
- Müllera, D., Rambo, C.R., Recouvreur, D.O.S., Porto, L.M., Barra, G.M.O., 2011. Chemical in situ polymerization of polypyrrole on bacterial cellulose nanofibers. *Synth. Met.* 161 (1–2), 106–111.
- Maity, S., Chatterjee, A., Singh, B., Singh, A.P., 2014. Polypyrrole based electro-conductive textiles for heat generation. *J. Text. Inst.* 105 (8), 887–893.
- Martins, C.R., do Almeida, Y.M., do Nascimento, G.C., de Azevedo, W.M., 2006. Metal nanoparticles incorporation during the photopolymerization of polypyrrole. *J. Mater. Sci.* 41, 7413–7418.
- Medina, S.H., El-Sayed, M.E.H., 2009. Dendrimers as carriers for delivery of chemotherapeutic agents. *Chem. Rev.* 109, 3141–3157.
- Morales, M.P., Bedard, M.F., Roca, A.G., de la Presa, P., Hernandez, A., Zhang, F., Zanella, M., Zahoor, A.A., Sukhorukov, G.B., del Mercato, L.L., Parak, W.J., 2009. Relaxation times of colloidal iron platinum in polymer matrixes. *J. Mater. Chem.* 19, 6381–6386.
- Morgan, T., Muddana, H., Altinoglu, E., Rouse, S., Tabaković, A., Tabouillot, T., Russin, T., Shanmugavelandy, S., Butler, P., Eklund, P., Yun, J., Kester, M., Adair, J., 2008. Encapsulation of organic molecules in calcium phosphate nanocomposite particles for intracellular imaging and drug delivery. *Nano Lett.* 12 (8), 4108–4115.
- Mura, P., Manderioli, A., Bramanti, G., Furlanetto, S., Pinzauti, S., 1995. Utilization of differential scanning calorimetry as a screening technique to determine the compatibility of ketoprofen with excipients. *Int. J. Pharm.* 119, 71–79.
- Nasongkla, N., Bey, E., Ren, J., Ai, H., Khemtong, C., Guthi, J., Chin, S., Sherry, A., Boothman, D., Gao, J., 2006. Multifunctional polymeric micelles as cancer-targeted, MRI-ultrasensitive drug delivery systems. *Nano Lett.* 11 (6), 2427–2430.
- Oh, W.K., Yoon, H., Jang, J., 2010. Size control of magnetic carbon nanoparticles for drug delivery. *Biomaterials* 31, 1342–1348.
- Petros, R.A., Ropp, P.A., DeSimone, J.M., 2008. Reductively labile PRINT particles for the delivery of doxorubicin to HeLa cells. *J. Am. Chem. Soc.* 130 (15), 5008–5009.
- Pope, M.R., Armes, S.P., Tarcha, P.J., 1996. Specific activity of polypyrrole nanoparticulate immunoreagents: Comparison of surface chemistry and immobilization options. *Bioconjugate Chem.* 7 (4), 436–444.
- Ramanathan, K., Bangar, M., Yun, M., Chen, W., Myung, N., Mulchandani, A., 2005. Bioaffinity sensing using biologically functionalized conducting-polymer nanowire. *J. Am. Chem. Soc.* 127, 496–497.
- Ranjha, N., Khan, I., Naseem, S., 2009. Encapsulation and characterization of flurbiprofen loaded poly( $\epsilon$ -caprolactone)-poly(vinylpyrrolidone) blend micropheres by solvent evaporation method. *J. Sol-Gel Sci. Technol.* 50, 281–289.
- Reece, D.A., Pringle, J.M., Ralph, S.F., Wallace, G.G., 2005. Autopolymerization of pyrrole in the presence of a Host/Guest calixarene. *Macromolecules* 38, 1616–1622.
- Sides, C., Martin, C., 2005. Nanostructured electrodes and the low-Temperature performance of Li-Ion batteries. *Adv. Mater.* 17, 125–128.
- Skotheim, T., Elsenbaumer, R., Reynolds, J., 1998. *Handbook of conducting polymers*, New York.
- Skotheim, T., 1986. *Handbook of conducting polymers*, New York.
- Soppimath, K., Aminabhavi, T., Kulkarni, A., Rudzinski, W., 2001. Biodegradable polymeric nanoparticles as drug delivery devices. *J. Control. Release* 70 (1–2), 1–20.
- Stupnisek-Lisac, E., Meticos-Hukovic, M., Lencic, D., Vorkapic-Furac, J., Berkovic, K., 2012. Structural investigation of N-arylpyrroles as iron corrosion inhibitors in hydrochloric acid. *Corrosion* 48, 924–930.
- Tarcha, P.J., Misun, D., Finley, D., Wong, M., Donovan, J.J., 1992. *Polymer Latexes: Preparation, Characterization and Applications*. Washington DC.
- Uva, M., Pasqui, D., Mencuccini, L., Fedi, S., Barbucci, R., 2014. Influence of alternating and static magnetic fields on drug release from hybrid hydrogels containing magnetic nanoparticles. *JBNB* 5, 116–127.
- Vicentini, D.S., Barra, G.M.O., Bertolino, J.R., Pires, A.T.N., 2007. Polyaniline/thermoplastic polyurethane blends: preparation and evaluation of electrical conductivity. *Eur. Polym. J.* 43, 4565–4572.
- Wadhwa, R., Lagenaur, C.F., Cui, X.T., 2006. Electrochemically controlled release of dexamethasone from conducting polymer polypyrrole coated electrode. *J. Control. Release* 110 (3), 531–541.
- Wang, H.-L., Fernandez, J.E., 1992. Conducting polymer blends: polypyrrole and poly(vinyl methyl ketone). *Macromolecules* 25, 6179–6184.
- Wang, X.D., Gu, X.S., Yuan, C.W., Chen, S.J., Zhang, P.Y., Zhang, T.Y., Yao, J., Chen, F., Chen, G., 2004. Evaluation of biocompatibility of polypyrrole in vitro and in vivo. *J. Biomed. Mater. Res.* 68A, 411–422.
- Wang, C., Xu, H., Liang, C., Liu, Y., Li, Z., Yang, G., Cheng, L., Li, Y., Liu, Z., 2013. Iron oxide @ polypyrrole nanoparticles as a multifunctional drug carrier for remotely controlled cancer therapy with synergistic antitumor effect. *ACS Nano* 7 (8), 6782–6795.
- White, A., Slade, R., 2004. Carbon papers with conductive polymer coatings for use in solid-state supercapacitors. *Macromol. Symp.* 212 (1), 275–280.
- Xu, C., Sun, J., Gao, L., 2011. Synthesis of novel hierarchical graphene/polypyrrole nanosheet composites and their superior electrochemical performance. *J. Mater. Chem.* 21, 11253–11258.
- Yang, X., Lu, Y., 2005. Preparation of polypyrrole-coated silver nanoparticles by one-step UV-induced polymerization. *Mater. Lett.* 59 (19), 2484–2487.
- Yang, K., Xu, H., Cheng, L., Sun, C., Wang, J., Liu, Z., 2012. In vitro and in vivo near-infrared photothermal therapy of cancer using polypyrrole organic nanoparticles. *Adv. Mater.* 24, 5586–5592.
- Ye, F.R., Ke, T.Y., Jeong, E.K., Wang, X.L., Sung, Y.G., Johnson, M., Lu, Z.R., 2006. Noninvasive visualization of in vivo drug delivery of poly(L-glutamic acid) using contrast-enhanced MRI. *Mol. Pharm.* 3, 507–515.
- Zong, B.Y., Ho, P., Wuang, S.C., 2015. Synthesis and multi-applications of conductive magnetic stable polypyrrole dispersion with phase-convertible characteristics. *Mater. Chem. Phys.* 149–150, 156–163.



*Conclusion and  
perspectives*

This PhD topic aimed to develop iodine-based nano-emulsions as new targeted X-ray contrast agents used for preclinical imaging. The main objectives of this subject are concluded in the following points: i) Generating nontoxic contrast agents with prolonged blood circulation ( $t_{1/2} = 8-9$  hours), so-called blood pool contrast agents (BPCAs). ii) Augmentation of their efficiency achieved by incorporating high concentrations of the radiopaque materials to deliver low amounts of the injected doses, providing low toxicity and improves the contrast enhancement of blood vessels, soft tissues and specific lesions. iii) As well as the efficiency enhanced either by active or passive targeting mechanisms to precisely deliver those nanoparticulate systems to the body site and avoiding the undesired bindings. iv) Engineering liver and spleen specific CAs *via* passive accumulation mechanism. v) Studying in depth the pharmacokinetics, the biodistribution and the toxicity profiles of different iodinated nano-emulsions in function of their physico-chemical parameters such as molecular structure, nanometric size, and surface charge. vi) Designing multifunctional nanoparticles in one-pot synthesis to afford the nanocomposite (NC) with many advantages like improving the hydrophilicity of the lipophilic loaded drugs, imparting the conductivity and the magnetic properties to the NCs rendering them excellent candidate for MRI applications.

Various iodinated molecules i.e. lipids and vitamins were simply synthesized and then formulated as a part of the nano-emulsions core by using spontaneous emulsification methods.

The first study investigated the significant impact of the chemical nature of the oily cores of the nano-emulsions on their biodistribution and pharmacokinetic. For that, two novel PEGylated nanodroplets nano-emulsions, 131 nm and 200 nm of sizes were formulated, their cores constituted of hexaiodinated monoglyceride (Capmul MCM C8) and hexaiodinated triglyceride (Castor oil) respectively. They were obtained at SOR = 60% for monoglyceride and SOR = 65% in case of castor oil and at constant SOWR = 40% for both emulsions. The X-ray attenuation values (HU) for both NEs revealed higher contrast than Fenestra® VC which determined by *in vitro* X-ray preclinical imaging, this is due to the high iodine concentration loaded in the nano-emulsions. The cytotoxicity MTT experiments were proceeded against HeLs cells, hepatocytes, and spleenocytes, showing negligible toxicity. The viscosity, the PH, and the osmolality of the formulations were adjusted to be suited to the biological medium before injection. They were intravenously injected to mice revealing remarkable contrast enhancement in heart indicated that

---

they circulated in the bloodstream and persisted up to half-lives of 8-9 hours. After blood elimination, they tended to passively accumulate mainly in liver in case of monoglycerides NEs and the castor oil is potentially accumulated into spleen. The mice scanned after 50 days and showed no contrast, meaning that they were entirely eliminated from the body. The *in vitro* results were coherent with *in vivo* data, because the uptaking of nano-emulsions including iodinated vitamin E were studied against two cell lines, hepatocytes (BNL-CL2) and macrophages (RAW264.7) displaying clear uptake of the monoglycerides to hepatocytes much higher than spleenocytes, however the triglycerides only uptaked by spleenocytes, in contrast the iodinated vitamin E showed high penetration only to the hepatocytes. The outcome of this study is that those new CAs can help us to deliver the molecules of interest very precisely to MPS systems like liver and spleen via passive targeting mechanism.

The second purpose of the thesis focused on varying the size of the NPs and follows the biodistribution and the toxicity because it has been approved in the literature that the size plays an important role in this process. We covalently grafted the free OH group of the vitamin D<sub>3</sub> with triiodobenzoic acid. The final iodine content in the triiodinated-cholecalciferol was around 43.6 wt.%, and the stable nano-emulsions were obtained only if mixing with Labrafac oil to increase the homogeneity with the surfactant (Cremophore ELP®) affording monodisperesed particles suited for *i.v.* injection. Two different nano-emulsions prepared, NE1 of a size 55 nm that composed of SOR = 40%, and cholecalciferol/Labrafac oil (OR = 66%) at SOWR = 40%. In parallel, the size of the NE2 was around 100 nm due to varying only the OR% ratio that became 33%. The iodine contents in both nano-emulsions were sufficient to provide high X-ray signals. *In vitro* experiments were carried out on two cell lines, namely hepatocytes (BNL-CL2) and macrophages (RAW264.7). Cell viability studies, cell uptake observations by confocal microscopy, and cellular uptake quantification by fluorimetry, displayed clear differences between the two formulations, as well as between the two types of cell lines. After *i.v.* injection of the two iodinated nano-emulsions in mice, CT scans provided the quantification of the pharmacokinetics and biodistributions. We finally approved that the size in the nano-emulsions has not a real impact on biodistributions, but has a strong influence on their toxicity, corresponding to the *in vitro* results.

---

The third objective was working on the surface chemistry of the nanoparticles which is a key factor impacting their biological pathways, because the external surface is the first part interact with the biological fluids. Due to many factors like NPs interaction with plasma proteins, surface ligand functionalization (active targeting) or even their uptake by RES system, all affect the *in vivo* journey of the delivered particles. Surface charge one of the physico-chemical parameters which has strong impact on the biodistribution and pharmacokinetics of the nanoparticulate systems. Considering the high lipophilicity properties of the oleic acid as oily core allows production efficient nano-emulsion coated with PEG molecules. But the resulted nano-emulsion presented viscous solution and high PDI properties led to be non-injectable suspension. Whereas, the iodinated oleate molecule obtained after modification of oleic acid tended to afford very interesting nano-emulsion with controlled size of around 60 nm and low PDI. The iodine content of the final CA solution was about 10%, which is too high to provide clear X-ray signals by CT scanner. Three different nano-emulsions were prepared i) neutral nanodroplets coated with PEG shell, ii) negative nano-emulsions by using poly(maleic anhydride-alt-1-octadecene) (PMAO C18) carboxylic polymer in the composition of the formulation and anchored carboxylic groups on the surface at the end of the process. iii) Fabrication of positive charge nanoemulsion through deposition of chitosan layer on the carboxylic groups. *In vitro* cellular uptake assessment performed on HeLa cells demonstrated low penetration of the neutral charge NEs, and the negative charge NEs were significantly internalized in the cells. However the positive chitosan NEs not interacted with the cells at all. The neutral and negative charge NEs were intravenously administrated to mice observing high contrast after injection immediately for both NEs and possessing prolonged blood circulation, but the difference in the charge affects largely on the toxicity.

The fourth study aimed to allowing successful functionalization to the nanodroplet nanoemulsion by using silica shell coated the droplet surface and bearing amino groups for grafting ligands. The idea came from the active targeting mechanism and how they facilitate the selectivity of the nanoparticles to specific receptors. The formulation was prepared thanks to sono-chemistry within the spontaneous emulsification process in the presence of the silane candidate (APTES). Various spectroscopic and microscopic techniques exploited to characterize the functionalized nanocapsules and quantify of the NH<sub>2</sub> groups. Next, they were grafted by a model fluorescent

---

ligand (activated coumarin blue dye) yielding 41% efficiency. This simple protocol opens the door to functionalize the lipid droplets that may exhibit a real advance regarding potential applications that need efficient decoration of droplets nano-emulsion with ligands.

The last goal of this topic was concerned to develop multifunction polymeric nanocomposites by one-step synthesis *via* in situ chemical oxidative process. Taking the benefit of the simple and the numerous methods to polymerize the conductive polypyrrole polymer in order to encapsulate hydrophobic drugs (ketoprofen model) and having magnetic particles as well. The designed nanoparticles is constituted of encapsulated ketoprofen and iron oxide NPs into the polypyrrole polymer and decorated by polyethylene glycol chains. The purpose of this study was i) encapsulate lipophilic drugs with very high concentrations reached to 95% and 98%, ii) improve the biocompatibility and the hydrophilicity of the components that resulted from the PEG molecules, iii) adding iron oxide NPs to the NCs making them potentially used for magnetic resonance imaging applications. Gathering both therapeutic agent and imaging agent in one particle is of great importance to follow up the treatment progression by the imaging modality what so-called theranostics.

To conclude, the successful one-step development of multifunctional nanocarrier containing drug, X-ray or MRI contrast agent and coated by neutral PEG shell, opens the door to utilize another PEGylated molecules ended by active groups such as OH, NH<sub>2</sub>, COOH, etc. This adds further advantage to the result nanocarrier to functionalize specific ligands and bioconjugate with such receptors, performing active targeting *in vivo*.

Finally, since these synthesized iodine-containing nano-emulsions provide significant contrast for X-ray micro-CT imaging. Taking the benefit of the passive accumulation of the CAs to liver and spleen, they can be exploited not only for diagnosis of both organs, but also for treatment through co-administration of such spleen or liver specific anticancer drug along with the CA in single platform. This helps to evaluate its therapeutic efficacy over the time.

Of particular interest is developing bimodal imaging agent for X-ray CT / fluorescence imaging. Nanoemulsions are promising candidate to achieve that, through loading of lipophilic fluorescent dye along with the iodinated molecules in the oily core of the nanodroplets.

---

One of our current research nowadays, for the first time, applying liver-targeted contrast agents as excellent imaging probe to study the evolution of the liver tumor in mice by using X-ray CT. We were able to inject the CA to tumor-bearing mice in order to follow the tumor evolution from zero time up to one month, demonstrating clear growth of the tumor over the time by X-ray scanner.



# *Appendices*

### Oral communications

- [Mohamed F. Attia](#), Nicolas Anton, and Thierry F. Vandamme. Contrast agents based on nano-emulsions for targeted Biomedical Imaging. *International Conference on Nanotechnology in Medicine (NANOMED)*. Manchester Conference Centre, **Manchester, UK**. November 23-25, **2015**.
- [Mohamed F. Attia](#), Nicolas Anton, and Thierry F. Vandamme. Nano-emulsions for Targeted Biomedical Imaging. “5th International Conference on Nanotek and Expo”. Hilton San Antonio Airport, San Antonio, **Texas, USA**. November 16-18, **2015**.
- [Mohamed F. Attia](#), Nicolas Anton, and Thierry F. Vandamme. Journée des doctorants en chimie. Novel contrast agents for targeted X-ray micro computed tomography. *Ecole doctorale Européenne*. **Strasbourg, France**. November 13, **2015**.
- [Mohamed F. Attia](#), Nicolas Anton, and Thierry F. Vandamme. Contrast agents for targeted biomedical imaging. *Journées du campus d’Illkirch (JCI)*, **Strasbourg, France** April 13-14, **2015**.

### Posters communications

- Nicolas Anton, [Mohamed Attia](#) and Thierry. F. Vandamme. Novel Contrast Agents for Targeted Biomedical Imaging. *The 43th Annual Meeting & Exposition of the Controlled Release Society. Washington State Convention Center Seattle*, **Washington, U.S.A.** July 17–20, **2016**.
- [Mohamed F. Attia](#), Nicolas Anton, and Thierry F. Vandamme. Novel iodinated contrast agents for Targeted Biomedical Imaging: Studying their biodistribution and pharmacokinetics by X-ray CT. *Clinical Nanomedicine and Targeted Medicine (CLINAM 9)*. **Basel, Switzerland**. June 26-29, **2016**.
- Nicolas ANTON, [Mohamed ATTIA](#), Xiang LI, Thierry VANDAMME. Nano-emulsions for biomedical imaging. *The 41st Annual Meeting & Exposition of the Controlled Release Society*. **Chicago, U.S.A.** July 13-16, **2014**.

### Original research articles

- Shukai Ding, [Mohamed F. Attia](#), Nicolas Anton, Justine wallyne, Christophe Serra and Thierry F. Vandamme. *Preparation of SPIONPs-encapsulated polymethyl-methacrylate nanoparticles by microfluidics as contrast agents for MR imaging*. (In progress)

- 
- [Attia, M. F.](#); Dieng, S.M.; Anton, N.; Collot, M.; Klymchenko, A.; Bouillot, C.; Serra, C.A.; Schmutz, M.; Er-Rafik, M.; Vandamme, T.F. **Surface modification of nano-emulsions post-formulation with lipophilic polymer: potential for droplet functionalization and impact on the biodistribution and pharmacokinetics on mice.** (In review)
  - [Mohamed F. Attia](#), Nicolas Antona, Ikram Ullah Khan, Christophe A. Serra, Nadia Messaddeq, Anshuman Jakhmola, Raffaele Vecchione, Thierry Vandamme. **One-step synthesis of iron oxide polypyrrole nanoparticles encapsulating ketoprofen as model of hydrophobic drug.** *International journal of pharmaceutics*. 508, 61-70, 2016.
  - [Mohamed F. Attia](#), Nicolas Anton, Roman Akasov, Manuela Chiper, Elena Markvicheva, Thierry F. Vandamme. **Biodistribution and toxicity of X-ray iodinated contrast agent in nano-emulsions in function of their size.** *Journal of Pharmaceutical Research*. 33(3), 603-614, 2015.
  - [Mohamed F. Attia](#), Nicolas Anton, Redouane Bouchaala, Pascal Didier, Youri Arntz, Nadia Messaddeq, Andrey S. Klymchenko, Yves Mély and Thierry F. Vandamme. **Functionalization of nano-emulsions with an amino-silica shell at the oil-water interface.** *RSC Advances journal*. Vol. 5, 74353–74361, 2015.
  - [Mohamed F. Attia](#), Nicolas Anton, Manuela Chiper, Roman Akasov, Halina Anton, Nadia Messaddeq, Sylvie Fournel, Andrey S. Klymchenko, Yves Mély, and Thierry F. Vandamme. **Biodistribution of X-Ray Iodinated Contrast Agent in Nano-Emulsions Is Controlled by the Chemical Nature of the Oily Core.** *ACS Nano journal*. Vol. 8, No. 10, 10537-10550, 2014.

#### Review articles

- [Mohamed F. Attia](#), Nicolas Anton, Justine Wallyn, Thierry F. Vandamme. Inorganic nanoparticles for targeted CT imaging. (In review)
- [Mohamed F. Attia](#), Nicolas Anton, Justine Wallyne, Ziad Omran and Thierry F. Vandamme. Targeting agents conjugated to carriers to increase drug sensitivity. (In review)

#### Book chapters

- Nicolas Anton, François Hallouard, [Mohamed F. Attia](#) and Thierry F. Vandamme. **Nano-emulsions for drug delivery and biomedical imaging.** (Accepted)



## Contrast agent based on nano-emulsion for targeted biomedical imaging

### Abstract

X-ray imaging agents are essential in combination with X-ray computed tomography to improve contrast enhancement aiming at providing complete visualization of blood vessels and giving structural and functional information on lesions allowing the detection of a tumor. As well as it is fundamental tool to discriminate between healthy cells and pathogens. We successfully limit the problems presented in commercial X-ray contrast agents like poor contrasting in Fenestra<sup>®</sup> VC associated with short blood circulation time and to avoid rapid renal elimination from the body as found in Xenetix (Iobitriol). We developed nontoxic and blood pool iodine-containing nano-emulsion contrast agents serving in preclinical X-ray  $\mu$ -CT imaging such as,  $\alpha$ -Tocopherol (vitamin E), Cholecalciferol (vitamin D<sub>3</sub>), Castor oil, Capmul MCMC8 oil and oleic acid. Those formulated nanoemulsions were prepared by low energy spontaneous emulsification technique with slight modification for each platform. They showed new specific features rendering them promising agents in *in vivo* experiments as improving the balance between the efficacy and the toxicity of targeted therapeutic interventions. We investigate the effect of size and the chemical composition of the nanoparticles on their biodistribution, pharmacokinetics and toxicity. They demonstrated that the chemical structures of the droplet's cores have significant role in targeting for example vitamin E was mainly accumulated in liver and castor oil formulation was passively accumulated in spleen explaining the proof-of-concept of EPR effect. On the other hand, two different platform sizes of Cholecalciferol molecule revealing that no real impact on the pharmacokinetics and biodistribution but presented remarkable effect on the toxicity. Of particular interest is studying the effect of the surface charge of nanoparticles on their biodistribution, this is why oleic acid nano-emulsion was selected to proceed this study by presence of amphiphile polymer poly(maleic anhydride-alt-1-octadecene) (PMAO). The *in vitro* results and *in vivo* evaluations were completely coherent approving that the neutral charged NPs are less toxic compared to the negatively charged ones that were highly uptaken in the cells causing stress to the cells and thereby affecting the toxicity. As a result they are different in biodistribution and pharmacokinetics. In this context, for the first time, we were able to functionalize the nano-emulsion droplets with ligand molecules by covalent bonds. Likewise we designed nano-droplets and coated by silica shell ended by amino groups and then followed by formation of amide bonds with grafting to dye ligand model (coumarin blue dye). The quantification of amino groups was performed by using spectroscopic and microscopic techniques, with a grafting efficiency as high as 41%. This process improves the targeting properties of such chemotherapeutic agents to the location of interest following active targeting mechanism (ligand receptor strategy). One of our achieved objectives was to engineer multifunctional polymer-based NPs encapsulating hydrophobic drug model as DDs and iron oxide NPs as a theranostic model. To conclude, novel contrast agents and delivering systems were synthesized with outstanding physico-chemical characteristics and suitable for *in vivo* medium with high efficacy and low toxicity.

**Keywords:** Contrast agents,  $\mu$ -CT imaging, passive targeting, active targeting, ligand surface functionalization, drug delivery, lipid, nano-emulsion, polymer, pharmacokinetics, biodistribution, toxicity.

### Résumé

Les agents d'imagerie aux rayons X sont essentiels en combinaison avec la tomodensitométrie pour améliorer le contraste de manière à permettre la visualisation complète des vaisseaux sanguins et de fournir l'information structurelle et fonctionnelle de lésions permettant la détection d'une tumeur. Ces outils fondamentaux permettent également de faire la distinction entre les cellules et les agents pathogènes sains. Les agents de contraste aux rayons X commercialisés sont limités dans leur succès dans le cas du Fenestra<sup>®</sup> VC par le temps court de circulation dans le sang et celui qui est lié à l'élimination rénale rapide du corps comme dans le cas du Xenetix<sup>®</sup> (Iobitriol). Nous avons développé des agents de contraste à base d' $\alpha$ -tocophérol (vitamine E), de Cholécalférol (vitamine D<sub>3</sub>), d'huile de ricin, de Capmul<sup>®</sup> MCMC8 et d'acide oléique qui sont tous dénués de toxicité, qui contiennent de l'iode sous forme de nano-émulsion et qui sont destinés à l'imagerie préclinique en  $\mu$ -CT. Ces nano-émulsions formulées ont été préparées par la technique d'émulsification spontanée de basse énergie avec une légère modification pour chaque composé iodé. Ces formulations ont montré de nouvelles caractéristiques spécifiques les rendant prometteuses dans des expérimentations *in vivo* avec une augmentation du rapport de la toxicité et de celui des interventions thérapeutiques visées. Nous avons étudié l'effet de la taille et de la composition chimique des systèmes nanoparticulaires sur leur biodistribution, leur pharmacocinétique et leur toxicité. Ces études ont permis de mettre en évidence l'importance de la constitution chimique des agents iodés utilisés avec par exemple la vectorisation du foie dans le cas de la vitamine E et une accumulation passive dans la rate pour les formulations à base d'huile de ricin, faisant la preuve-de-concept de l'effet EPR. D'autre part, des formulations identiques ayant deux tailles de gouttelettes différentes et contenant du cholécalférol indiquent qu'il n'y a pas de réels impacts sur la pharmacocinétique et la biodistribution mais présentaient une augmentation importante de la toxicité. Une autre étude a consisté à étudier l'effet des charges de surface des systèmes nanoparticulaires sur leur biodistribution, c'est pourquoi la nano-émulsion a été sélectionnée pour réaliser cette étude en présence d'un polymère amphiphile tel que le poly (anhydride-alt-1-octadecene maléique) (PMAO). Les résultats *in vitro* et les évaluations *in vivo* étaient tout à fait cohérents sachant que les systèmes nanoparticulaires neutres présentent moins de toxicité comparée à celles qui sont chargés négativement qui ont été capturés de manière plus importante dans les cellules causant un stress cellulaire et delà affectent la toxicité. Selon les résultats, elles présentent des biodistributions et des pharmacocinétiques différentes. Dans ce contexte, pour la première fois, nous avons pu fonctionnaliser les nanogouttes des nanoémulsions en fixant des ligands par des liaisons covalentes. Nous avons conçu des nanogouttes enrobées avec un enrobage de silice terminé par des groupements aminés et ainsi réalisé la formation de liaisons amides avec le greffage d'un colorant modèle (colorant bleu coumarine). La quantification des groupements aminés a été réalisée à l'aide de techniques spectroscopiques et microscopiques ainsi que la détermination de l'efficacité du greffage déterminé à 41%. Ce processus améliore les propriétés de vectorisation des agents chimio-thérapeutiques à la localisation qui présente un intérêt en suivant le mécanisme de vectorisation active (stratégie de réception du ligand). Un de nos objectifs réalisés était de concevoir des systèmes nanoparticulaires polymères multifonctionnels qui peuvent encapsuler des principes actifs hydrophobes modèles et des agents de contraste pour l'imagerie à rayons X, de sorte à construire des dispositifs théranostiques. Pour conclure, de nouveaux agents de contraste et des systèmes de délivrance ont été synthétisés ayant des caractéristiques physico-chimiques exceptionnelles et acceptables pour être utilisées *in vivo* avec une grande efficacité et une faible toxicité.

**Mots-clés:** agents de contraste, imagerie  $\mu$ -CT, vectorisation passive, vectorisation active, fonctionnalisation de surface avec ligand, libération de principe actif, lipide, nano-émulsion, polymère, pharmacocinétique, biodistribution, toxicité.